ABSTRACT

Title of Document: **WIND TUNNEL BLOCKAGE CORRECTIONS FOR PROPELLERS**

Ryan Elizabeth Fitzgerald,
Master of Science, 2007

Directed By: Dr. Jewel Barlow
Associate Professor
Department of Aerospace Engineering and
Director of Glenn L. Martin Wind Tunnel

Early in the twentieth century, Glauert developed a still widely used correction methodology for blockage in wind tunnels. Since then, several improvements to this method as well as new methods have been developed. For this thesis, powered propeller data was gathered in two wind tunnels of significantly different size. The Glauert correction, Hackett-Wilsden correction, and one of the newest corrections, developed by Sørensen and Mikkelsen, was applied to the data. Additionally, predictions of the pressure change in the tunnel due to the energy of the propeller were calculated.
The data, when corrected using each method, are essentially identical up to a thrust coefficient of approximately 1.2. Beyond this value, the correction data begins to diverge. The pressure predictions are inaccurate when compared to experimental data and it is suggested that this be an area for further study.

WIND TUNNEL BLOCKAGE CORRECTIONS FOR PROPELLERS

By

Ryan Elizabeth Fitzgerald

Thesis submitted to the Faculty of the Graduate School of the
University of Maryland, College Park, in partial fulfillment
of the requirements for the degree of
Masters of Science
2007

Advisory Committee:
Dr. Jewel Barlow, Chair
Dr. John D. Anderson, Jr.
Dr. Alan Winkelmann

ACKNOWLEDGEMENTS

I would like to sincerely thank my advisor, Dr. Jewel Barlow, for his continual support and guidance in this endeavor. Though I have never had the pleasure of having Dr. Barlow as a professor, I have, nevertheless, been a student of his since the moment he accepted me as his graduate student. His active participation in preparation and execution of our wind tunnel tests is greatly appreciated; certainly I could not have done either so successfully on my own. In addition to being a supportive and encouraging advisor, Dr. Barlow is a kind-hearted man who exercises patience in frustrating circumstances and thoughtfulness in difficult situations. Dr. Barlow, thank you for your investment in this project and in me, as a graduate student!

I would also like to thank Terrence Ghee, of the Naval Aerodynamics Test Facility. His expertise in wind tunnel testing prevented me from making easily-made mistakes. His interest and excitement in his field makes him a pleasure to work with. Terry, thank you for everything!

I would also like to thank the US Navy, particularly my supervisor, Steven Donaldson, and my team leader, Marjorie Draper-Donley, for the professional support of my studies and the US Navy Air Vehicle Engineering Department for the funding provided to enhance those studies. Additionally, thank you to Glenn L. Martin Wind Tunnel for financial support of this project.

TABLE OF CONTENTS

LIST OF SYMBOLS

A	propeller disk area, feet
B	span of wind tunnel, feet
C	tunnel cross sectional area, feet
C_D	coefficient of drag
C_p	coefficient of pressure, $(p - p_\infty)/ \frac{1}{2} \rho U_\infty^2$
C_{bp}	base-pressure coefficient, uncorrected
C_{bpc}	base-pressure coefficient, corrected
C_{pc}	coefficient of pressure, corrected
C_{pu}	coefficient of pressure, uncorrected
ΔC_p	C_p increment relative to empty tunnel value at same location
D	Propeller diameter used for non-dimensionalization, ft
ϵ	blockage factor
J	advance ratio
q	dynamic pressure, pounds/square foot
Δq	change in dynamic pressure, pounds/square foot
S	reference area of model, square feet
T	thrust, feet
U_∞	free stream velocity, feet/sec
Δu	induced velocity in direction of tunnel axis, feet/sec
V'	equivalent free airspeed, feet/sec
V	wind tunnel datum velocity, feet/sec
x/B	non-dimensionalized coordinate along test section, normalized by tunnel span
x/D	non-dimensionalized coordinate along test section, normalized by propeller diameter
y/B	non-dimensionalized coordinate spanwise in test section, normalized by tunnel span
z/B	non-dimensionalized coordinate vertically in test section, normalized by tunnel span
x, y, z	coordinates along tunnel axis, spanwise, and vertically, feet
x_o, y_o, z_o	coordinates of solid body singularity, feet
x_1, y_1, z_1	coordinates of wake-simulating singularity at propeller location
x_2, y_2, z_2	coordinates of wake-simulating singularity far downstream

Greek Symbols

α_1	factor used in Glauert correction= A/C
ρ	density, slug/ft^3
σ	strength of source/sink
τ_4	factor used in Glauert correction, $T / (\rho A V^2)$
Φ	velocity potential
Ψ	stream function

Subscripts

ss	solid body blockage source
sk	solid body blockage sink
ws	wake body blockage source
wk	wake body blockage sink

LIST OF FIGURES

LIST OF ABBREVIATIONS

ESC	Electronic Speed Control
GLMWT	Glenn L. Martin Wind Tunnel
NATF	Naval Aerodynamics Test Facility
RAE	Royal Aircraft Establishment
RC	Remote Control
RPM	Revolutions Per Minute
WOZ	Wind Off Zero

CHAPTER 1 INTRODUCTION AND CORRECTION METHODOLOGIES

1.1 Purpose

Past efforts have been made to generate a suitable wind tunnel blockage correction methodology using wind tunnel wall pressure signatures. Most notable among these efforts has been those of Glauert, Maskell, Ashill and Keating, Hensel, Hackett-Wilsden, and Sørensen and Mikkelsen. Most of the methods from these sources do not make use of measured wall pressures. The analyses used infer what tunnel wall pressure is expected to be, but they do not use measured values except for Ashill and Keating and Hackett-Wilsden. It was the purpose of this thesis to collect high quality powered propeller data for a wide range of size of propeller relative to the wind tunnel so that wall correction methods could be evaluated and, perhaps, extended. To this end, powered propeller data was collected in the Glenn L. Martin Wind Tunnel at the University of Maryland and at the Naval Aerodynamics Test Facility at Patuxent River Naval Air Station; the blockage of the first was negligible. The data resulting from this test was taken as baseline data. The blockage of the second was non-negligible and the Hackett-Wilsden and Sørensen and Mikkelsen correction methods and Glauert methods were employed, separately, to examine the calculated blockage correction and compare the methodologies. Critiques and conclusions are drawn about the quality of this correction methodology, particularly as it applies to the powered propeller model.

1.2 Glauert Correction

Glauert was among the first aerodynamicists to explore propeller blockage corrections. In one of his early publications, *The Elements of Aerofoil and Airscrew Theory*, Glauert presents the derivation of his correction. This correction determines an "equivalent free airspeed, V', corresponding to the tunnel datum velocity V, at which the airscrew, rotating with the same angular velocity as in the tunnel, would produce the same thrust and torque."[1] This equivalent free airspeed can be found by applying momentum theory to the case of an airscrew rotating in a wind tunnel. In a closed jet, under positive thrust conditions, the propeller slipstream accelerates and maintains a velocity greater than the wind tunnel datum velocity, V. Due to continuity, the same volume of air must pass just ahead of the propeller as passes just aft of the propeller. Therefore, it follows that the velocity outside the slipstream will be less than V. Due to its lower velocity, the static pressure outside of the slipstream has a higher static pressure. Using Bernoulli and taking into account a pressure discontinuity across the propeller disc, Glauert shows that the static pressure of the air within the slipstream must be identical to that outside of the slipstream. This higher static pressure "reacts back to the propeller so that it develops thrust that is greater than would be developed in an unrestricted flow of the same speed with the same propeller rotation rate and blade angle. Or it can also be said the thrust developed would be equal to that which would be expected at a lower V' in free air."[2] Glauert's correction follows:

$$V/V' = [1 - (\tau_4 \alpha_1 / (2*(1+2*\tau_4)^{1/2}))]^{-1} \quad (1)$$

Where V' is the equivalent free airspeed

V is the wind tunnel datum velocity

$$\tau_4 = T / (\rho A V^2) \quad (2)$$

T = thrust, lbs

ρ = density, lbs/ft^3

A = cross-sectional area of propeller, ft^2

V = wind tunnel datum velocity, ft/s

$$\alpha_1 = A/C \quad (3)$$

C = cross-sectional area of wind tunnel, ft^2

Glauert's results are shown in figure 1.

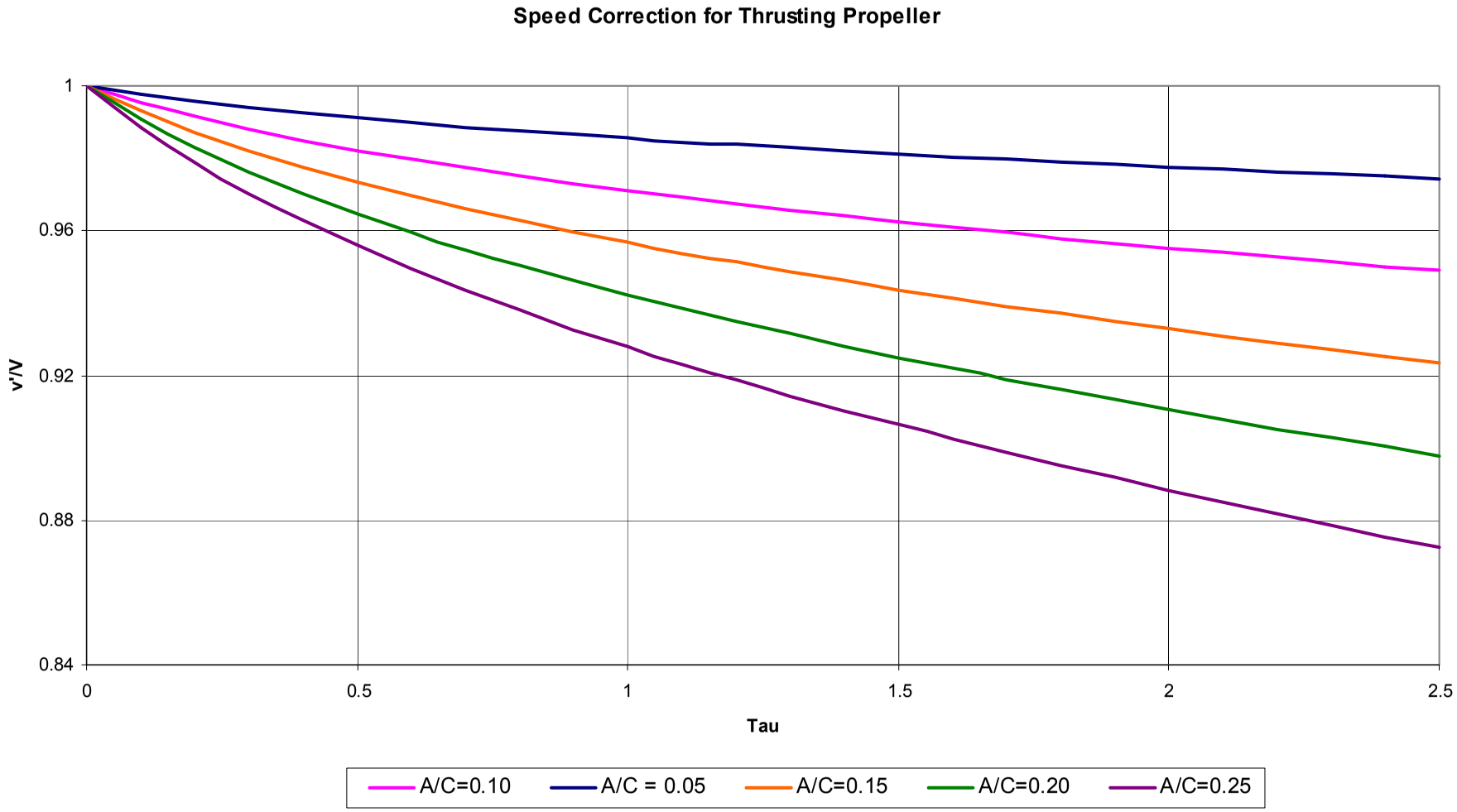

Figure 1. Speed correction for thrusting propeller. Glauert Correction.

It can be seen that V', the equivalent free airspeed, is less than V, the tunnel datum speed, for any positive thrust conditions. Negative values of thrust are not shown as the propeller is no longer in a positive thrust condition, resulting in the above slipstream model being invalidated. Glauert's correction is a classic and simple correction that is used in modern-day testing to correct for wind tunnel interference.

1.3 Maskell Correction

Maskell developed a theory of blockage correction for bluff bodies in closed wind tunnels based on an approximate relation describing the momentum balance in the flow outside the wake of a bluff body and two auxiliary equations. This theory was the first to address blockage corrections for non-streamline flow, including addressing flow over partially stalled shapes, such as wings. In both flow cases, streamline and non-streamline flow, the wake aft of a bluff body has a tendency towards axial symmetry. Additionally, through experiments conducted at the Royal Aircraft Establishment (RAE), it was shown that the wall constraint can be regarded as equivalent to a simple increase in velocity of the undisturbed stream. Using conservation of momentum over a control surface which is bound by the solid walls of the wind tunnel, the surface of the body, and the constant-pressure surface bounding the effective wake and two planes normal to the undisturbed velocity vector—one lying upstream of the body and the other located where the cross-sectional dimensions of the bubble are greatest--Maskell developed a relation for the drag coefficient based on base-pressure measurements of the model in the tunnel[3]. This relationship is affirmed by further RAE experiments. Maskell then uses

relationships describing the distortion of the wake due to wall constraint, combined with the drag coefficient relationship to generate a blockage correction expression. This expression is

$$\Delta q/q = \epsilon (C_D S/C) \quad (4)$$

Where ϵ is the blockage factor

C_D is the drag coefficient

S is the reference area of the model

C is the cross-sectional area of the wind tunnel

$\Delta q = q_c - q$ is the effective increase in dynamic pressure of the undisturbed stream due to constraint

The blockage factor is dependent on the base-pressure coefficient

$$\epsilon = 1/(\kappa_c^2 - 1) \quad (5)$$

Where $\kappa_c^2 = 1 - C_{pbc}$ and is found iteratively

C_{pbc} is the corrected base-pressure coefficient

"The factor ϵ is shown to range between a value of a little greater than 5/2 for axi-symmetric flow to a little less than unity for two-dimensional flow. But the variation from 5/2 is found to be small for aspect ratios in the range of 1 to 10.[3]" To show the validity of the theory, data was collected for the two extremes for which this theory purportedly is valid: axi-symmetric flow and two-dimensional flow. The results show

that "in the interval A=(1,10) the blockage factor lies roughly in the range $\epsilon = 5/2 \pm$ ¼. And the constant value $\epsilon=5/2$ leads to errors of only $\pm 0.1\Delta q$ at the extreme points of the range." "Therefore, the theory holds for almost all two-dimensional bluff-body flows, and for the wide range of three-dimensional flows for which the wake is closely axi-symmetric at the downstream plane." However, it must be noted that there is an important possible exception to this rule. An implied assumption in the theory is that the origin of the wake is independent of constraint. And so it may be necessary to exclude well-rounded bluff bodies for which a small change in pressure distribution might lead to a significant movement of the separation front. This also limits the confidence in correction of partially-separated flows such as those over stalled wings.

Maskell's method is not designed for, or easily adaptable to, application of powered propellers and therefore this methodology was not used for blockage corrections in this powered propeller test. Its description is included here because it uses a measured value of drag to infer an addition to blockage of the solid object in the test section. This is somewhat analogous to the Glauert propeller blockage approach.

1.4 Ashill and Keating Correction

Ashill and Keating, of the Royal Aircraft Establishment, build off of Maskell's work in development of their correction theory. As Maskell did, Ashill and Keating create a method of correction which does not require modeling of flows in the tunnel. This eliminates the difficulty of modeling separated and complicated flows. Instead, they use a 'two-component' method in which the knowledge of two components of flow

velocity at the outer boundary must be known. These components are that normal to the boundary and that in the stream wise direction. For low speed wind tunnels that have solid walls and thin wall boundary layers, the outer boundary of the 'two-component' method may be taken to coincide with the tunnel walls and the normal component assumed to be zero. Hence only the stream wise component is required for tunnels of this type, and this component can be inferred from static-pressure measurements at the walls[4].

Using the two-component method as described above, Ashill and Keating use equations for the perturbation potential in free air flow and that due to wall constraint. They show that the difference in perturbation potential between free air and the constrained condition is entirely due to wall interference. They use Bernoulli's equation to calculate the stream wise velocity increment from the corresponding increment in static pressure. This increment can be used to asses the difference in perturbation potential, and thus wall interference.

To test this theory, Ashill and Keating test two types of plates in the RAE tunnel; one of aspect ratio of one and the other with aspect ratio of three. They also test a combat-aircraft half-model. In each case, wall static-pressure taps were used to asses changes in pressure along the wall. Base-pressure coefficients are also measured. This data allows for calculation of corrected base-pressure coefficients and blockage effects[4]. The comparisons of Ashill and Keating's corrected base-pressure coefficients against Maskell's show good agreement with Maskell's theory for the flat plates. However, for the combat-aircraft half-model the blockage corrections are significantly smaller than those given by Maskell's method.

As with Maskell's method, Ashill and Keating's correction methodology was not developed with powered propeller testing and blockage effects in mind and its application to propeller corrections has not been reported in the literature. It could be adapted to propeller corrections using an approach analogous to the that used in this study with the Hackett-Wilsden method as discussed in later sections.

1.5 Hensel's Area-Ratio Method

Hensel's 1951 technical note reports a method for calculating the "ratios of the velocity increments at test bodies to those at the tunnel walls caused by the solid blocking of these bodies within the walls of a closed rectangular wind tunnel."[5] Hensel builds strongly off the methods in Thom[6] in which point and line sources are used to model bodies of revolution, finite straight wings, and finite swept wings.

1.6 Hackett-Wilsden Method

In 1979, Hackett, Wilsden, and Lilley released a NASA report[7] describing an expansion on Hensel's correction methodology. Instead of using doublets to create an "equivalent body" outline, they used sources and sinks to do so. In their experiments, they used models that produced varying blockage ratios; some models were small enough such that they were in a "free air" state. The largest models were up to 10% of the total tunnel cross section. During these experiments, they measured wall pressures along the center line of the tunnel walls or the roof, and on the floor when necessary. In cases where the body created lift, the mean of the roof and floor pressures was used. These pressures were then "used to determine source or sink

strengths, spans, and locations on the tunnel center line which define a body outline which 'is equivalent' to the test model and its wake.[7]"

The Hackett-Wilsden method employs an iterative scheme to resolve the pressure signatures into symmetric and anti-symmetric parts. The symmetric part represents the solid blockage while the anti-symmetric part reflects the wake blockage. Once these parts are resolved and the necessary parameters are deduced from the parts, a set of equations and a chart look-up technique is employed to obtain singularity strengths, spans, and locations. Using these parameters, a velocity increment $\Delta u/U_\infty$ is calculated. This is the velocity increment calculated from the singularity strengths, spans, and locations which represent an "equivalent body" outline; therefore, this is also the velocity increment caused by the model in the tunnel.

Using the calculated velocity increment, the Hackett-Wilsden method then employs one of two correction methods. For models with predominately attached flow, a global correction can be used. To do this, a source-panel model of the body may be generated and the three components of interference velocity at each panel center is calculated. These are then input to a source panel program together with the panel geometry and mainstream velocity to obtain corrected pressure coefficients.

For models that do not have predominately attached flow, a point-by-point correction equation is used to obtain corrected pressure coefficients. It follows:

$$C_{pc}(x) = [(C_{pu}(x) - 1) / (1 + (\Delta u(x)/U_\infty)^2)] + 1 \qquad (6)$$

To prove the validity of the point-by-point correction, in-tunnel pressure coefficients taken with a checkout sphere installed were corrected using the above equation and compared with a corresponding free-air calculation. The resulting error in C_p was 0.013, at most. Along the equator of the sphere, the error was less than 0.005 at all positions. Though the blockage ratio for this checkout sphere is not explicitly stated, results do state that bearing in mind the large size of the model used for checkout, it may be concluded that the above equation corrects measured pressures sufficiently accurately for most practical purposes.

For instance, for models occupying up to 13.7% of the tunnel cross section, the Hackett-Wilsden methodology produced results comparable with, and no less credible than, results from similar test in a large wind tunnel. This allows for more confidence in conducting blockage corrections for relatively large models. Additionally, for models with predominately attached flow, a global correction may be used successfully.

1.7 Sørensen and Mikkelsen Method

In 2002, Sørensen and Mikkelsen presented a method to model wind tunnel blockage with particular attention to the testing of wind turbines. This method is based on the axial momentum theory and employs a series of five equations to obtain a closed-form solution of the equations of the axial momentum theory[8]. It incorporates Hackett's method of using source and sink singularities to model the contraction or expansion of the wake of the propeller. Using the strength of the specific singularity which accurately models this expansion or contraction, Sørensen and Mikkelsen

introduce an explicit formula for calculating an intermediate value, ũ, such that the velocity through the propeller disc can be calculated directly and all five equations derived from the axial momentum theory can be solved simultaneously. This intermediate value is also used to obtain the correction synonymous to Glauert's correction formula. This explicit equation, as well as the five momentum equations, and the Sørensen and Mikkelsen's correction formula are shown below:

Intermediate Variable Equation

$$\tilde{u} = (\sigma (\beta\sigma^2 - 1)) / (\beta\sigma (3\sigma - 2) - 2\sigma + 1) \quad (7)$$

Where $\beta = S/C$ (8)

S = propeller cross sectional area, ft^2

C = tunnel cross sectional area, ft^2

σ = strength of singularity, S_1/S

S_1 = cross sectional area of slip stream far downstream, ft^2

$$\tilde{u} = u/V_o \quad (9)$$

u = velocity of air through propeller, ft/sec

V_o = wind tunnel datum velocity, ft/sec

Five Momentum Equations

$$\tilde{u}_1 = \sigma\tilde{u} \quad (10)$$

Where $\tilde{u}_1 = u_1/V_o$

u_1 = slip stream airspeed far downstream, ft/sec

$$\tilde{u}_2(1-\beta\sigma) = 1 - \beta u \quad (11)$$

Where $\tilde{u}_2 = u_2/V_o$

u_2 = airspeed outside of slip stream far downstream, ft/sec

$$C_T = \tilde{u}_1^2 - \tilde{u}_2^2 \quad (12)$$

Where C_T = coefficient of thrust

$$C_P = 1 - \tilde{u}_2^2 \quad (13)$$

Where C_P = coefficient of power

$$-\beta C_T - C_P = 2u_1\beta\sigma(\tilde{u}_1 - 1) - 2\tilde{u}_2(1-\beta\sigma)(1 - \tilde{u}_2) \quad (14)$$

Correction Formula

$$V'/V_o = \tilde{u} - (¼ * C_T / \tilde{u}) \quad (15)$$

Where V' is the equivalent free airspeed

1.8 Summary

Chapter 2 of this document describes the experimental set up of the test, description of test facilities, and the steps taken to reduce the data from the experiment. Chapter 3 gives detailed analysis steps and methodology that was used to first mathematically simulate the physical phenomena in the wind tunnel using the Hackett-Wilsden approach and to calculate the Hackett-Wilsden and Sørensen and Mikkelsen corrections. The Glauert correction is also presented. Pressure predictions using Glauert and Sorensen and Mikkelsen equations are explained. Discussion on the corrections and the pressure predictions is given. Finally, Chapter 4 offers conclusions and Chapter 5 proposes recommendations for future work.

It should be noted that for each propeller, nine successful conditions were desired for execution of analysis. These conditions, corresponding to three wind tunnel speeds, each at three RPM settings, would be simulated using sources and sinks. With nine runs for each of four propellers, a total of thirty-six potential runs could be analyzed and mathematically simulated. However, in some cases, high speed/high RPM runs were unable to be completed successfully; the motor overheated prior to the successful completion of the run. As many consistent conditions as possible were identified and analyzed.

In the body of this document, experimental data, calculations, corrections, and predictions are shown for only the 18”x8” propeller runs. Other propeller data, calculations, etc, are not shown unless specific attention is required in analysis or explanation. All data for the 14”x8”, 22”x8”, and 24”x8” propellers can be found in Appendix B.

CHAPTER 2 DESCRIPTION OF TEST

2.1 Description of Test Articles

2.1.1 Propellers

The Scimitar Series propellers used were acquired from Windsor Propeller Company. The four propellers had diameters of 14", 18", 22", and 24" and identical airfoil shapes. All propellers are fabricated from hard wood maple. A drill guide balance system, purchased from Windsor Propeller Company, was used to balance the propellers. The balance stand allowed tip-to-tip and chord-wise balancing, while the drill guides and bushings provided a guide though which to drill the centered mounting hole, using the included 3/8" drill bit. The figures in Appendix A show the experimental set up and articles.

2.1.2 Motor and Electronic Speed Controller

An AXI 5330-18 outrunner brushless motor was used to drive the propellers. The motor is 2.5" in diameter and 2" in length. The maximum power output is approximately 3.5 horsepower (2.6 kW). The propeller shaft was 12 mm in diameter (0.47") when purchased, but was turned down to 3/8" to mount the propellers. The motor is controlled by a Jeti Advance PLUS 90 Opto Control brushless electronic speed controller (ESC). The remote control receiver was connected to the ESC, allowing the ESC to be controlled by the remote control exterior to the tunnel.

2.1.3 Torquemeter

The torque cell used during testing was a 5330 Hollow Flange Reaction Torque Cell, manufactured by Interface. Its maximum capacity is 60 in-lb. The diameter of the torque cell is 2.5" in diameter and 2.125" in length.

2.1.4 Power Supply

The power supply was rented from Elgar Electronics. It requires 200/208 volt, three-phase input and is capable of providing 4 kW of power. The maximum voltage was set for 42.3 volts and the amperage was varied from 0 to 50 amps based on demand from the ESC, which was controlled by the remote control. This voltage and amperage limitation was introduced so as not to exceed the motor limitation of 2kW of power input.

2.1.5 Remote Control

A typical 2-channel RC car or plane remote control was used. It was bought from Tower Hobbies and included the necessary signal receiver. Modifications were made to channel 2, throttle. The throttle stick was replaced with a trim pot so that a power setting could be set and the knob released without the setting changing.

2.1.6 Stroboscope

A 1531A type stroboscope, manufactured by General Radio and owned by the Glenn L. Martin Wind Tunnel (GLMWT) at the University of Maryland was used to assess the RPM of the propellers during testing.

2.1.7 Pressure Board

A pressure board, owned by GLMWT, was mounted on the ceiling of each tunnel to record the pressure signature during running. In the GLMWT, two pressure boards were used. These boards, together, are 12' long and have 24 pressure ports spaced every 6" along the center of the board. It was mounted with bolts and sealed on the sides with aluminum tape. The pressure tubes were taped to the side of the tunnel and run through the floor to the sensing equipment.

One of these two boards was transported for use at NATF. The board used is 7' long and has 14 pressure ports spaced every 6" along the center of the board. It was also mounted on the center of the wind tunnel test section ceiling and sealed with aluminum tape. Pressure tubes were routed out of the ceiling of the wind tunnel.

2.2 Experimental Setup

2.2.1 Support Structure

The motor was attached to a bearing and housing which was fabricated to prevent cantilevered loads on the torque cell. This housing was attached to a horizontal support, which was then mounted to a vertical circular steel support. For use in the GLMWT, this support was approximately 4' tall which allowed for the propeller to be in the center of the tunnel. An aerodynamic fairing was used to cover the bottom two feet of this support to aid in drag reduction and shield the more bulky remote control receiver. This support was mounted to the tunnel balance.

The three power wires protruding from the motor were soldered to the three wires coming from the ESC. The ground lines from each were soldered together, and the

remaining wires were attached such that the motor turned in a counter clockwise direction (from the front). The wires protruding from the opposite side of the ESC were soldered to longer lengths of wire fed through the floor of the tunnel. These lines were attached to the output of the power source. The remote control receiver was plugged into the ribbon wire coming from the ESC.

A terminal block was mounted on the back of the housing. This was used to connect the torque cell output wires to the wires fed into the instrumentation, which were also fed through the floor of the tunnel.

The full support structure, as installed in the GLMWT and Naval Aerodynamic Test Facility (NATF) are show in figures in Appendix B.

2.3 Description of Wind Tunnels

2.3.1 Physical Characteristics

The Glen L. Martin Wind Tunnel at the University of Maryland and the Naval Aerodynamic Test Facility Subsonic Wind Tunnel at Patuxent River Naval Air Station, MD, were used for testing. The GLMWT is a closed-return tunnel and has a 7.75H x 11.04W foot test section that is 13.25 feet long. It has corner fillets and a turbulence intensity factor of 0.21%. The test section area is 85.04 sq feet. The speed range is from 3 ft/s to 337 ft/s.

The Naval Aerodynamic Test Facility Subsonic Wind Tunnel at Patuxent River Naval Air Station has a 4 x 4 foot test section that is 8 feet long. It has sharp corners and a turbulence intensity factor of 0.6%. The test section area is 16 sq feet. The speed range is from 40 ft/s to 200 ft/s.

For data reduction purposes, dimensions of the NATF tunnel were normalized in several ways. For modeling of solid blockage, calculation of velocity increment at the tunnel ceiling, and method of images calculations, wind tunnel dimensions were normalized by the test section span. The position of x/B = 0 was assigned to the center of the model length, slightly upstream of the mid-length position in the tunnel. Using this position, the beginning of the wind tunnel test section occurs at x/B = -0.85 and ends at x/B = 1.148. The height of the test section is z/B = -0.5 to z/B = 0.5 and the width of the test section is y/B = -0.5 to y/B = 0.5.

To provide comparison of measured pressure data, experimental results were normalized by propeller diameter, D. The x/D = 0 was assigned to the location of the propeller in this case.

2.3.2 Data Acquisition Hardware

GLMWT uses a six component yoke type balance. Pressure measurements are obtained using an Electronically Scanned Pressure system made by Pressure System Inc., coupled with pressure boards, as described previously. Up to 144 static pressure measurements may be obtained. Twenty-four measurements were obtained for this test.

NATF uses a three component platform type balance to measure side force, yaw force, and axial force. Pressure measurements are obtained using a system identical to that at GLMWT, the PSI 8400 Electronically Scanned Pressure system made by Pressure System, Inc., coupled with the pressure board mounted at NATF. The

pressure system is capable of taking up to 256 pressure port measurements. Fourteen pressure measurements were obtained for this test.

NATF has a Hitachi HV-D5W digital/analog broadcast quality camera that can be placed for optimum visualization. A Panasonic analog camera is also mounted looking into the test section from the top.

2.3.3 Data Acquisition Software

GLMWT uses a Hewlett Packard 743 VXI bus workstation. Customized data acquisition systems and graphical user interfaces may be designed using icon-driven software VEETEST.

The data acquisition software and systems at NATF are dependent on the data acquisition instrumentation used. For this experiment, a 486 PC Autonet system was used.

2.4 Test Execution

Three RPM settings were used for testing each propeller. These RPM settings corresponded to set current on the power supply. The power supply was set for a maximum voltage of 42.3 at all times due to the model motor limitations. Using the remote control, the amperage output was selected and set, a complete wind tunnel velocity sweep was conducted with stabilized points for data collection, and then the amperage was increased or decreased for a different RPM setting. Three amperage settings were used to obtain three RPM settings: low, medium, and high. Because the power required to rotate the propeller was greater at low wind tunnel speeds than high

speeds, current settings, particularly the high current setting, were set at a low tunnel speed. This guaranteed that the power required by the motor did not exceed the 2kW from the power supply as the tunnel speed varied and allowed for a full range of tunnel speeds to be tested at a consistent power setting.

The trim pot on the modified remote control proved to be very sensitive and it was difficult to set power supply current in a repetitive and efficient fashion. Additionally, the actual power required by the propeller, for a given setting of the remote trim pot, increased as wind tunnel speed decreased. Therefore, because of this sensitivity, the change in required power, and for efficiency, tests were conducted by setting a current setting with the remote control and varying wind tunnel speed. First, the current was set at the lowest setting possible with the wind tunnel velocity at a high speed. This is the minimum power required by each propeller in the sequence of testing and resulted in the low RPM setting. The low current setting was maintained as the tunnel velocity was decreased. While the setting on the remote control was never changed, the power required by the motor increased and the curent drawn from the power supply increased. The resulting current required at the low wind tunnel speed then defined the "low power setting" boundary. By knowing that the maximum power output of the power supply was limited to 2kW and the maximum voltage setting was 42.3 volts, limited by the motor, the maximum current available could be calculated as 50 amps. With this knowledge, an intermediate current setting was then deduced. The low wind tunnel speed was maintained as the intermediate current was applied, and thus the intermediate RPM setting was obtained. Time was given for the propeller to attain a constant RPM and then data was taken at the intermediate RPM

setting as the tunnel was increased in speed. Finally, because the power required was greatest at low wind tunnel speeds, the tunnel speed was brought back down to a low speed and the maximum current of 50amps was set. The tunnel was again increased in speed as data was taken for the high RPM setting.

To define the highest wind tunnel speed at which data was taken for each of the RPM settings, the tunnel speed was varied from the minimum speed to a speed such that the propeller no longer produced thrust. This was determined by noting the measured drag at each test point, subtracting the appropriate drag tare value, and determining if zero thrust condition had been reached. The tunnel speed was increased and test points taken until this occurred.

During each test point measurements of drag and torque was recorded. The pressure at each tap along the pressure board was also recorded.

Wind tunnel testing was first conducted at GLMWT. Testing was begun with a drag tare run. The 18" x 8" propeller was run first, and was followed by the 22" x 8" and 24" x 8" propellers. Next the 14" x 8" propeller was tested to complete the 8" pitch propeller group. The 18" x 8" propeller was re-tested to provide for examination of repeatability.

At NATF, the first run was also a drag tare run. Again, the 18" x 8" propeller was tested first. It was tested as a "check run" to compare against the GLMWT running. When the test was completed successfully and the data examined, it was determined that both the installation and data collected was sound. The experiment proceeded with the testing of the 14" x 8", 22" x 8" and 24" x 8" propellers. For the 24" x 8" propeller, a static thrust run was also completed. That is, the tunnel was left turned

off and data was collected as the current setting, and thus propeller RPM, was varied. This completed the testing of the 8" pitch propeller group.

Finally, for repeatability, the 18" x 8" propeller was re-tested. A static thrust run and windmill run was included. The final run was the drag tare run with the motor spinning. This concluded the experiment.

2.5 Data Reduction

2.5.1 Wind Off Zero

Wind off zero (WOZ) points were taken before each run at GLMWT. The data acquisition software at GLMWT corrected for the WOZ points automatically. The data that was obtained by the experimenter included this correction.

Wind off zero points were taken before and after each run at NATF. Drag values varied insignificantly between the WOZ points before and after the respective run. To correct for the WOZ drag values, the first and last points were averaged and subsequently subtracted from each drag value collected during the run.

In some cases, there was a significant difference in torque values between the WOZ points before and after the each run. A "step-methodology" was used. That is, an equal step was added or subtracted to the first WOZ torque value at each point such that the last WOZ torque value was reached by the end of the run. This value was subsequently subtracted from each torque value collected during the run. This provided for an equal change in WOZ torque value as the run progressed.

2.5.2 Drag Tare

A drag tares was taken at both GLMWT and NATF. At both tunnels, these were taken without the motor running at a range of tunnel dynamic pressures. A drag tare run was also taken at NATF with the motor running to determine if there was an appreciable difference in drag due to the spin of the motor. As shown in the first figure in Appendix B, there was no appreciable difference in these drag tares. The drag tares were corrected for WOZ points as described above.

2.5.3 Pressure Signatures

The pressure signature measurements required reduction in order to use them with the wall interference correction methodology. The raw data received from NATF was the difference between the pressure measured at the pressure board tap and the reference pressure. The reference pressure was the barometric pressure of the day. This data is divided by the dynamic pressure in the tunnel to obtain the coefficients of pressure at the ceiling along the length of the tunnel.

For comparison to the simulated model and wake, the pressure signatures were converted to velocity increments. To do so, the pressure signature was measured at a range of dynamic pressures without the model present in the wind tunnel. These were converted to coefficients of pressure, as stated above. Then, the difference between the coefficients of pressure with the model and without the model, at approximately the same dynamic pressure, was calculated. Finally, this was turned into a velocity increment using Wilsden/Hackett's equation[7] as below:

$$\Delta u / U_\infty = (1-\Delta C_p)^{1/2} - 1 \quad (16)$$

This quantity is used later for comparison purposes.

2.6 Data Uncertainty

Uncertainty exists in all instrumentation used in the test set up. At GLMWT, the uncertainty in the pressure data is ±0.0015 psi and the uncertainty in the drag data, measured by the yoke balance, is ±0.015 pounds. More information on the GLMWT and its data acquisition system can be found at http://windvane.umd.edu/index.php.

At NATF, the uncertainty in the pressure data is ±0.1% of the full scale value and the uncertainty drag data is ±0.818% of the full scale value, corresponding to ±0.49 pounds. The uncertainty in the tunnel velocity is 0.75% of the full scale value, corresponding to 1.5 ft/s. More information on the NATF tunnel and its data acquisition equipment can be found at http://sata.tamu.edu/members/tunnels/138.html and in reference 9 and 10.

The torquemeter mounted on the model also has uncertainty. According to the manufacturer's data sheet, the uncertainty in torque measurements is 0.25% full scale, corresponding to 0.15 lb-in.

CHAPTER 3 MATHEMATICAL SIMULATION OF PHYSICAL PHENOMENA

3.1 Model and Wake Simulation

3.1.1 Solid Body Simulation

The volume of the model, as mounted at NATF, was simulated by a three-dimensional source and sink pair. The pair was placed on the centerline of the tunnel, as the model was. This results in the position of any source or sink $[x_o, y_o, z_o]$ equal to $[x_o, 0, 0]$, where x_o gives the position of the singularity along the test length of the test section. The source and sink pair is superimposed with a one-dimensional uniform velocity, which simulates the free stream flow inside the wind tunnel. Derived from Katz and Plotkin[11], the velocity potential for a free stream flow superimposed with a source of strength σ_{ss} at position $[x,y,z] = [-x_o,0,0]$ and a sink of strength σ_{sk} at position $[x,y,z] = [x_o,0,0]$ is

$$\Phi(x,y,z) = U_\infty x - \sigma_{ss} / \{(4\pi)[(x+x_o)^2+(y)^2+(z_o)]^{1/2}\}$$
$$+ \sigma_{sk} / \{(4\pi)[(x-x_o)^2+(y)^2+(z)]^{1/2}\} \quad (17)$$

The stream function, with cylindrical coordinates of the source and sink of $[x,r] = [-x_o,0]$ and $[x,r] = [x_o,0]$, respectively, is

$$\Psi(x,r) = U_\infty r - \sigma_{ss} / \{2[(x+x_o)^2+(r)^2]^{1/2}\}$$
$$\sigma_{sk} / \{2[(x-x_o)^2+(r)^2]^{1/2}\} \quad (18)$$

The strengths and spacing of the pair was then adjusted such that a stagnation streamline, representative of the model volume, was formed. The stagnation streamline is located at the x, and r locations such that $\Psi=0$.

3.1.2 Wake Simulation

To simulate the wake of the propeller, a source or sink placed at the propeller location is superimposed with uniform flow and the solid body source and sink pair. The determination of which singularity sign for superimposition with uniform flow at the propeller location depends on the speed of the wind tunnel, and the advance ratio, and thus the thrust being produced by the propeller. The propeller itself produces drag for advance ratios above a critical value determined by the pitch of the propeller. If the propeller is unpowered, the advance ratio will be above this critical value and thrust will be produced. Therefore, at a low RPM settings and low wind tunnel speed, the propeller produces drag, rather than thrust, and the wake is decelerated when the net streamwise force on the propeller and nacelle is in the drag direction. In this case, it is appropriate to simulate the wake as a source. At a mid power setting and low wind tunnel speed, the wake is faster than the surrounding air. A sink accurately simulates the wake. At a high power setting, the wake is speeded up the most and again a sink simulates the wake accurately.

By the momentum theorem, the wake will be, on average, faster than the free stream if the propeller is producing a net thrust and the wake will, on average, be slower than the free stream if the propeller is producing drag. With the addition of a source or

sink placed at the propeller location for wake simulation purposes, a singularity of opposite sign and equal strength must be placed at infinity downstream.

The velocity potential for a point source of strength σ_{ws}, located at $[x,y,z] = [-x_o,0,0]$ is

$$\Phi(x,y,z) = - \sigma_{ws} / \{(4\pi)[(x+x_o)^2+(y)^2+(z)]^{1/2}\} \quad (19)$$

The velocity potential for a point sink of strength σ_{wk}, located at $[x,y,z] = [-x_o,0,0]$ is

$$\Phi(x,y,z) = \sigma_{wk} / \{(4\pi)[(x+x_o)^2+(y)^2+(z)^2]^{1/2}\} \quad (20)$$

The corresponding stream function, with source and sink locations of $[x,r] = [-x_o,0]$ and $[x,r] = [x_o,0]$, respectively, is

$$\Psi(x,r) = -\sigma_{ws} (x+x_o) / \{2[(x-x_o)^2 + r^2]^{1/2}\} \quad (21)$$

$$\Psi(x,r) = \sigma_{wk} (x-x_o) / \{2[(x-x_o)^2 + r^2]^{1/2}\} \quad (22)$$

It should be noted that the stream function is expressed in cylindrical coordinates due to the model being simulated as a body of revolution and thus being axi-symmetric. The stream function, in three-dimensions, only applies to axisymmetric flow; it is an approximate description of axi-symmetric body in a rectangular wind tunnel.

3.2 Velocity Increment Calculation

The velocity increment induced by the above superimposition of uniform flow, solid body source and sink pair, and wake source and sink pair was calculated next. The velocity induced by the singularities was derived from the velocity potential and stream function of the combination of the singularities, as given previously. The induced velocity equations due to the singularities follow.

Induced velocity for a point source at $[x,y,z] = [x_o,0,0]$

$$\Delta u(x,y,z) = \sigma(x-x_o) / \{(4\pi)[(x-x_o)^2+(y)^2+(z)^2]^{3/2}\} \quad (23)$$

Induced velocity for a point sink at $[x,y,z] = [x_o,0,0]$

$$\Delta u(x,y,z) = - \sigma(x-x_o) / \{(4\pi)[(x-x_o)^2+(y)^2+(z)^2]^{3/2}\} \quad (24)$$

Induced velocity for uniform flow

$$\Delta u(x,y,z) = U_\infty \quad (25)$$

Since the model was mounted in the center of the tunnel, all singularities lie at the center of the tunnel. Using a subscript of ss to indicate a solid body source, a subscript of sk to indicate a solid body sink, a subscript of ws to indicate a wake blockage source, a subscript of wk to indicate a wake blockage sink, a subscript of 0 to indicate the coordinates of the solid body singularities , a subscript of 1 to indicate

the coordinates of the wake singularity at the propeller, and a subscript of 2 to indicate the coordinates of the wake singularity placed far downstream, the total induced velocity for uniform flow superimposed with a solid body source and sink pair, a point source located at the at the propeller, and a point sink far downstream is

$$\Delta u(x,y,z) = U_\infty + \sigma_{ss}(x+x_o) / \{(4\pi)[(x+x_o)^2+(y)^2+(z)^2]^{3/2}\} -$$
$$\sigma_{sk}(x-x_o) / \{(4\pi)[(x-x_o)^2+(y)^2+(z)^2]^{3/2}\} +$$
$$\sigma_{ws}(x-x_{o1}) / \{(4\pi)[(x-x_{o1})^2+(y)^2+(z)^2]^{3/2}\} -$$
$$\sigma_{wk}(x-x_{o2}) / \{(4\pi)[(x-x_{o2})^2+(y)^2+(z)^2]^{3/2}\} \quad (26)$$

The total induced velocity for uniform flow superimposed with a solid body source and sink pair, a point sink located at the at the propeller, and a point source far downstream is

$$\Delta u(x,y,z) = U_\infty + \sigma_{ss}(x+x_o) / \{(4\pi)[(x+x_o)^2+(y)^2+(z)^2]^{3/2}\} -$$
$$\sigma_{sk}(x-x_o) / \{(4\pi)[(x-x_o)^2+(y)^2+(z)^2]^{3/2}\} -$$
$$\sigma_{wk}(x-x_{o1}) / \{(4\pi)[(x-x_{o1})^2+(y)^2+(z)^2]^{3/2}\} +$$
$$\sigma_{ws}(x-x_{o2}) / \{(4\pi)[(x-x_{o2})^2+(y)^2+(z)^2]^{3/2}\} \quad (27)$$

In this test, the pressure signature was taken along the ceiling of the wind tunnel at the center span. The coordinates which describe the pressure taps depend both on the pressure board's location at the ceiling as well as the location of the pressure taps along the wind tunnel test section length. The ceiling location and this "length" location were both normalized by the wind tunnel span. This results in the first tap on the pressure board being located at [x/B, y/B, z/B] = [-0.6914, 0, 0.5]. The last tap is located at [x/B, y/B, z/B] = [0.9336, 0, 0.5]. Pressure taps are separated by x/B = 0.0125, with consistent y/B and z/B coordinates. These are the locations at which the induced velocity must be calculated. These values were substituted into the above appropriate induced velocity equation and the equation was further divided by the given uniform flow speed and square of the tunnel span to non-dimensionalize the induced velocity equations. The velocity increment term, $\Delta u / U_\infty$, resulted.

The full non-dimensional equation for the total induced velocity for uniform flow superimposed with a solid body source and sink pair, a point source located at the at the propeller, and a point sink far downstream is

$$\begin{aligned}\Delta u/ U_\infty = 1 &+ \sigma_{ss}(x/B+x_o/B) / \{(4\pi^* U_\infty{*}B^2)[(x/B+x_o/B)^2 + (z/B)^2]^{3/2}\} - \\ &\sigma_{sk}(x/B-x_o/B) / \{(4\pi^* U_\infty{*}B^2)[(x/B-x_o/B)^2 + (z/B)^2]^{3/2}\} + \\ &\sigma_{ws}(x/B-x_{o1}/B) / \{(4\pi^* U_\infty{*}B^2)[(x/B-x_{o1}/B)^2 + (z/B)^2]^{3/2}\} - \\ &\sigma_{wk}(x/B-x_{o2}/B) / \{(4\pi^* U_\infty{*}B^2)[(x/B-x_{o2}/B)^2 + (z/B)^2]^{3/2}\} \qquad (28)\end{aligned}$$

The full non-dimensional equation for the total induced velocity for uniform flow superimposed with a solid body source and sink pair, a point sink located at the at the propeller, and a point source far downstream is

$$\Delta u/ U_\infty = 1 + \sigma_{ss}(x/B+x_o/B) / \{(4\pi^* U_\infty^* B^2)[(x/B+x_o/B)^2 + (z/B)^2]^{3/2}\} -$$

$$\sigma_{sk}(x/B-x_o/B) / \{(4\pi^* U_\infty^* B^2)[(x/B-x_o/B)^2 + (z/B)^2]^{3/2}\} -$$

$$\sigma_{wk}(x/B-x_{o1}/B) / \{(4\pi^* U_\infty^* B^2)[(x/B-x_{o1}/B)^2 + (z/B)^2]^{3/2}\} +$$

$$\sigma_{ws}(x/B-x_{o2}/B) / \{(4\pi^* U_\infty^* B^2)[(x/B-x_{o2}/B)^2 + (z/B)^2]^{3/2}\} \quad (29)$$

To completely and correctly calculate the induced velocity due to the wake of the propeller, the method of images must be used to simulate the solid boundaries of the wind tunnel walls. This is presented next.

3.3 Method of Images

The method of images is a technique used to simulate solid boundaries, such as wind tunnel walls, around a model and to calculate wall interference velocities and blockage effects. In this case, the wake of the propeller is simulated with either a point source or point sink, depending on the working state of the propeller. Using this singularity as a starting point, a set of opposing singularities are placed at an appropriate distance from the original singularity to produce a zero streamline at the location of the solid boundaries, successfully simulating the wind tunnel walls.

However, these additional singularities introduce effects that must be cancelled by placing another set of opposing singularities at twice the distance of the first. These new singularities also produce additional effects and another set of opposing singularities are added to the system. This obviously becomes an infinite process; point sources and sinks are alternately placed at appropriate distances from the original singularity to simulate the solid boundaries and while producing zero net effect due to these singularities. The same process must be followed to simulate wind tunnel walls at the singularity of opposite strength far downstream. In theory, sources and sinks should be placed in an infinite grid. In this case, 22,500 singularities were placed around the original singularity.

Once these singularities are placed and the image system is established, its effect on the model is the same as that of the boundary it represents[2]. Following this establishment, the velocity increment produced by each singularity, including those that simulate the solid body and wake, is calculated. These increments are summed, plotted over the length of the test section, and compared to that calculated from the measured pressure signature. These increments match when the model and wake has been accurately simulated with the source and sink singularities. Since the model is accurately simulated by the solid body source and sink pair, the source and sink pair that simulate the wake is the only singularity strength that is adjusted such that the velocity increments match.

3.4 Deduction of Singularity Strength

With the singularities which correctly simulate solid blockage, wake blockage singularity strength and sign must be found such that the velocity increment calculated using these singularities matches the velocity increment derived from pressure measurements at the wall. As aforementioned, the sign of the upstream singularity is easily deduced from examining the velocity increment trend. If the increment decreases over the length of the test section, the propeller is simulated by a sink. If the increment increases over the length of the test section, the propeller is simulated by a source. As expected, the magnitude of the singularity increases with an increase in magnitude of the velocity increment.

For each data run that was selected for analysis, singularity strengths were found using trial and error. Initially, the mathematically simulated velocity increments matched well in shape but not in absolute value. As is described in Hackett, et al.,

> On the majority of occasions, the test section will be too short in relation to the model and its wake for the asymptote to be well established at both ends. Designated points may therefore be selected at the upstream and downstream ends of the signature. On the first attempt to match the curve, these points are assumed to be asymptotes. Miss-distances are next determined, between the designated points and the fitted curve and the curve is adjusted so that the fitted cure intersects the designated points. This correction is made just once and is not iterated.[5]

Though the downstream velocity increments appear to establish asymptotic behavior, the upstream asymptote is not realized and determination of this "miss distance" was

necessary. Once it was established for each curve, the velocity increment calculated from the singularities matched the experimentally velocity increments very well.

For purposes of demonstration, data will be presented for the 18" x 8" propeller experimentation. All other data may be found in Appendix B. Figures 2 through 9 show the velocity increment calculated using the singularities to simulate solid body blockage and wake blockage as compared to experimental data. Each figure shows the components which contribute to the total velocity increment at the ceiling of the tunnel, however, the miss distance is not applied to the components. The miss distance is applied to the total velocity increment. It should be noted that the velocity increment caused by the solid body blockage was virtually zero and therefore is not shown. During the 18" x 8" propeller testing, there was no high speed, high RPM run that was successfully completed at NATF. The motor overheated on each attempt; there are eight figures below showing all other speed and RPM runs selected for analysis.

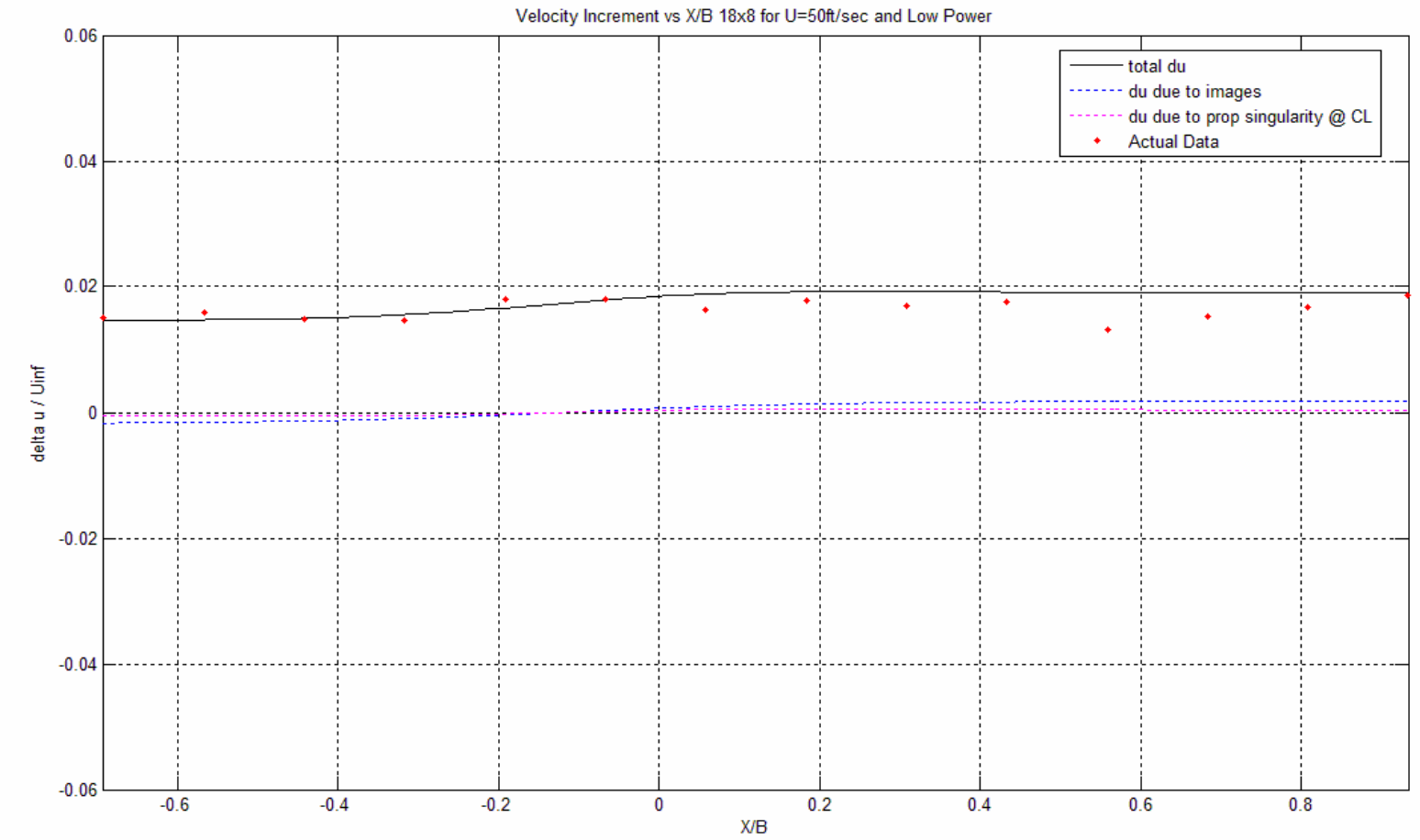

Figure 2. Velocity increment calculated from mathematical simulation model and propeller plotted against experimentally produced velocity increment for 18”x8” propeller rotating at low RPM and wind tunnel speed of 50ft/s.

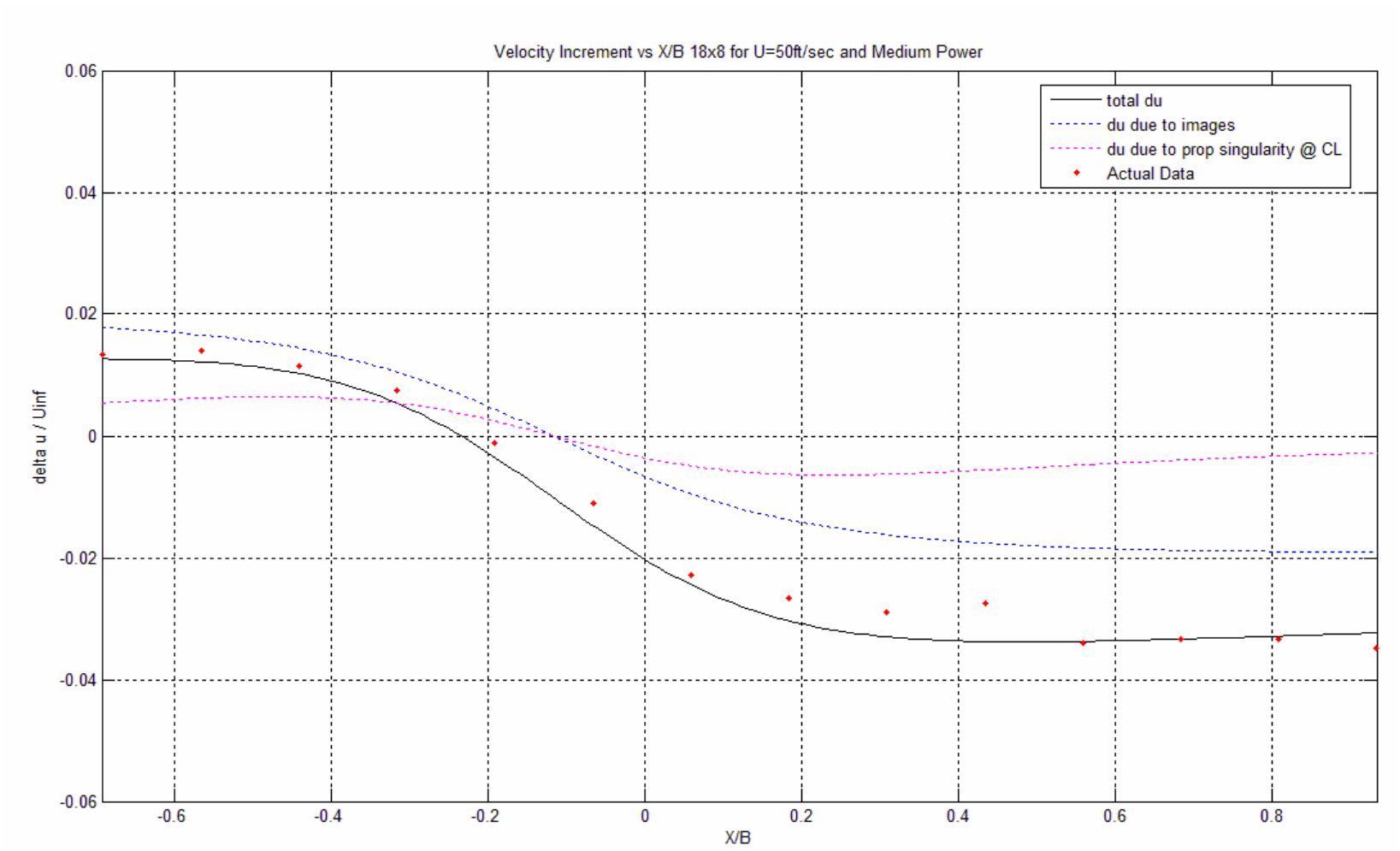

Figure 3. Velocity increment calculated from mathematical simulation model and propeller plotted against experimentally produced velocity increment for 18”x8” propeller rotating at medium RPM and wind tunnel speed of 50ft/s.

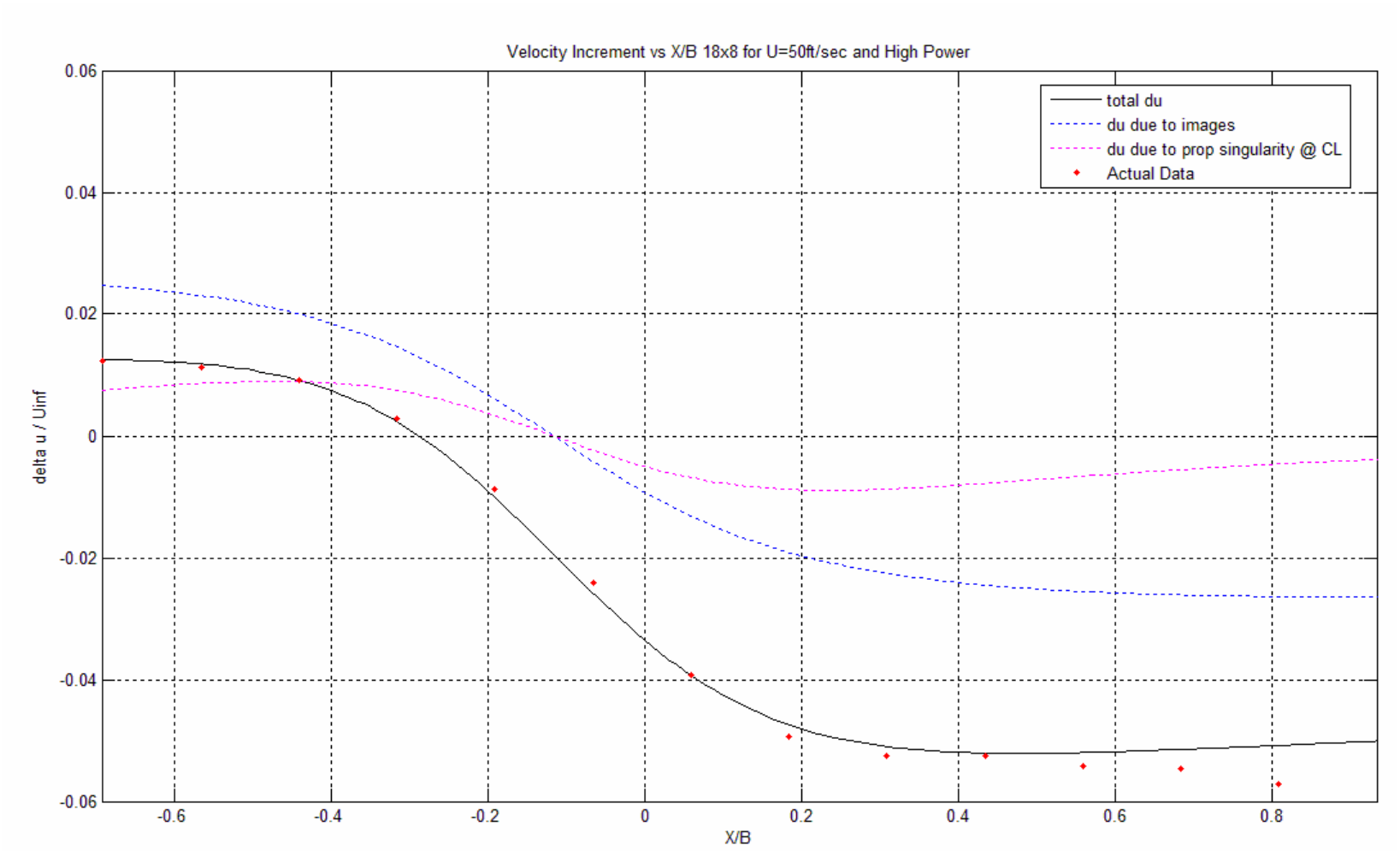

Figure 4. Velocity increment calculated from mathematical simulation model and propeller plotted against experimentally produced velocity increment for 18”x8” propeller rotating at high RPM and wind tunnel speed of 50ft/s.

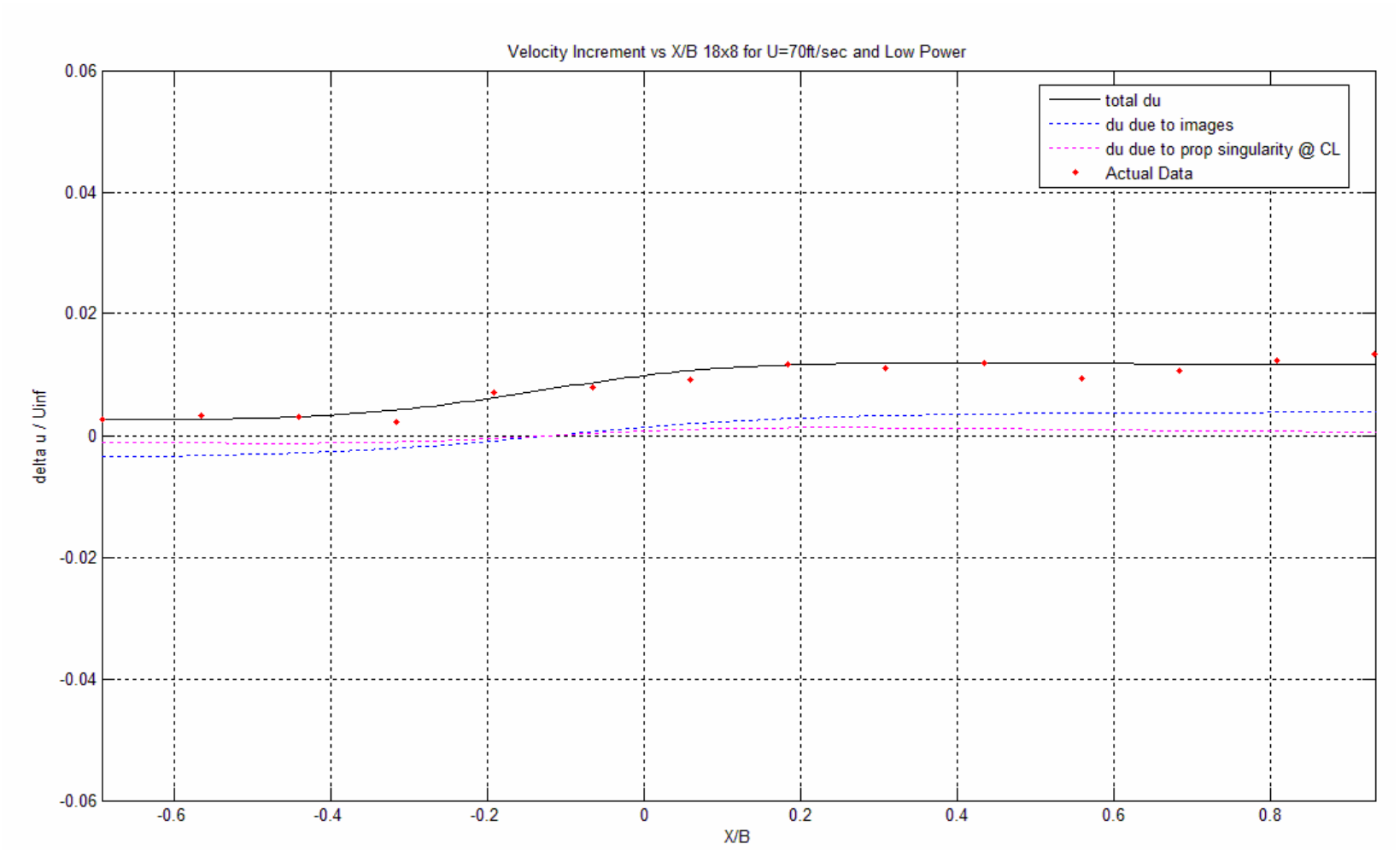

Figure 5. Velocity increment calculated from mathematical simulation model and propeller plotted against experimentally produced velocity increment for 18"x8" propeller rotating at low RPM and wind tunnel speed of 70ft/s.

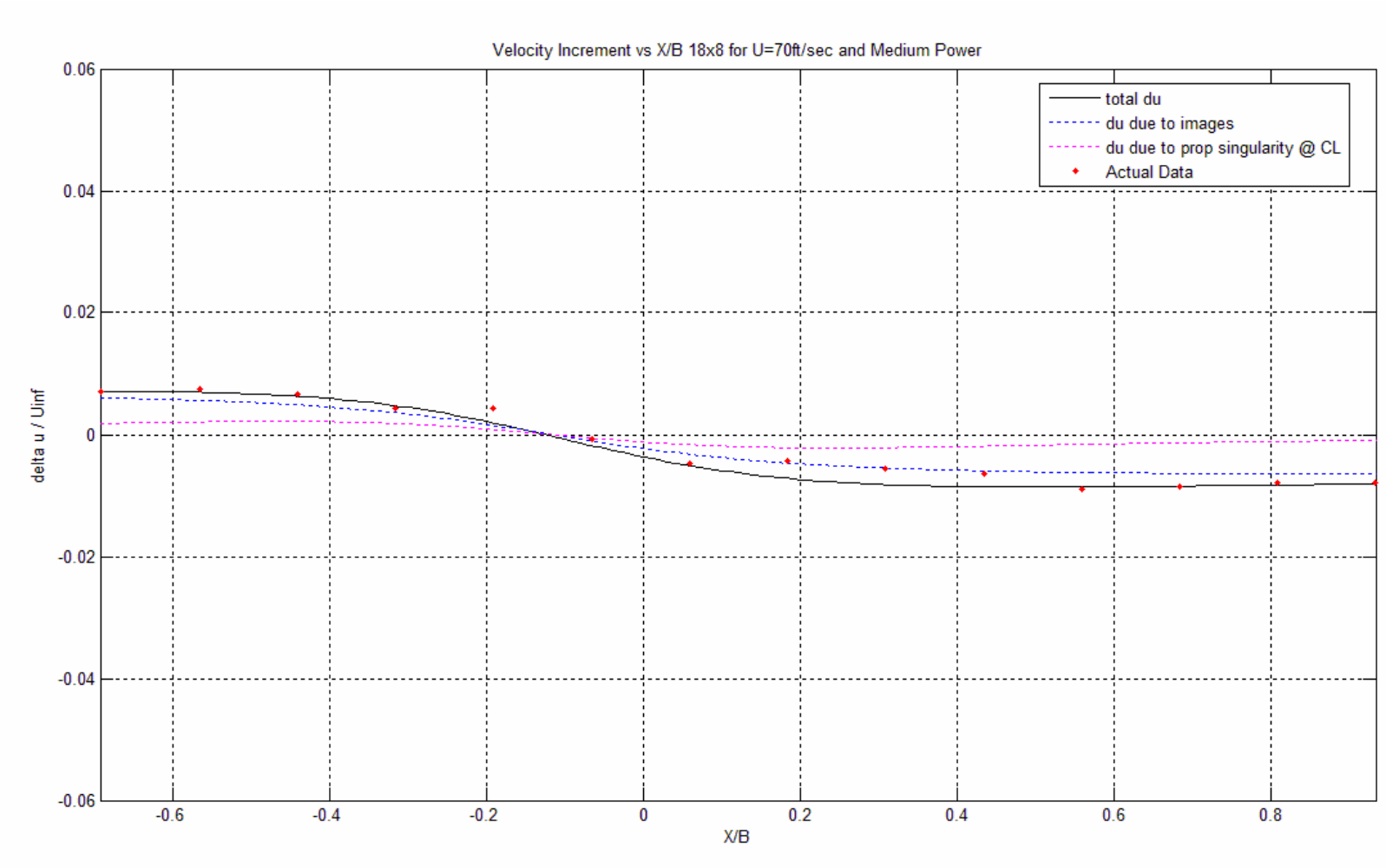

Figure 6. Velocity increment calculated from mathematical simulation model and propeller plotted against experimentally produced velocity increment for 18”x8” propeller rotating at medium RPM and wind tunnel speed of 70ft/s.

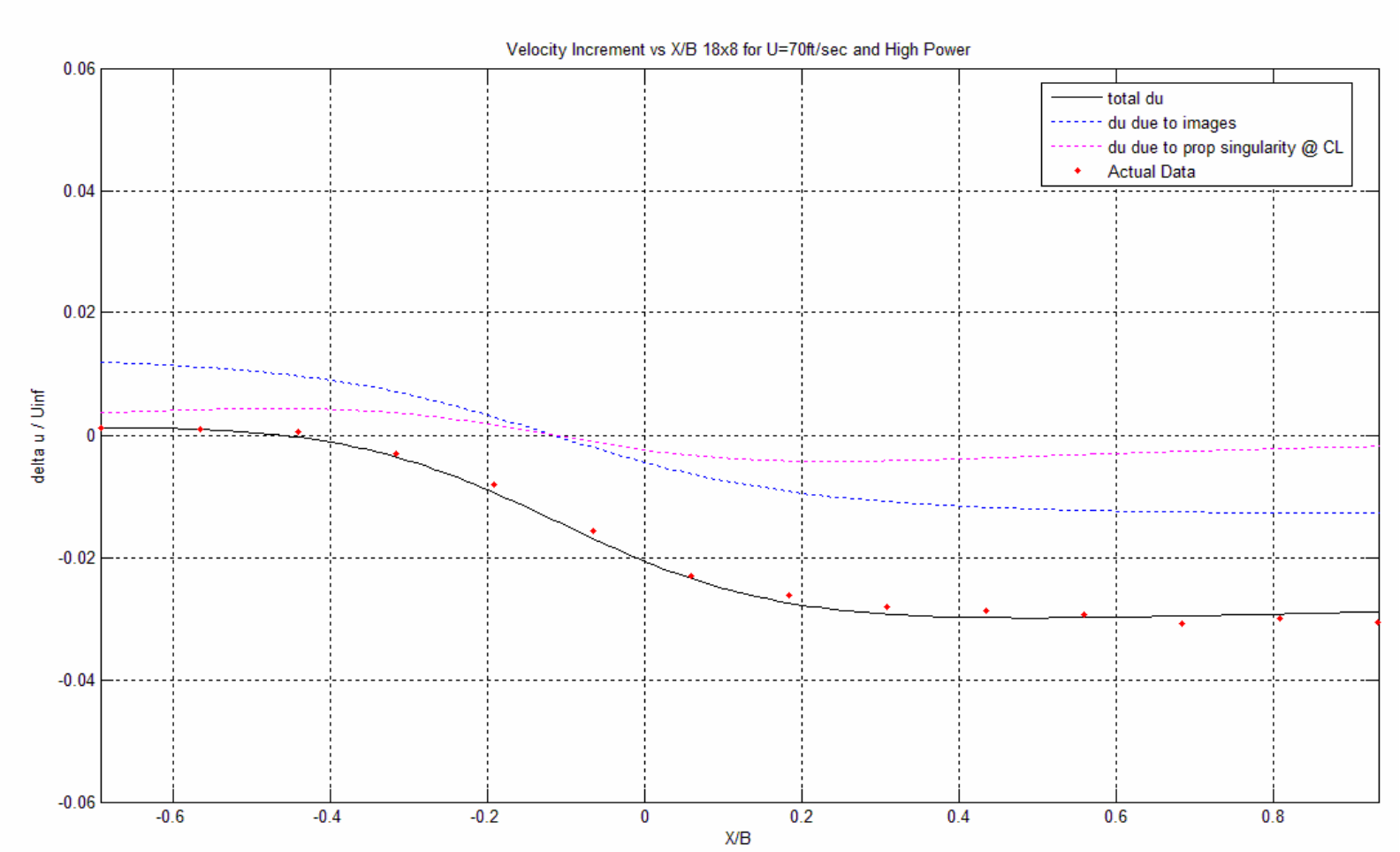

Figure 7. Velocity increment calculated from mathematical simulation model and propeller plotted against experimentally produced velocity increment for 18"x8" propeller rotating at high RPM and wind tunnel speed of 70ft/s.

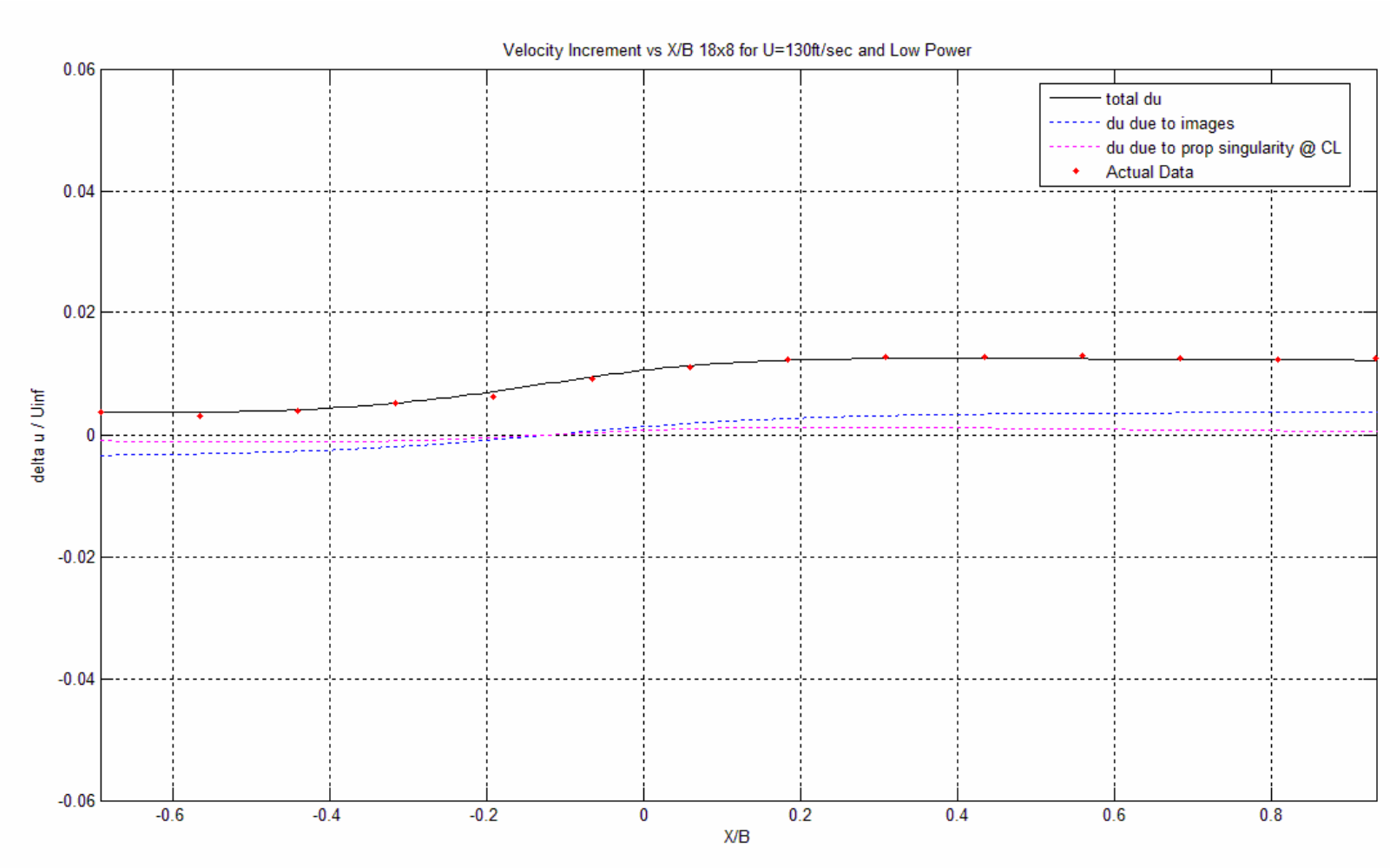

Figure 8. Velocity increment calculated from mathematical simulation model and propeller plotted against experimentally produced velocity increment for 18”x8” propeller rotating at low RPM and wind tunnel speed of130ft/s.

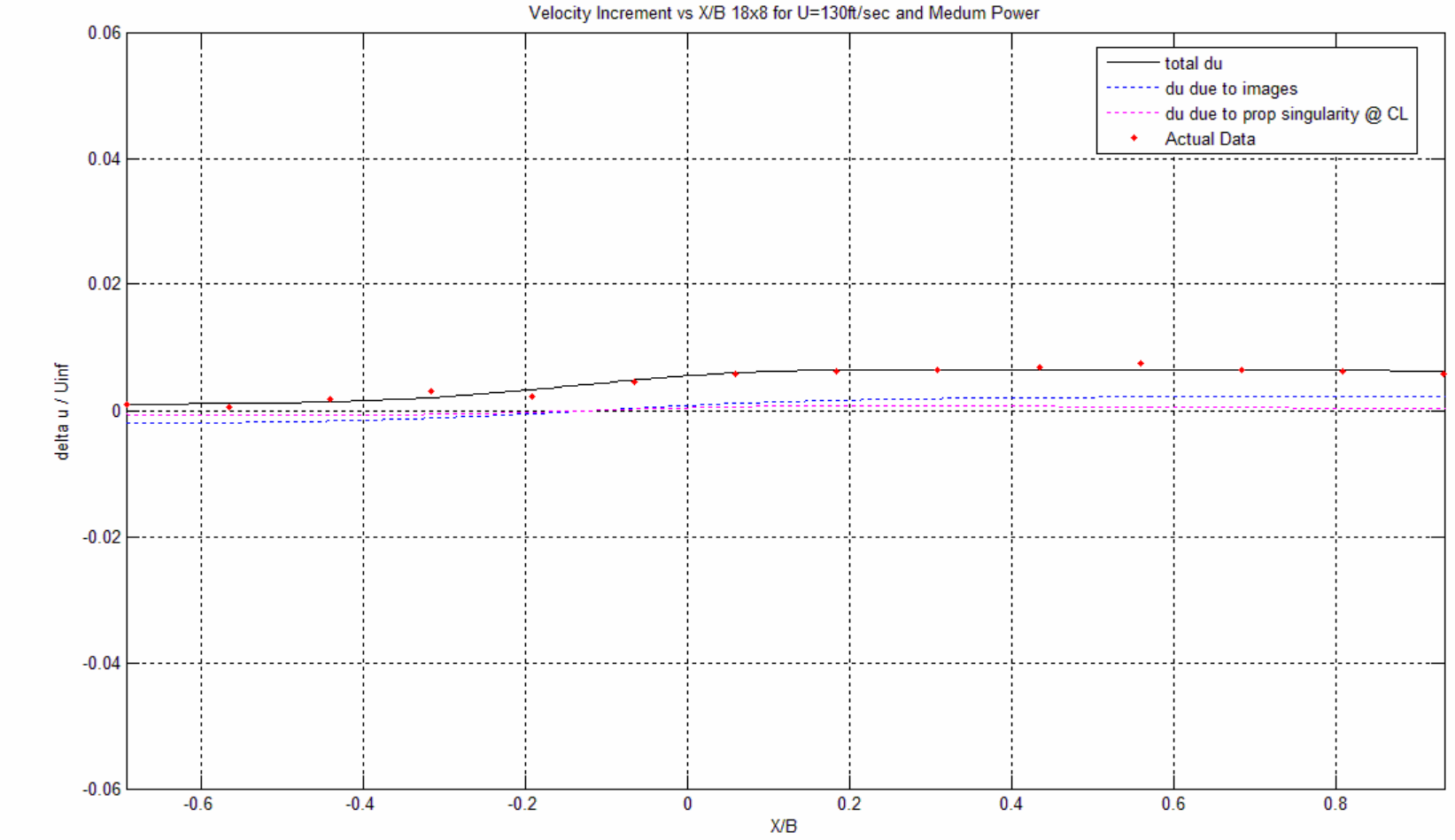

Figure 9. Velocity increment calculated from mathematical simulation model and propeller plotted against experimentally produced velocity increment for 18"x8" propeller rotating at medium RPM and wind tunnel speed of130ft/s.

Two assessments may be made from the above figures. First, the methodology used to simulate the solid body and the wake with singularities is sound; the calculated velocity increment matches experimental data well in most cases. Some cases show data scatter which cannot be identically matched by the mathematical calculations. This is likely a result of data scatter inherent in the data collection system. Second, one can observe that as the power setting increases, with wind tunnel speed held constant, thrust increases. However, as wind tunnel speed increases, given the same power setting, thrust produced decreases. This is an expected result.

Figures 2 through 9 show data gathered from NATF. Comparable simulation of solid body and wake blockage were not performed for data collected from GLMWT. This is because there was no blockage effect at GLMWT. This can be seen by examining the incremental velocity data from GLMWT against NATF. Figures 10 through 12 show the velocity increments from GLMWT as compared to that at NATF. The GLMWT velocity increments show that there is no appreciable velocity increment caused by the propeller thrust at any wind tunnel velocity or RPM setting. There is a brief drop in velocity increment at x/B=0, which coincides with the propeller location. This is due to the pressure increase through the propeller disc. Aside from this change, the velocity increments from the GLMWT data show no appreciable slope. If one attempted to model this velocity increment with singularities, as is done for the NATF velocity increment, one would discover that the singularity strength would be essentially zero. This is indicative of zero blockage. In some cases, successful runs at NATF were not able to be successfully completed at GLMWT and vice versa. Corresponding data for all other propellers can be found in Appendix B.

Additionally, the Glauert correction was applied to the GLMWT test data to prove that no blockage corrections were necessary. Figure 13-16 show these corrections. In all cases, the corrected data lies directly on top of the experimental data, or very close to it. In one case, for the 18”x8” propeller, two runs were completed. These are designated by the diamonds and triangles. The repeatability of the runs was not as desired and caused scatter. This is shown in figure14.

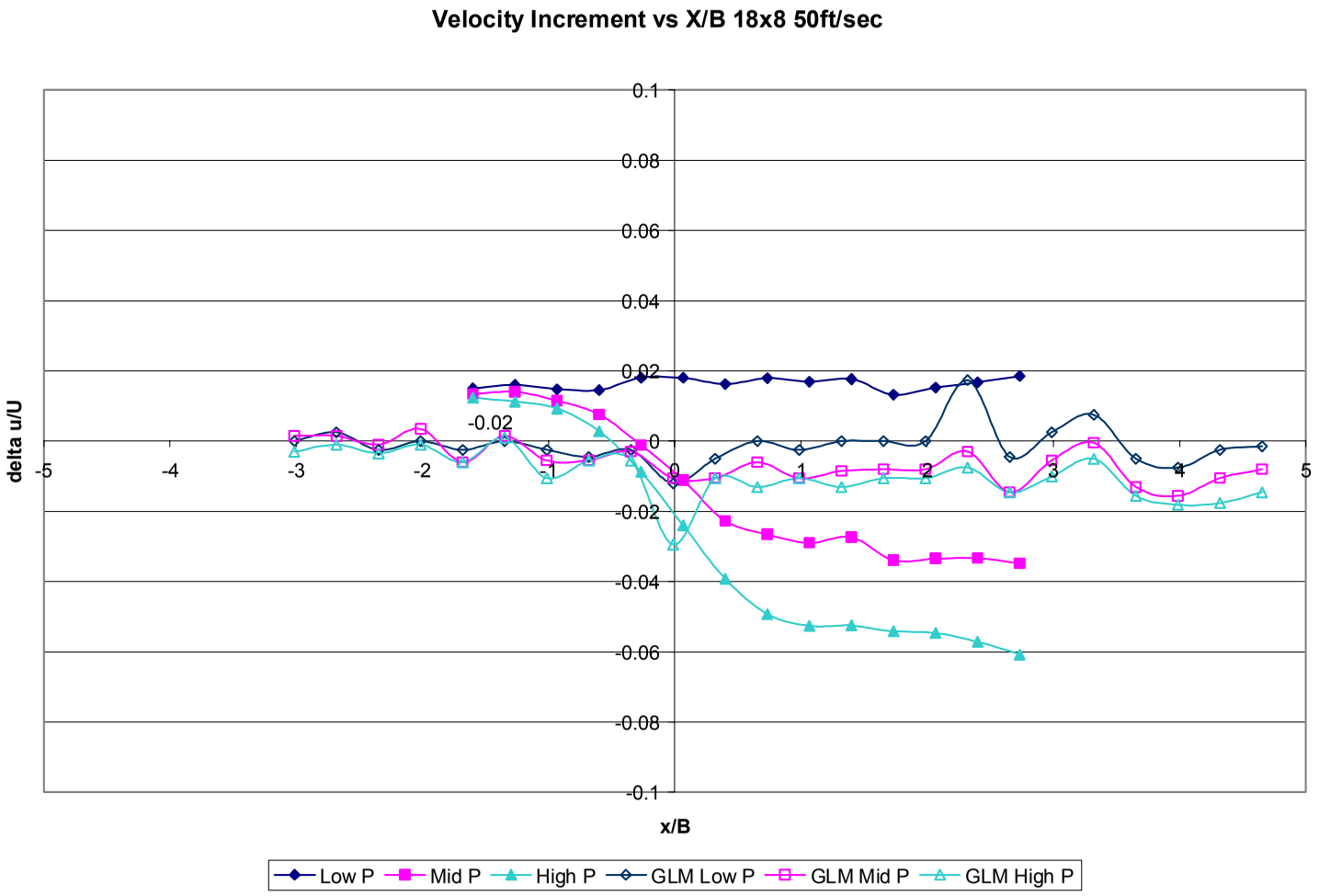

Figure 10. Velocity increment calculated from pressure data collected at NATF and GLMWT for the 18"x8" propeller and wind tunnel speed of 50ft/s.

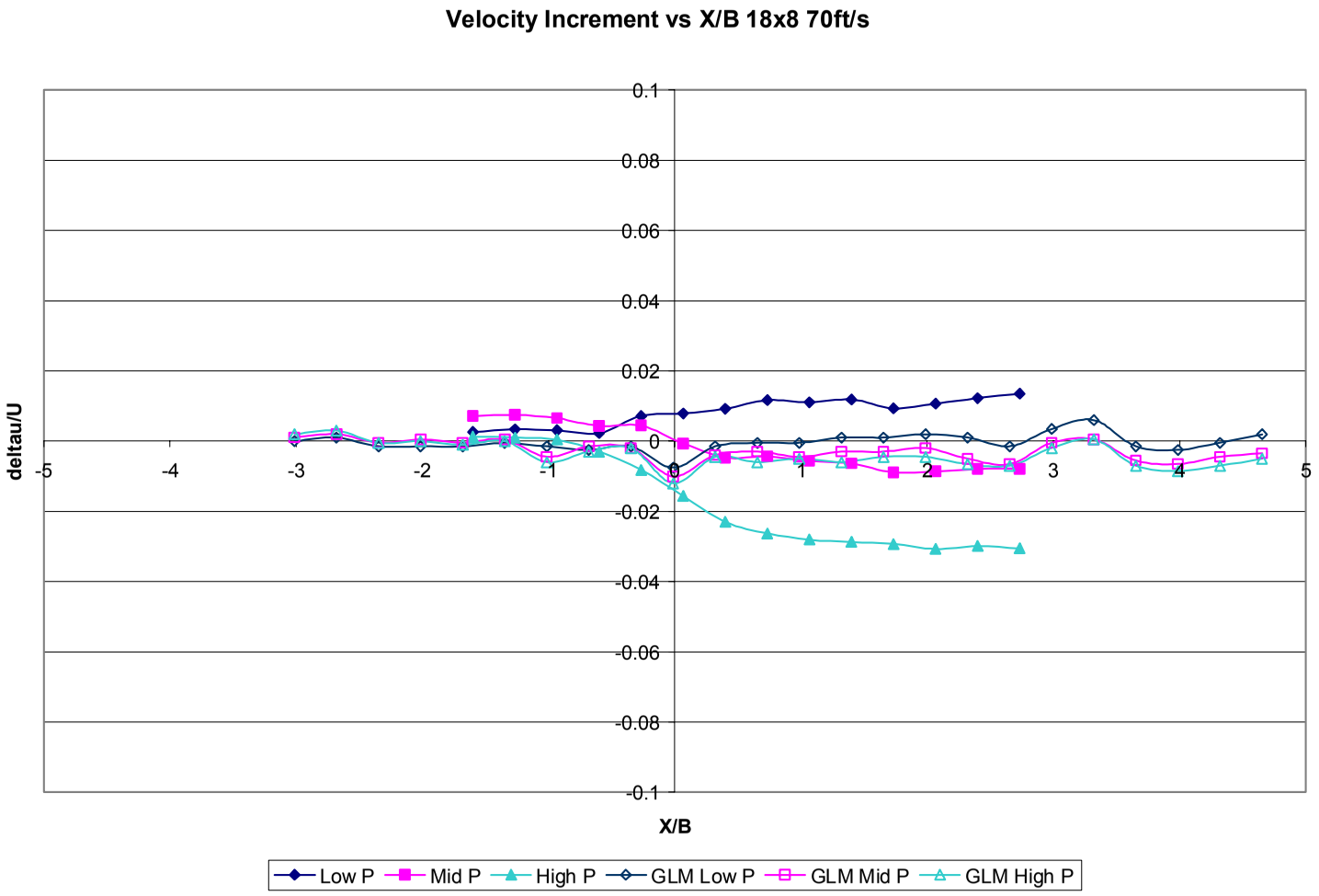

Figure 11. Velocity increment calculated from pressure data collected at NATF and GLMWT for the 18"x8" propeller and wind tunnel speed of 70ft/s.

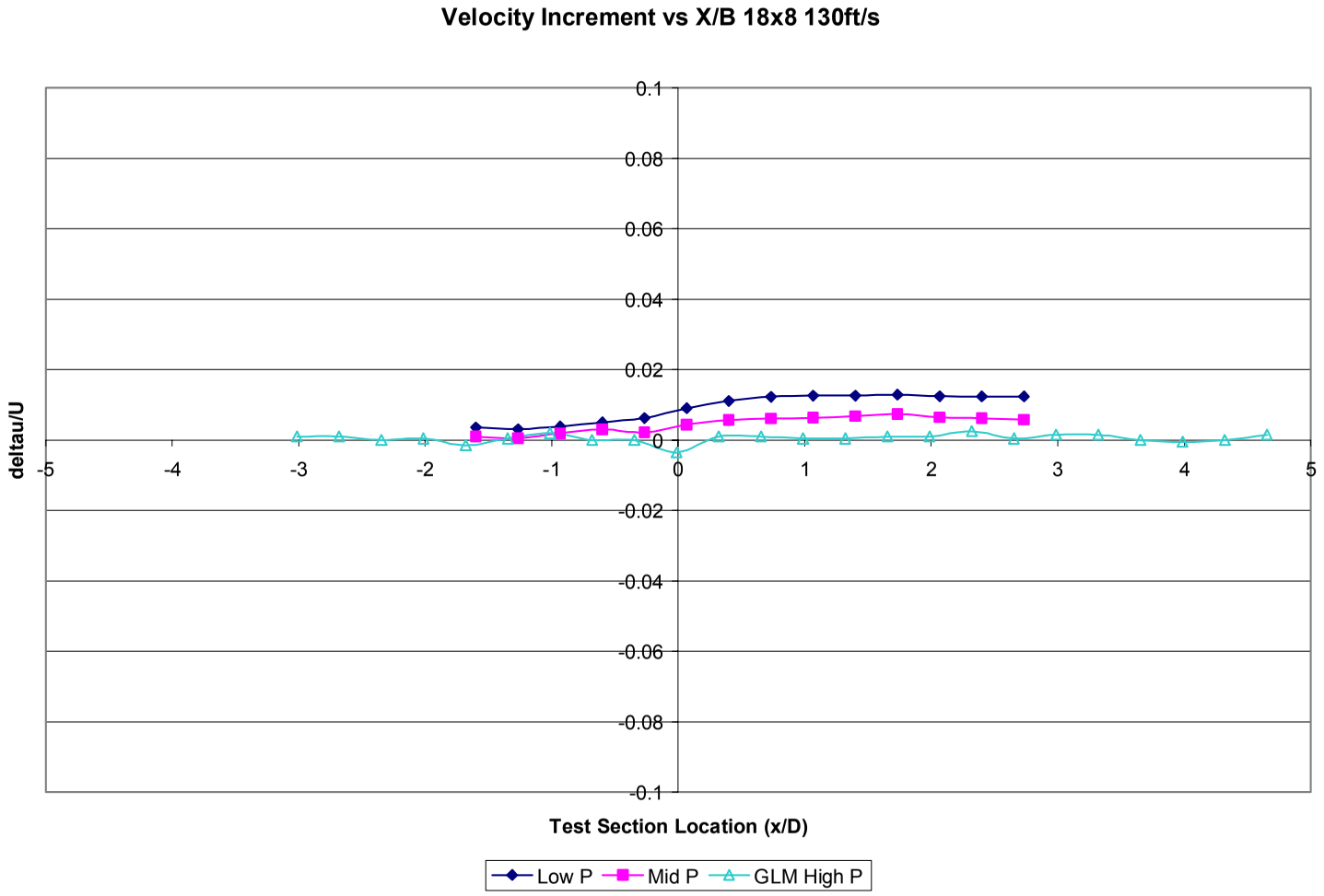

Figure 12. Velocity increment calculated from pressure data collected at NATF and GLMWT for the 18"x8" propeller and wind tunnel speed of 70ft/s.

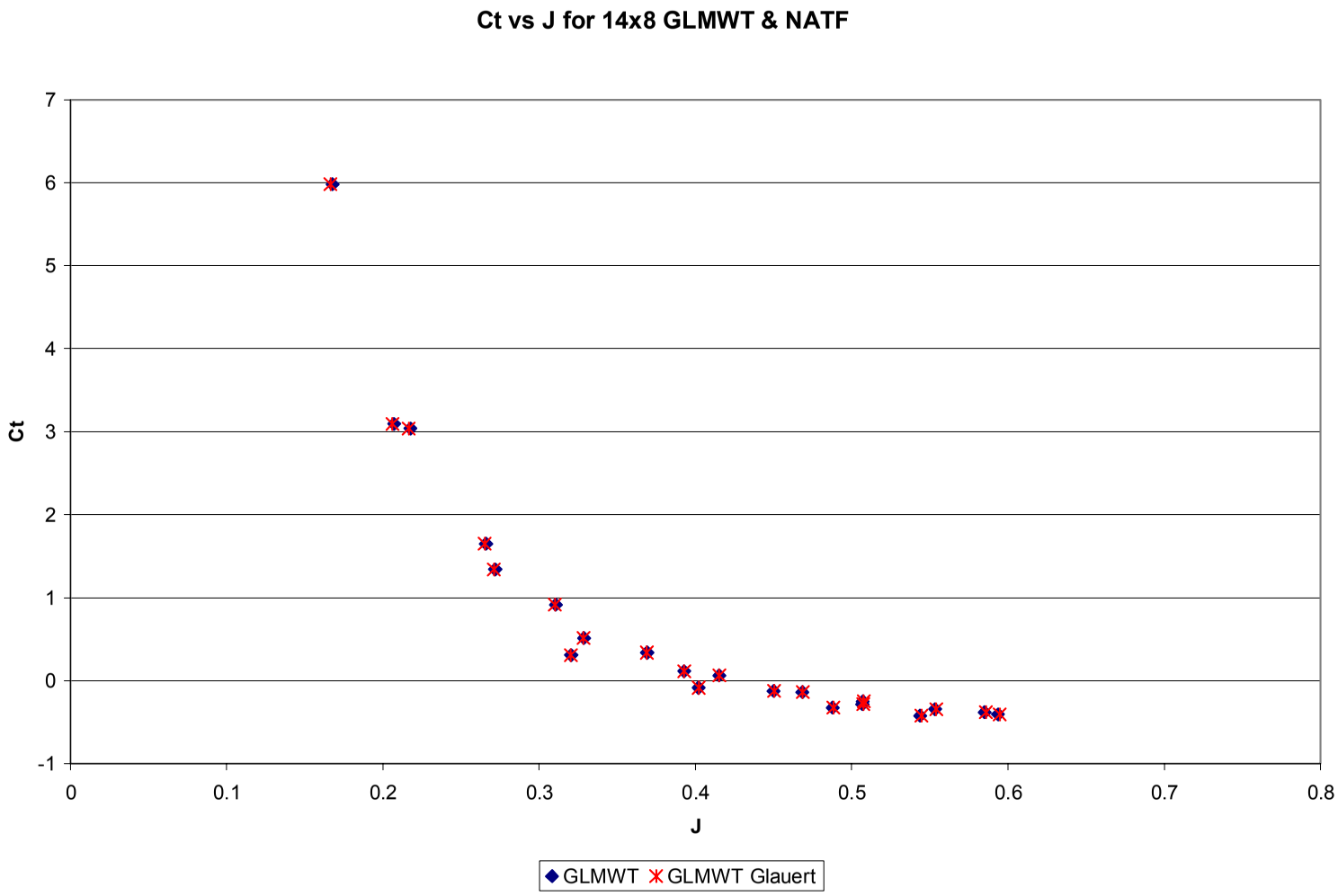

Figure 13. GLMWT experimental data compared to Glauert-corrected GLMWT data.

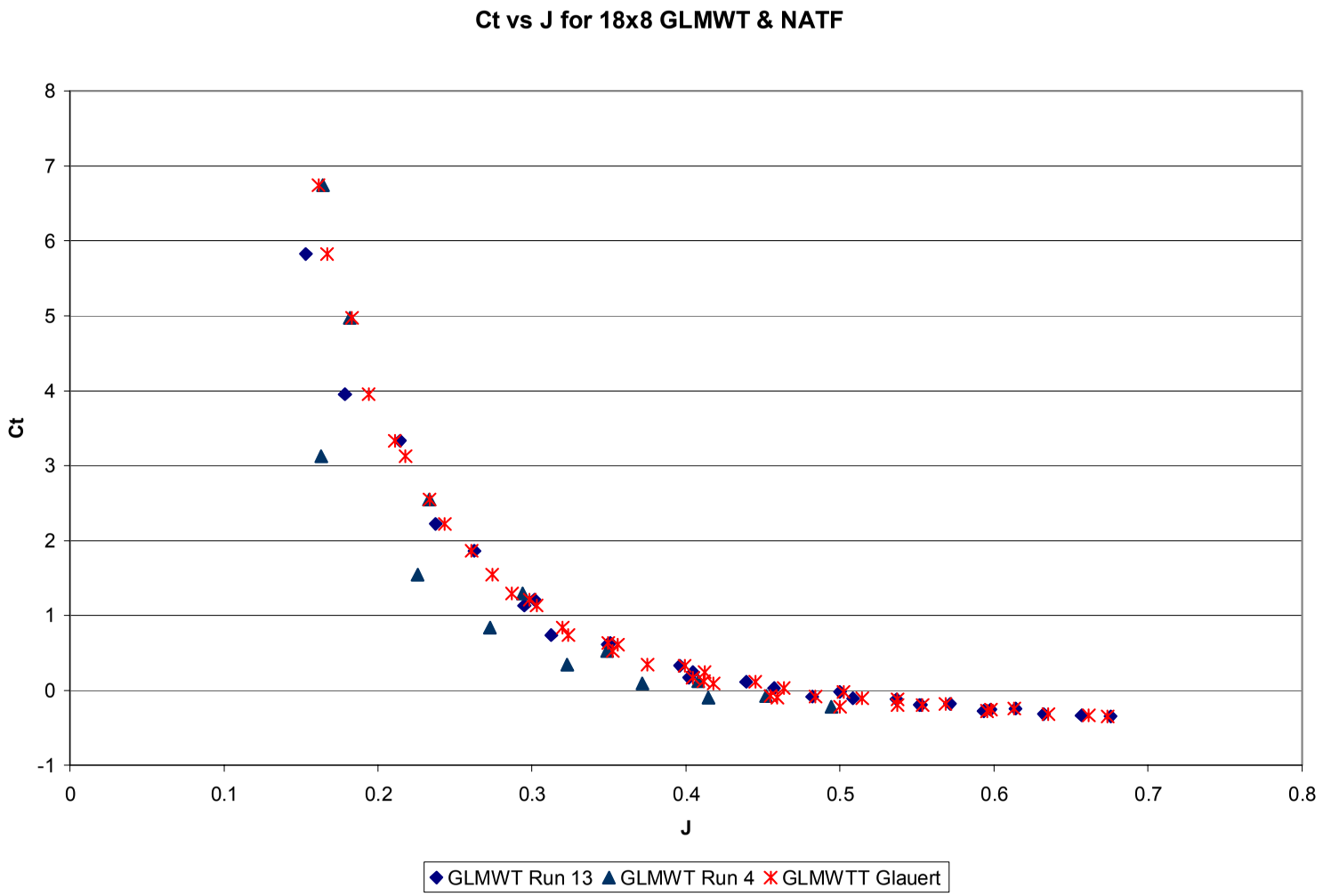

Figure 14. GLMWT experimental data compared to Glauert-corrected GLMWT data.

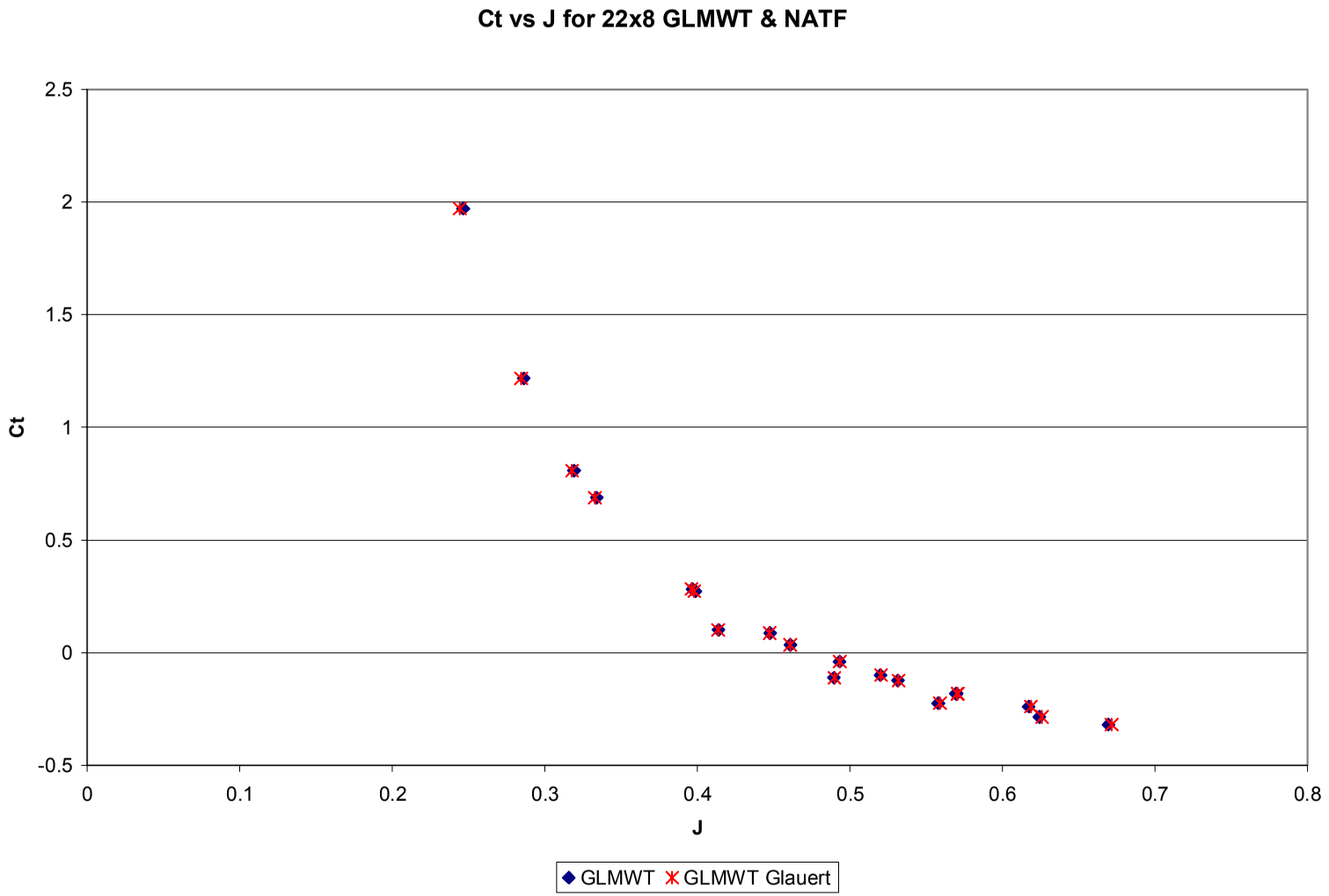

Figure 15. GLMWT experimental data compared to Glauert-corrected GLMWT data.

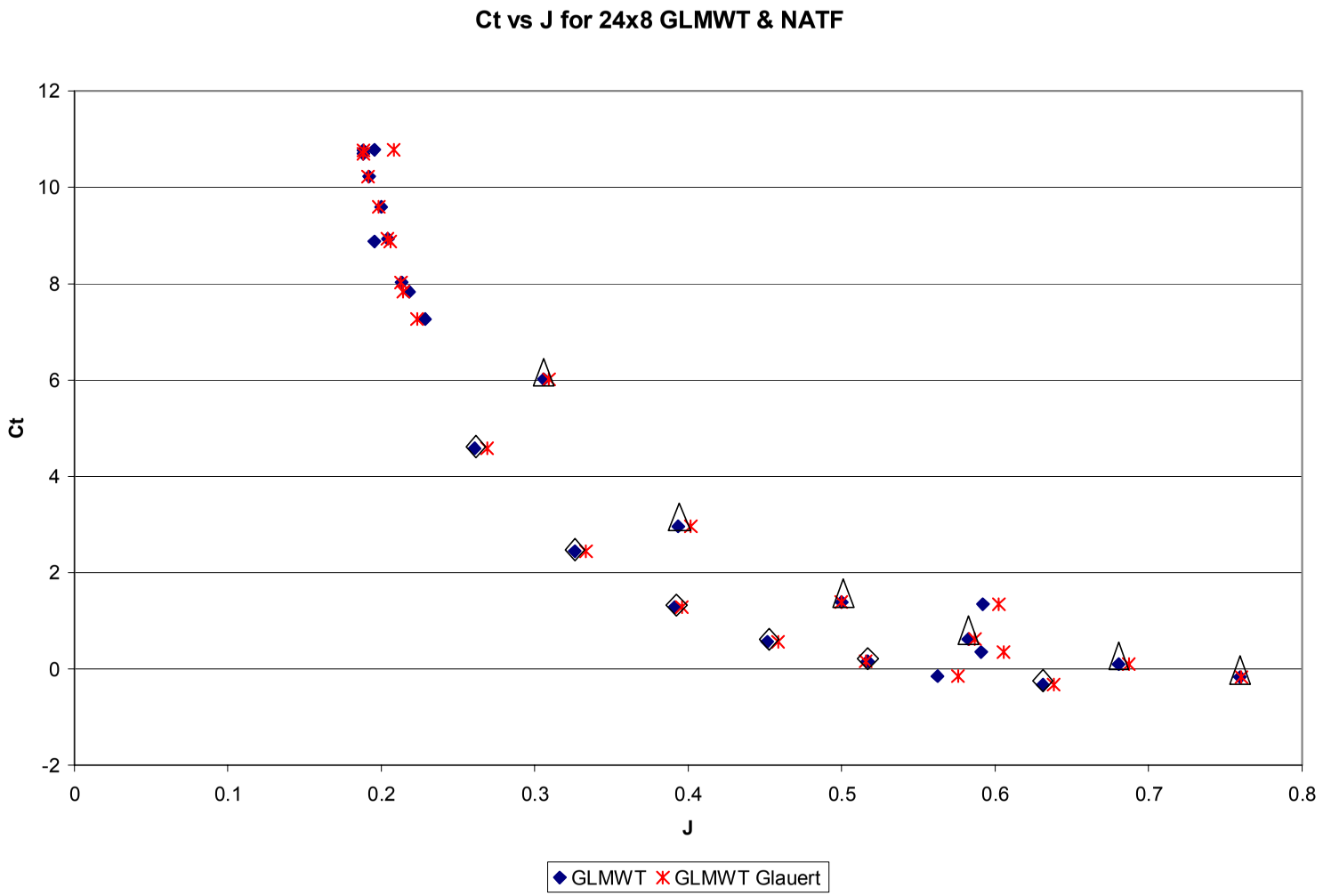

Figure 16. GLMWT experimental data compared to Glauert-corrected GLMWT data.

3.5 Velocity Increment at Wind Tunnel Centerline

As is done in the Hackett-Wilsden method, velocity increments at the tunnel centerline are calculated. This is done simply using the x/B locations of the pressure taps while setting the z/B coordinate at which the velocity increment is calculated to the centerline location of z/B = 0. The singularities that simulate the solid blockage and the wake blockage are removed for this calculation, and only the increment caused by the image system is calculated. The increments are calculated as in equation 28, for each singularity in the infinity of images. As is described in the method of images, location of each image varies in y/B and z/B coordinates. Additionally, the "miss distance" is included in the calculation of the velocity increment to capture the aforementioned effect of test section length.

The centerline velocity increments are shown for the 18" x 8" propeller in figures 17 through 24. Centerline velocity increments for all other propellers can be found in Appendix B.

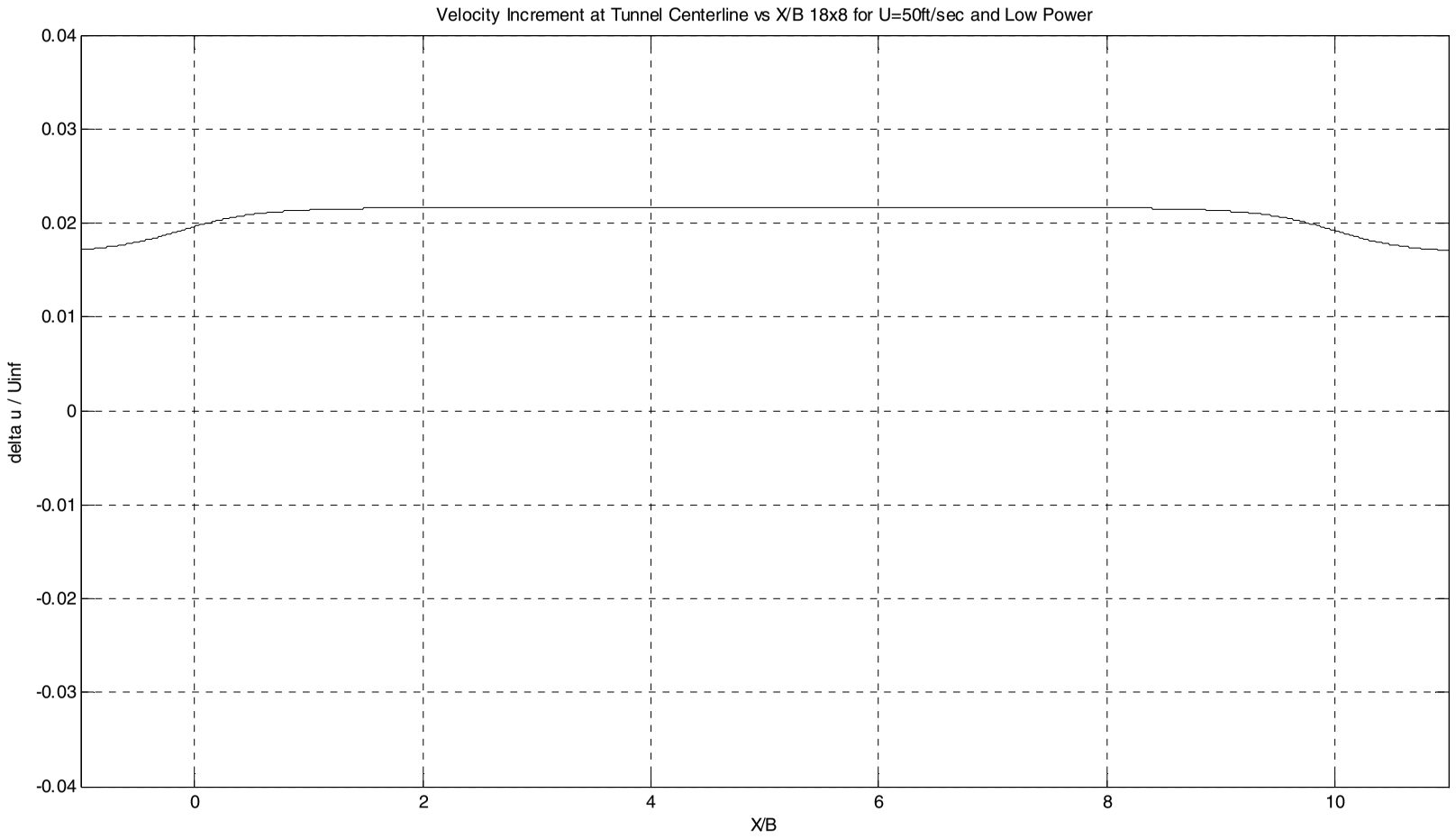

Figure 17. Centerline velocity increment for 18” x 8” propeller at 50ft/sec at low RPM.

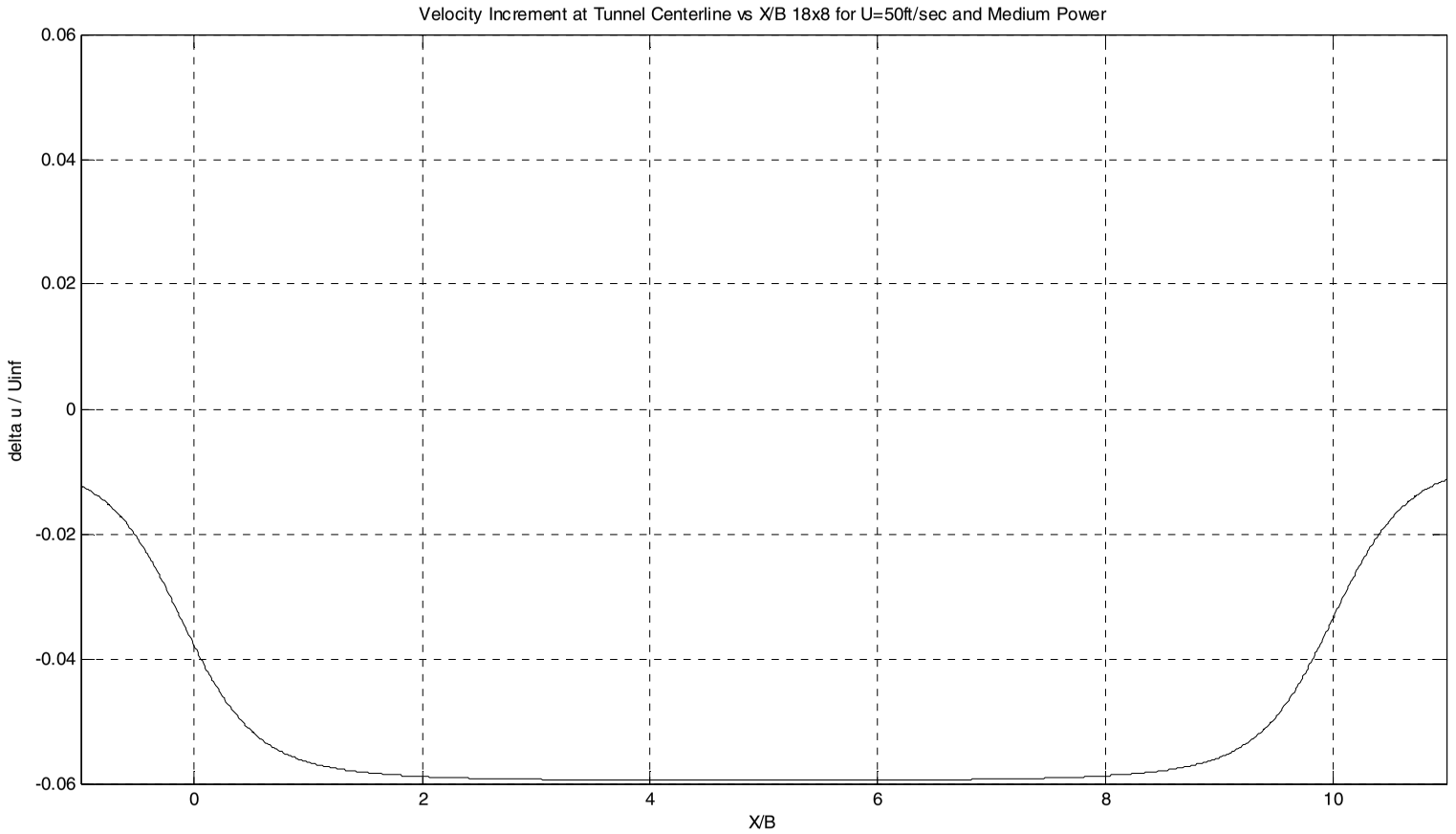

Figure 18. Centerline velocity increment for 18” x 8” propeller at 50ft/sec at medium RPM.

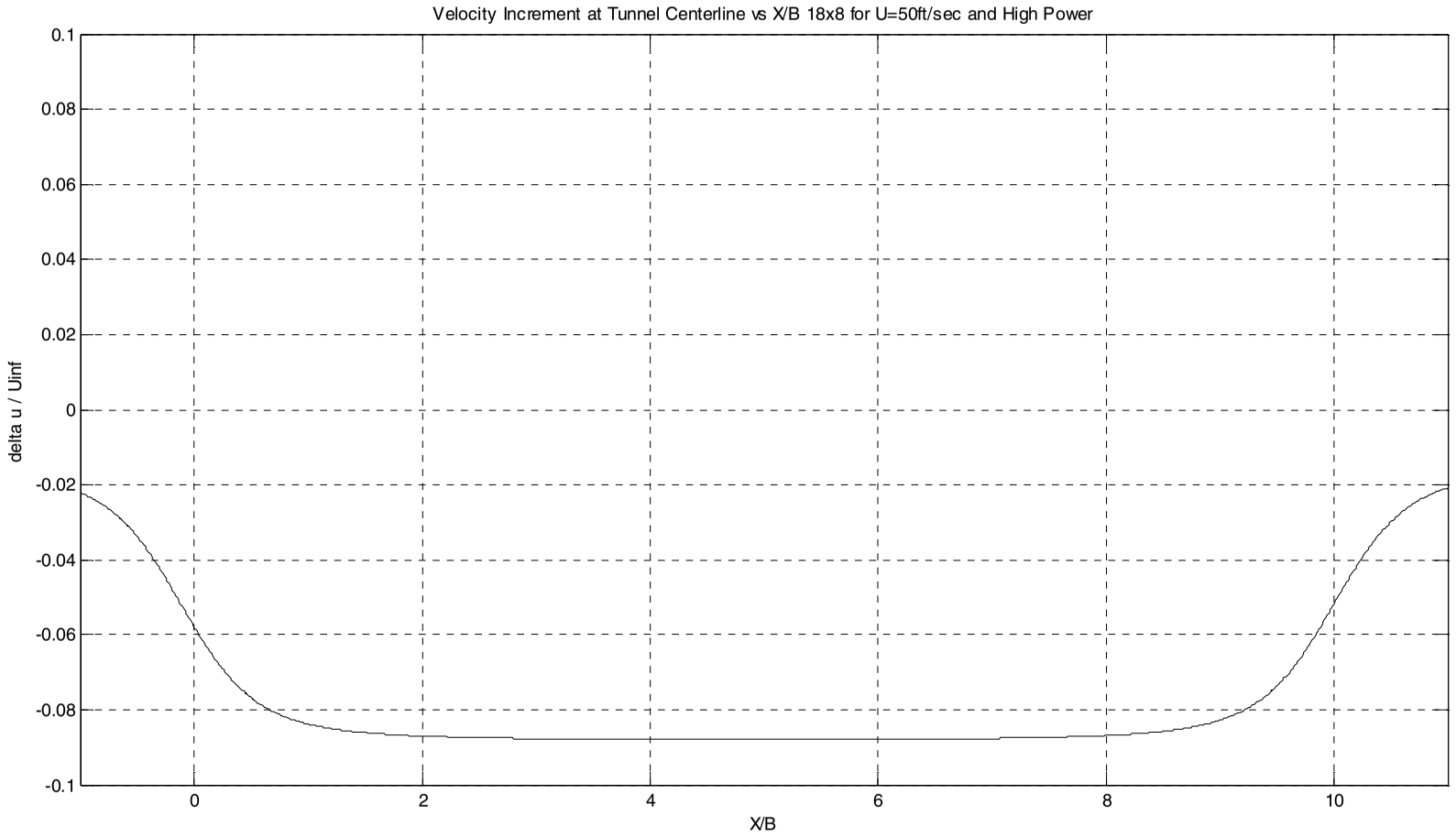

Figure 19. Centerline velocity increment for 18” x 8” propeller at 50ft/sec at high RPM.

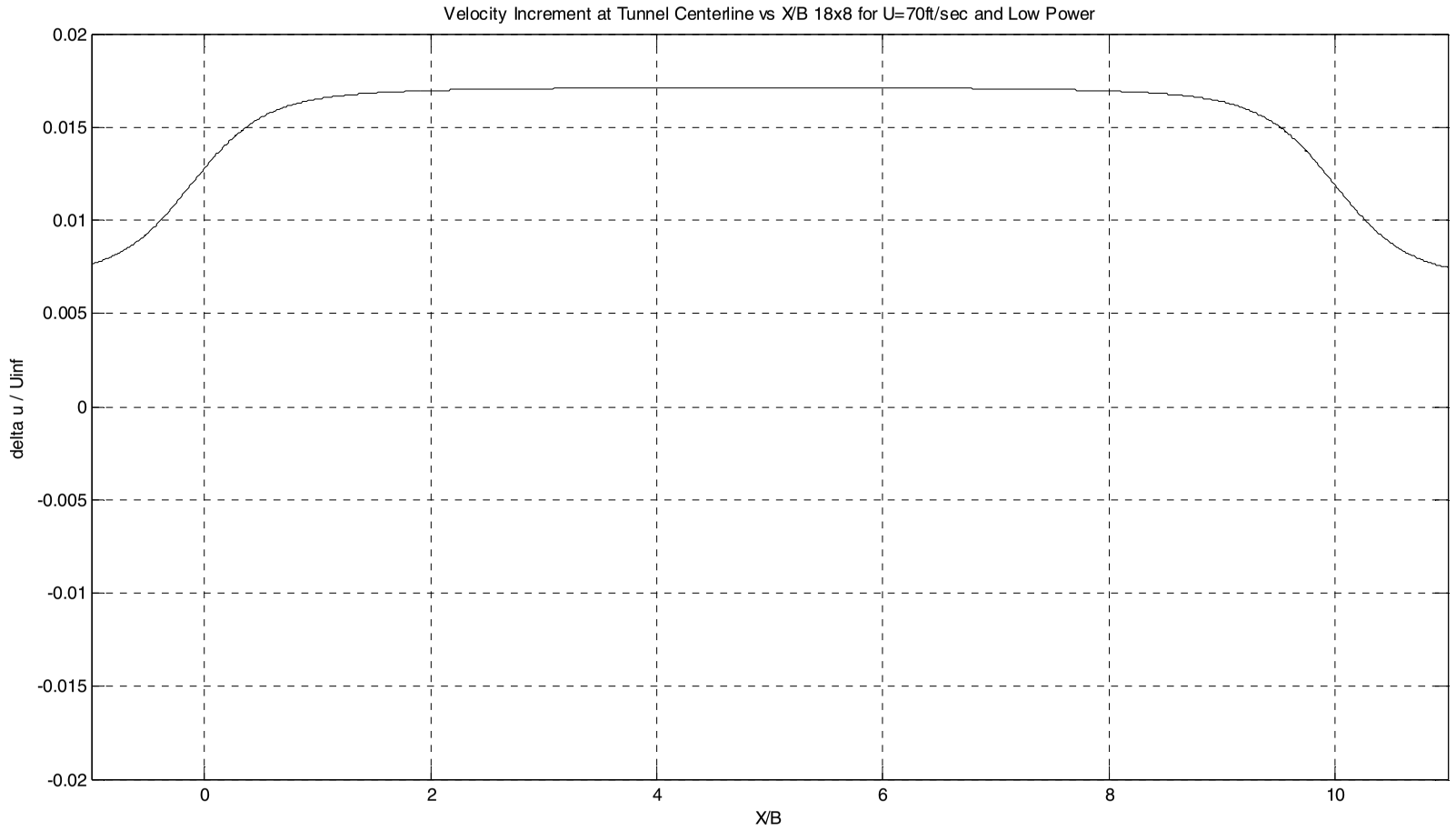

Figure 20. Centerline velocity increment for 18” x 8” propeller at 70ft/sec at low RPM.

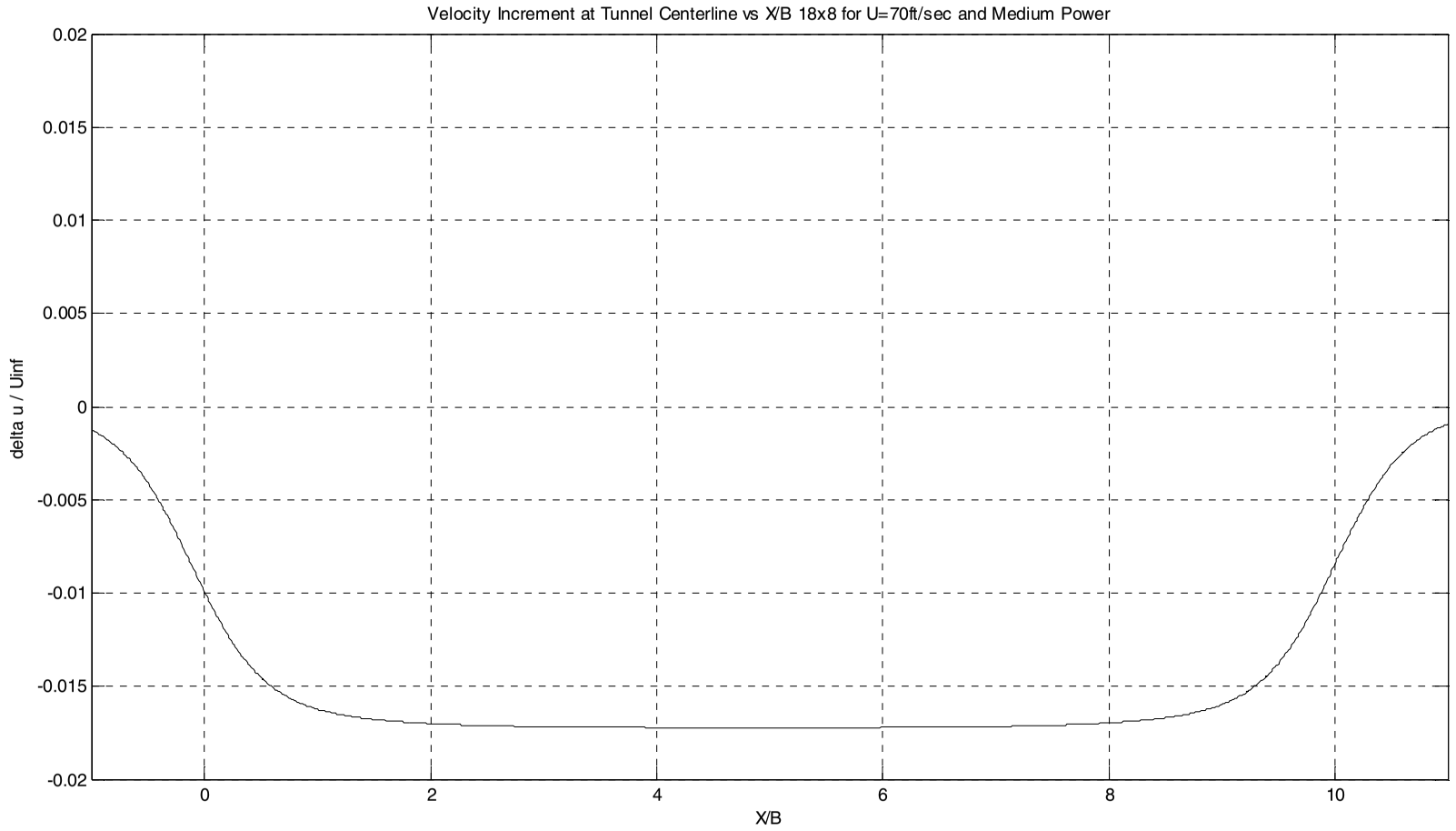

Figure 21. Centerline velocity increment for 18” x 8” propeller at 70ft/sec at medium RPM.

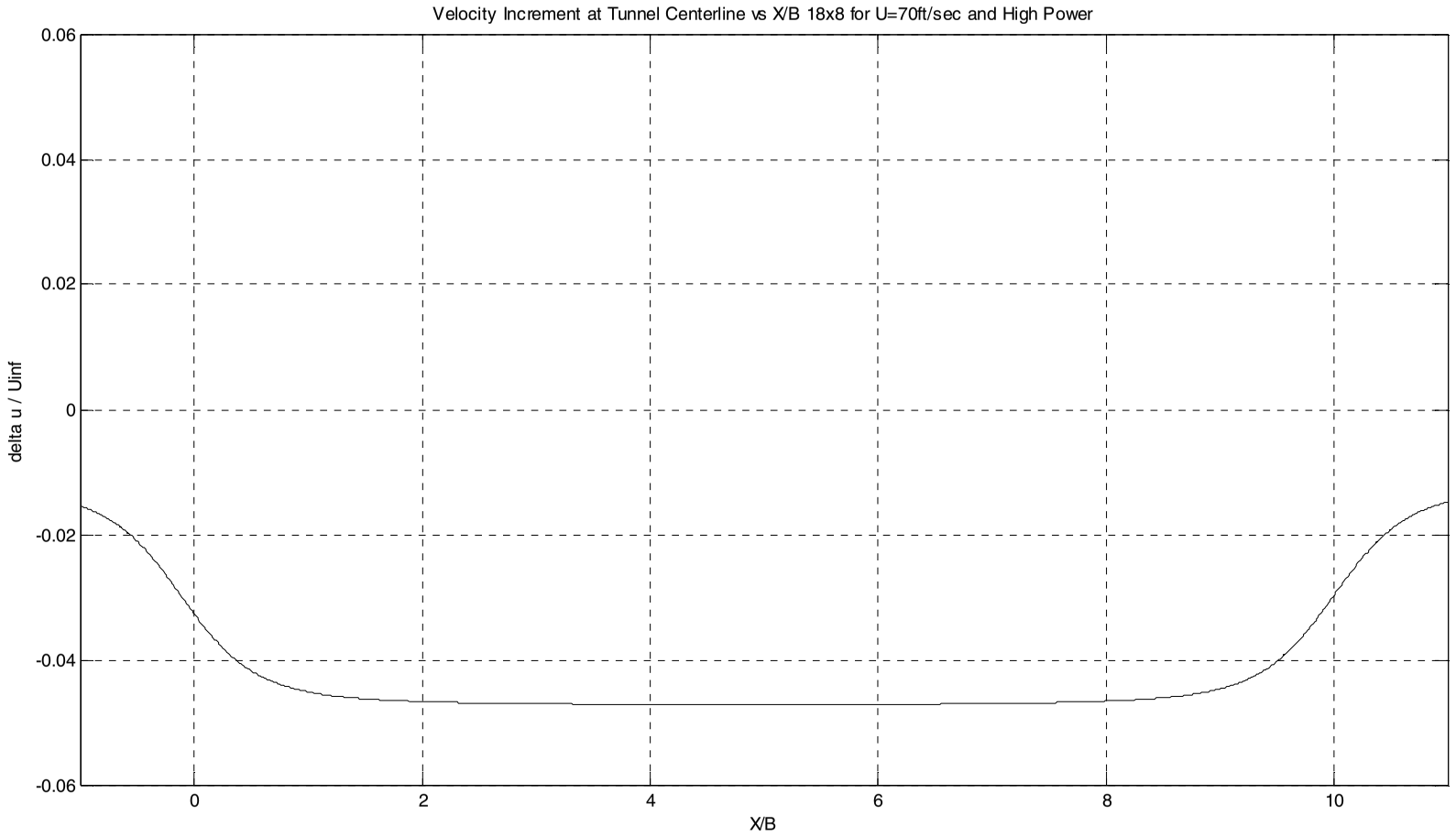

Figure 22. Centerline velocity increment for 18” x 8” propeller at 70ft/sec at high RPM.

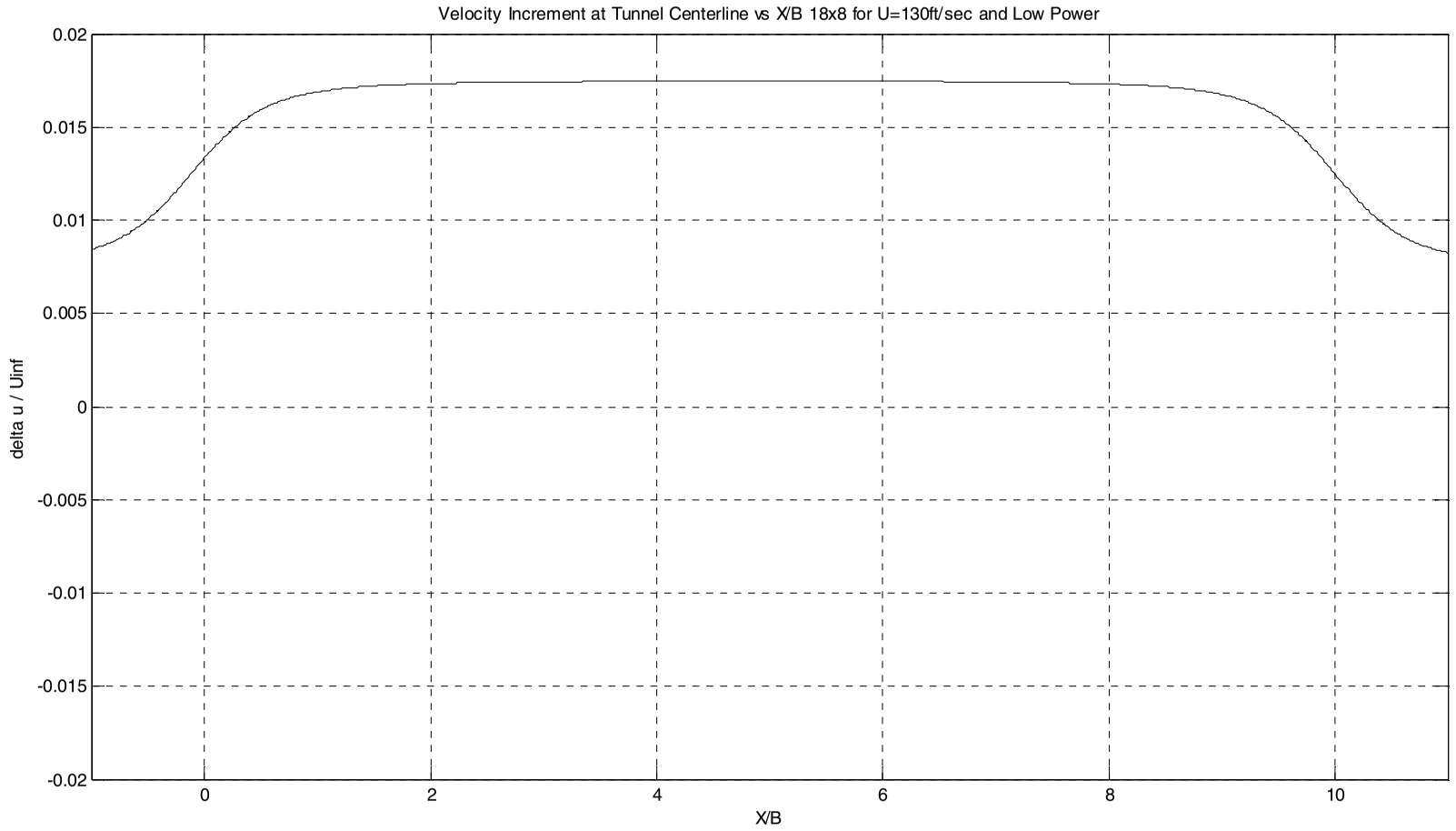

Figure 23. Centerline velocity increment for 18" x 8" propeller at 130ft/sec at low RPM.

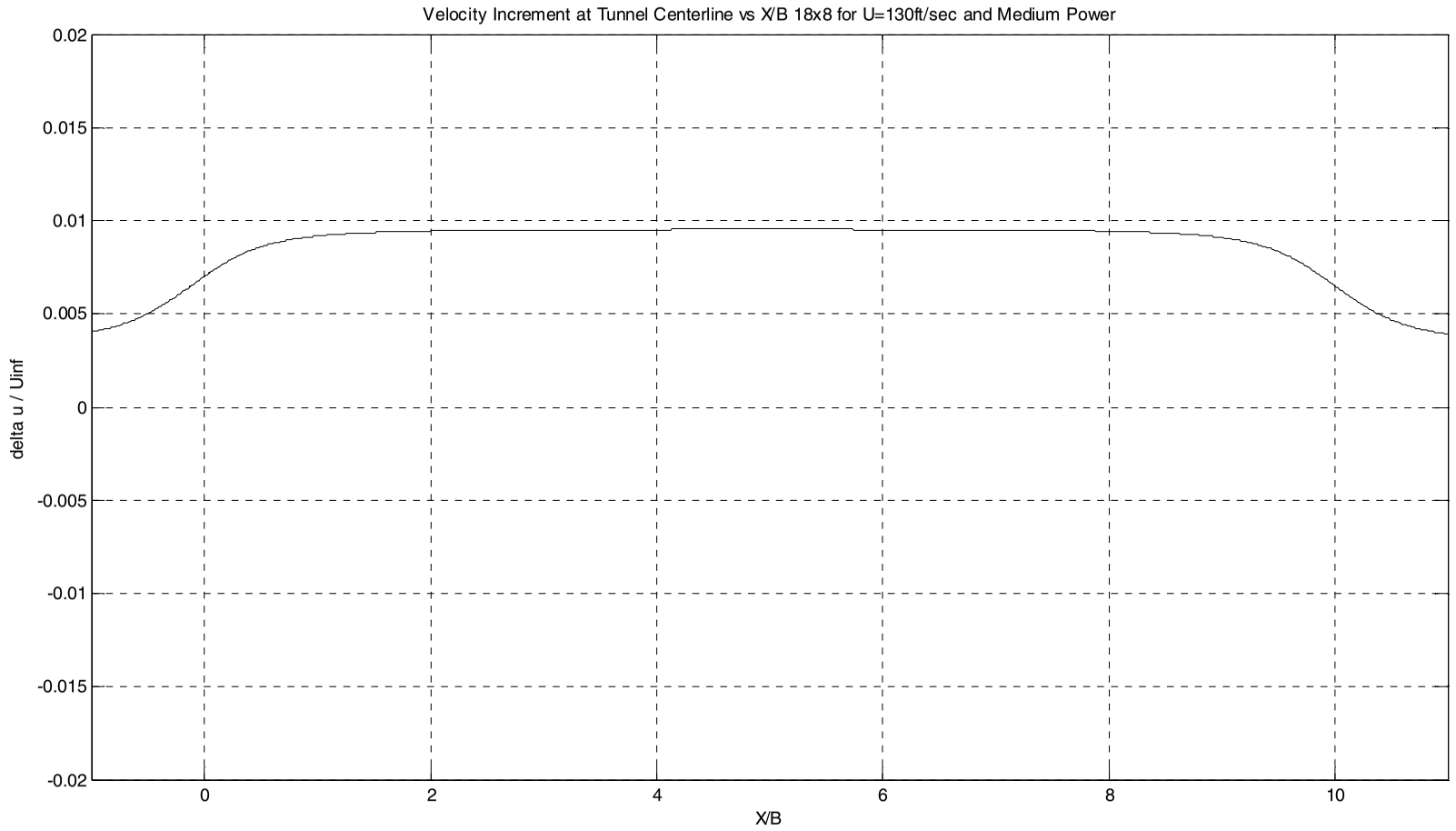

Figure 24. Centerline velocity increment for 18” x 8” propeller at 130ft/sec at medium RPM.

3.6 Calculation of Corrections

Following the successful modeling of the model and propeller wake, the classical Glauert correction was calculated as described in chapter 1, section 1.2. As previously stated, this calculation provides the speed at which the experiment should be run to develop the forces corresponding to those that would be obtained in unrestricted flow, at the same operating conditions.

It should be noted that Glauert's correction is useful both for positive and negative thrust cases, as is Sørensen and Mikkelsen's. However, at $C_T = -1$, Glauert's correction becomes singular. Sørensen and Mikkelsen state that the correction formula they developed allows for a closed-form solution of the equations of axial momentum. They claim, "With the new approach, there is no longer any need for introducing approximate correction formulas for the wind speed through the rotor disk. Furthermore, the singularity problem is solved with the new solution.[8]" Therefore, corrections were calculated only both positive and negative thrust runs for comparison between methodologies. The Glauert correction calculated from experimental data was applied to negative thrust cases and plotted against the theoretical corrections. This is shown below in figure 25. Clearly, the Glauert corrections obtained with experimental data correspond with theoretical corrections at identical thrust conditions.

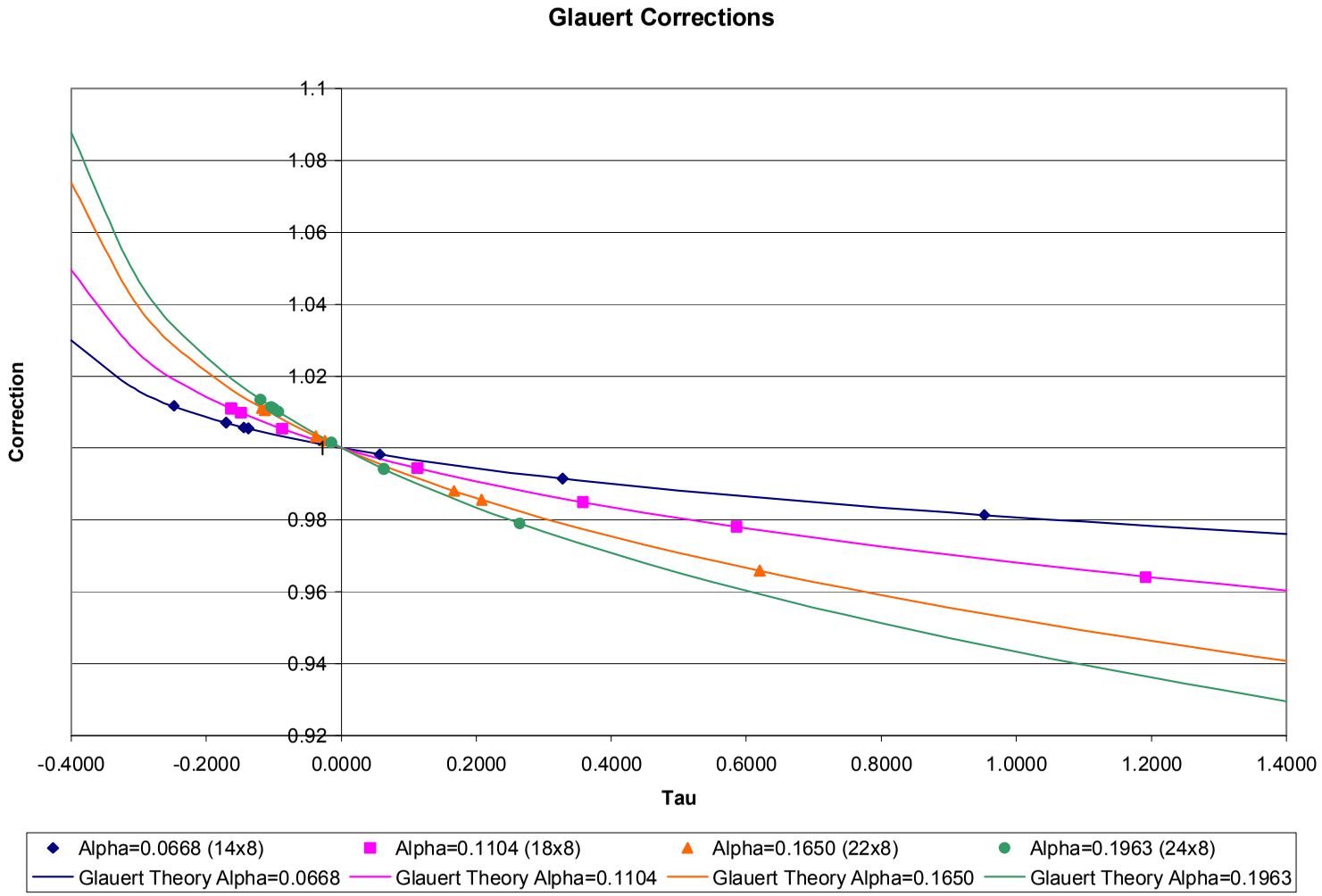

Figure 25. Glauert corrections plotted against experimental data.

To complete the Hackett-Wilsden correction method, the previously calculated centerline velocity increments are used. The value of the centerline velocity increment is added to the datum wind tunnel velocity to determine a corrected velocity, as is done in both the Glauert calculation. This gives the effective free stream flow needed to obtain the same thrust coefficients in free air as those obtained in the wind tunnel.

Lastly, Sørensen and Mikkelsen correction is performed. In order to carry out this correction, the singularities and their strengths which successfully model solid and wake blockage must be known. This is accomplished using the Hackett-Wilsden method. Next, to calculate the intermediate value, ũ, as is necessary in solving the first equation of the Sørensen and Mikkelsen methodology, the cross sectional area of the slip stream far downstream must be calculated. This was done using the conservation of momentum. Once the cross section area of the slip stream far downstream is known, the value β was easily found and used in equation 7, along with the strength of the propeller singularity to find ũ. With this variable calculated, the five momentum equations (10-14) were solved and all other variables calculated. Finally, the Sørensen and Mikkelsen correction formula, equation (15), was performed. Just as with the Glauert and Hackett-Wilsden correction, this formula provides the speed at which the experiment should be run to develop the forces corresponding to those that would be obtained in unrestricted flow.

Using the new airspeeds calculated from the Glauert, Hackett-Wilsden, and Sørensen and Mikkelsen correction formulas,corrected advance ratios were calculated. To compare the correction to the experimentally obtained data, and to compare the each

method against the others, experimental thrust coefficient was plotted against the experimental advance ratio and corrected points were super imposed on this plot. These comparisons are shown below in figures 26 through 29.

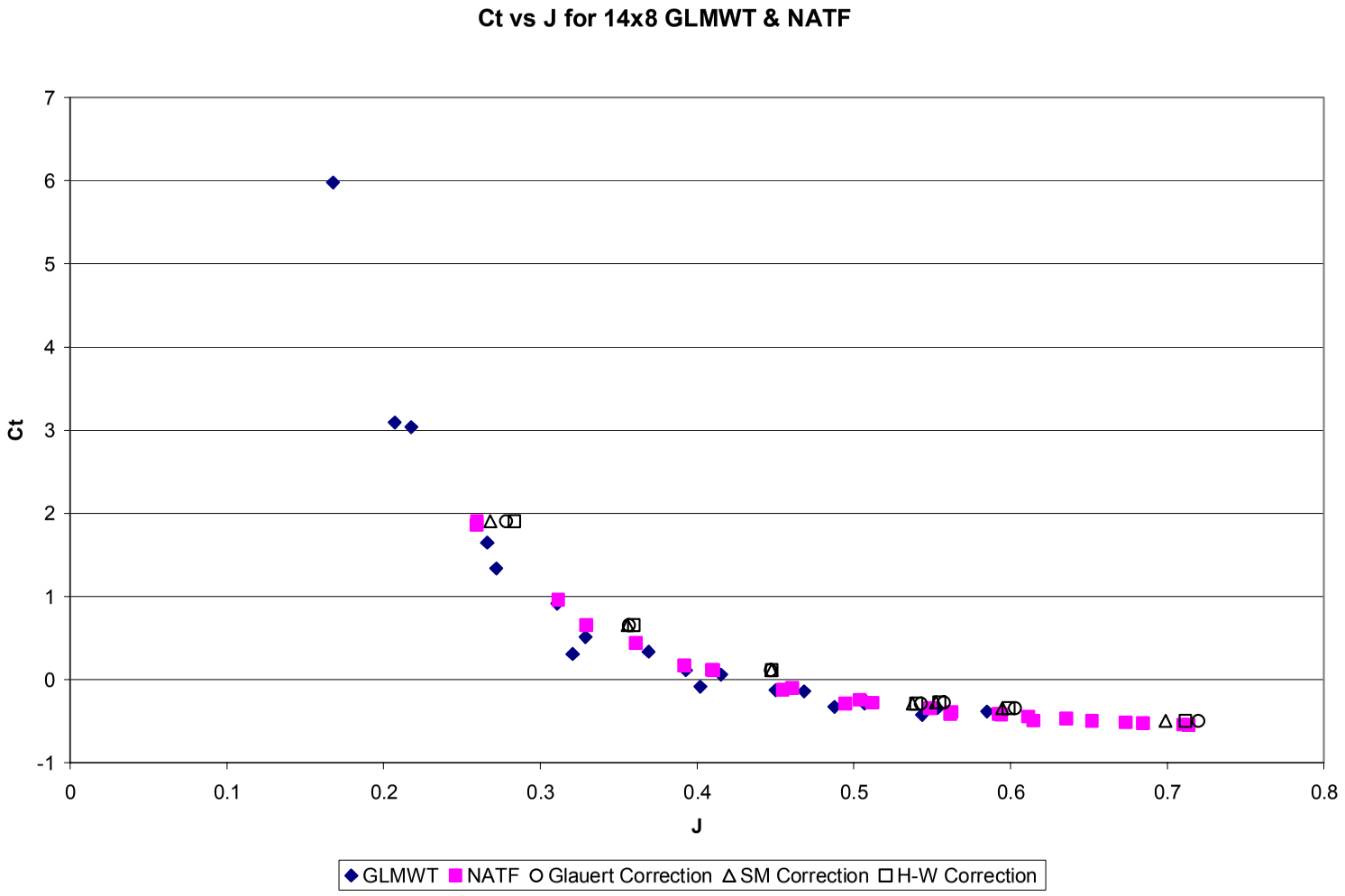

Figure 26. Data points corrected for wind tunnel blockage plotted against experimental data for the 14”x8” propeller.

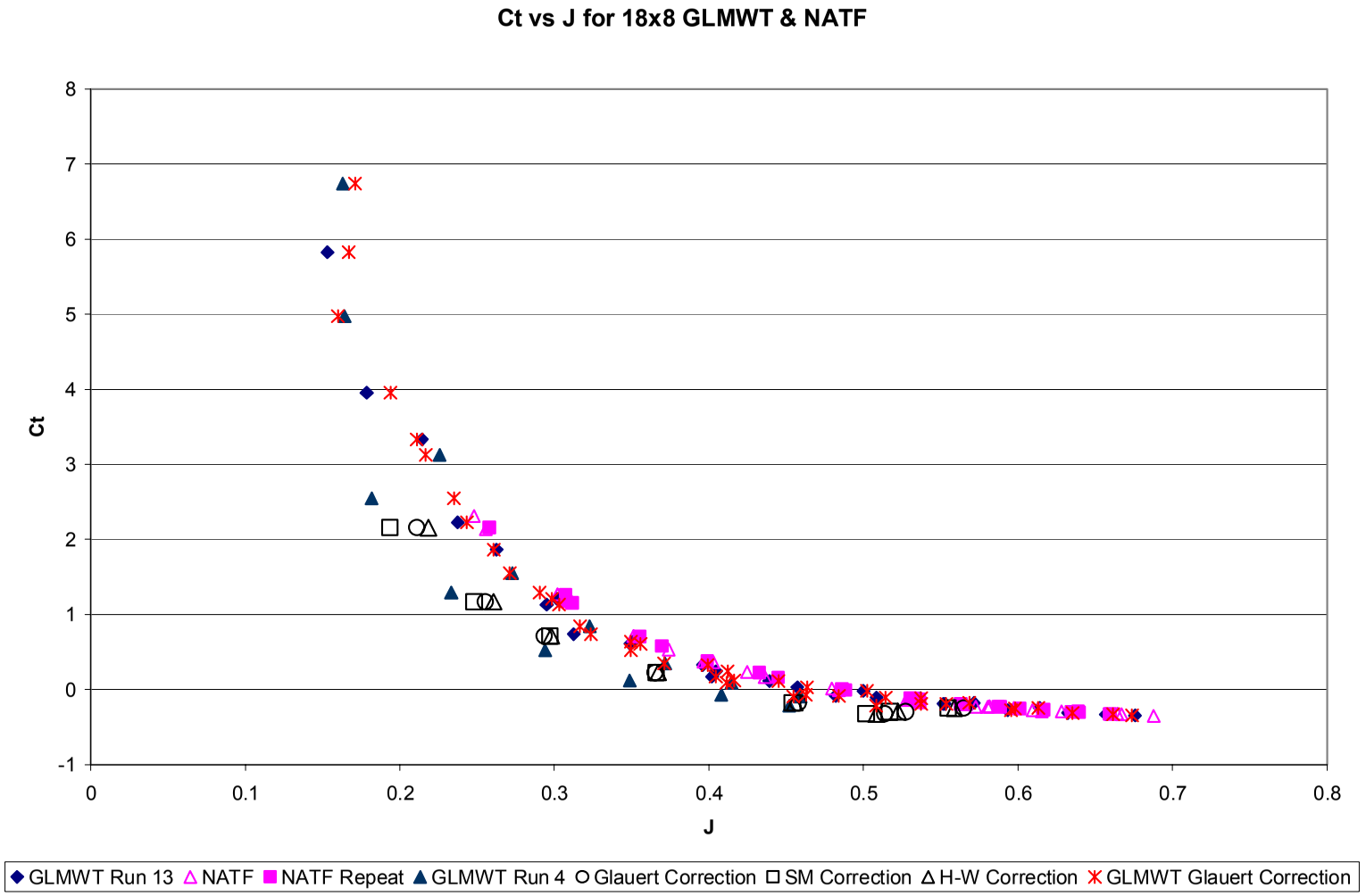

Figure 27. Data points corrected for wind tunnel blockage plotted against experimental data for the 18”x8” propeller.

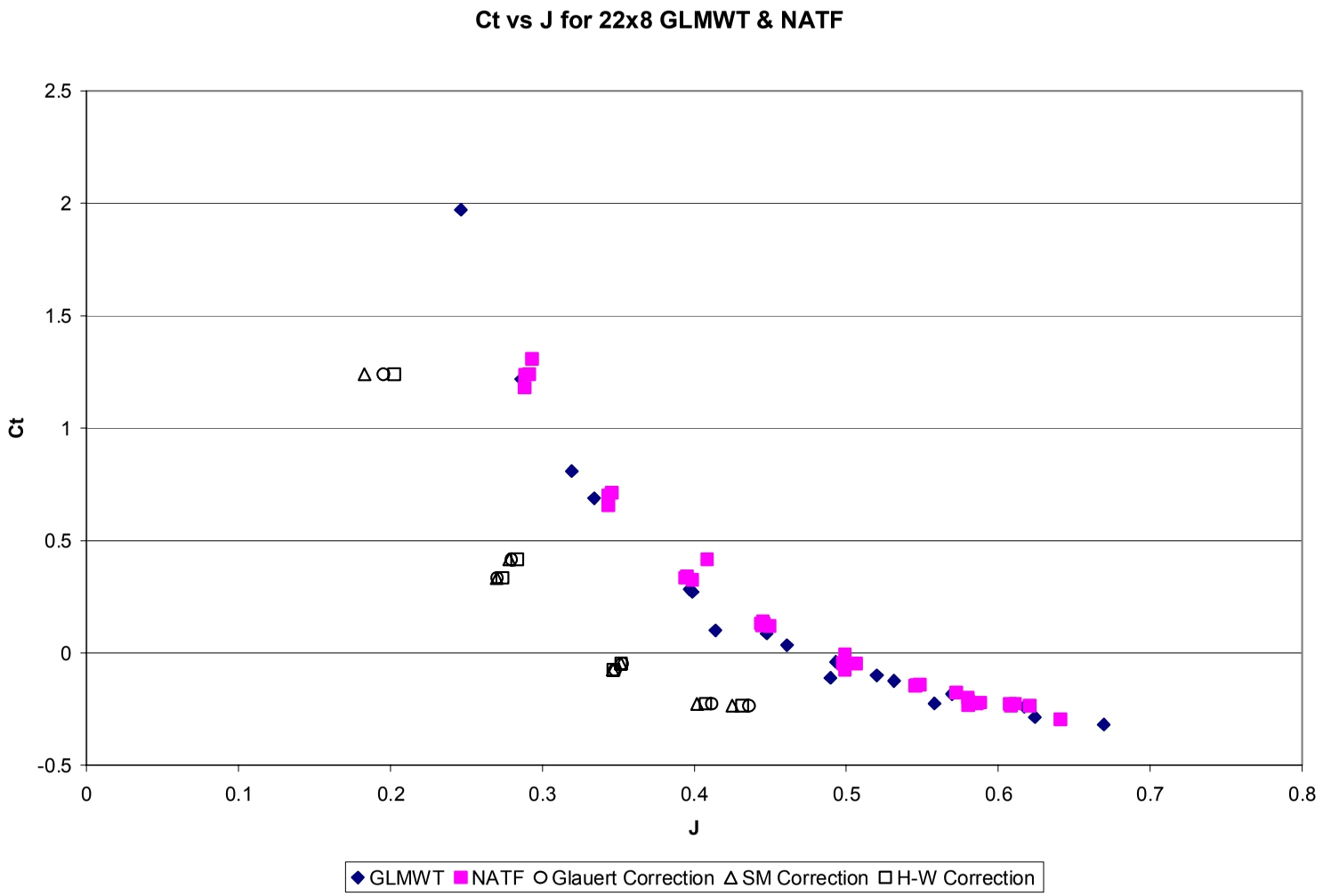

Figure 28. Data points corrected for wind tunnel blockage plotted against experimental data for the 22”x8” propeller.

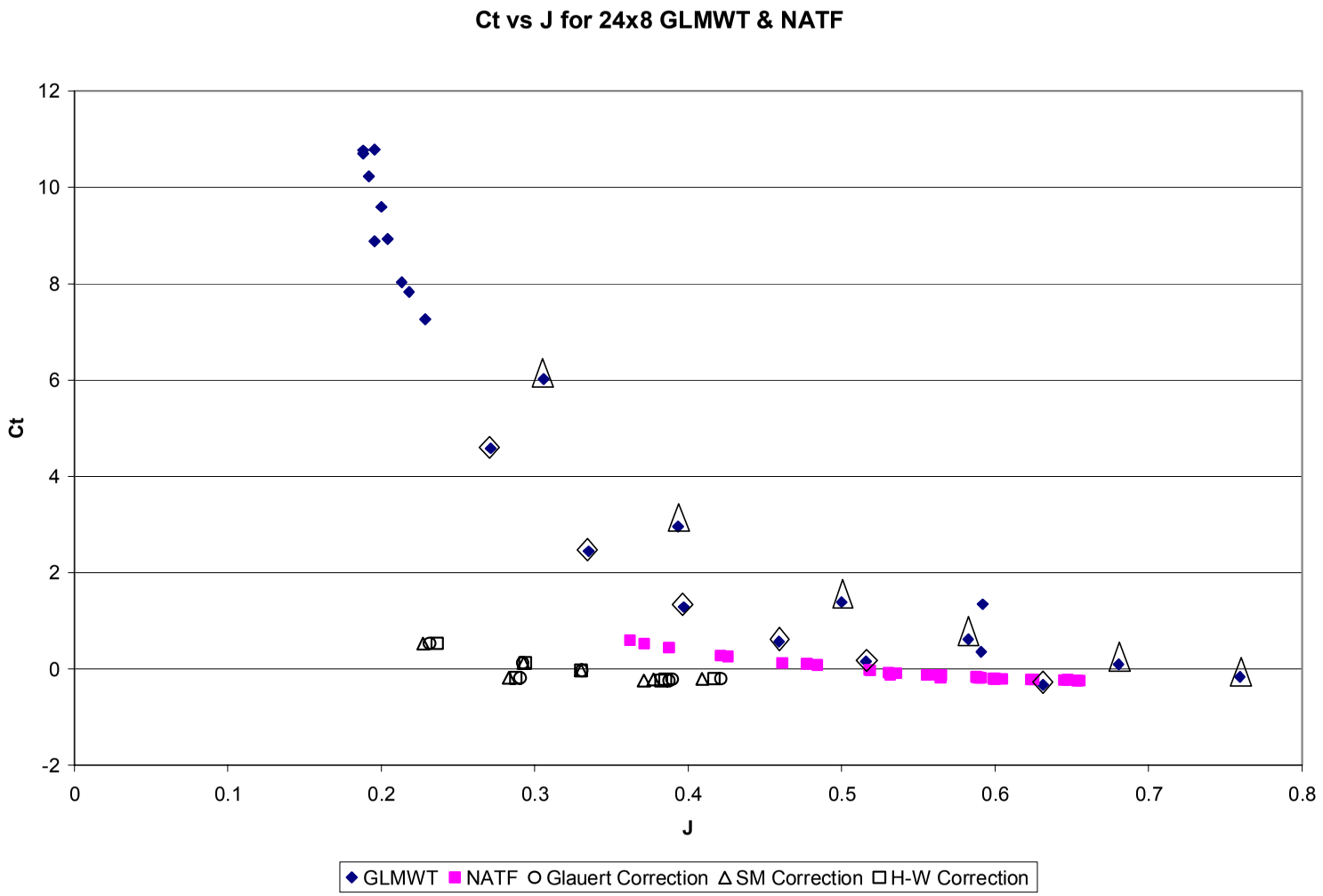

Figure 29. Data points corrected for wind tunnel blockage plotted against experimental data for the 24”x8” propeller.

As can be seen in the 24" x 8" propeller data, shown in figure 29, there appears to be two distinct thrust coefficient vs. advance ratio curves. They have each been delineated by a diamond and triangle around the data points. The cause of this "double curve" has been explored thoroughly. Based on this exploration, the most-likely cause of the double curve is due to hysteresis in the data collection equipment and scatter in the data. The examination of possible causes will be addressed later. Interestingly, this data split did not occur during testing of any other propellers or during NATF tests, though the same data collection technique was used.

3.7 Pressure Change Predictions

In each of Glauert's and Sorensen and Mikkelsen's derivation of their respective correction formula, an expression is derived for the pressure increase or decrease due to the total force the propeller exerts on the air in the wind tunnel test section. In Glauert's derivation, four equations and four unknowns can be used to solve for pressure differential. The first two equations are equations of continuity:

$$S_1 u_1 = Au \tag{30}$$

$$(C - S)\, u_2 = CV_o - Au \tag{31}$$

The second two equations are axial momentum equations:

$$T = S_1\rho u_1(u_1 - V_o) + (C - S)\rho u_2(u_2 - V_o) + C(p_2 - p_o) \quad (32)$$

Where T = thrust

p_o = wind tunnel datum pressure

p_2 = pressure far downstream of propeller

$$T = S_1\rho u(u_1 - V_o) + (C - S)\rho u_2(u_2 - V_o) + \tfrac{1}{2}C\rho(V_o^2 - u_2^2) \quad (33)$$

Using the equations of continuity to eliminate u solve for u_1 in terms of u_2 then substituting into equation 33, the pressure differential can be subsequently solved.

Sørensen and Mikkelsen have an explicit equation for predicting the pressure increase or decrease caused by the propeller. It is obtained by applying the momentum theorem on the wind tunnel:

$$T + (p_1 - p_o)C = \rho u_1 S_1(u_1 - V_o) - \rho u_2(C - S_1)(V_o - u_2) \quad (34)$$

All quantities are known and the pressure differential can be calculated directly.

These pressure differential predictions were transformed into velocity increment predictions using the same method as was used for experimental pressure measurement.

Table 1 shows side by side comparison of the calculated pressure, coefficient of pressure, and velocity increment differentials for the 18”x8” propeller. Additionally,

figures 30 through 32 show the velocity increment differential as predicted by Glauert's and Sørensen and Mikkelsen's methodology.

					Sorensen			Glauert		
Velocity (ft/sec)	Power Setting (1=L, 2=M, 3H)	Density (psf)	Thrust (pounds)	Ct	Delta P (psf)	Delta Cp	Deltau/U	Delta P	Delta Cp	Deltau/U
130.2705	1	0.00229	-11.07	-0.32281	0.06405	0.00330	-0.00165	-0.86165	-0.07300	0.03586
129.9858	2	0.00228	-8.427	-0.24866	0.22486	0.01165	-0.00584	-0.92014	-0.05456	0.02692
70.1400	1	0.00229	-2.93	-0.29694	0.09653	0.01716	-0.00862	-0.83666	-0.06623	0.03258
50.9636	1	0.00229	-0.9104	-0.17445	0.01635	0.00551	-0.00276	-1.02679	-0.03743	0.01854
70.2988	2	0.00229	2.246	0.226393	0.04087	0.00723	-0.00362	-1.18443	0.04141	-0.02092
49.9574	2	0.00229	5.87	1.171107	0.40192	0.14053	-0.07292	-1.55783	0.14501	-0.07534
70.2146	3	0.00229	7.112	0.71451	0.34392	0.06103	-0.03100	-1.31705	0.10709	-0.05506
50.2740	3	0.00228	10.97	2.159215	1.71408	0.59620	-0.36455	-2.07489	0.18139	-0.09523

Table 1. Predicted pressure, coefficient of pressure, and velocity increment differentials as predicted by Sørensen and Mikkelsen and Glauert's methods for the 18"x8" propeller.

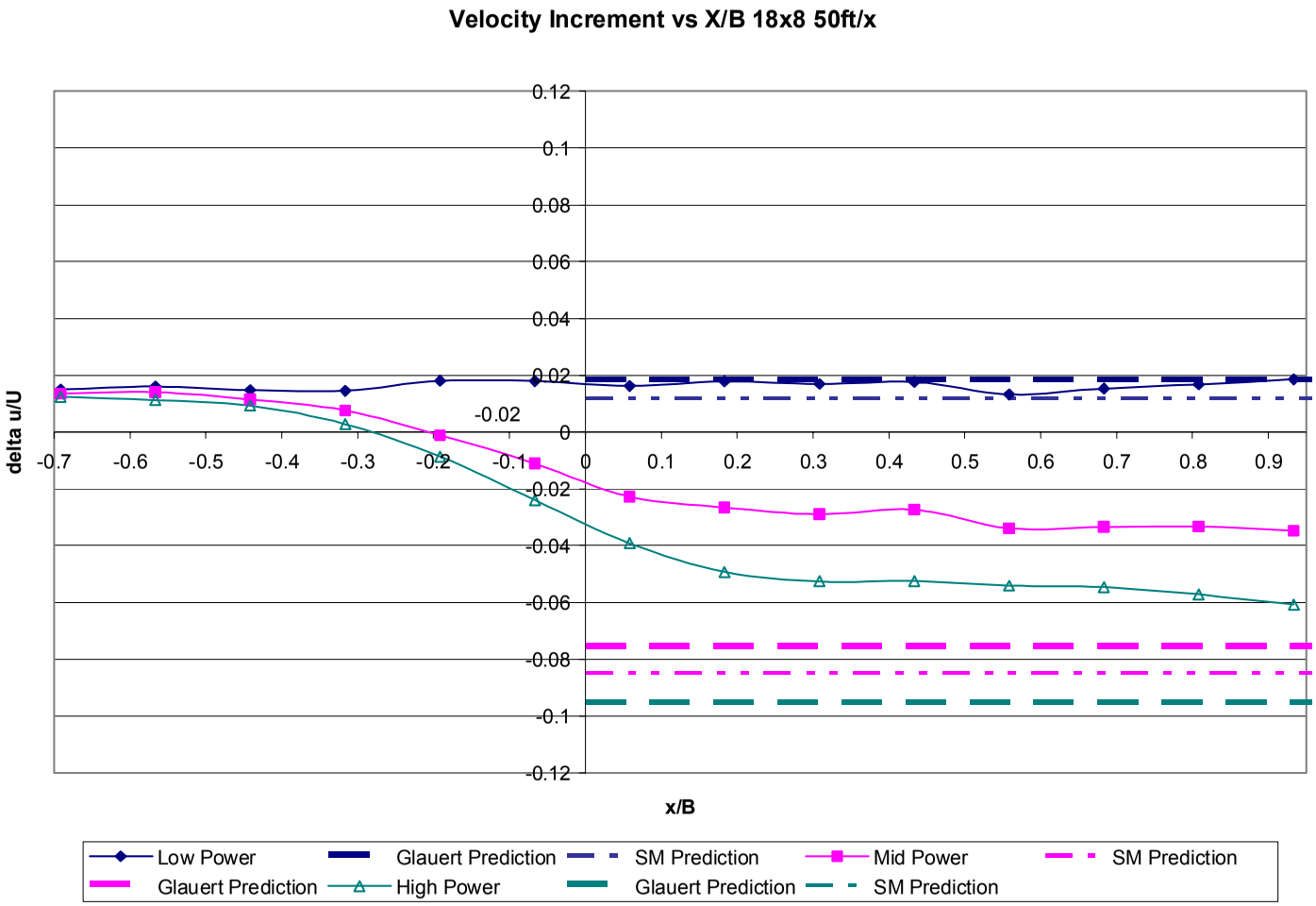

Figure 30. Predicted incremental velocity differentials plotted against velocity increments obtained from experimental data for the 18”x8” propeller and wind tunnel velocity of 50 ft/s.

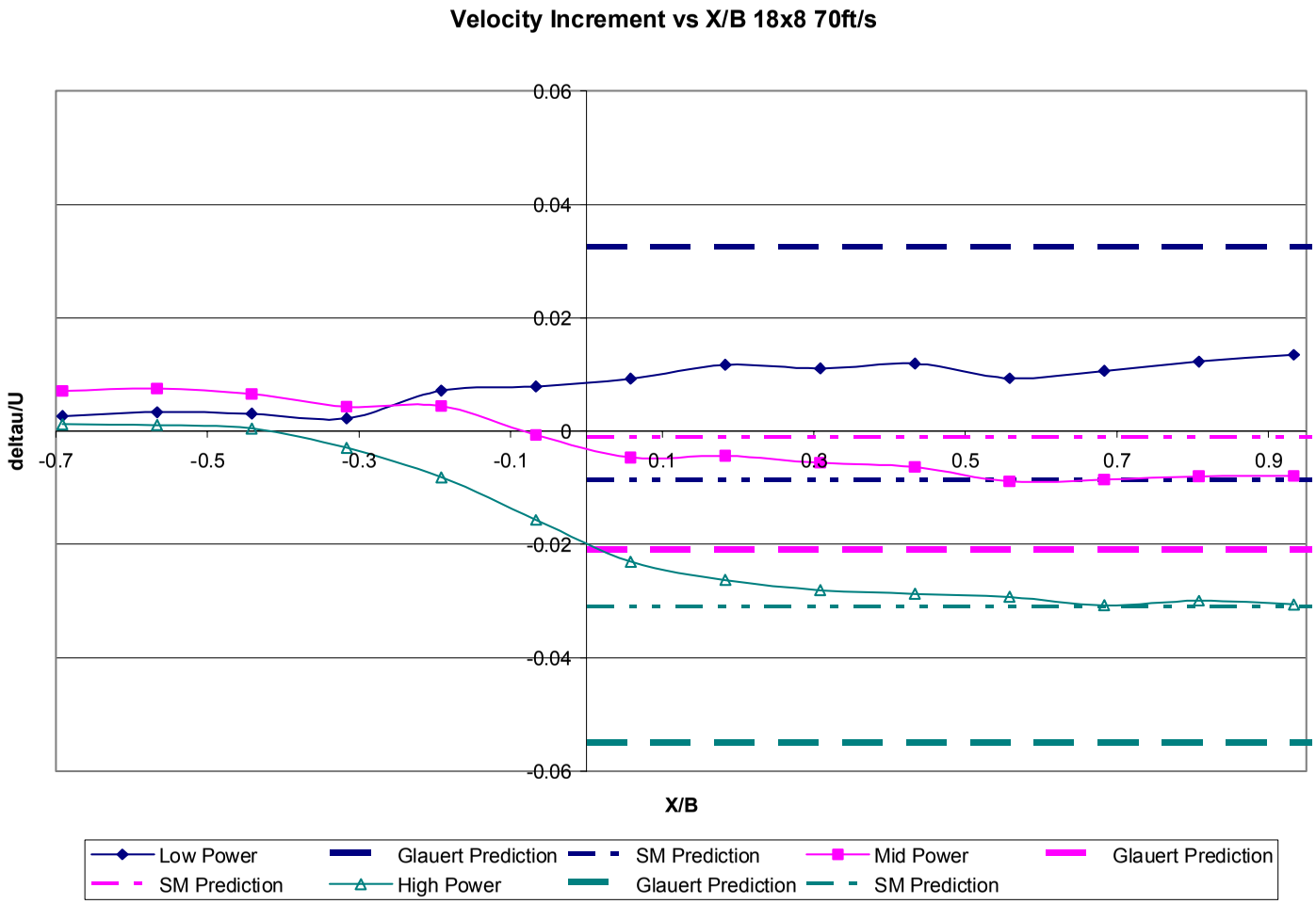

Figure 31. Predicted incremental velocity differentials plotted against velocity increments obtained from experimental data for the 18”x8” propeller and wind tunnel velocity of 70 ft/s.

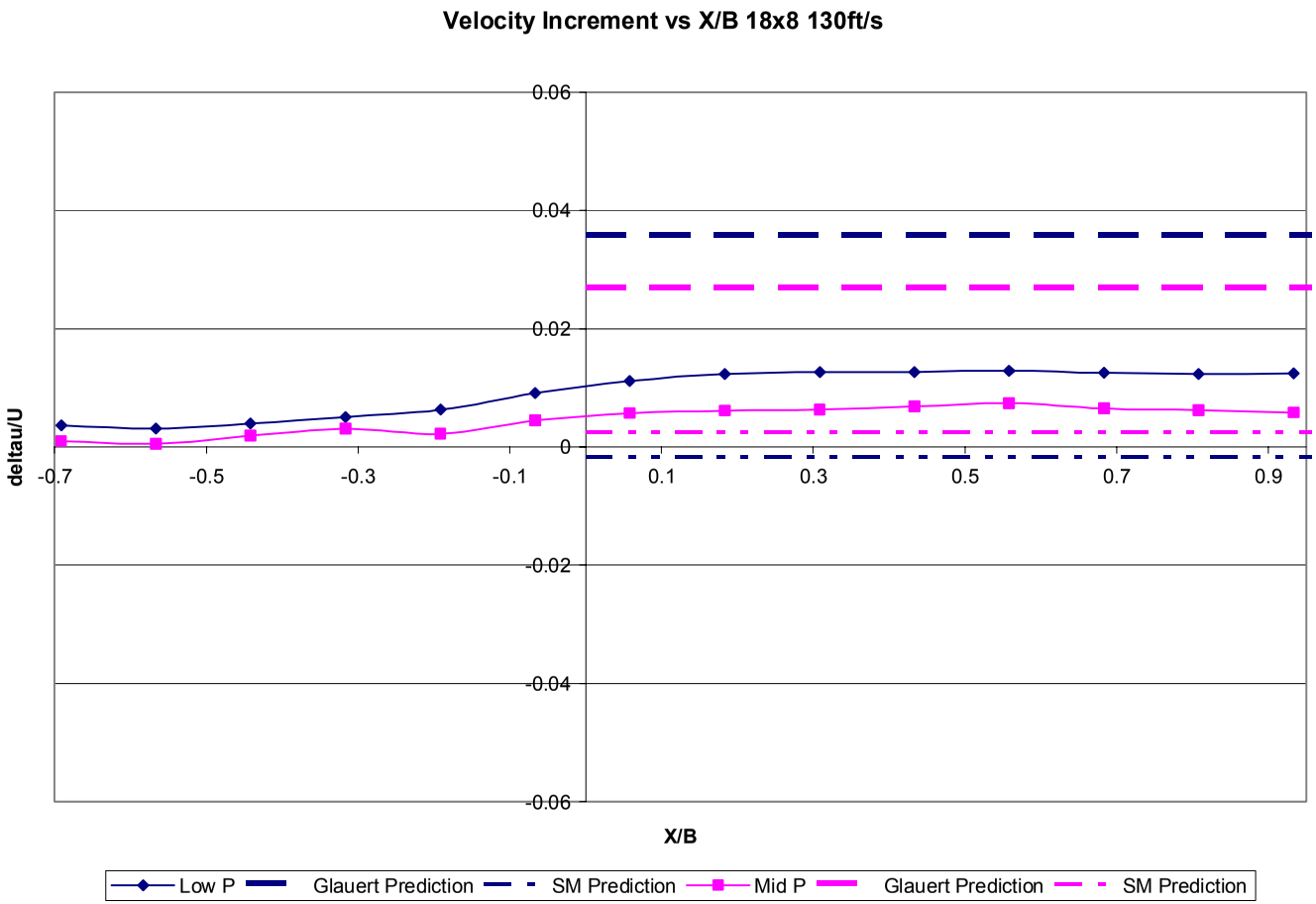

Figure 32. Predicted incremental velocity differentials plotted against velocity increments obtained from experimental data for the 18”x8” propeller and wind tunnel velocity of 130 ft/s.

3.8 Discussion

3.8.1 Corrected NATF Data

As stated, the purpose of this thesis was to collect high quality powered propeller data to which select correction methodologies may be applied. Glauert corrections, Hackett-Wilsden, and Sørensen and Mikkelsen correction methodologies were explored to assess the validity of the two latter against the widely used former correction method for wind tunnel blockage.

Due to blockage effects and consistent with Glauert's correction, higher thrust is expected to result in the model and tunnel configuration with higher blockage. Glauert's correction states that due to the necessary satisfaction of continuity, the discontinuity in pressure across the propeller blade, and changes in air velocity moving outside of the propeller slipstream, a higher thrust is developed by the propeller in the wind tunnel than otherwise would be in an unrestricted flow of the same speed with the same propeller rotation rate and blade angle. This is true when the propeller is operating such that positive thrust is produced. In this case, the negligibly small blockage ratio at GLMWT results in essentially unrestricted flow around the propeller. Conversely, at NATF, the blockage is high and more thrust is expected to be developed by the propeller at NATF than at GLMWT, at the same operating conditions.

Figures 26 through 29 provide comparisons for the correction methodologies. These figures show thrust coefficient vs. advance ratio data for both tunnels. Superimposed on this data is the corrected NATF data, resulting from calculated corrections using

the Glauert, Hackett-Wilsden, and the Sørensen and Mikkelsen methodologies. Three assessments can be made:

1) The magnitude of the corrections increase as propeller diameter increases.
2) Agreement between Glauert, Hackett-Wilsden, and Sørensen and Mikkelsen appear to be good at low positive thrust coefficients, but begin to diverge at thrust coefficients of about 1.2.
3) There appears to be better agreement between Glauert and Hackett-Wilsden corrections than between Glauert and Sørensen and Mikkelsen or Hackett-Wilsden and Sørensen and Mikkelsen.

Data from each propeller will be addressed separately. Figure 26 shows the coefficient vs. advance ratio data for the 14"x8" propeller. Clearly, there was little blockage effect even at NATF, as the area ratio was only 6.7%. The corrected data, indicated by the black outlined points on Figure 26, is very close to the actual data collected.

The data collected for the 18"x8" data, shown in figure 27, demonstrates that the thrust measured at NATF was not appreciably greater than that GLMWT, as expected. This is surprising considering the blockage for the 18"x8" propeller is 11%. However, this does not imply that there was no blockage correction needed. The corrected NATF data, shown in black outlined points, does correct the data. However, it brings the NATF data curve below that of the GLMWT data. This may lie in the scatter, but it does show the beginning of an unexpected trend.

Even though the blockage correction shows unexpected results, among the three correction techniques, good agreement is shown. Again, the correspondence of Glauert and Sørensen and Mikkelsen corrections diverge at a thrust coefficient of about 1.2.

It should be noted that in figure 27, both the repeat run for the 18"x8" propeller at GLMWT is shown as well as a repeat run for NATF. The NATF repeat run is shown by pink outlined triangles. The repeatability at NATF is outstanding. Additionally, the Glauert-corrected GLMWT data is shown for fully corrected comparison purposes.

Figure 28 shows the coefficient of thrust vs. advance ratio for the 22"x8" propeller. This data set continues to show unexpected results. First, the thrust coefficient data from NATF is not appreciably greater than the same data from GLMWT. This is unexpected, as blockage effects should be more pronounced with the large blockage ratio of 16.5% that the larger propeller casues. Additionally, the corrected data greatly reduces the thrust coefficient for the NATF data. This is a continuation of the unexpected trend in correction results. While care has been taken in examining data reduction and calculation techniques, the cause of the unexpected result has not been found. Possible causes will be addressed in a following section.

Finally, figure 29 shows the thrust coefficient vs. advance ratio data for the 24"x8" propeller. Again, the result is unexpected, but it is also consistent with the 18"x8" and 22"x8" data correction trend; the thrust coefficient data from NATF is less than that at GLMWT. Additionally, low advance ratio data was impossible to collect at NATF as the motor consistently overheated prior to a successful test point being

taken. Unfortunately, this prohibits comparison of data at advance ratios less than 0.37. The NATF data appears to lie within the "lower curve" of the GLMWT data at advance ratios of about 0.45 and greater. However, the trend shows that it begins to diverge below this advance ratio. Additionally, as in the 18"x8" and 22"x8" propeller data, the corrected NATF data further reduces the thrust coefficient data instead of correcting it to the GLMWT data.

3.8.2 Pressure Prediction Data

Table 1 shows the predicted pressure change and corresponding coefficient of pressure and velocity increment changes for the 18"x8" propeller. Additionally, figures 30 through 32 show the predicted velocity increment change. This data was calculated using intermediate equations in the Glauert and Sørensen and Mikkelsen correction methodologies.

Each of these figures shows a poor prediction of velocity increment change using either methodology. There appears to be no trend in terms of over prediction or under prediction of the velocity increment change. Hackett's suggestion that the test section length may cause lack of asymptote establishment potentially explains one possible contributor to these incorrect predictions. However, in the case of this experiment, it appears that the downstream asymptotic value is certainly established and the test section length is not a cause of the inaccuracy between the predicted downstream pressure values and the actual downstream pressure values. This is an area for further study.

3.8.3 Possible Reasons for Unexpected Data

3.8.3.1 "Double Curve" in 24"x8" Propeller Data

The double curve in the 24"x8" propeller data is unexpected and is not duplicated in any other test run at either tunnel. Several possibilities for this double curve behavior have been explored:

1) Due to time constraints, an RPM counter was not included in the wind tunnel model. This resulted in using the stroboscope for measurement of RPM. This proved to be very time consuming. Additionally, it was possible that if the stroboscope was not used properly, the wrong RPM could be measured. Great care was taken at NATF that this be avoided. However, the potential for this to occur was not realized at GLMWT and not as much care was used in measuring RPM. Therefore, it is possible that the RPM value recorded may be a blade passage frequency in error. However, after all data reduction and plotting was accomplished, a study was completed to assess the probability of RPM error being the source of the double curve. It was concluded that the RPM was reliable and correct and this possibility was discarded.

2) Hysteresis in the power setting mechanism on the remote control is a possible cause for the double curve. This was realized as a possibility only after observing the unusual behavior and there is no way to measure the probability of this cause as the remote control

has been dismantled. However, it very well may be the cause of the error and is assigned medium probability.

3) It is also possible that this double curve is due to RPM effects of the propeller. This was not explored and it is recommended that it be an area of further study.

4) Tip mach number effects may also cause this double curve. However, this has been assigned low probability based on the fact that the smaller diameter propellers, operating at higher RPMs did not display this behavior. The larger diameter propeller would have to be at a much higher RPM to cause tip mach number effects.

5) Due to the results shown in the 18"x8" propeller repeat runs, it is possible that the data scatter and/or lack of high quality repeatability at GLMWT causes data anomalies. A quality examination of the repeatability was not performed both due to time constraints and due to the lack of repeat runs to provide sufficient data for this study.

3.8.3.2 Blockage Corrections causing Unexpected Results

In addition to the double curve shown in the 24"x8", the results given by the blockage corrections at NATF are unexpected. The result desired in this study was to successfully correct higher-thrust NATF data to GLMWT data using the three methodologies. This clearly was not the result. It is difficult to understand why the

thrust values at NATF were not higher than those at GLMWT as is expected. Only a few possibilities exist for this:

1) The data gathered at GLMWT was not correct. Based on present and past performance at GLMWT, this is not highly probable. GLMWT is a well-known and well-respected facility that continuously provides high quality data to industry and research groups. The balance at GLMWT has a low uncertainty of only ±0.015 lb, in axial force, and continues to operate well through the present time.

2) The data gathered at NATF was not correct. This has a bit higher probability than at GLMWT based on the higher uncertainty of ±0.49 lb versus only ±0.015 lb at GLMWT. This approximate half-pound, if realized, may cause enough inaccuracy in the data to cause produce the unexpected results. However, as at GLMWT, the NATF tunnel is widely-used and well-respected for high quality data. It is unlikely that this is the cause in the unexpected data.

Neither of the above cases seem likely to have caused the unexpected results. It is suggested that this also be an area for future study.

CHAPTER 4 CONCLUSIONS

The method of mathematically simulating the solid body and wake blockage suggested by Hackett-Wilsden is a sound method. It provides for further calculation of pressures, using other methodologies, and velocity increments and allows one to compare the expected data to the experimentally obtained data.

For the 14”x8” propeller, little blockage is observed in the NATF tunnel. However, the blockage corrections increase as the propeller diameter increases. This is expected. However, the absolute value of the thrust data collected at NATF is unexpectedly low for all propellers from the 18”x8” propeller and larger

The Glauert and Sørensen and Mikkelsen correction methodologies appear to agree for thrust coefficients up to about 1.2. They begin to diverge above this value. Since Sørensen and Mikkelsen applied their correction methodology to wind turbines and not to thrust-producing propellers, perhaps there is an unexpected effect when the propeller is in a thrust-producing state. Because the Glauert correction has been used and accepted for over seventy-five years, this author believes that this is the correction that should be applied over the Hackett-Wilsden and Sørensen and Mikkelsen correction until the divergence between the corrections is understood.

The Glauert and Hackett-Wilsden corrections appear to agree up to a thrust coefficient of approximately 2. This shows better agreement than between Glauert and Sørensen and Mikkelsen.

It is interesting to note that although the corrections for the 18”x8”, 22”x8”, and 24”x8” propellers appear to be incorrect, all three methodologies resulted in

approximately the same correction. This comparison accomplishes the original goal of evaluation of two new correction methodologies to the relatively accepted Glauert correction.

CHAPTER 5 RECOMMENDATIONS FOR FUTURE WORK

It is recommended that in future propeller data collection that specific attention be paid to the methodology of collection. Specifically, experimentation can be executed to examine the effects of varying RPM settings with the wind tunnel speed consistently set at a low or high value. Avoidance of two "curves" in the data is desired. Exploration of possible tip mach effects and RPM effects should be conducted.

Examination into the cause of the divergence between Glauert and Sørensen and Mikkelsen corrections above the thrust coefficient value of 1.2 should also be completed.

Cause of the unexpectedly low thrust coefficient values for the 18"x8", 22"x8", and 24"x8" propeller data in NATF should be understood.

Finally, the change in pressure predictions calculated from the Glauert derivation and the Sørensen and Mikkelsen derivation should certainly be explored further. The lack of trends and accuracies is unexpected.

APPENDIX A

Scimitar series propellers with 8” geometric pitch.

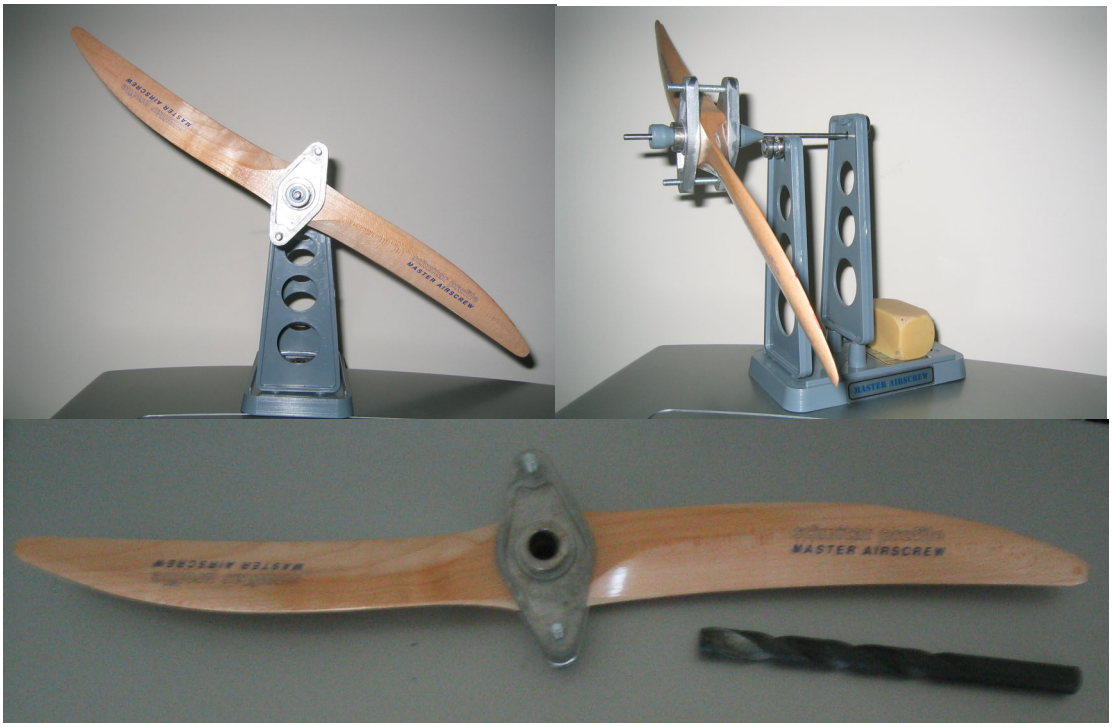

Propeller balance stand, drill guide bushing, and drill bit.

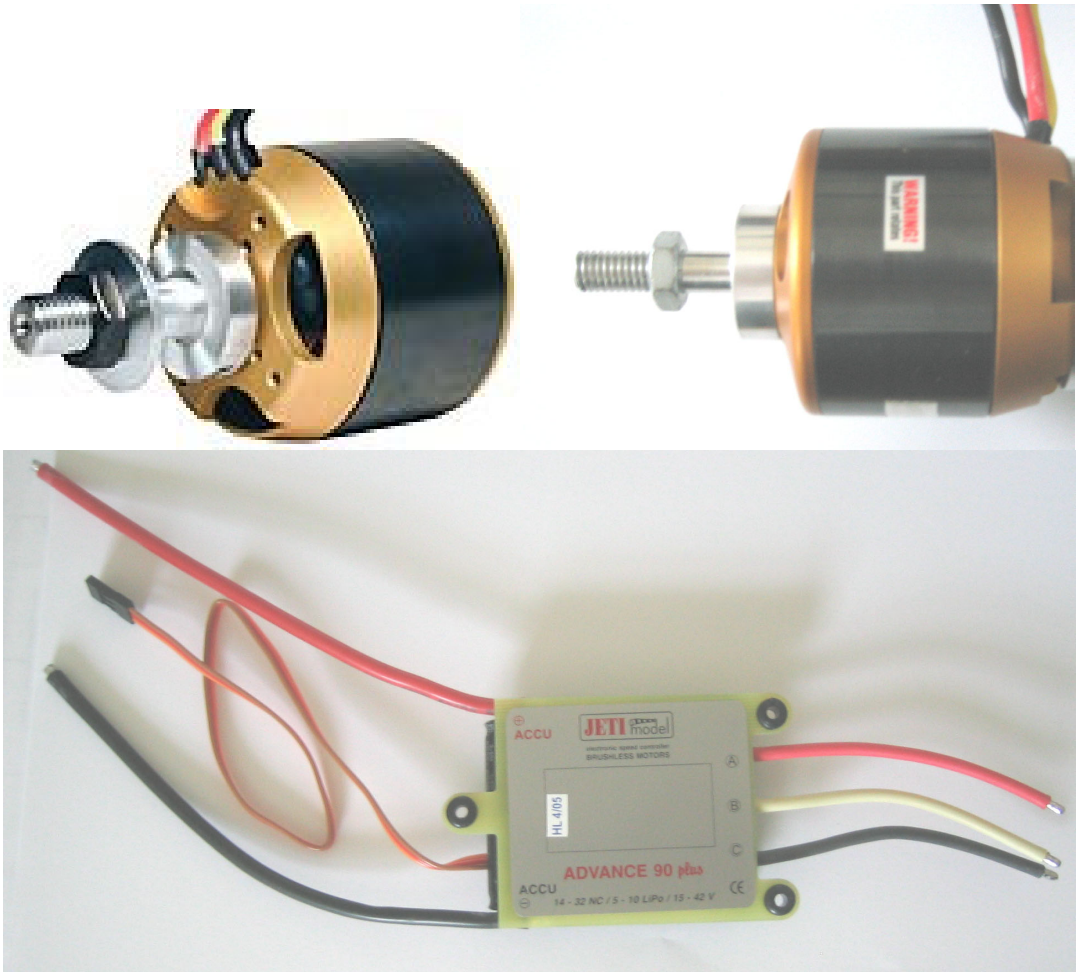

AXI Outrunner Motor and Jeti ESC.

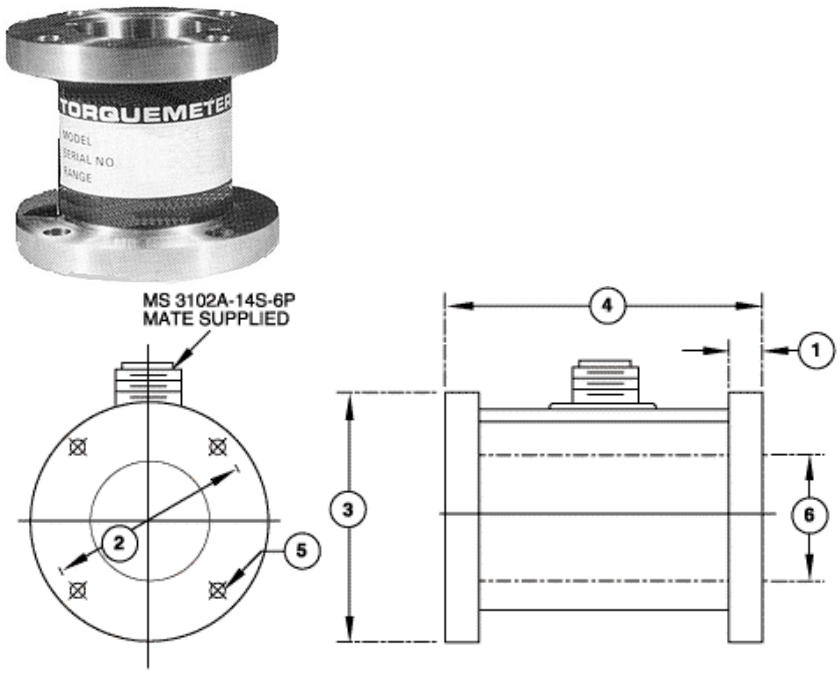
TORQUEMETER
MODEL
SERIAL NO.
RANGE
MS 3102A-14S-6P
MATE SUPPLIED
1
2
3
4
5
6

Torque cell.

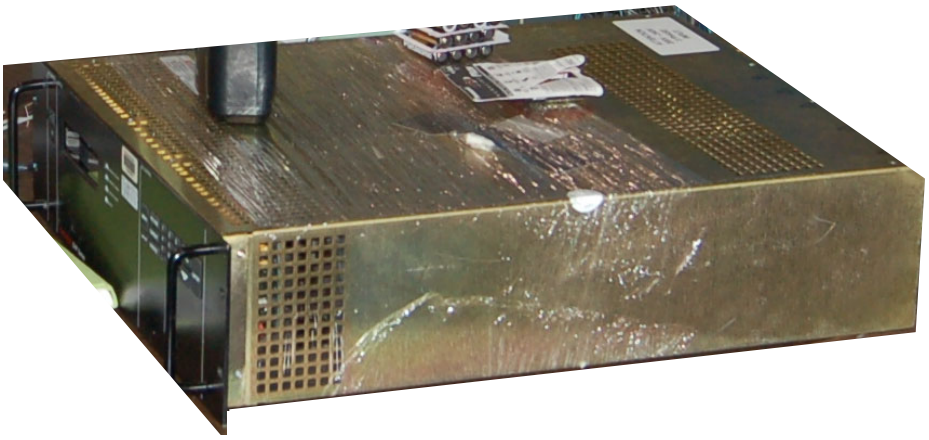

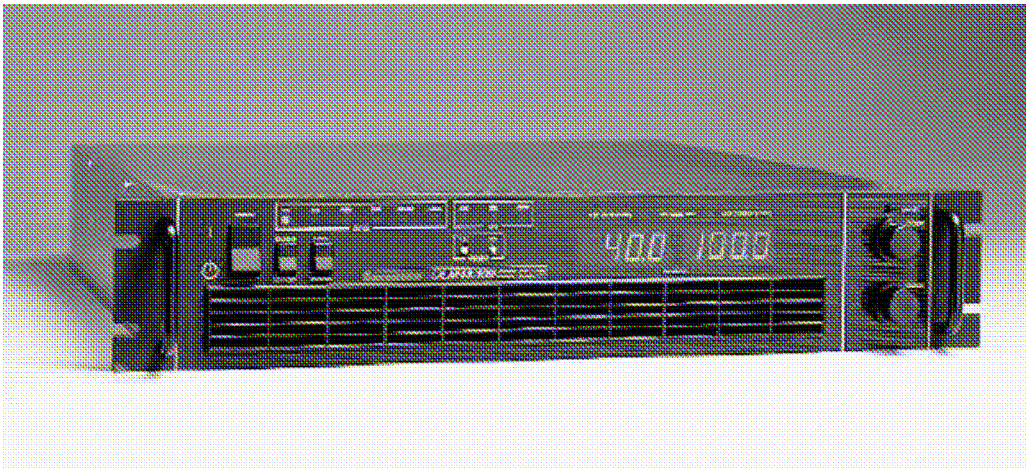

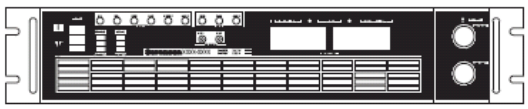

Front View

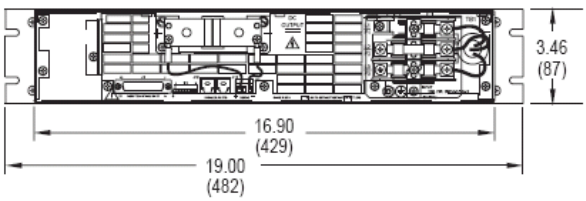

Rear View

Dimensions in inches (millimeters)

Power supply.

Remote control with trim pot modification.

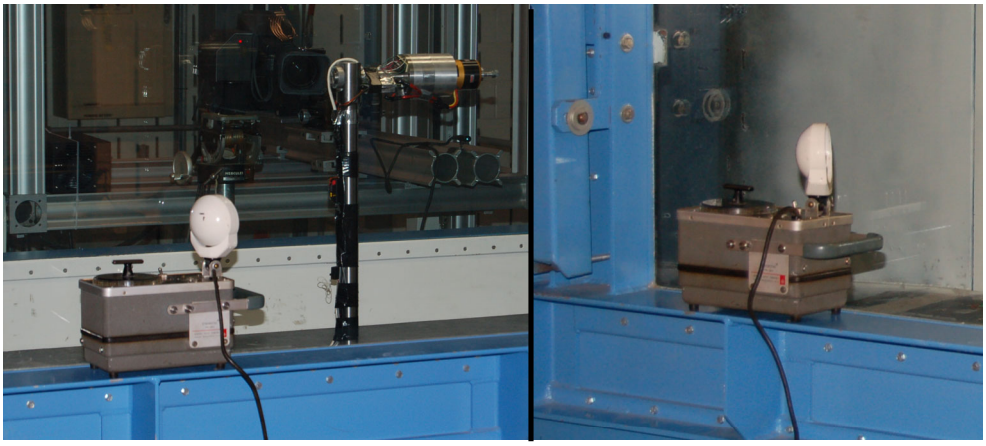

Stroboscope at NATF.

Pressure board installed at NATF

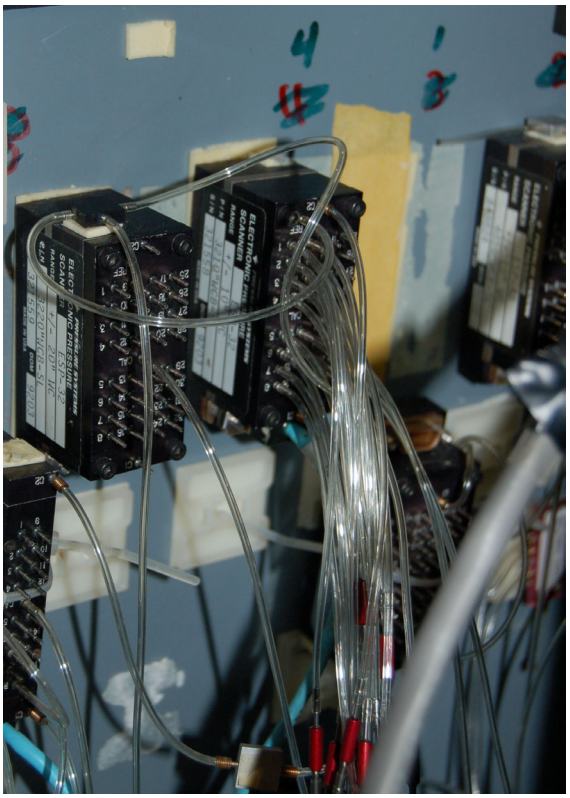
Sensing equipment for pressure tubes.

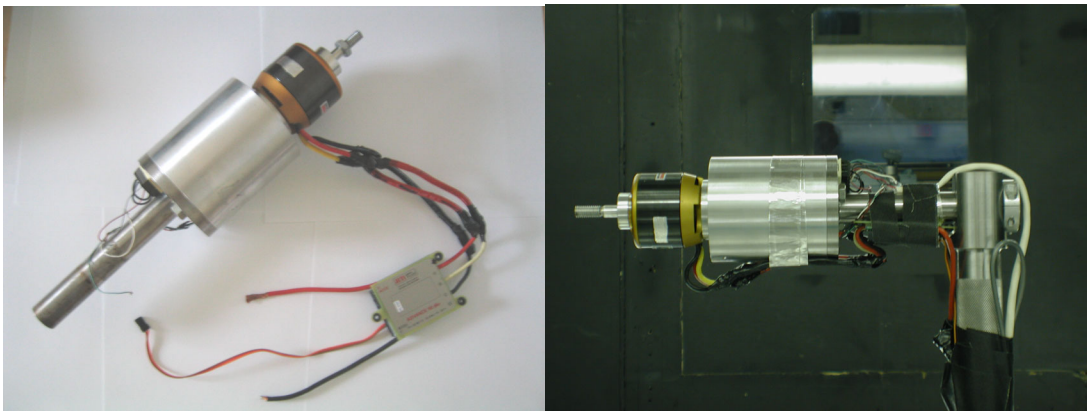

Motor with housing and ESC (left) and as installed (right).

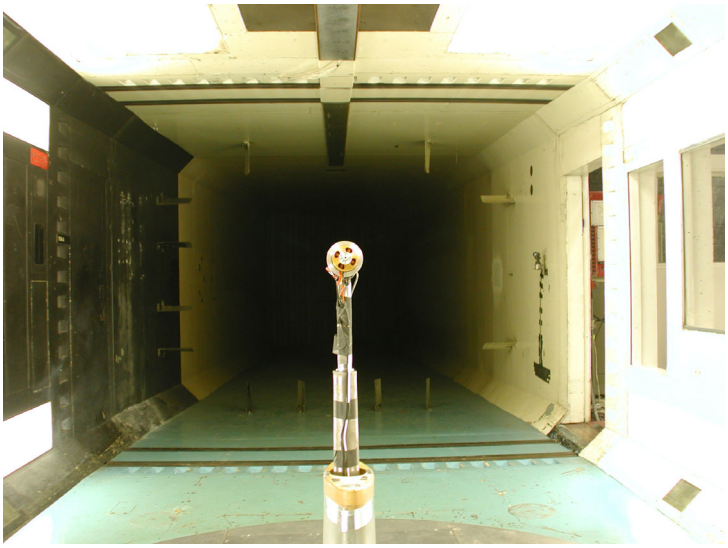

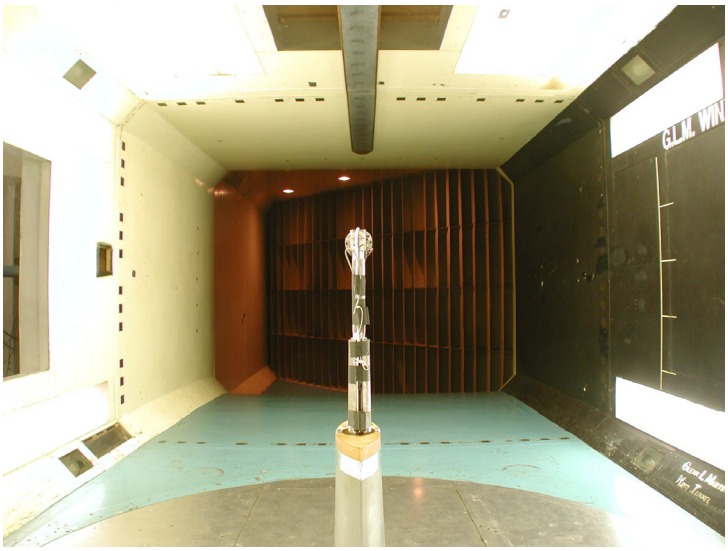

Motor and housing installed on support structure at GLMWT.

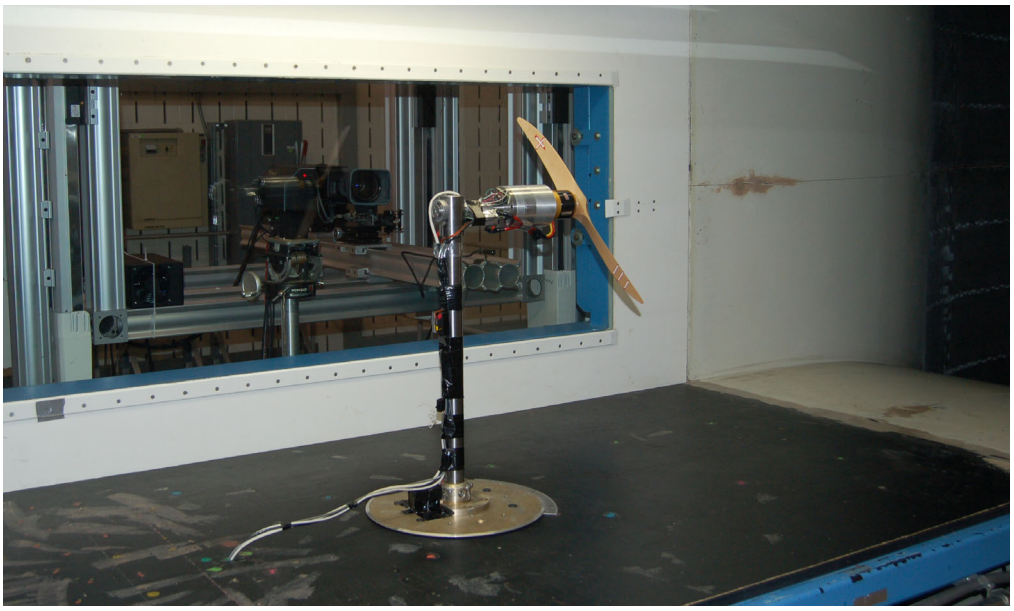

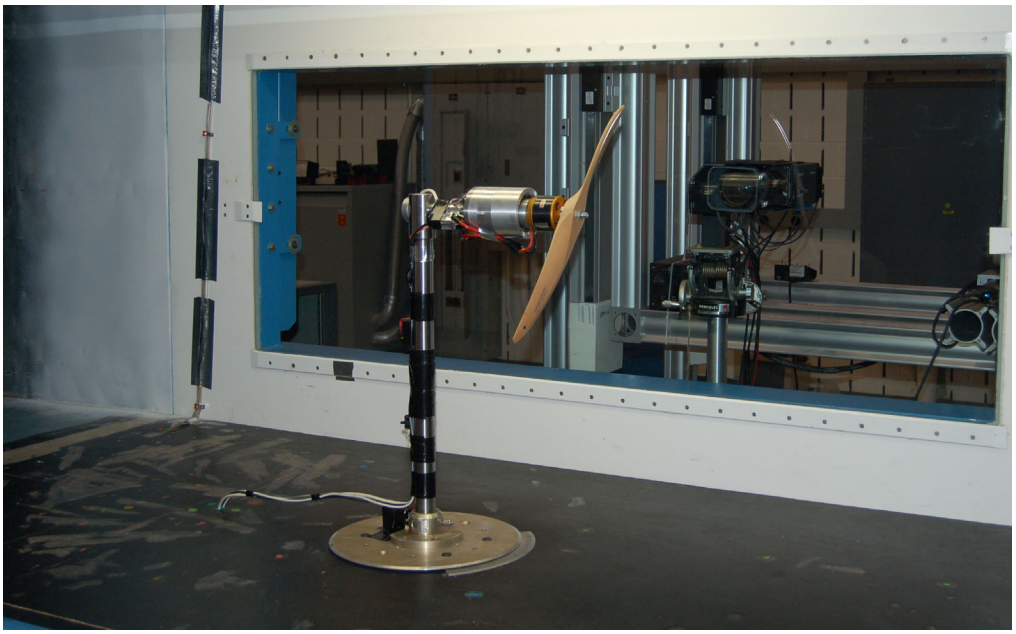

Motor and housing installed on support structure at NATF.

APPENDIX B

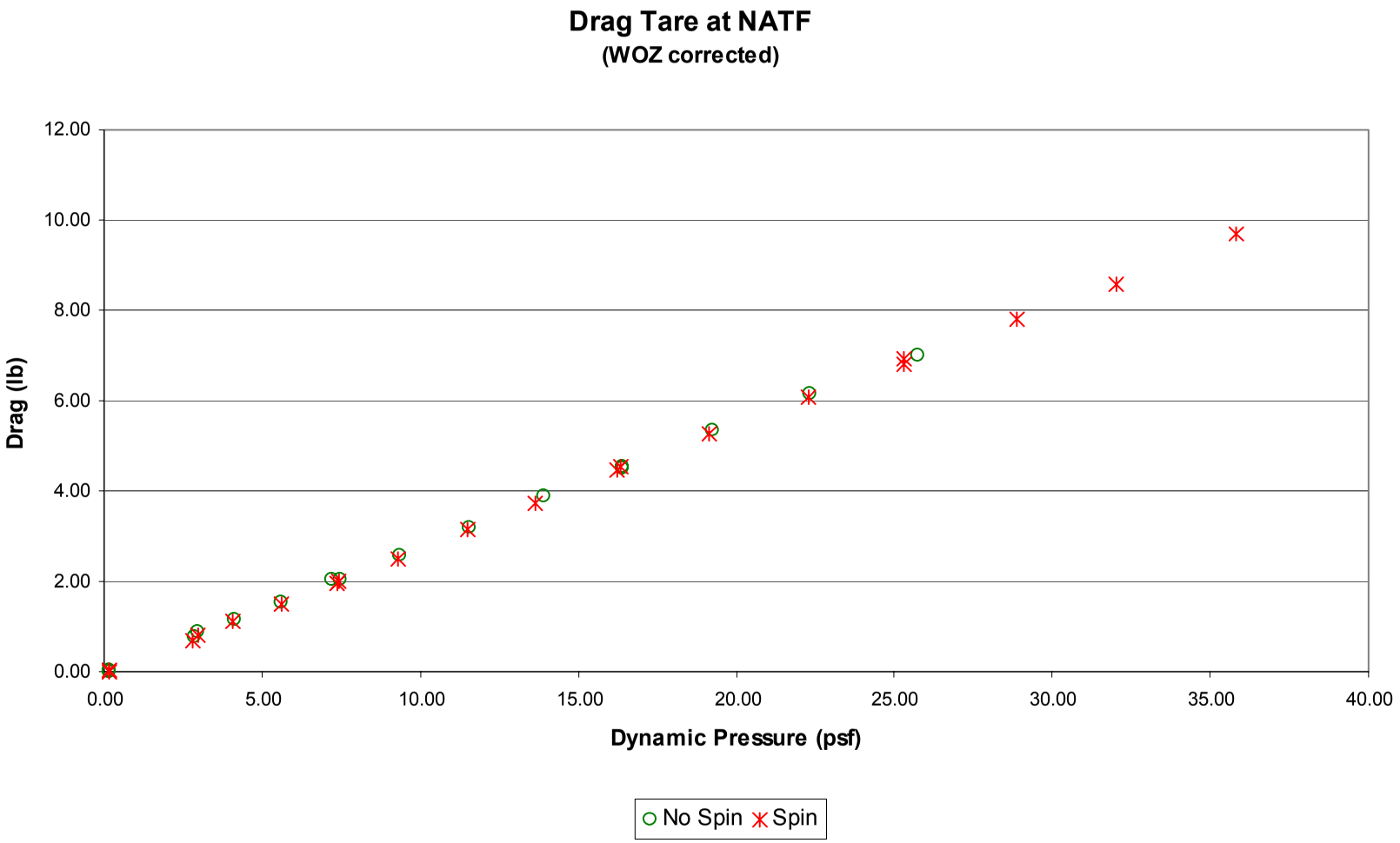

NATF drag tare, motor spinning and stationary.

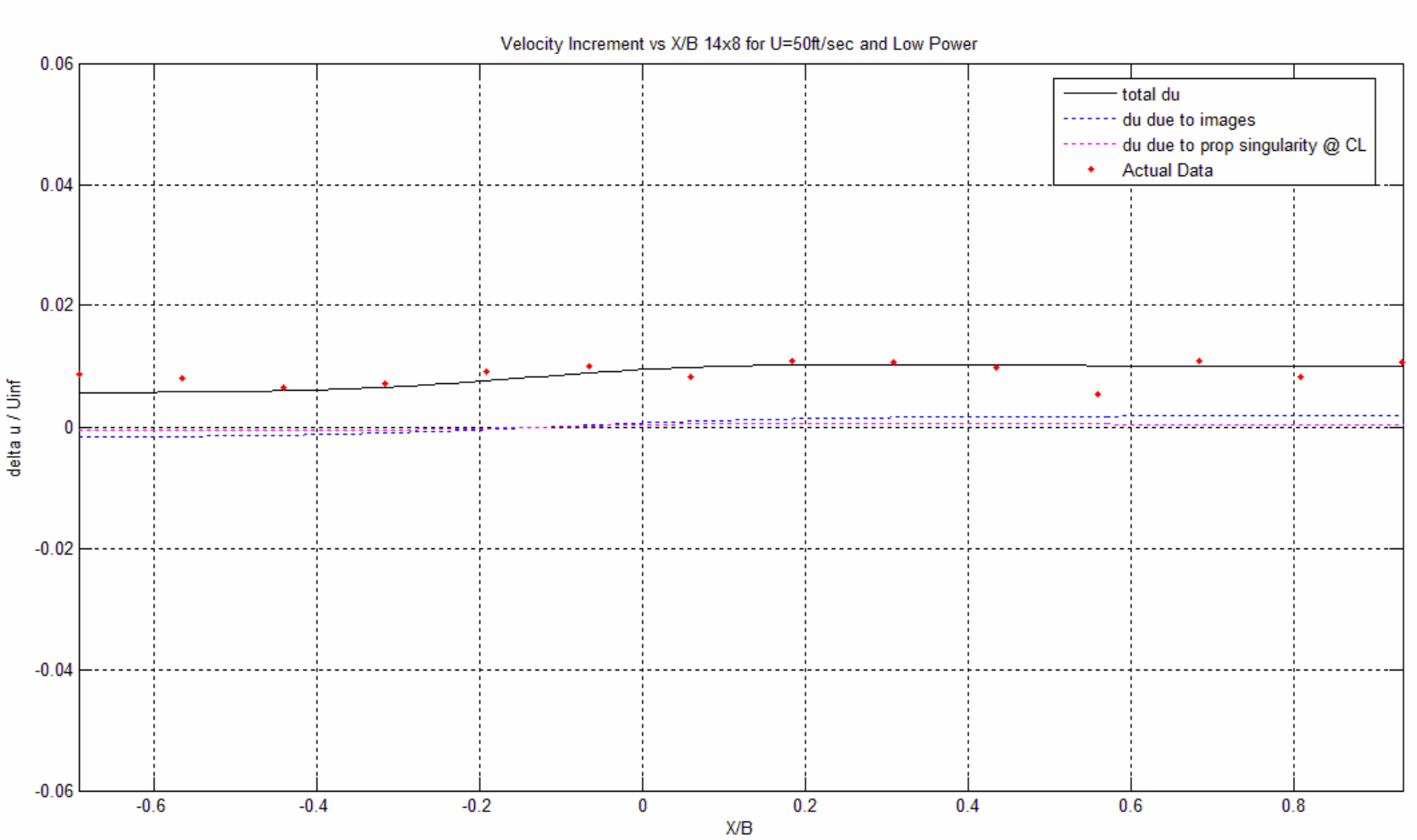

Velocity increment calculated from mathematical simulation model and propeller plotted against experimentally produced velocity increment for 14”x8” propeller rotating at low RPM and wind tunnel speed of 50ft/s.

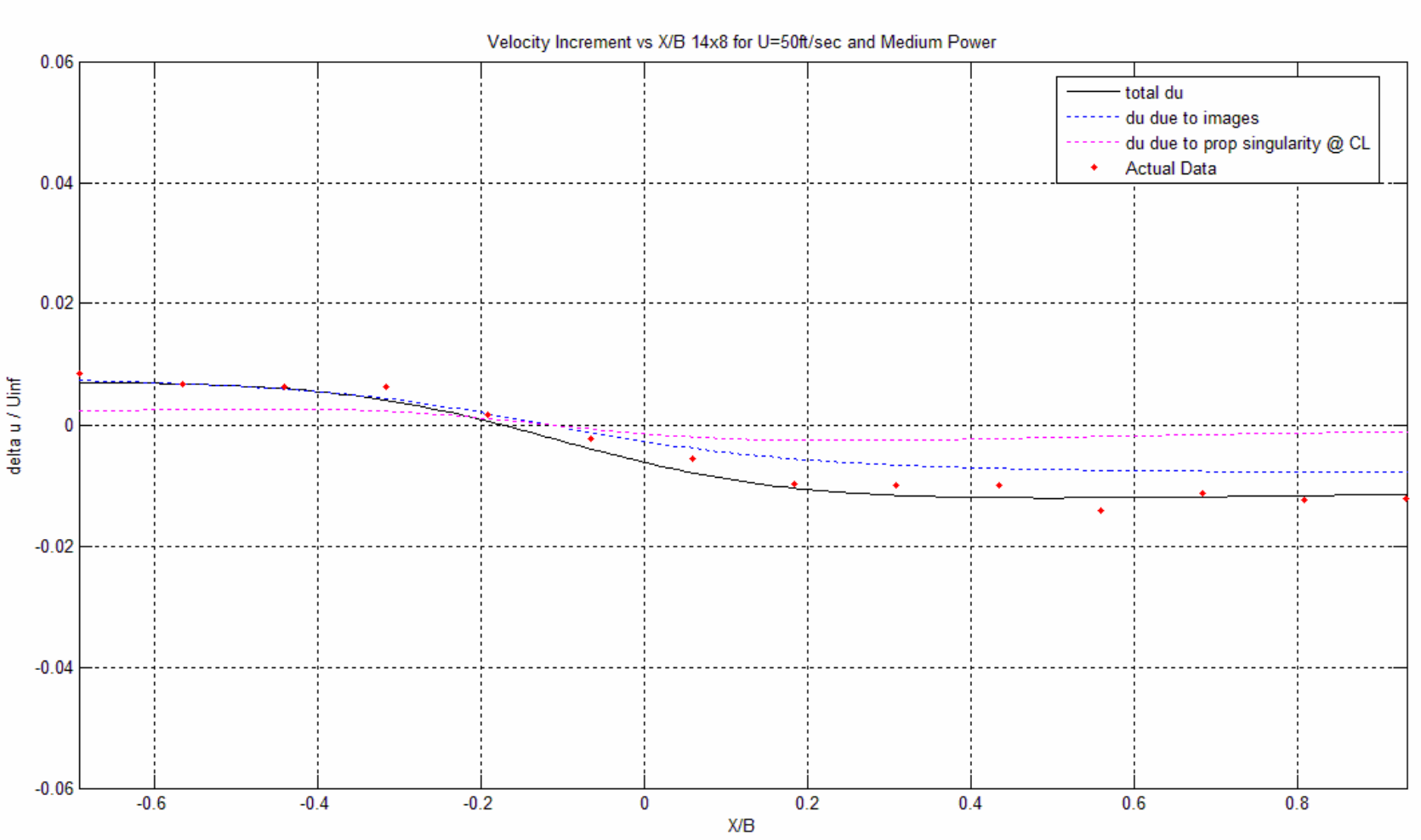

Velocity increment calculated from mathematical simulation model and propeller plotted against experimentally produced velocity increment for 14”x8” propeller rotating at medium RPM and wind tunnel speed of 50ft/s.

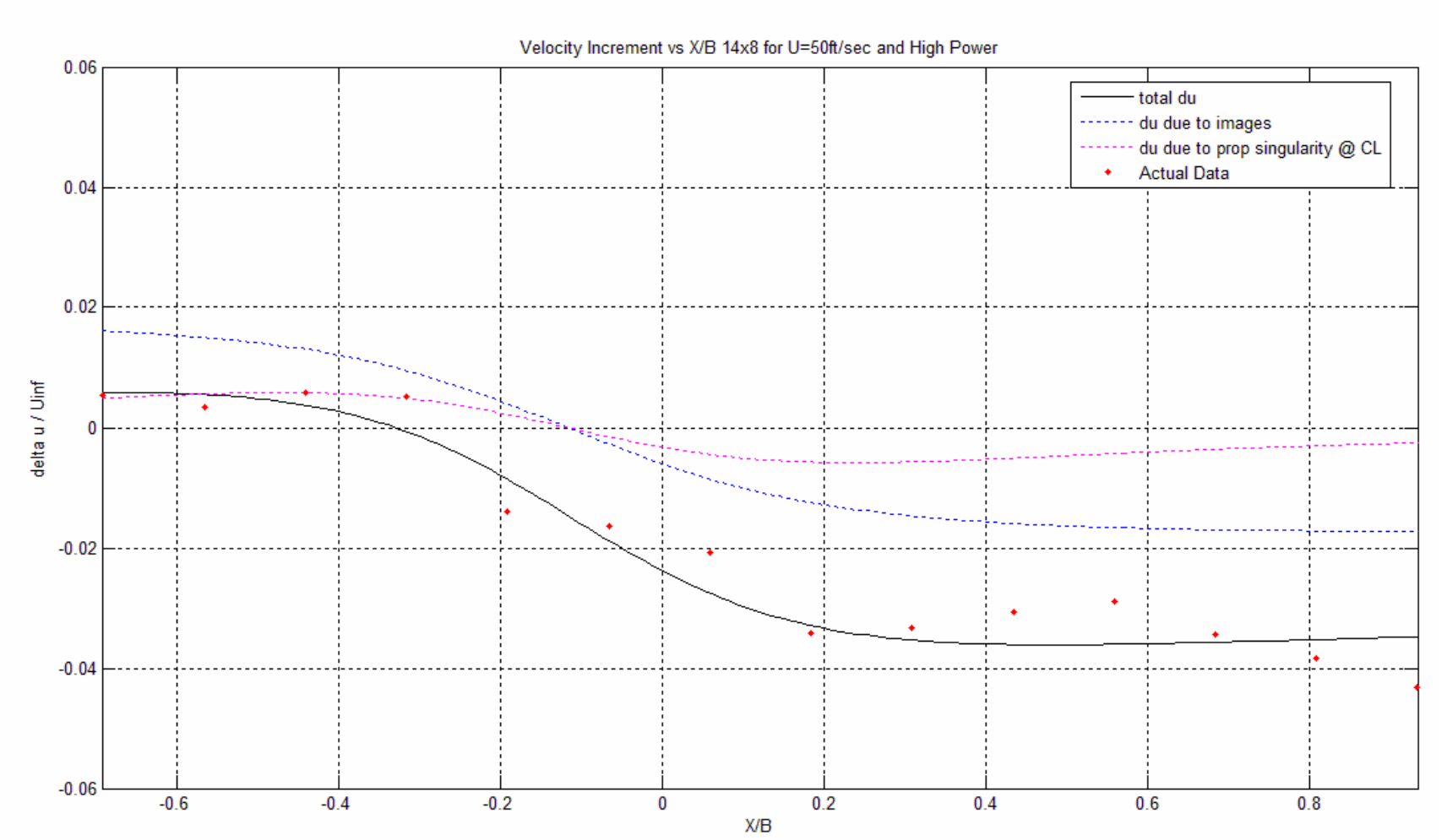

Velocity increment calculated from mathematical simulation model and propeller plotted against experimentally produced velocity increment for 14”x8” propeller rotating at high RPM and wind tunnel speed of 50ft/s.

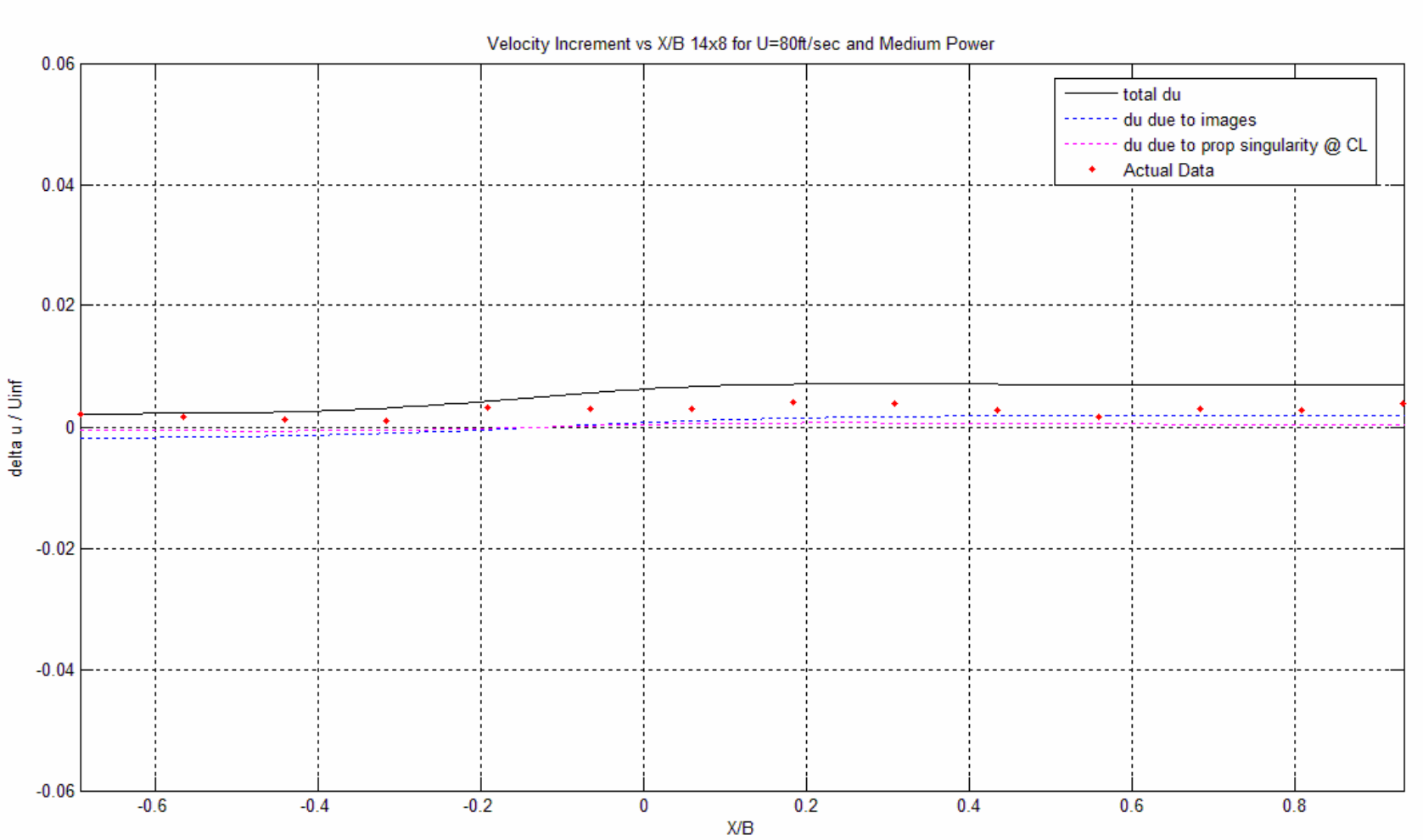

Velocity increment calculated from mathematical simulation model and propeller plotted against experimentally produced velocity increment for 14”x8” propeller rotating at medium RPM and wind tunnel speed of 80ft/s.

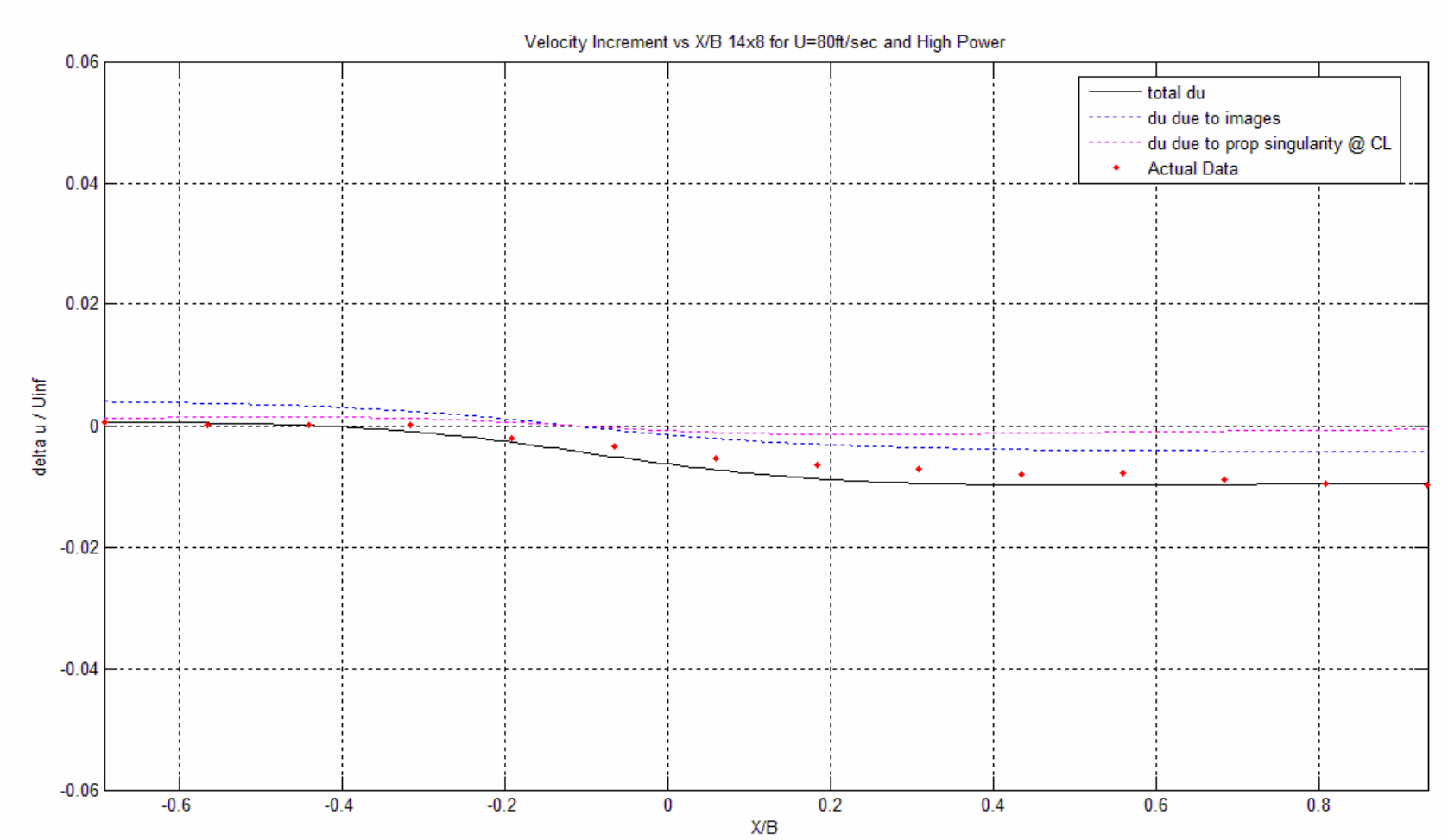

Velocity increment calculated from mathematical simulation model and propeller plotted against experimentally produced velocity increment for 14”x8” propeller rotating at medium RPM and wind tunnel speed of 80ft/s.

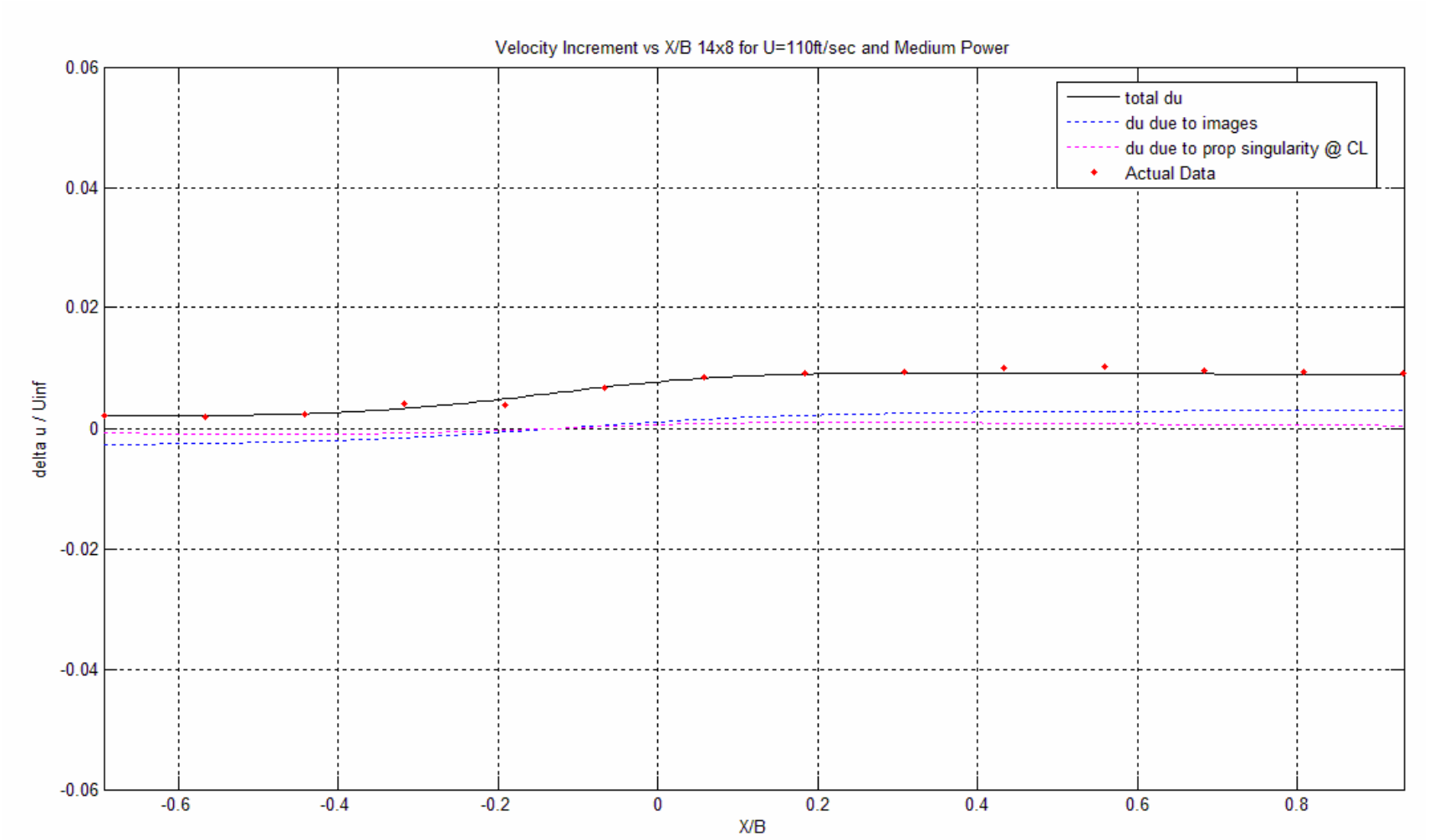

Velocity increment calculated from mathematical simulation model and propeller plotted against experimentally produced velocity increment for 14”x8” propeller rotating at medium RPM and wind tunnel speed of 110ft/s.

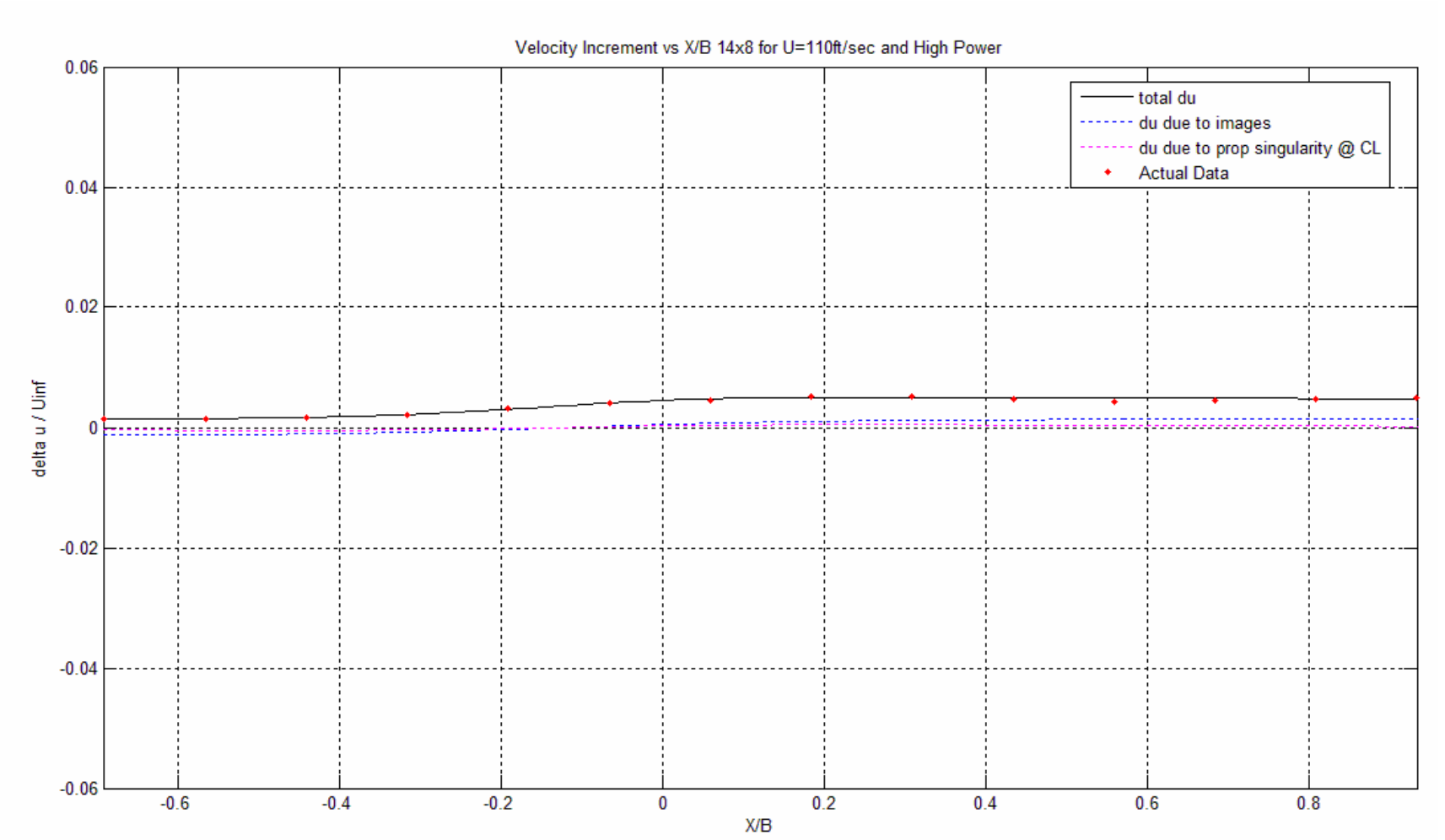

Velocity increment calculated from mathematical simulation model and propeller plotted against experimentally produced velocity increment for 14”x8” propeller rotating at high RPM and wind tunnel speed of 110ft/s.

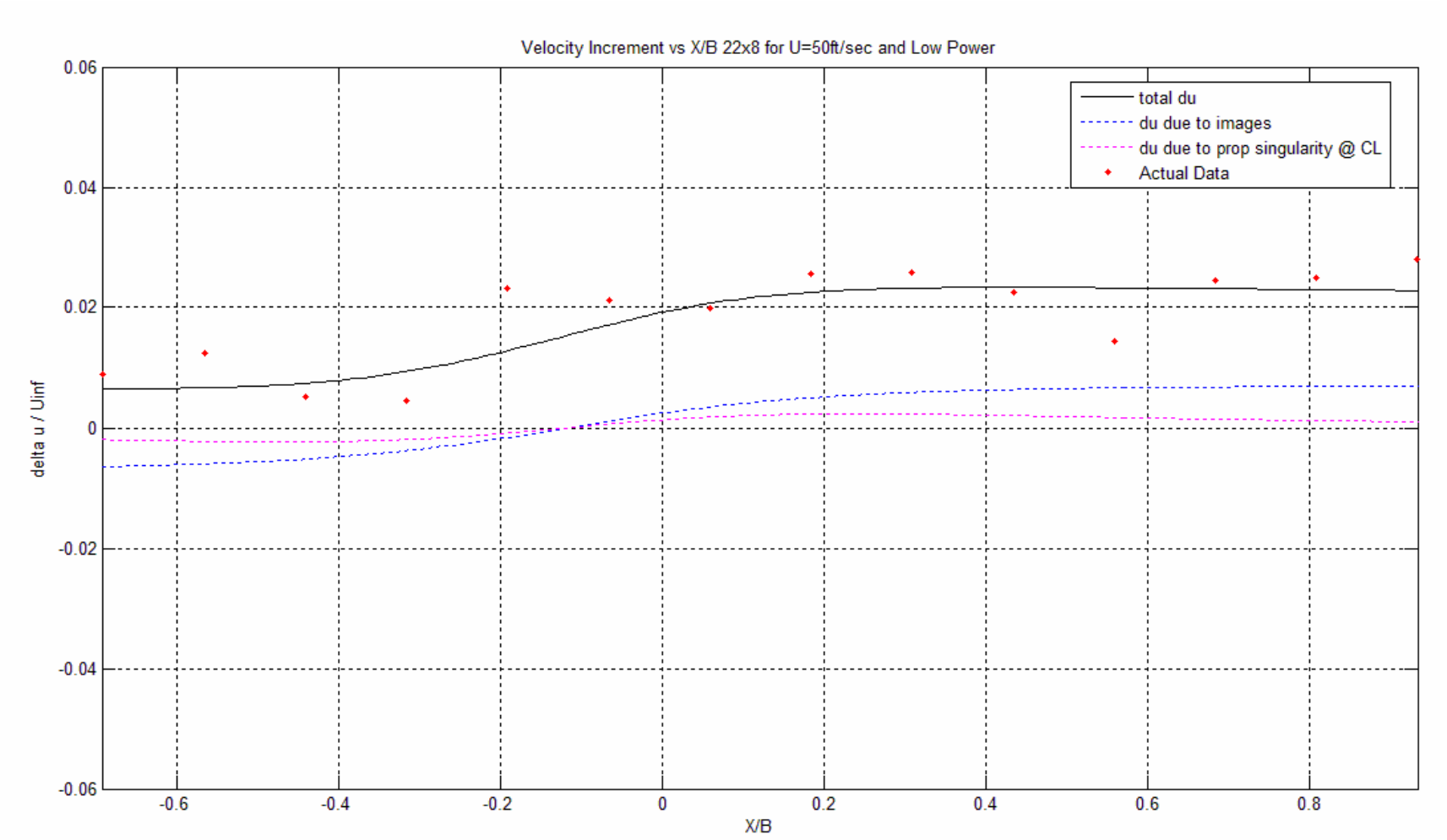

Velocity increment calculated from mathematical simulation model and propeller plotted against experimentally produced velocity increment for 22”x8” propeller rotating at low RPM and wind tunnel speed of 50ft/s.

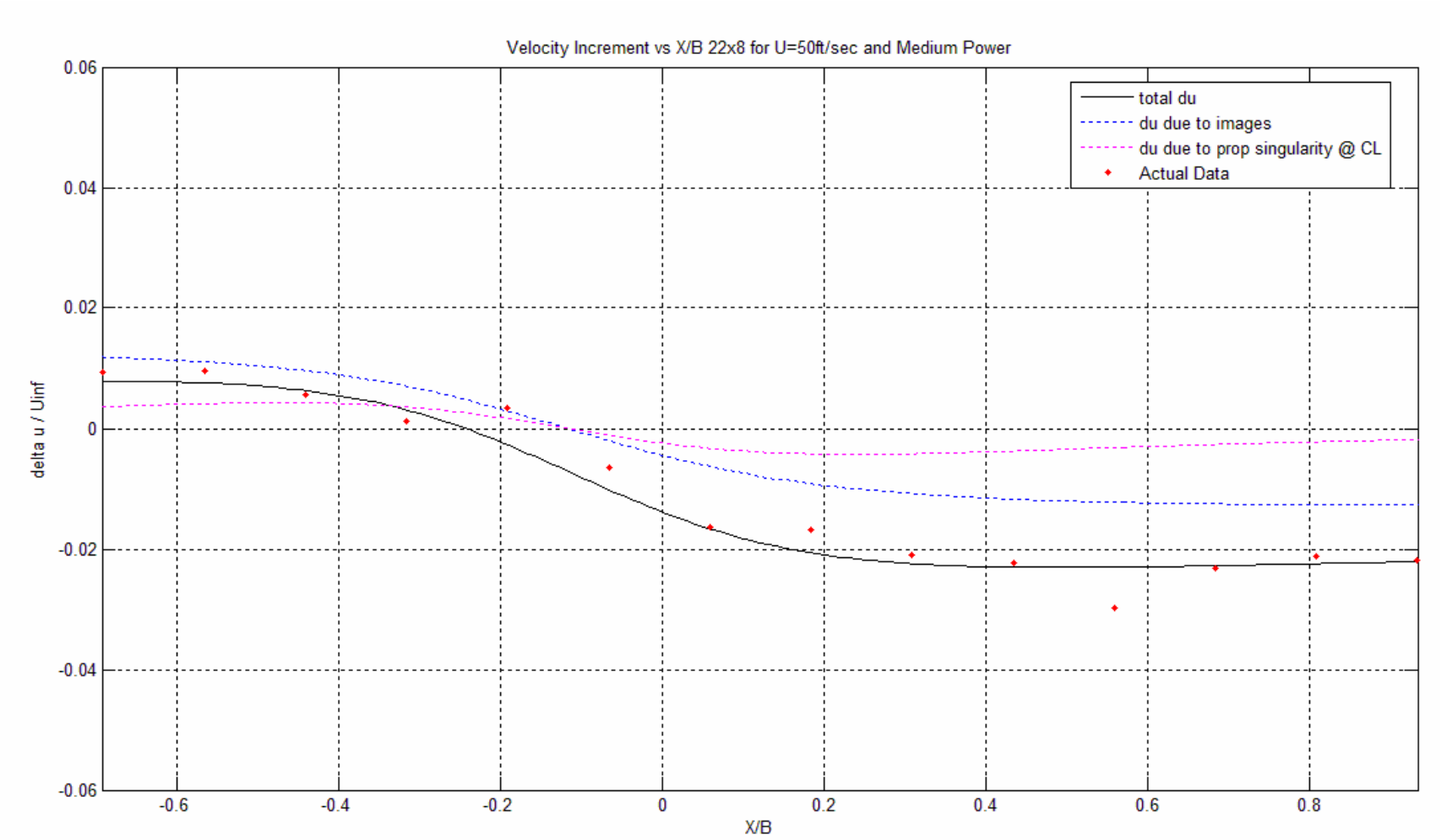

Velocity increment calculated from mathematical simulation model and propeller plotted against experimentally produced velocity increment for 22”x8” propeller rotating at medium RPM and wind tunnel speed of 50ft/s.

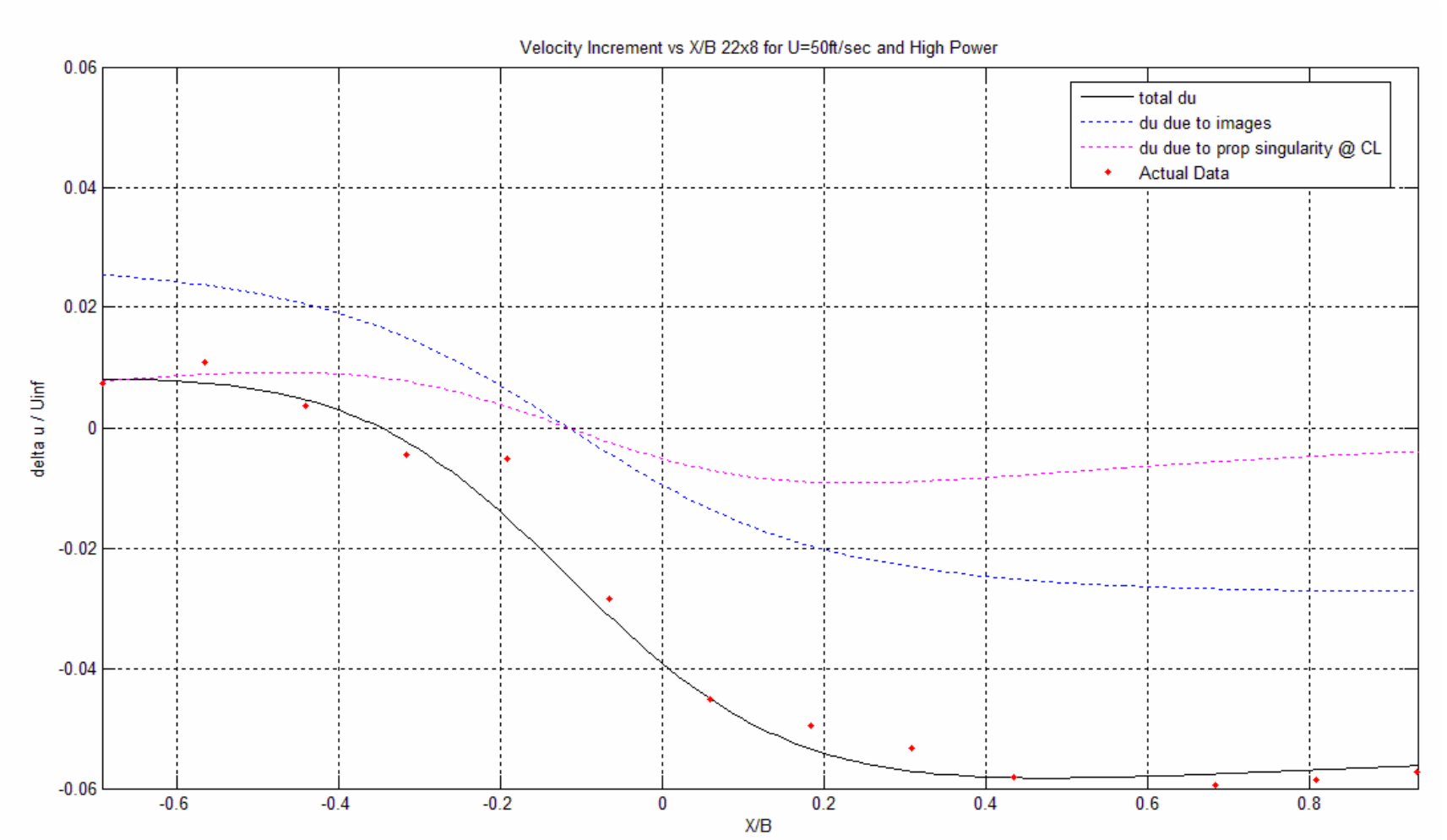

Velocity increment calculated from mathematical simulation model and propeller plotted against experimentally produced velocity increment for 22”x8” propeller rotating at high RPM and wind tunnel speed of 50ft/s.

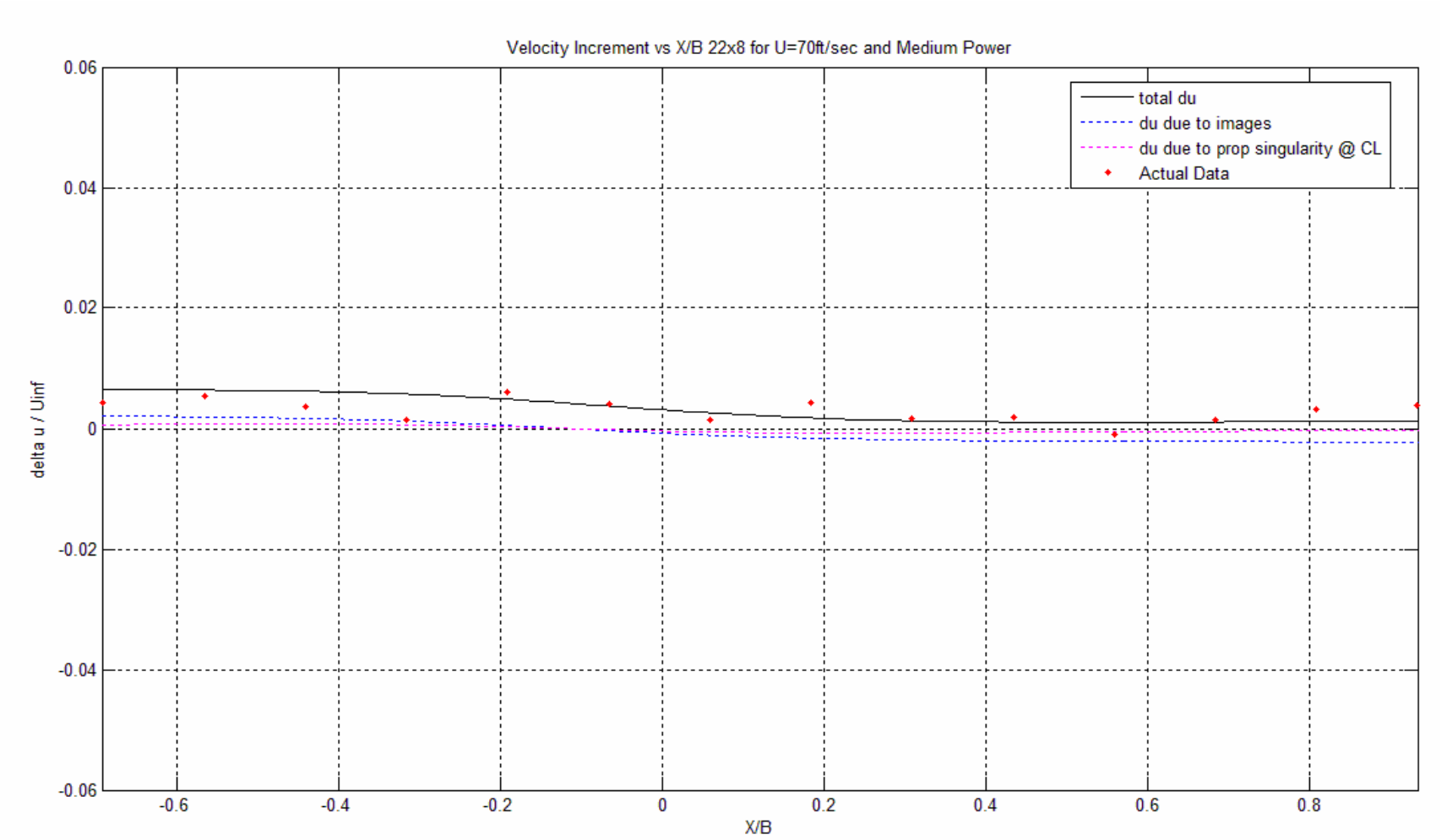

Velocity increment calculated from mathematical simulation model and propeller plotted against experimentally produced velocity increment for 22”x8” propeller rotating at medium RPM and wind tunnel speed of 70ft/s.

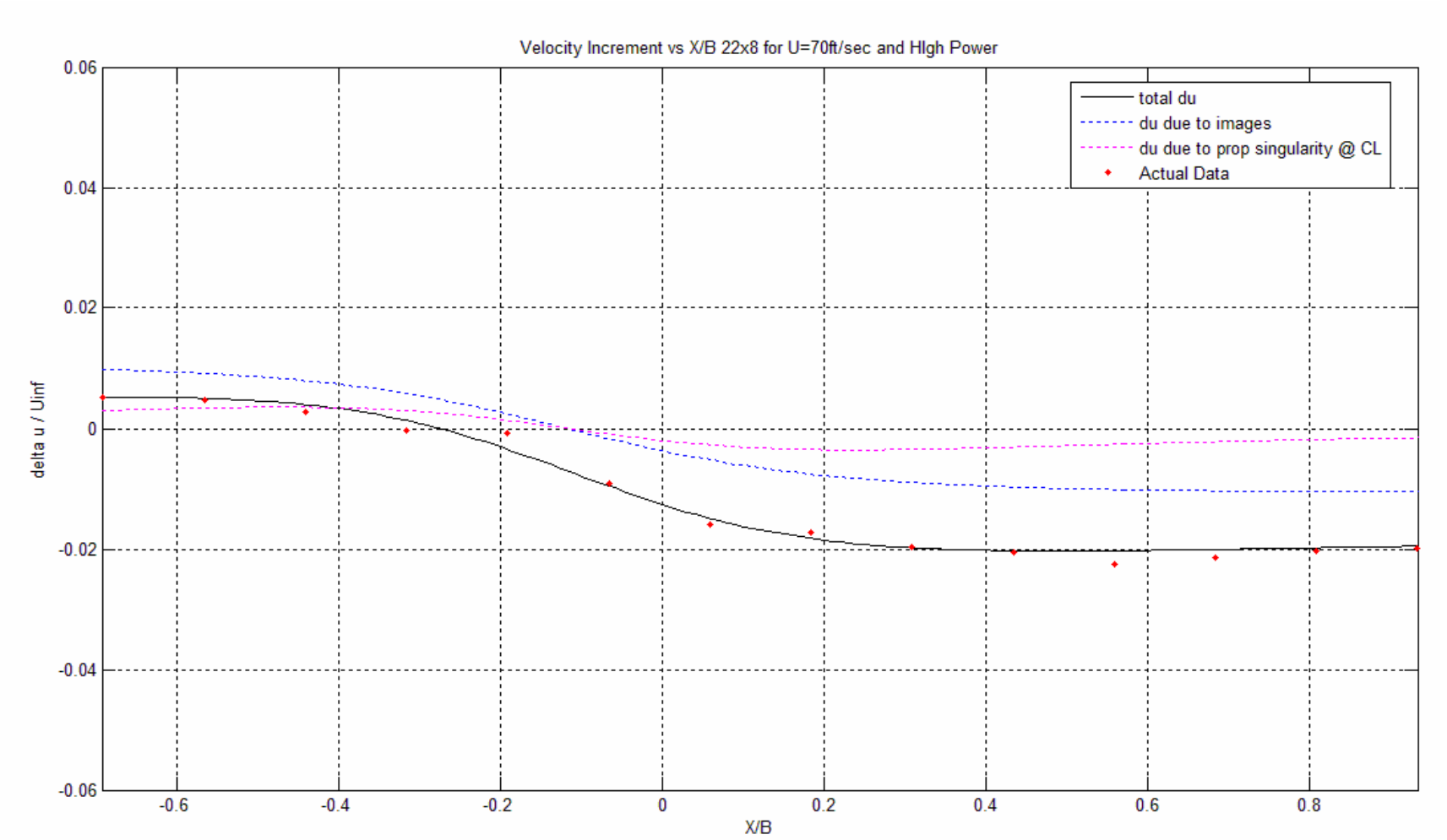

Velocity increment calculated from mathematical simulation model and propeller plotted against experimentally produced velocity increment for 22”x8” propeller rotating at high RPM and wind tunnel speed of 70ft/s.

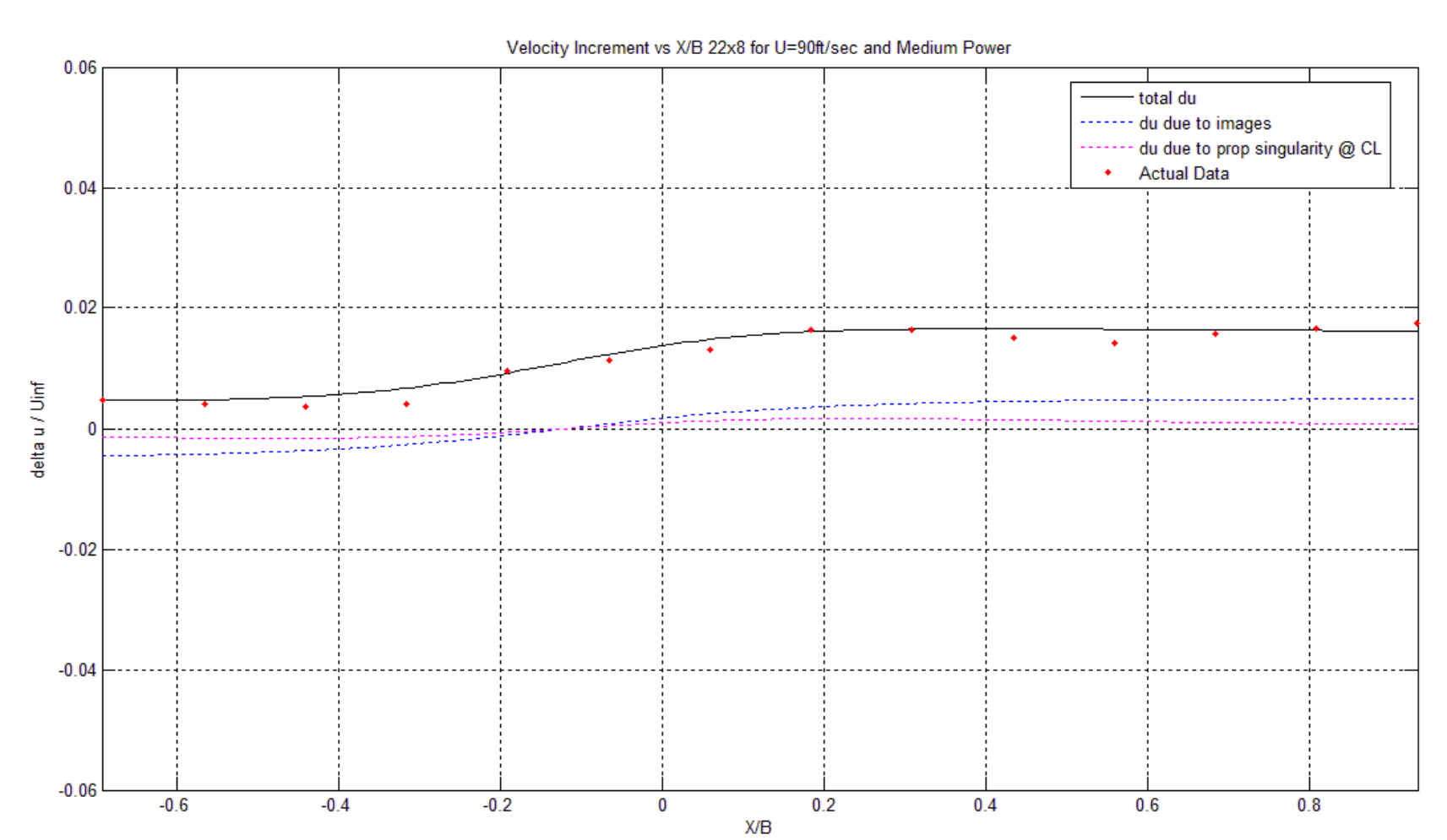

Velocity increment calculated from mathematical simulation model and propeller plotted against experimentally produced velocity increment for 22”x8” propeller rotating at medium RPM and wind tunnel speed of 90ft/s.

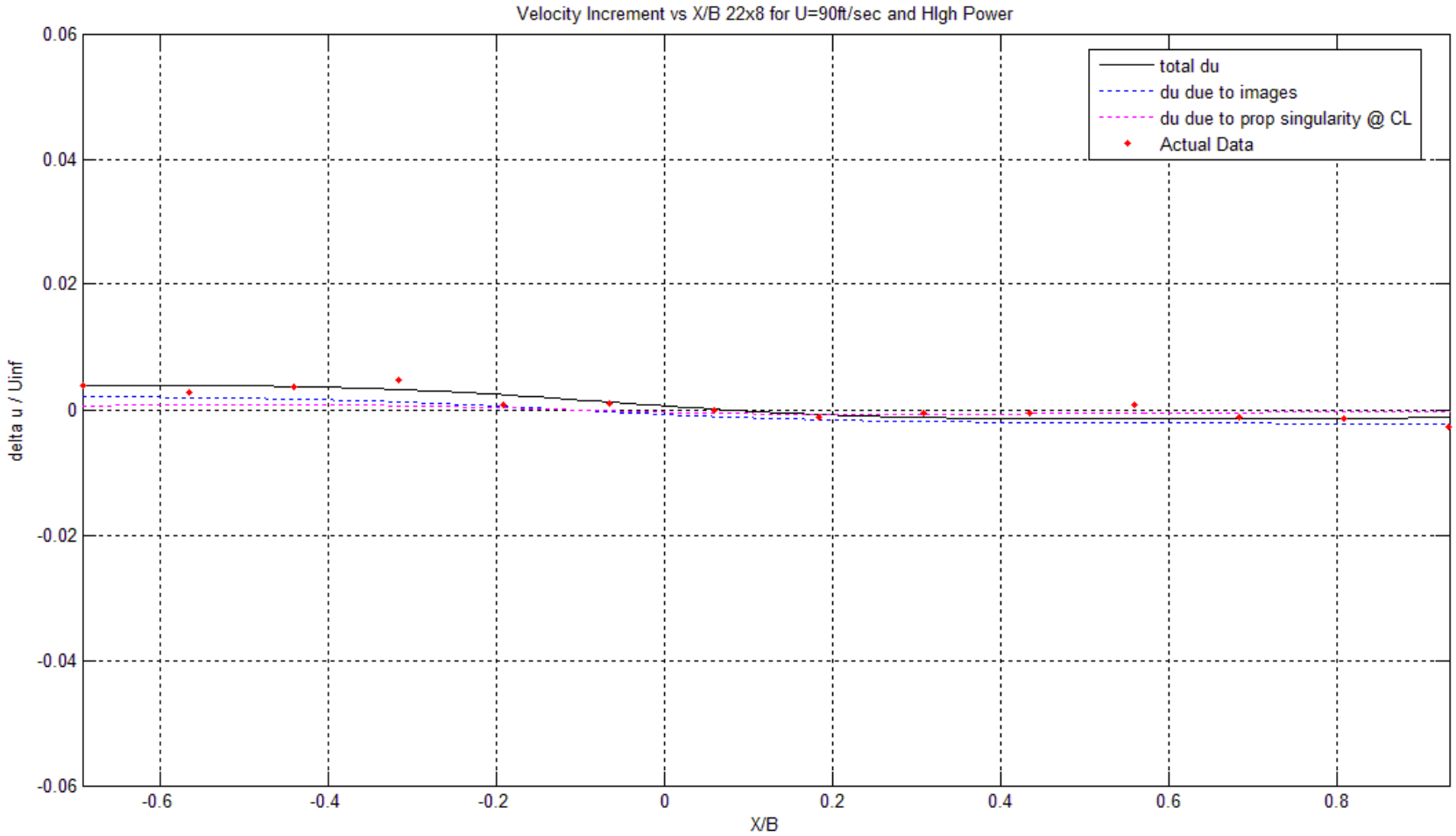

Velocity increment calculated from mathematical simulation model and propeller plotted against experimentally produced velocity increment for 22”x8” propeller rotating at high RPM and wind tunnel speed of 90ft/s.

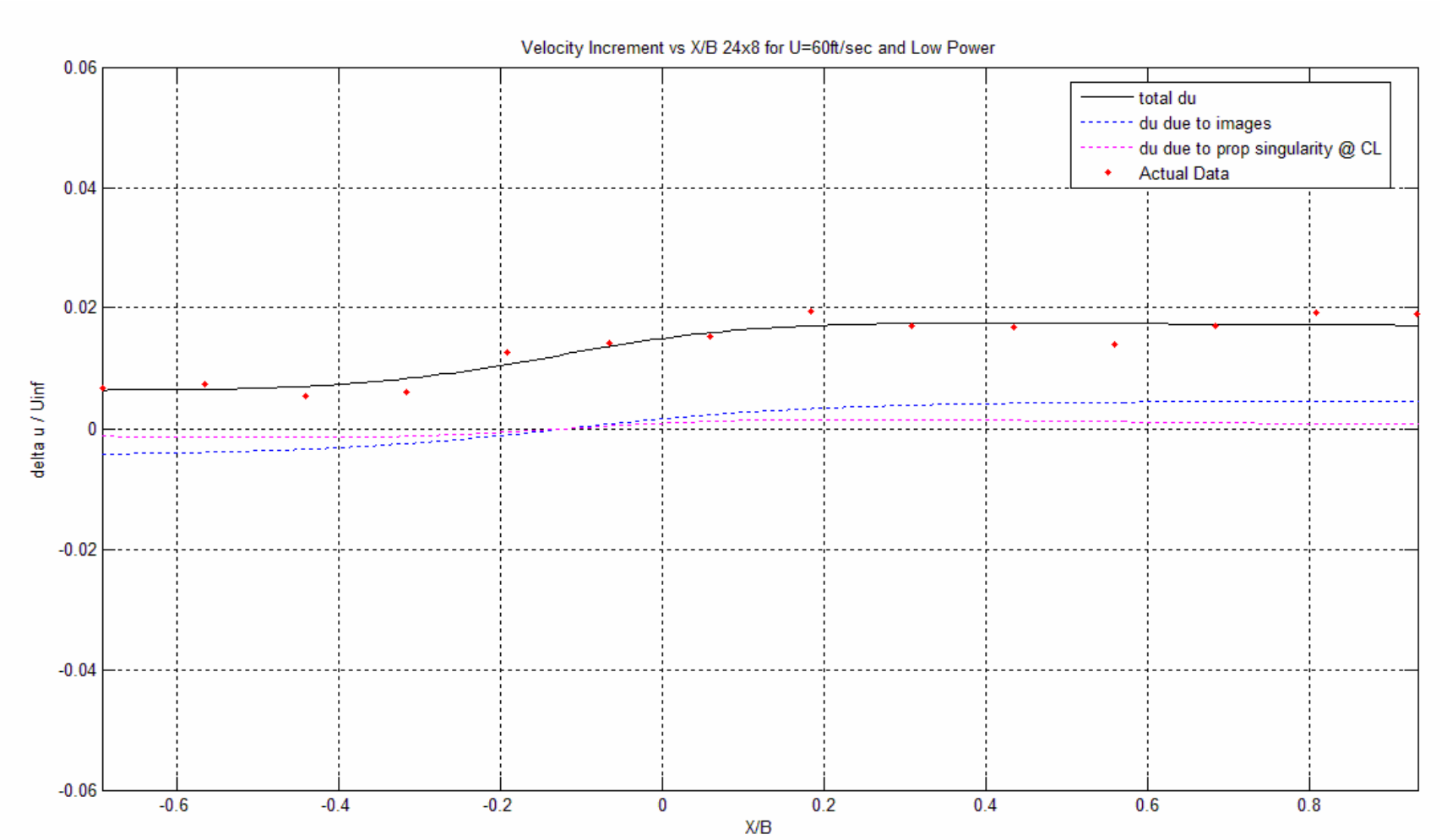

Velocity increment calculated from mathematical simulation model and propeller plotted against experimentally produced velocity increment for 24”x8” propeller rotating at low RPM and wind tunnel speed of 60ft/s.

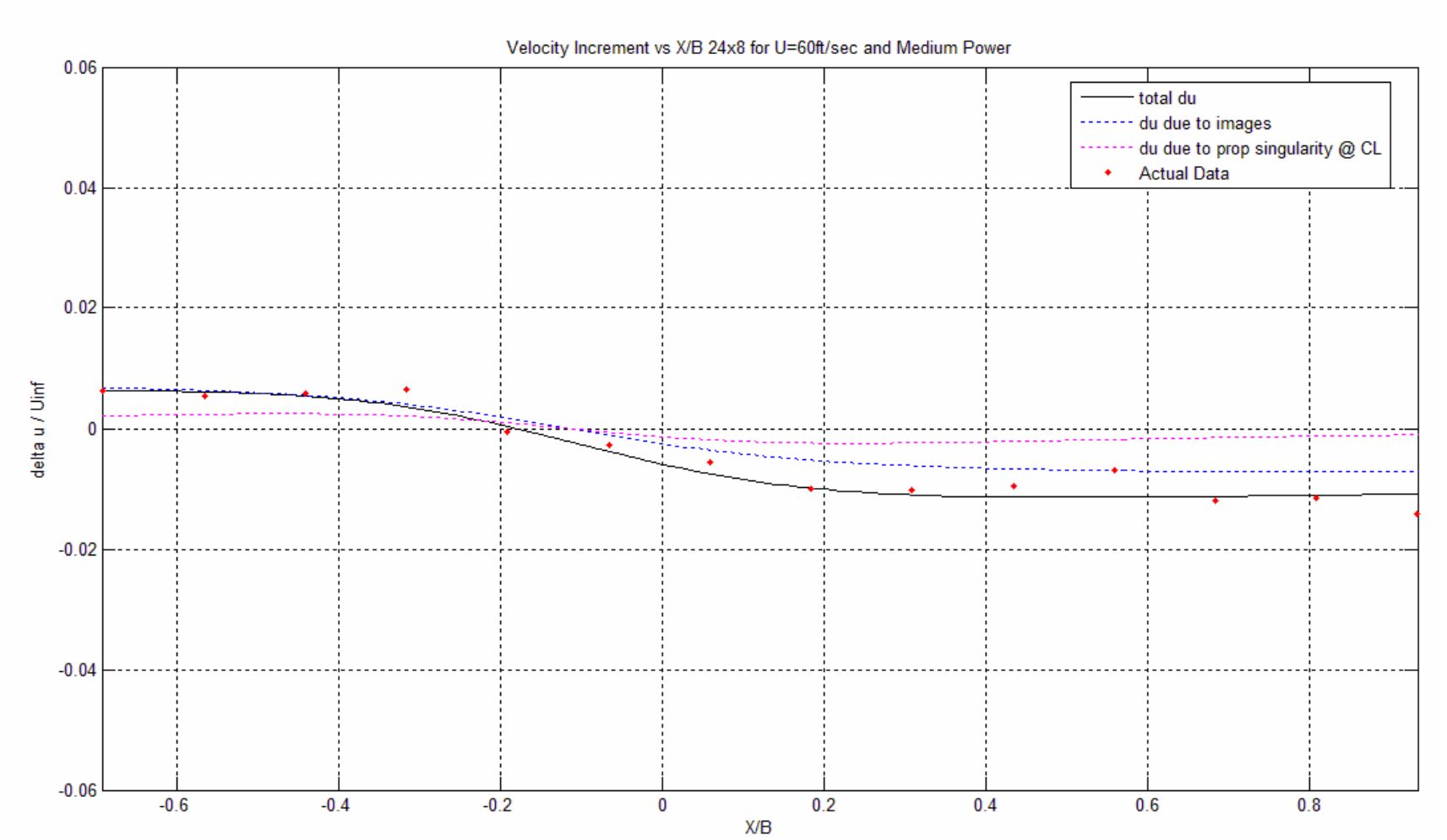

Velocity increment calculated from mathematical simulation model and propeller plotted against experimentally produced velocity increment for 24”x8” propeller rotating at medium RPM and wind tunnel speed of 60ft/s.

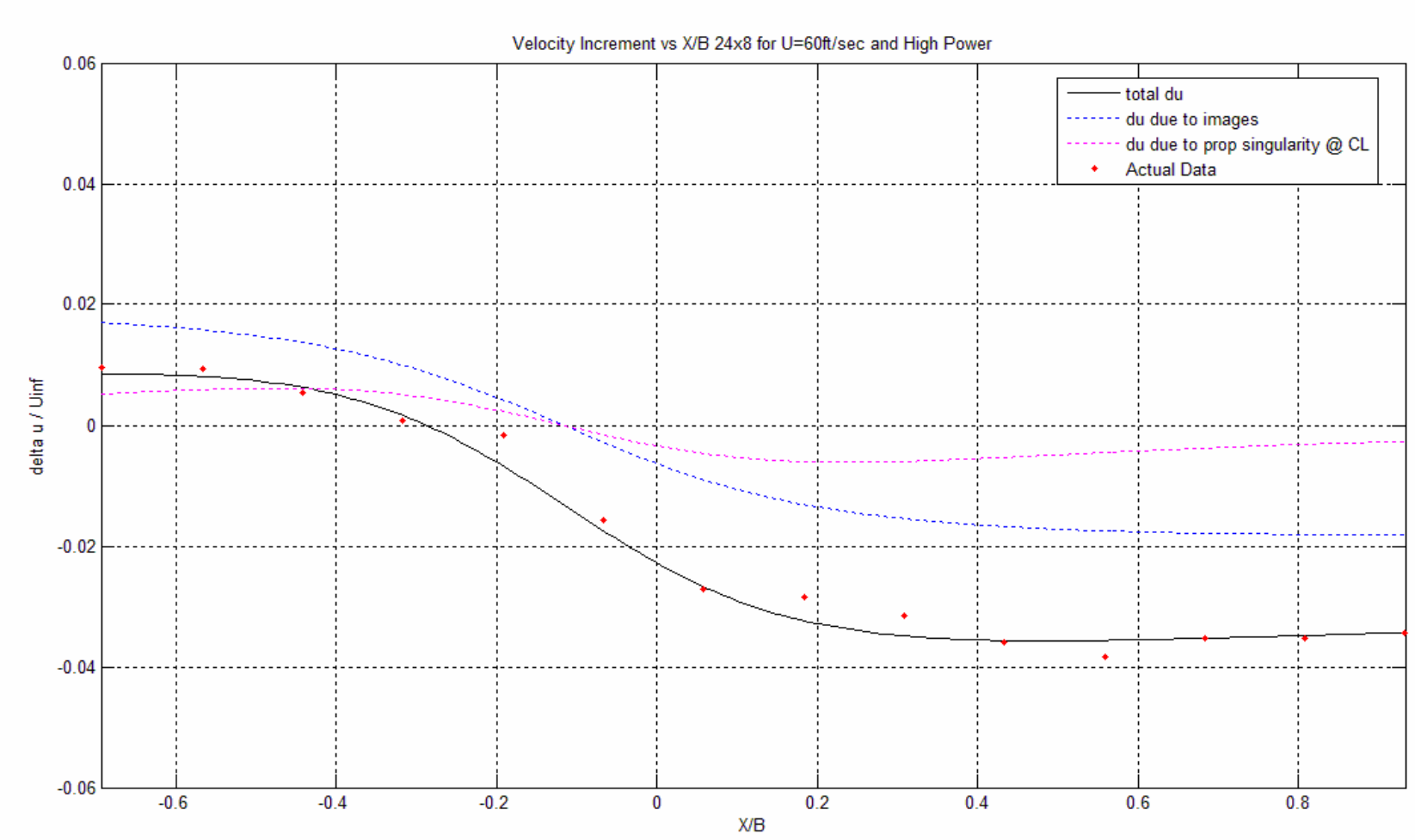

Velocity increment calculated from mathematical simulation model and propeller plotted against experimentally produced velocity increment for 24”x8” propeller rotating at high RPM and wind tunnel speed of 60ft/s.

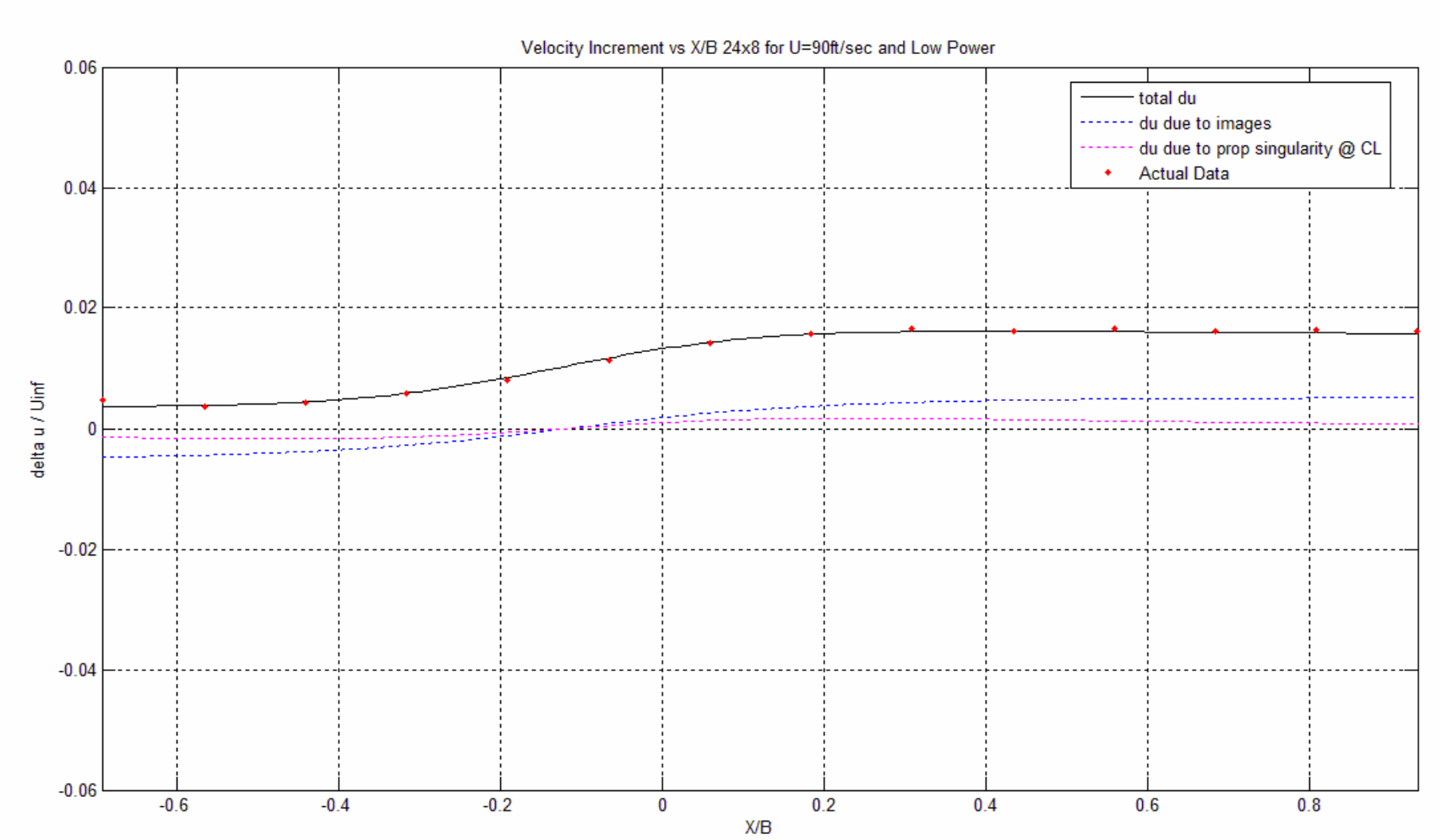

Velocity increment calculated from mathematical simulation model and propeller plotted against experimentally produced velocity increment for 24”x8” propeller rotating at low RPM and wind tunnel speed of 90ft/s.

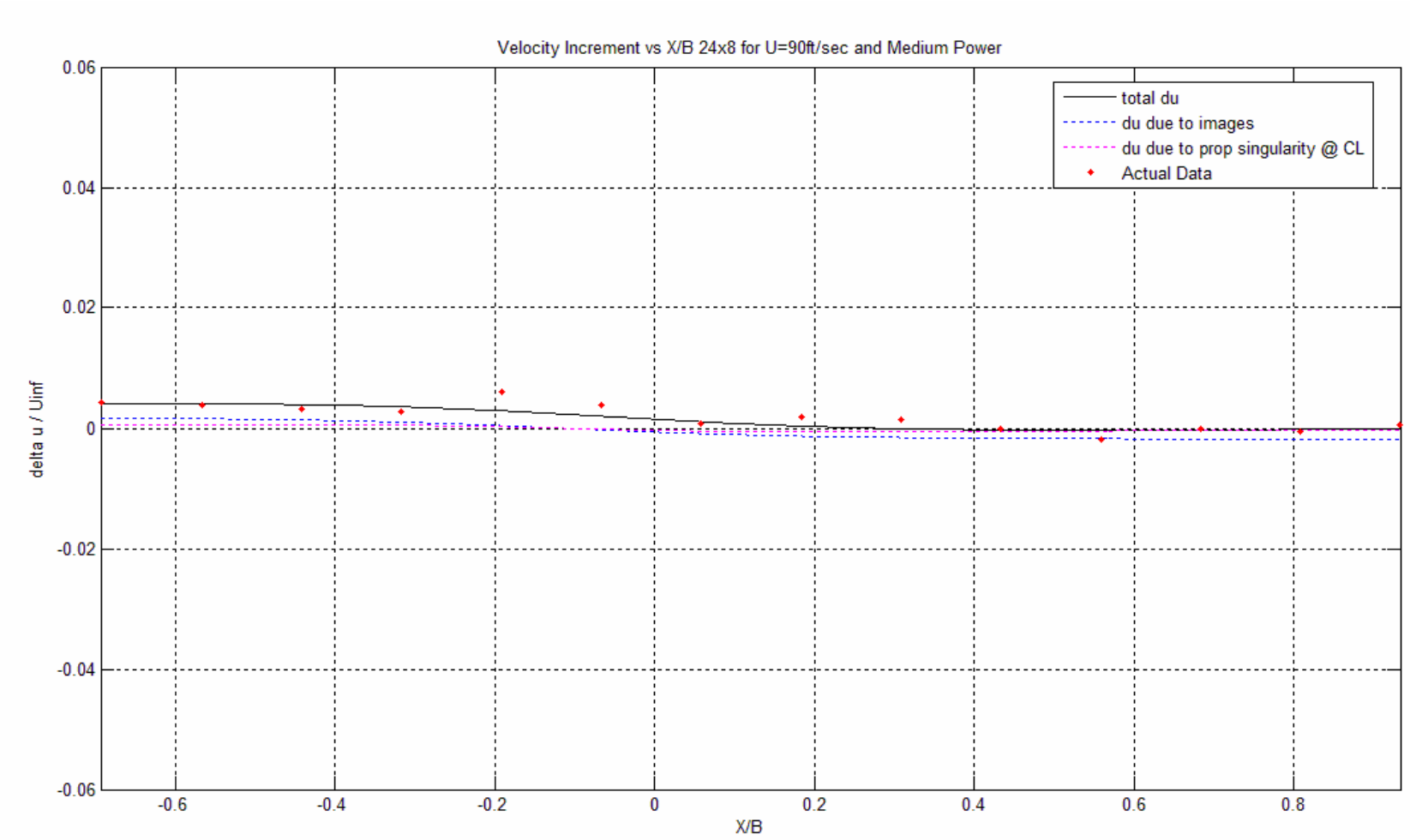

Velocity increment calculated from mathematical simulation model and propeller plotted against experimentally produced velocity increment for 24”x8” propeller rotating at medium RPM and wind tunnel speed of 90ft/s.

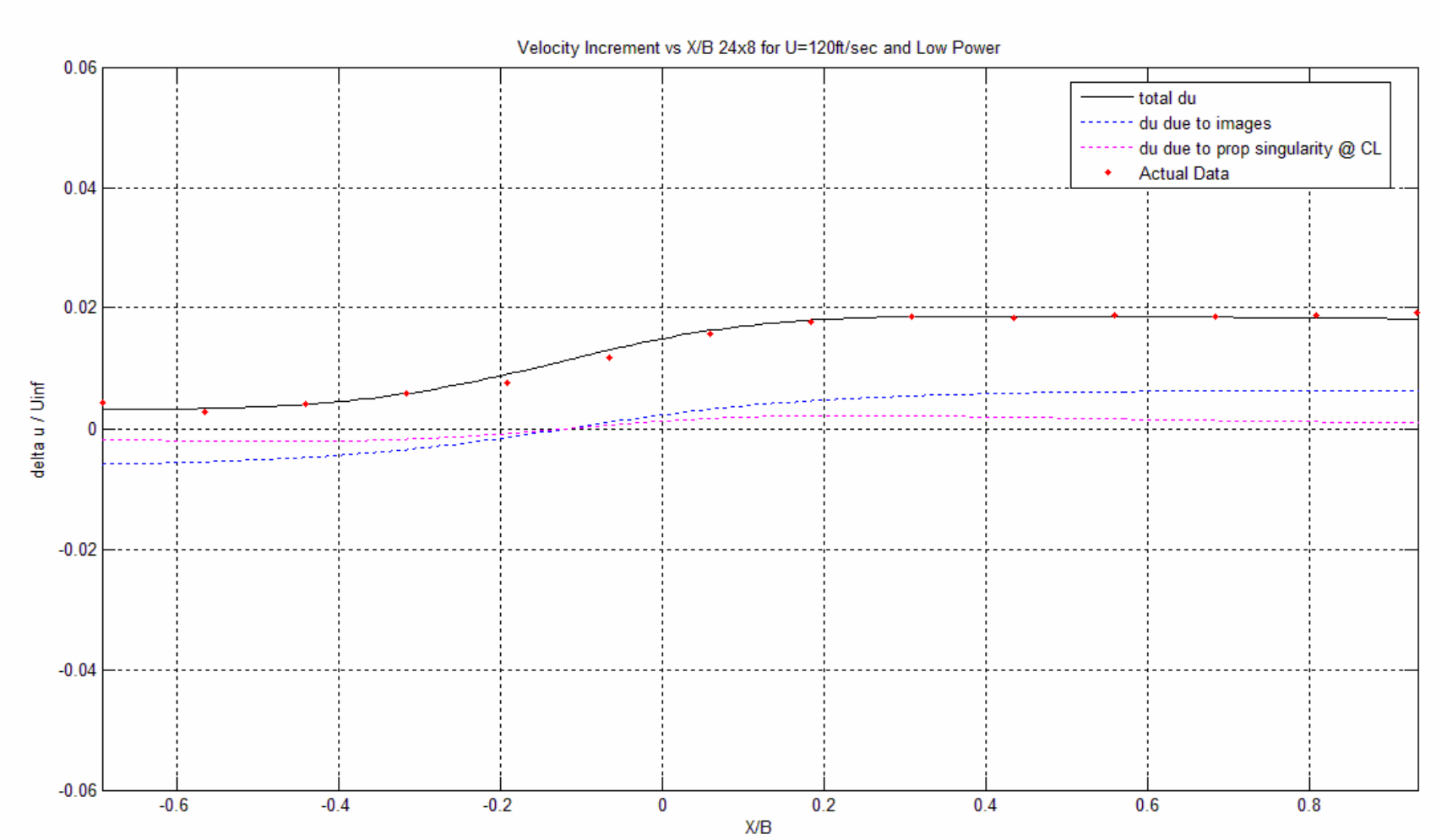

Velocity increment calculated from mathematical simulation model and propeller plotted against experimentally produced velocity increment for 24”x8” propeller rotating at low RPM and wind tunnel speed of 120ft/s.

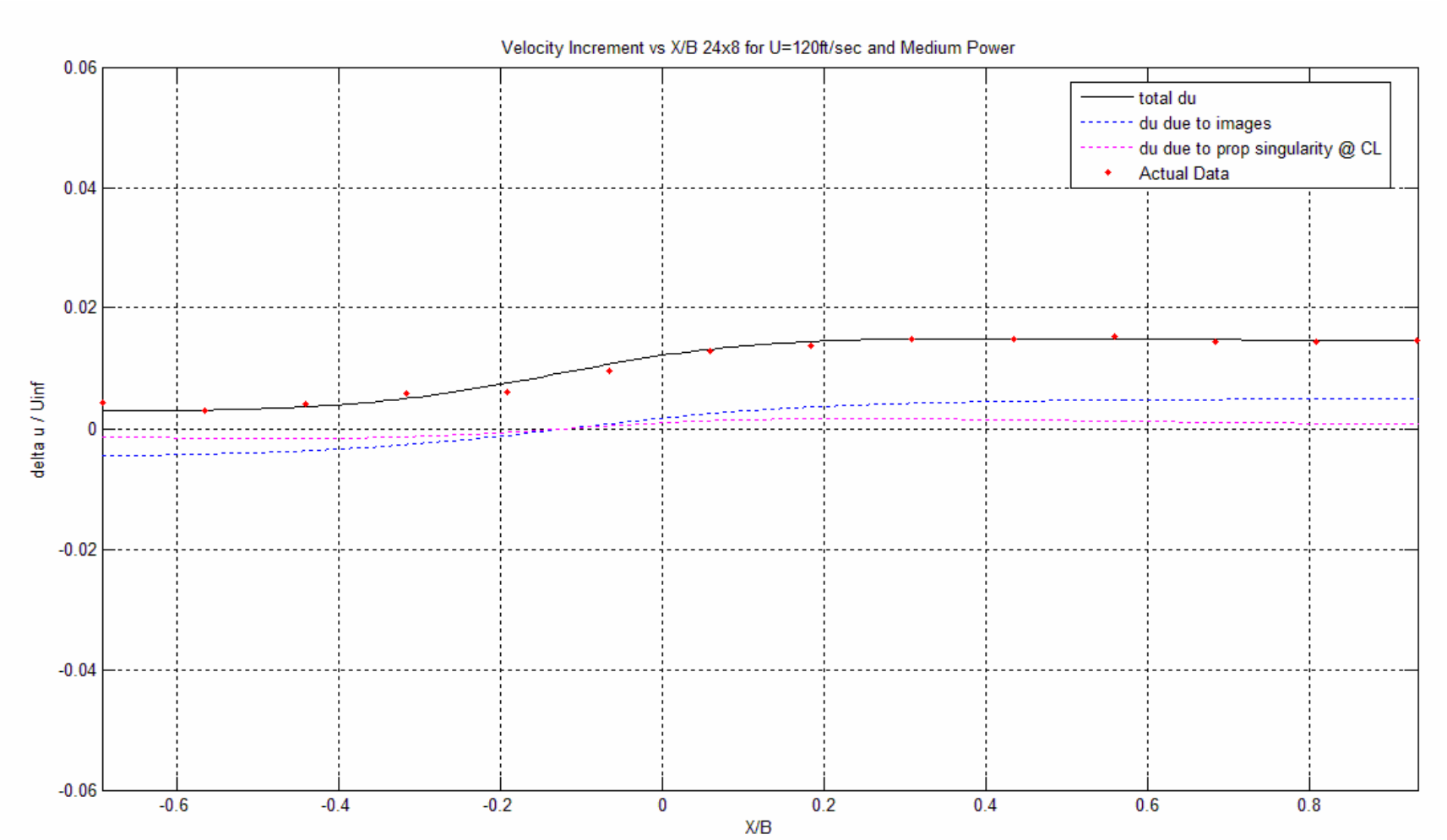

Velocity increment calculated from mathematical simulation model and propeller plotted against experimentally produced velocity increment for 24”x8” propeller rotating at medium RPM and wind tunnel speed of 120ft/s.

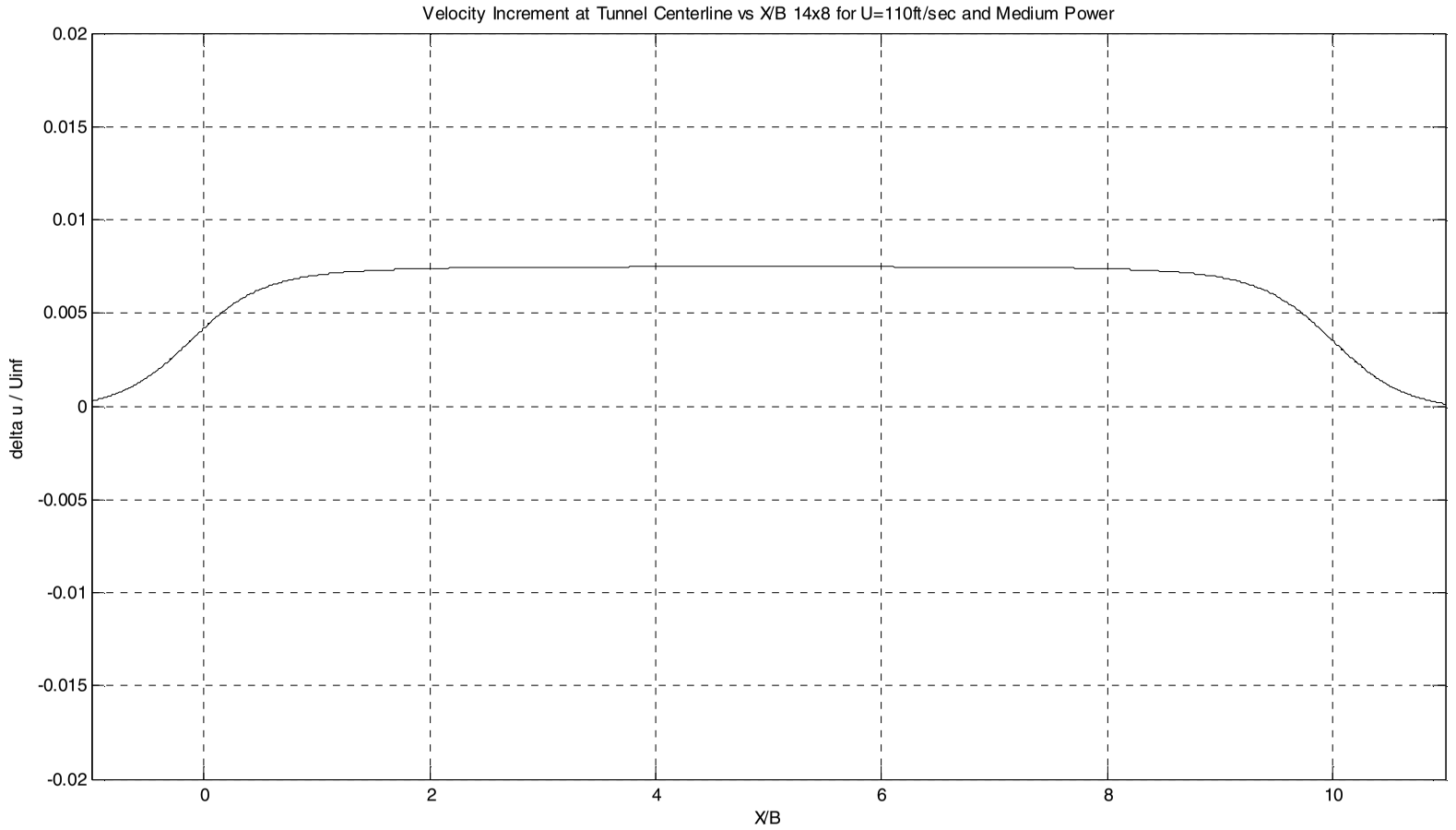

Centerline velocity increment for 14” x 8” propeller at 110ft/sec at medium RPM.

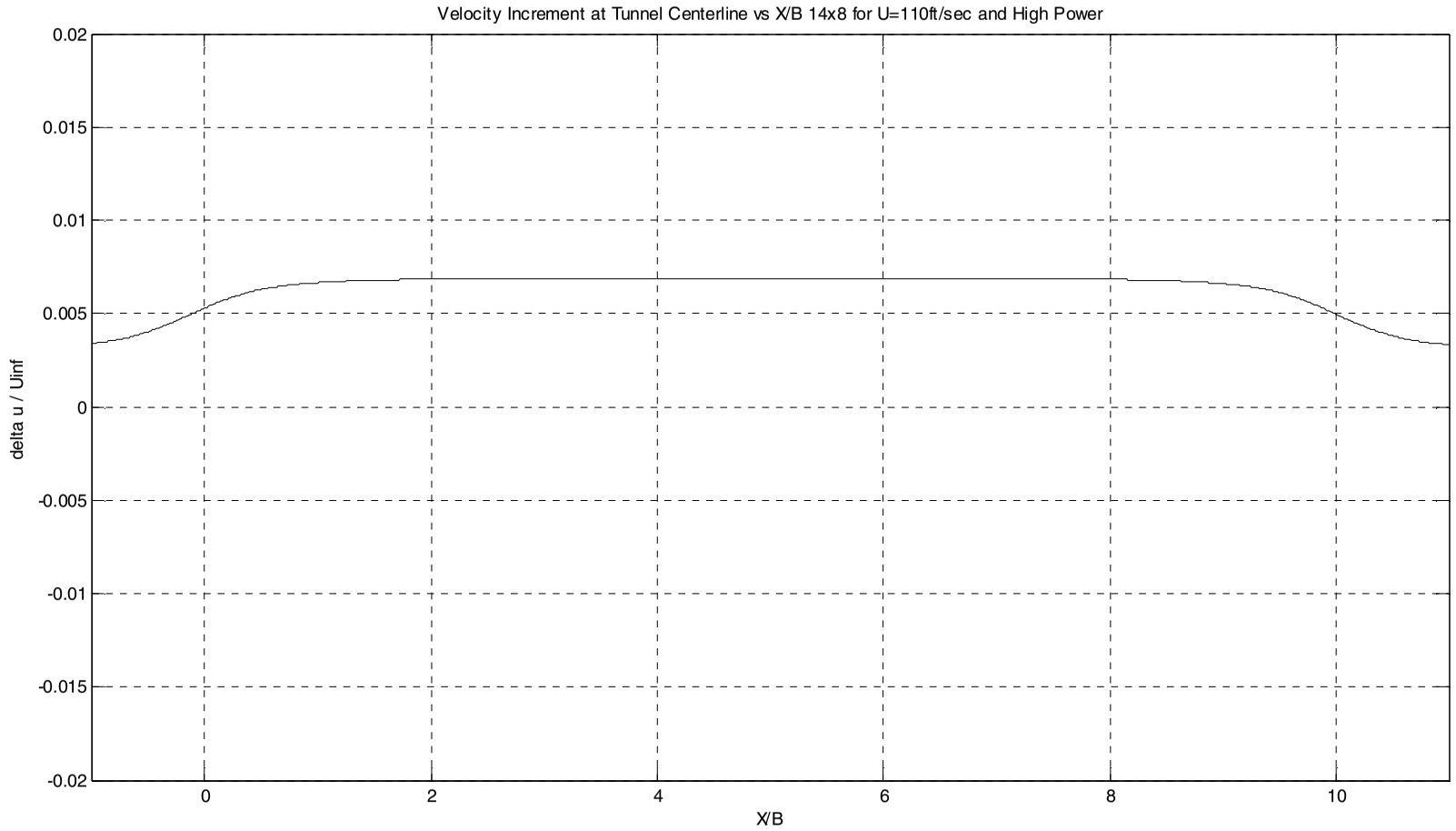

Centerline velocity increment for 14” x 8” propeller at 110ft/sec at high RPM.

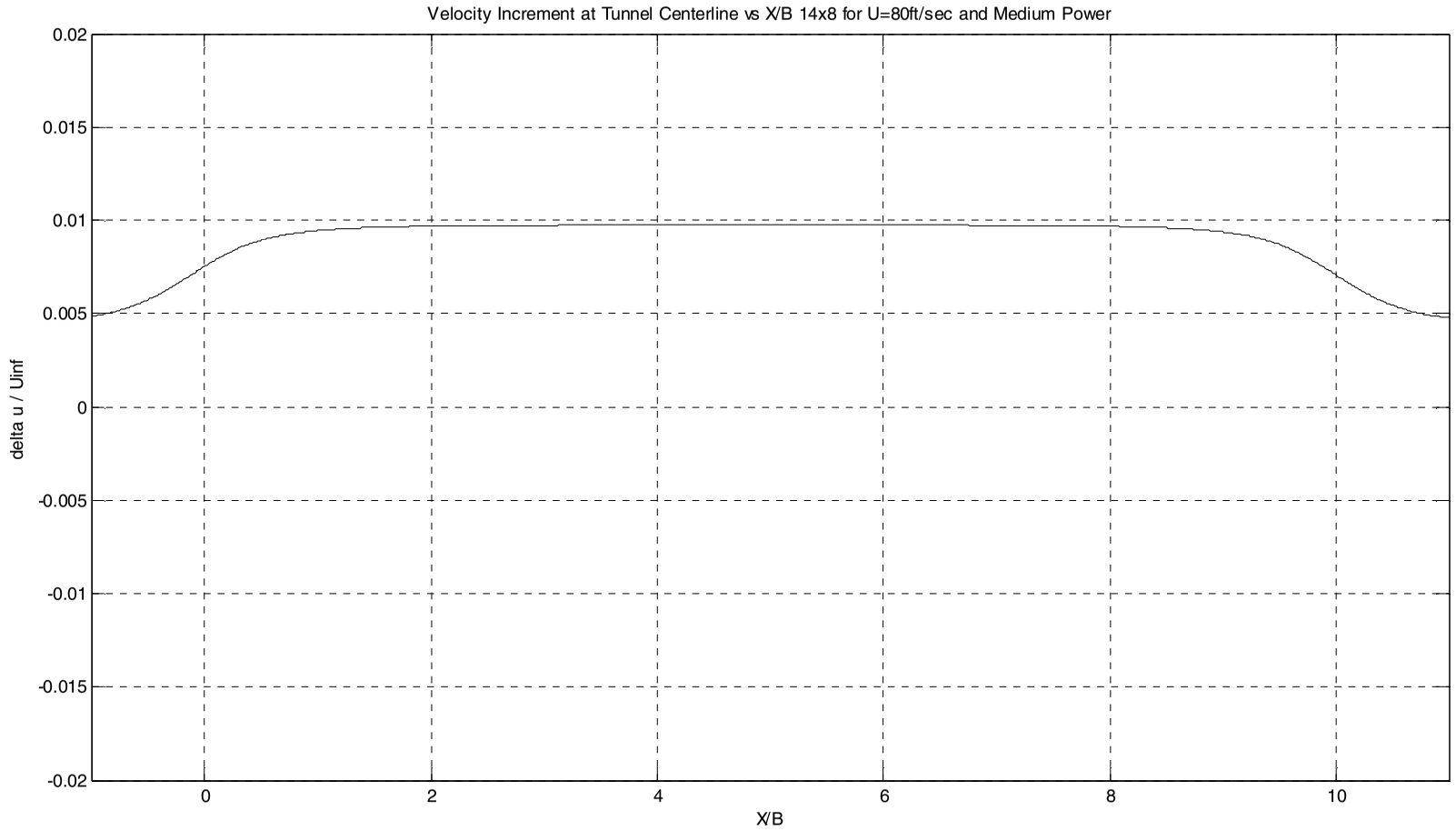

Centerline velocity increment for 14” x 8” propeller at 80ft/sec at medium RPM.

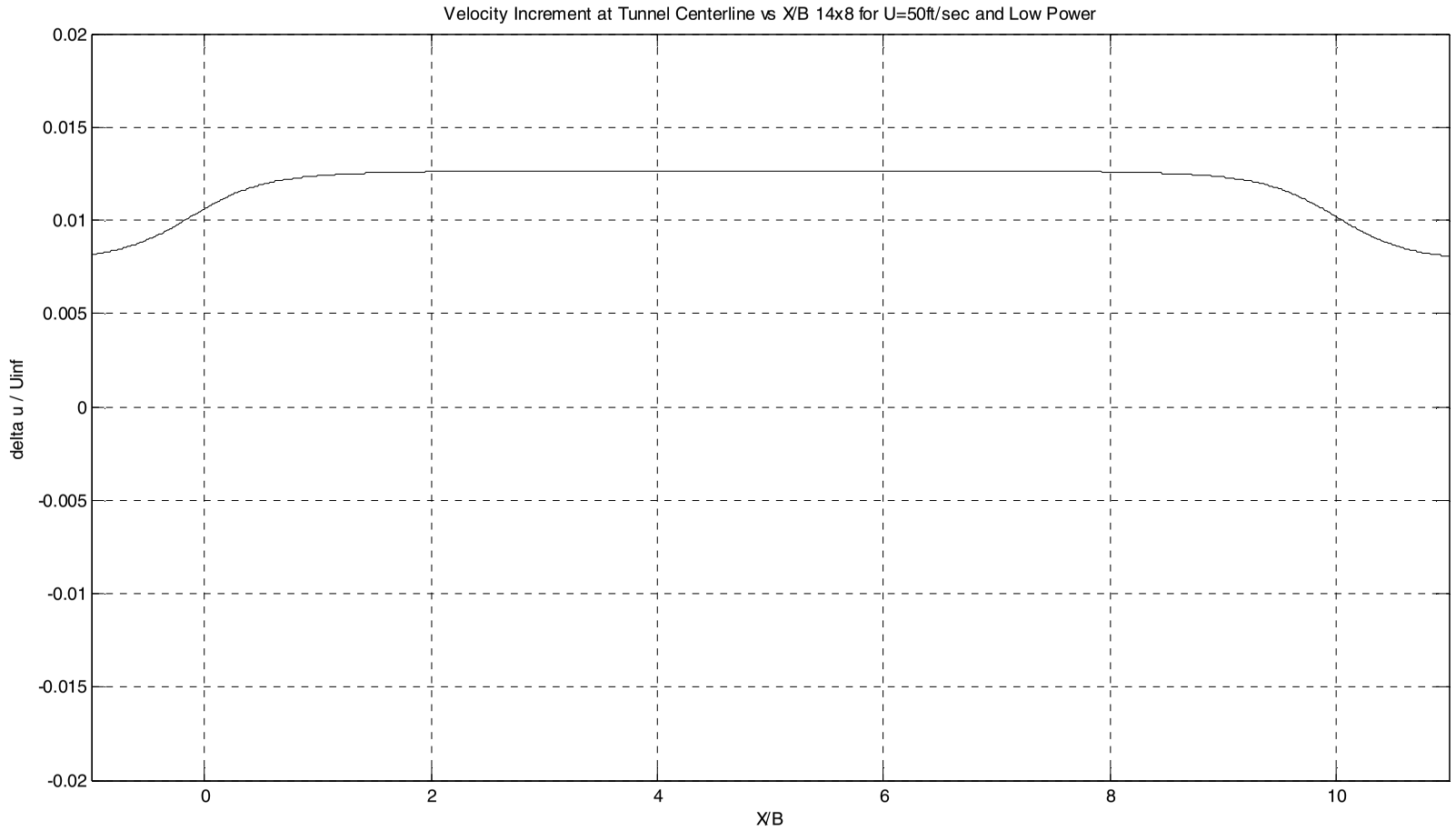

Centerline velocity increment for 14” x 8” propeller at 50ft/sec at low RPM.

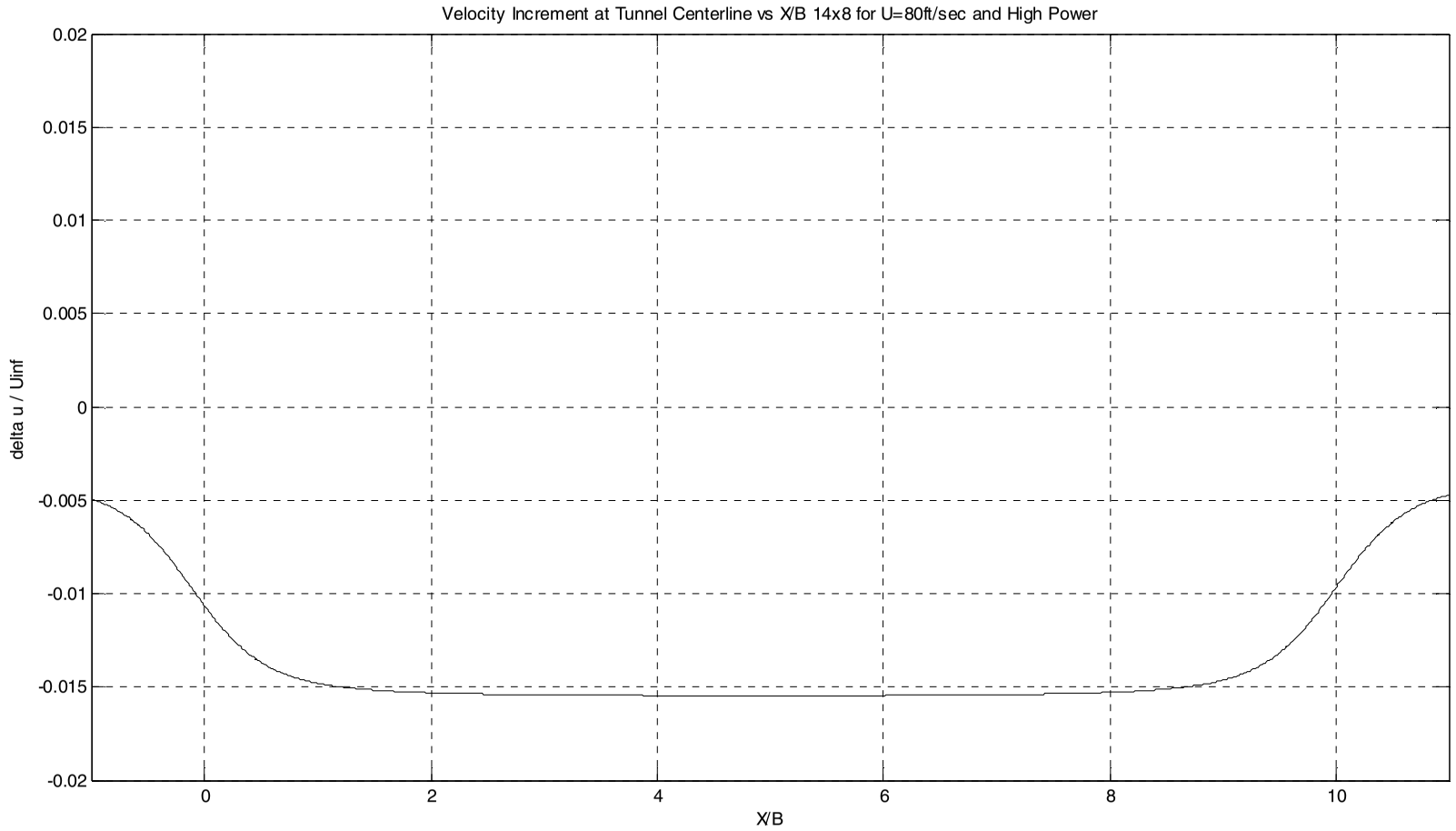

Centerline velocity increment for 14” x 8” propeller at 80ft/sec at high RPM.

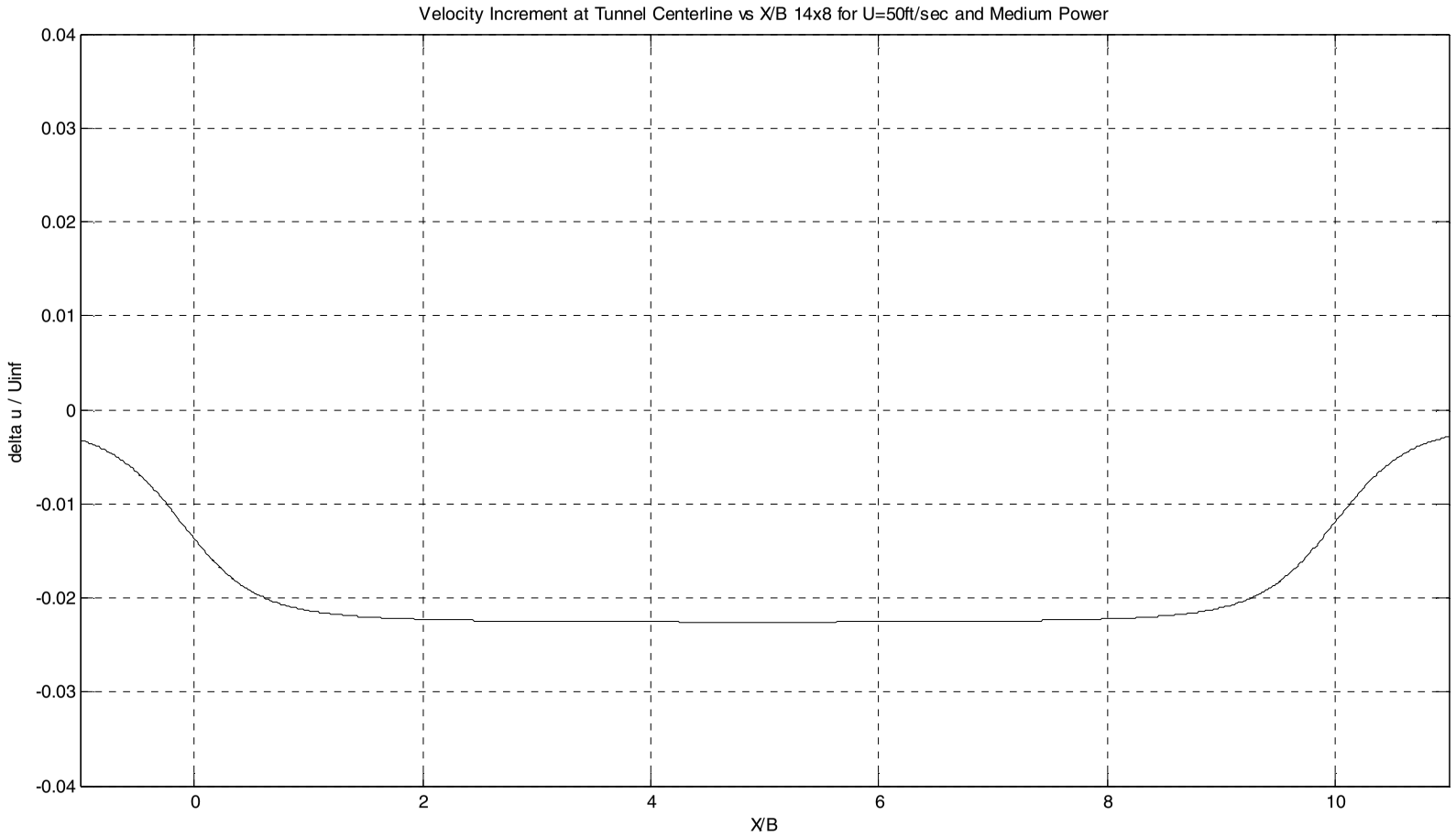

Centerline velocity increment for 14” x 8” propeller at 50ft/sec at medium RPM

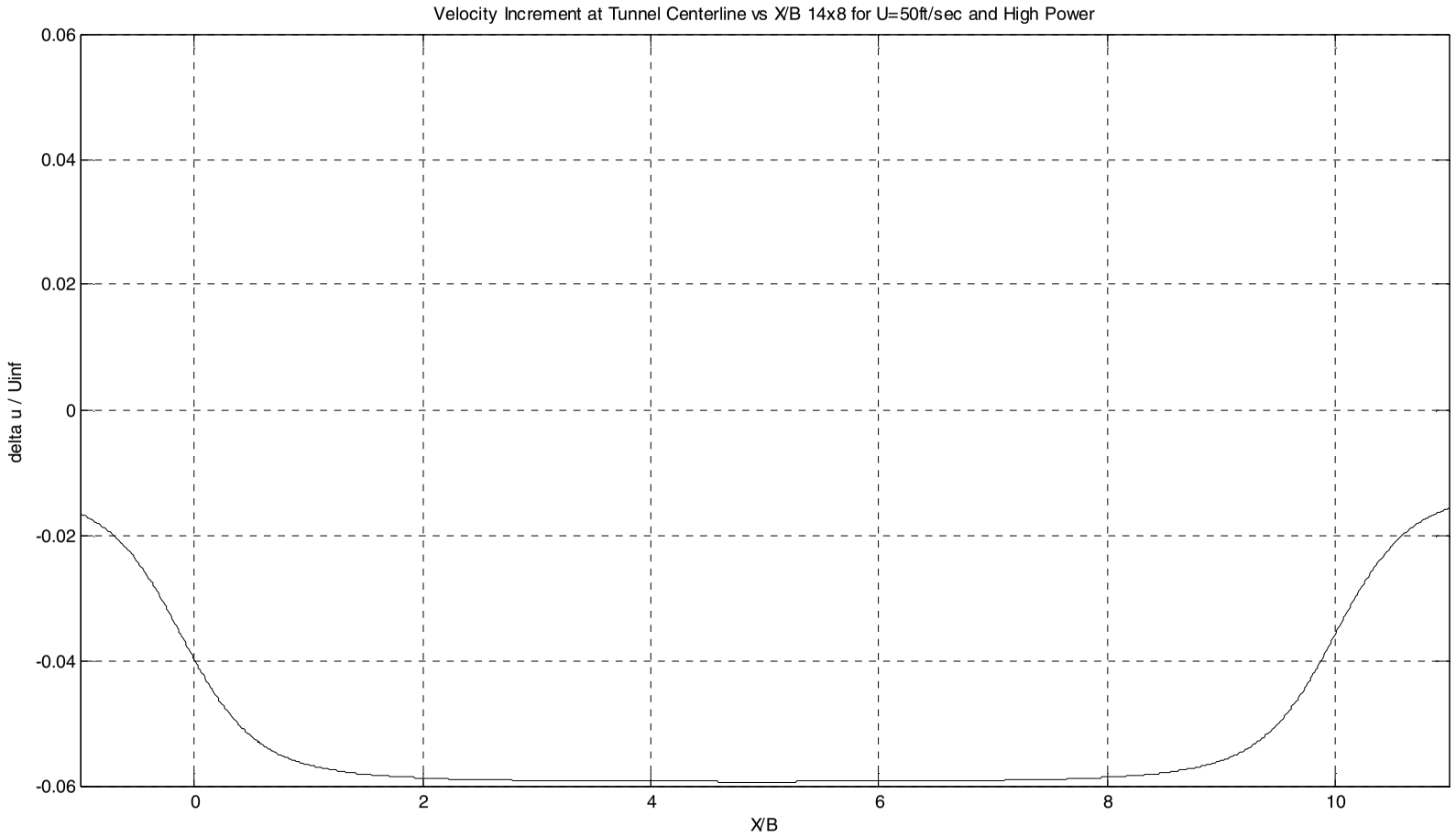

Centerline velocity increment for 14” x 8” propeller at 50ft/sec at high RPM.

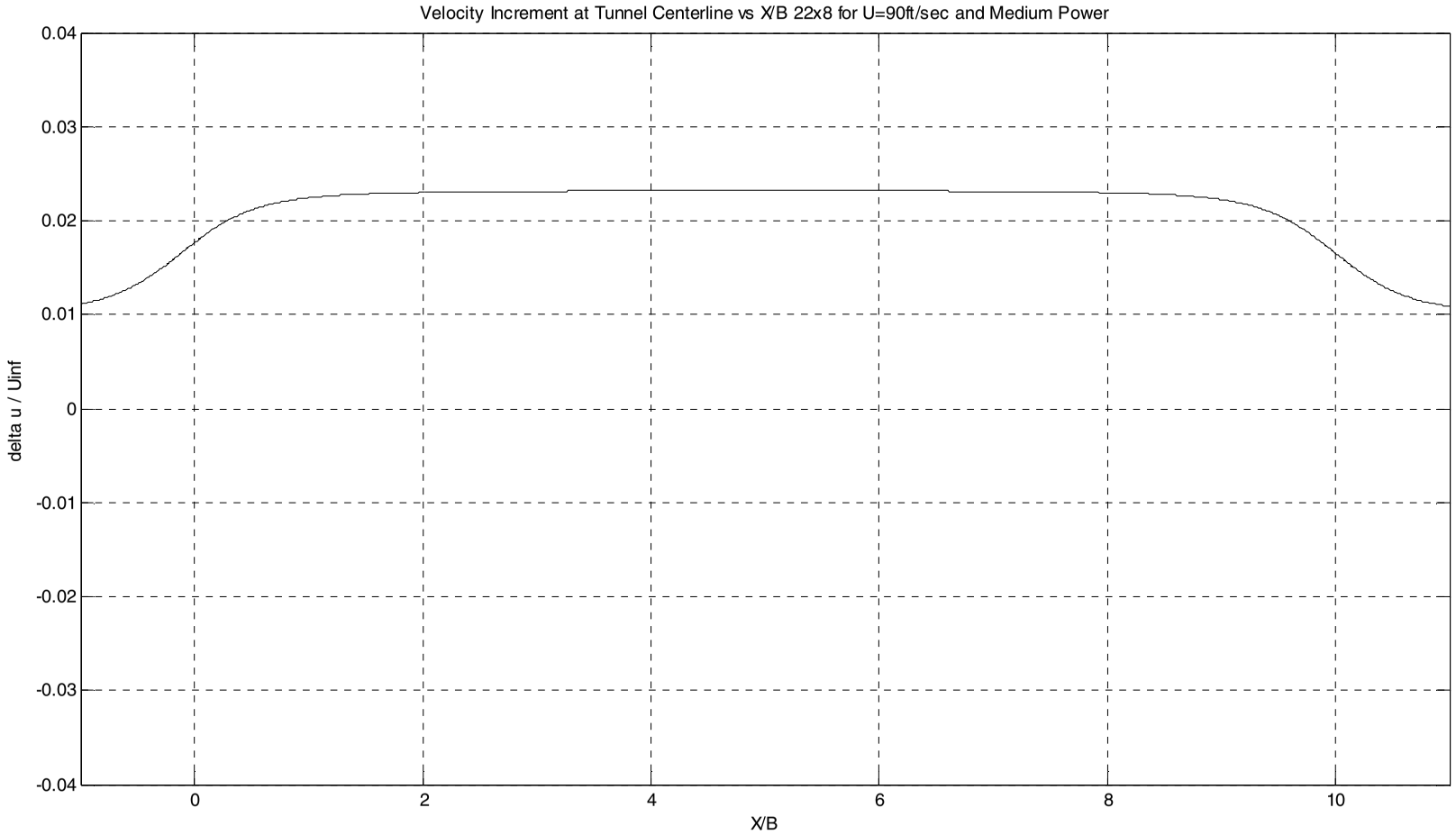

Centerline velocity increment for 22” x 8” propeller at 90ft/sec at medium RPM.

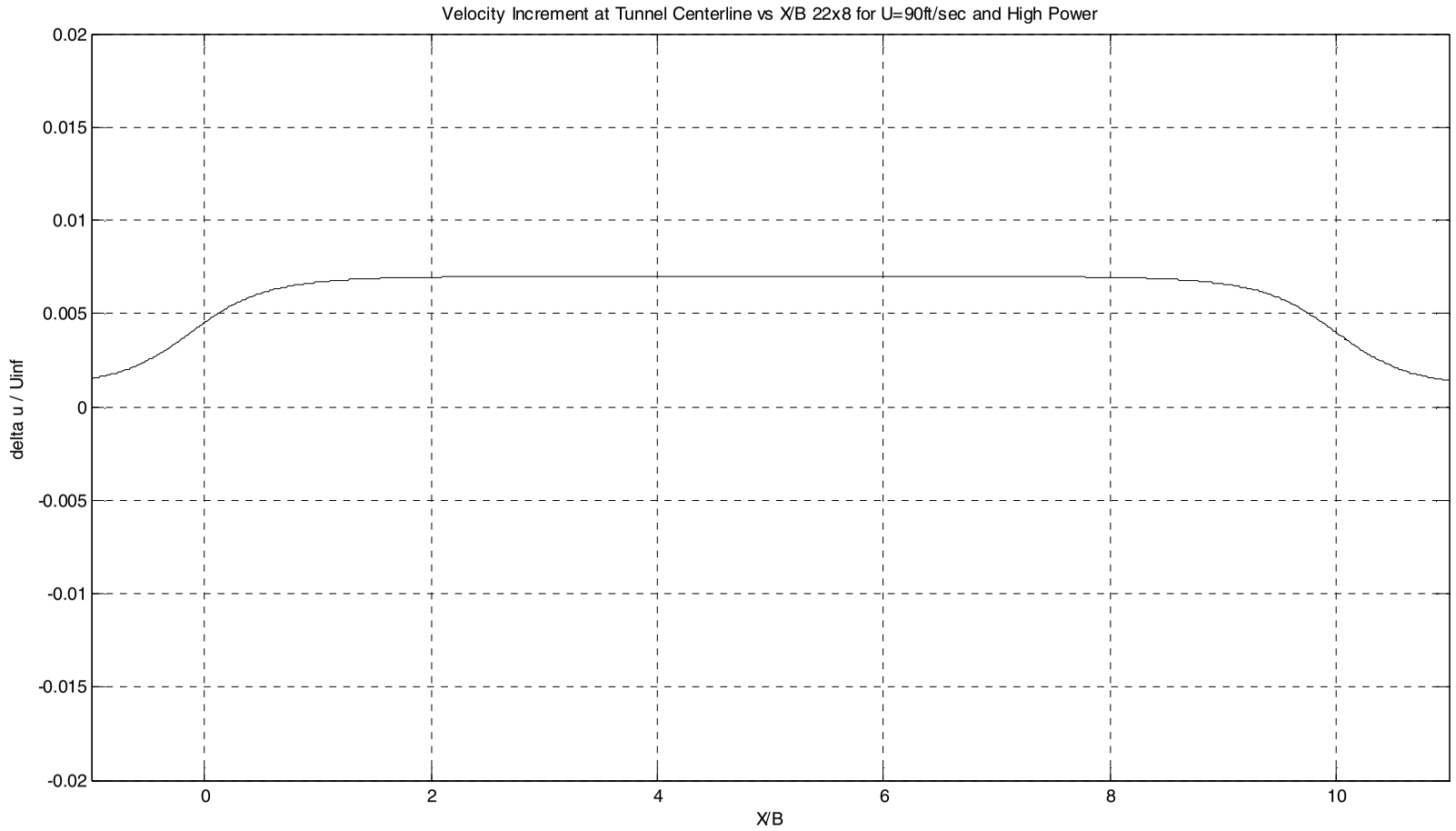

Centerline velocity increment for 22” x 8” propeller at 90ft/sec at high RPM.

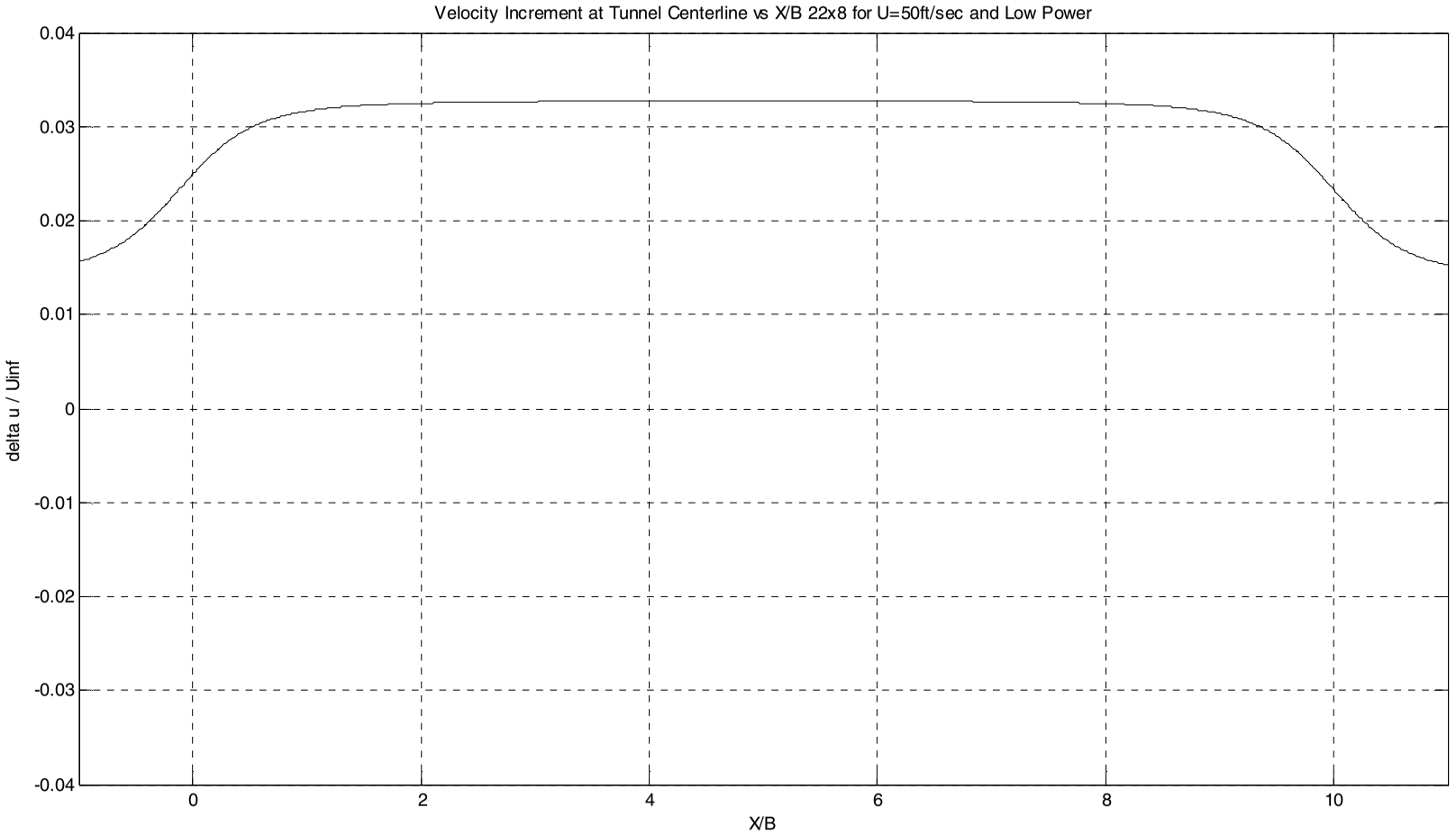

Centerline velocity increment for 22” x 8” propeller at 50ft/sec at low RPM.

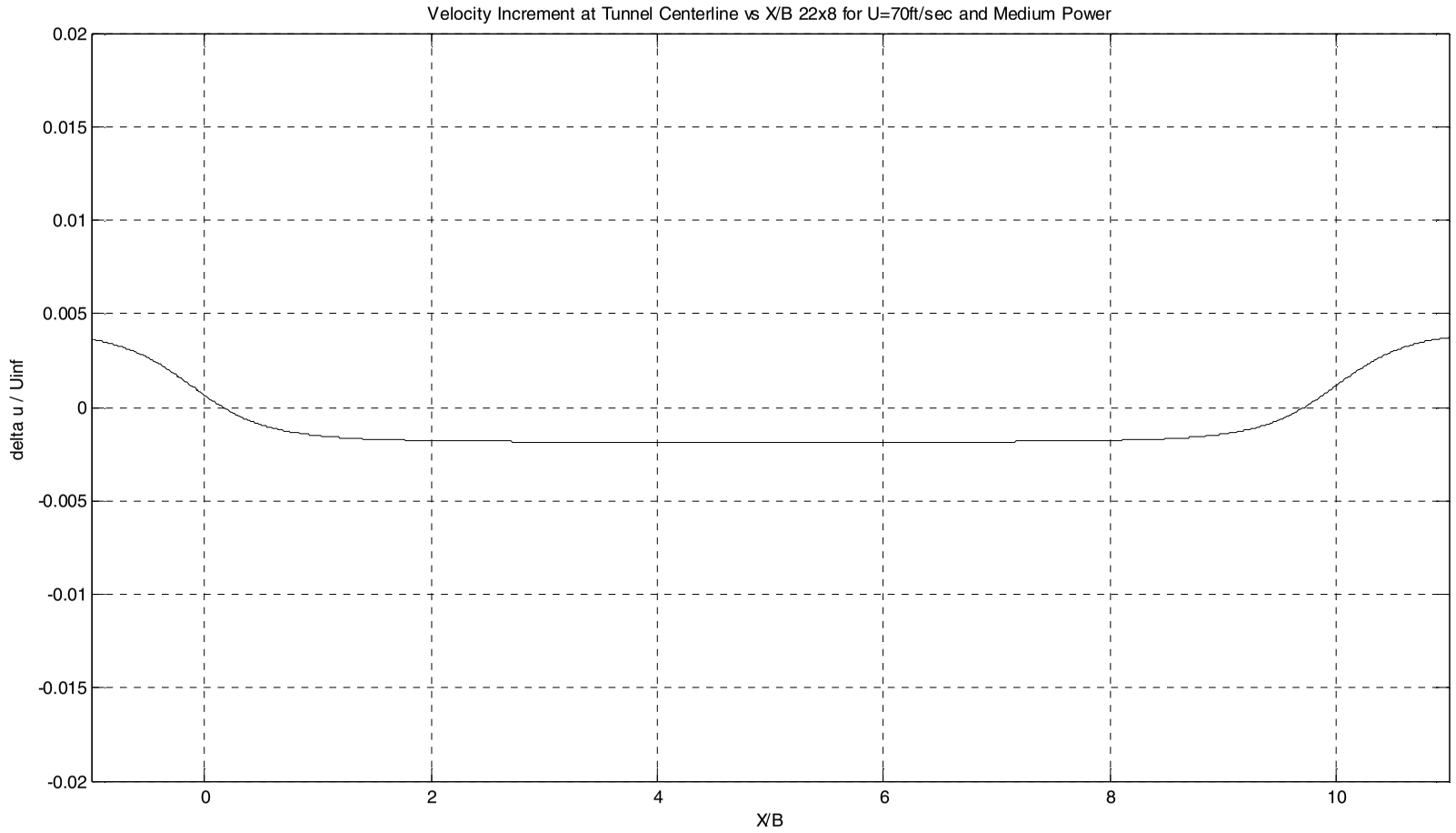

Centerline velocity increment for 22” x 8” propeller at 70ft/sec at medium RPM.

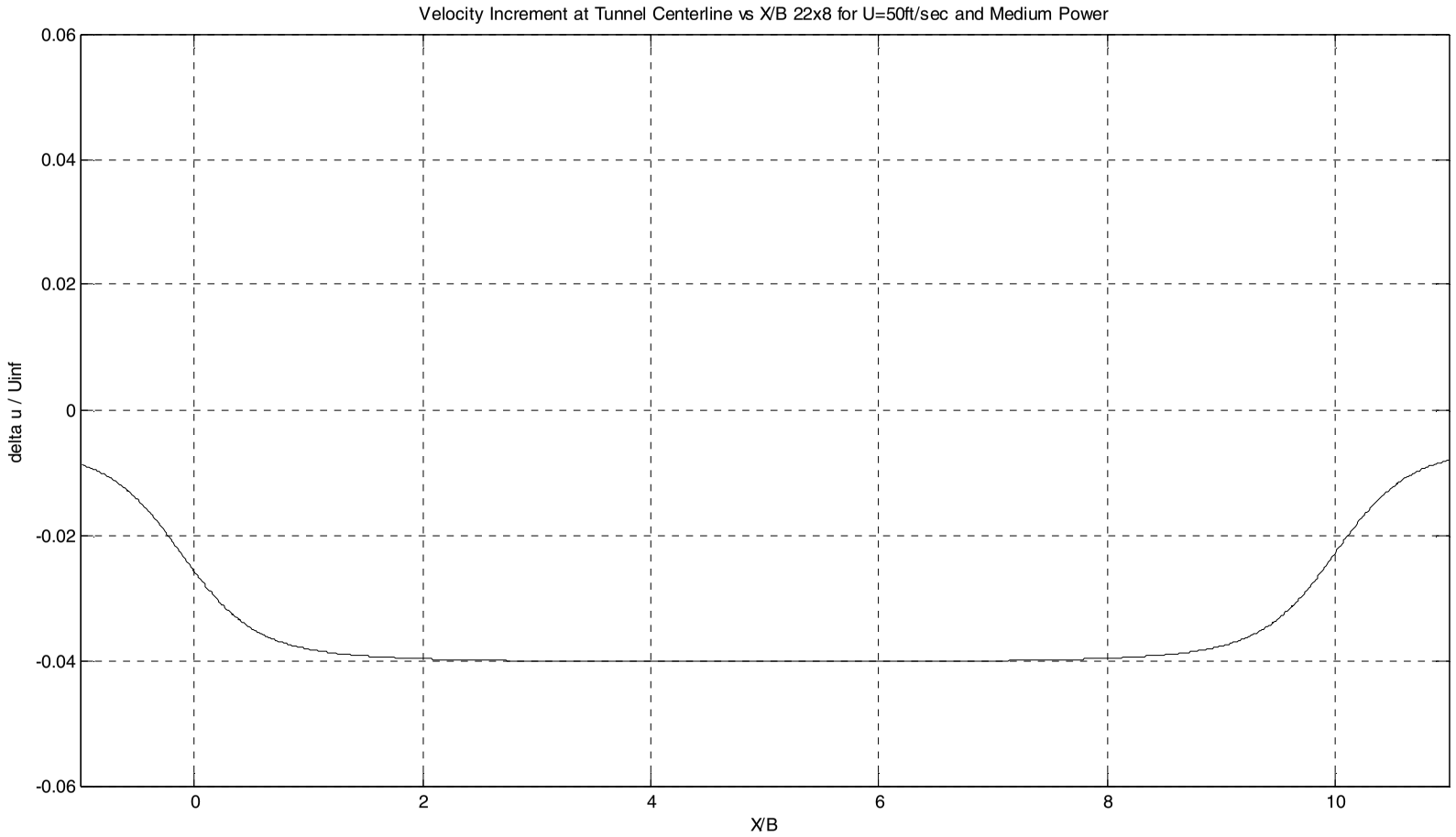

Centerline velocity increment for 22” x 8” propeller at 50ft/sec at medium RPM.

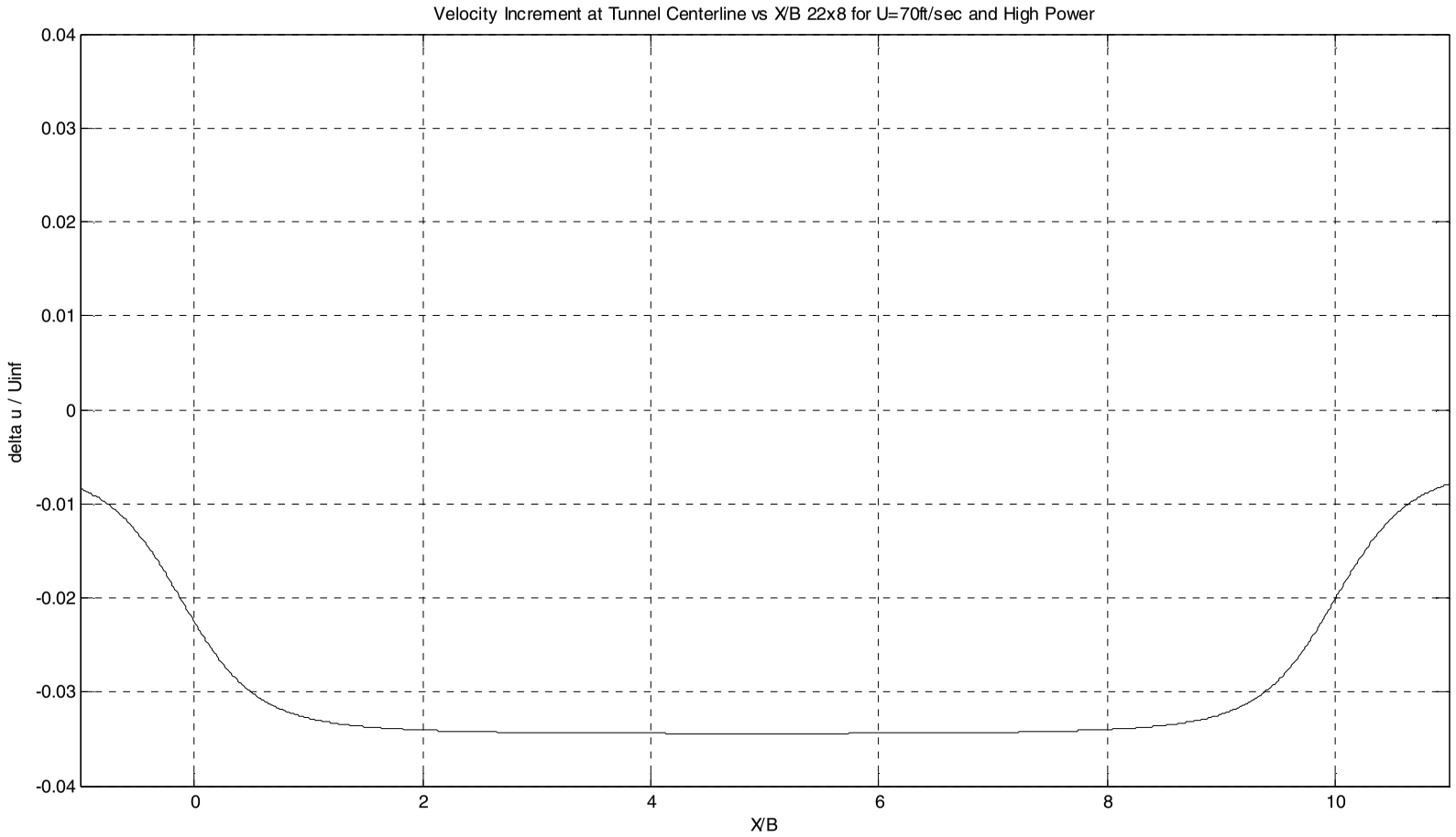

Centerline velocity increment for 22” x 8” propeller at 70ft/sec at high RPM.

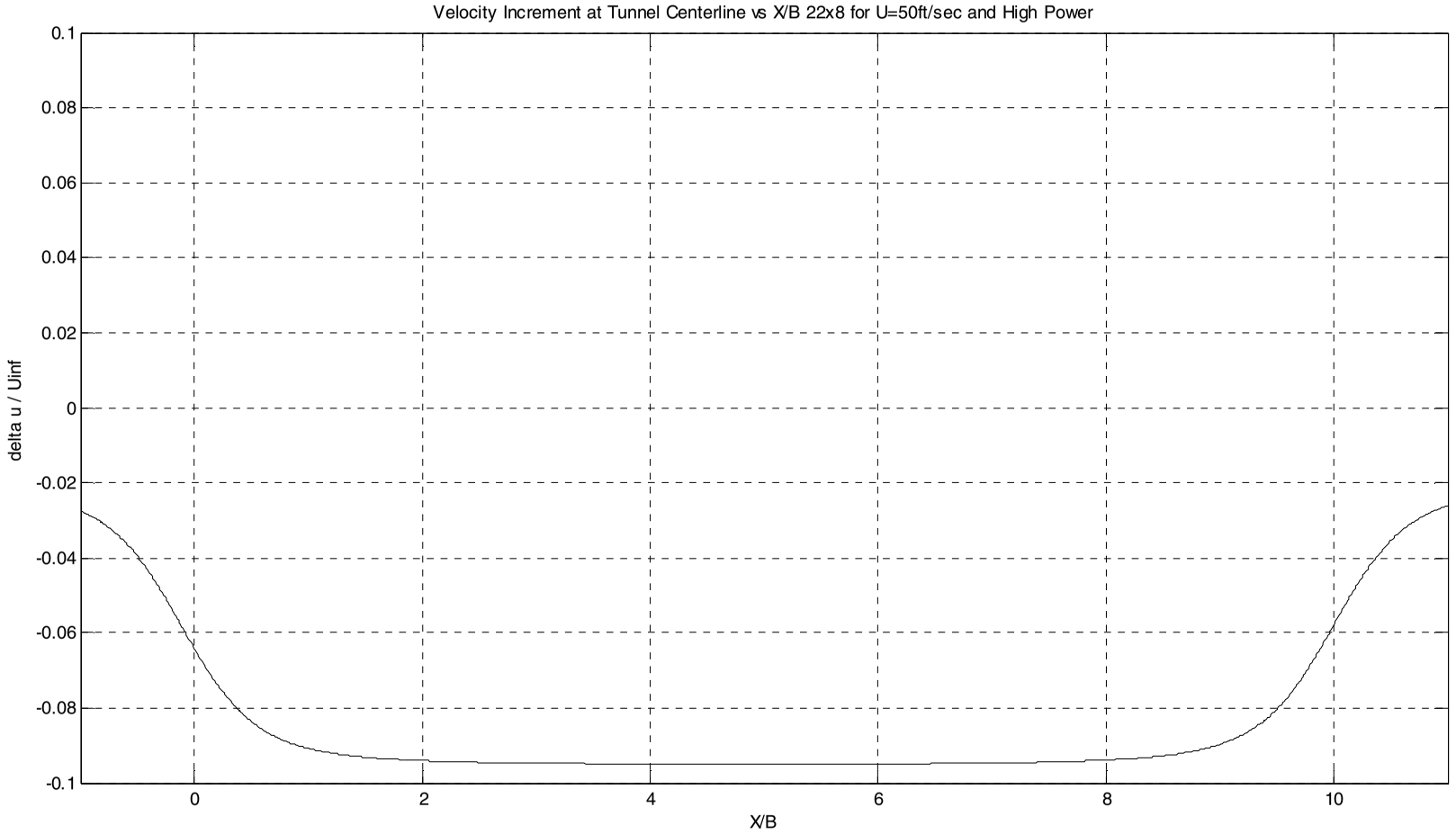

Centerline velocity increment for 22” x 8” propeller at 50ft/sec at high RPM.

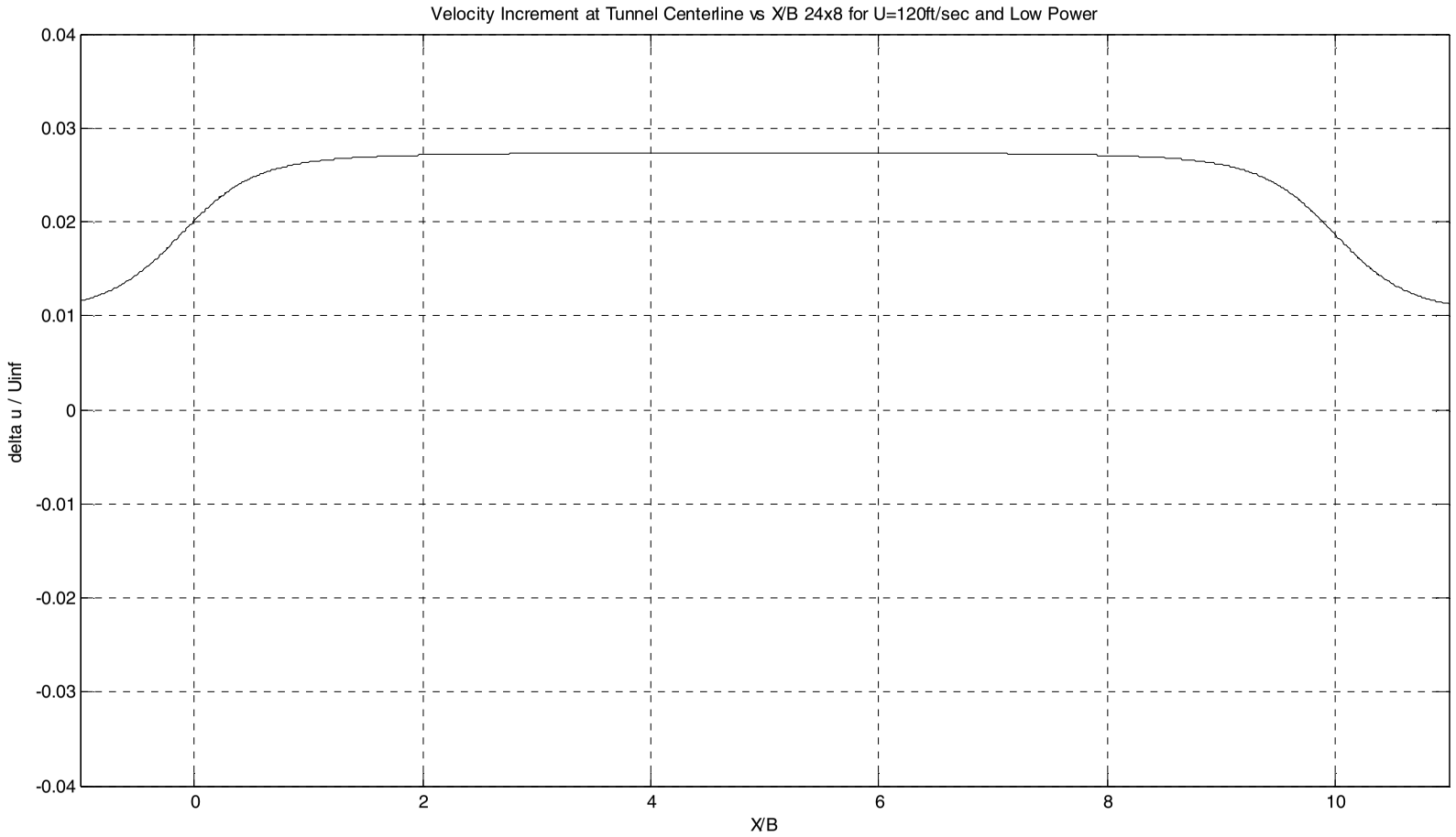

Centerline velocity increment for 24” x 8” propeller at 120ft/sec at low RPM.

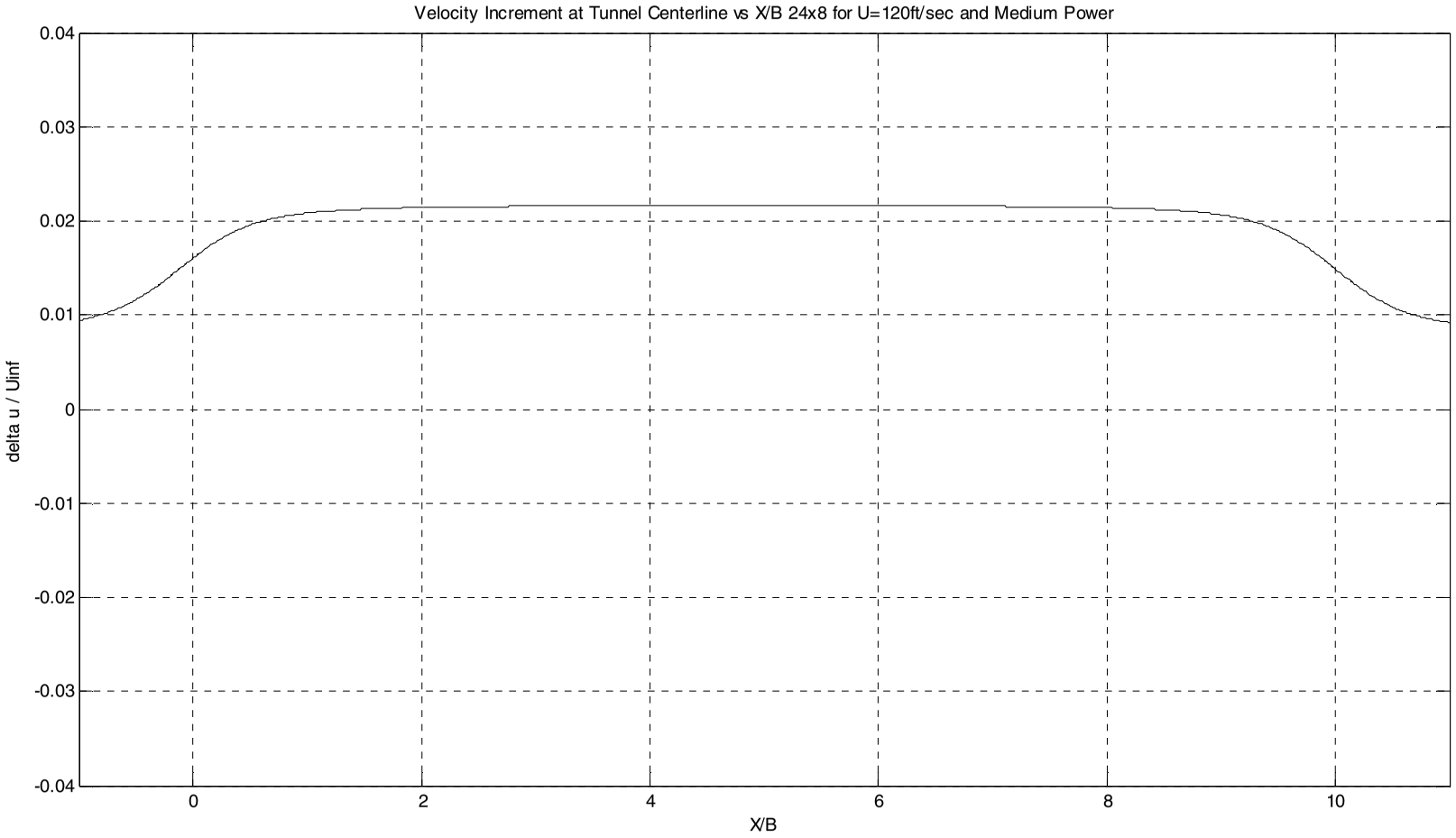

Centerline velocity increment for 24” x 8” propeller at 120ft/sec at medium RPM.

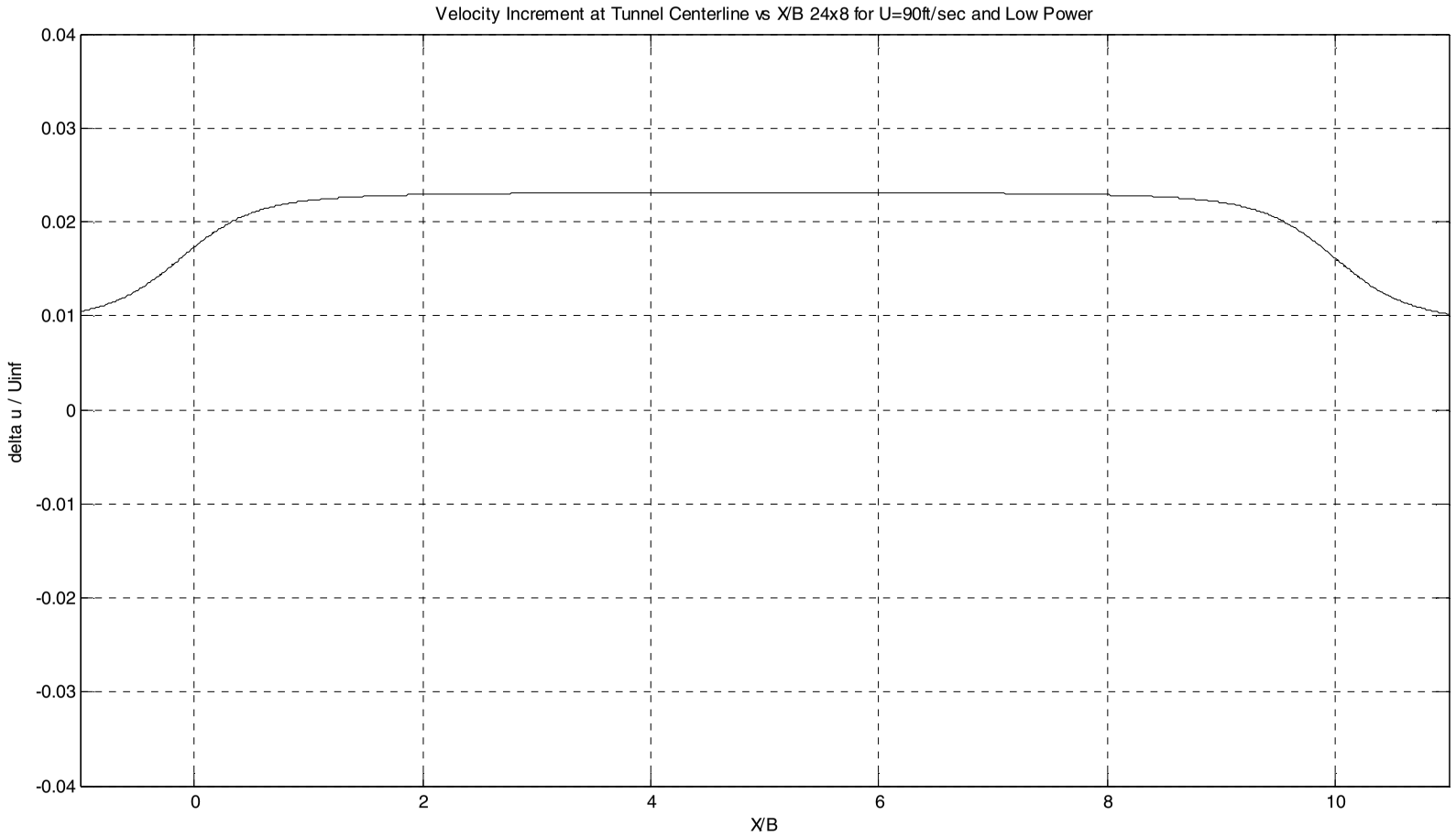

Centerline velocity increment for 24” x 8” propeller at 90ft/sec at low RPM.

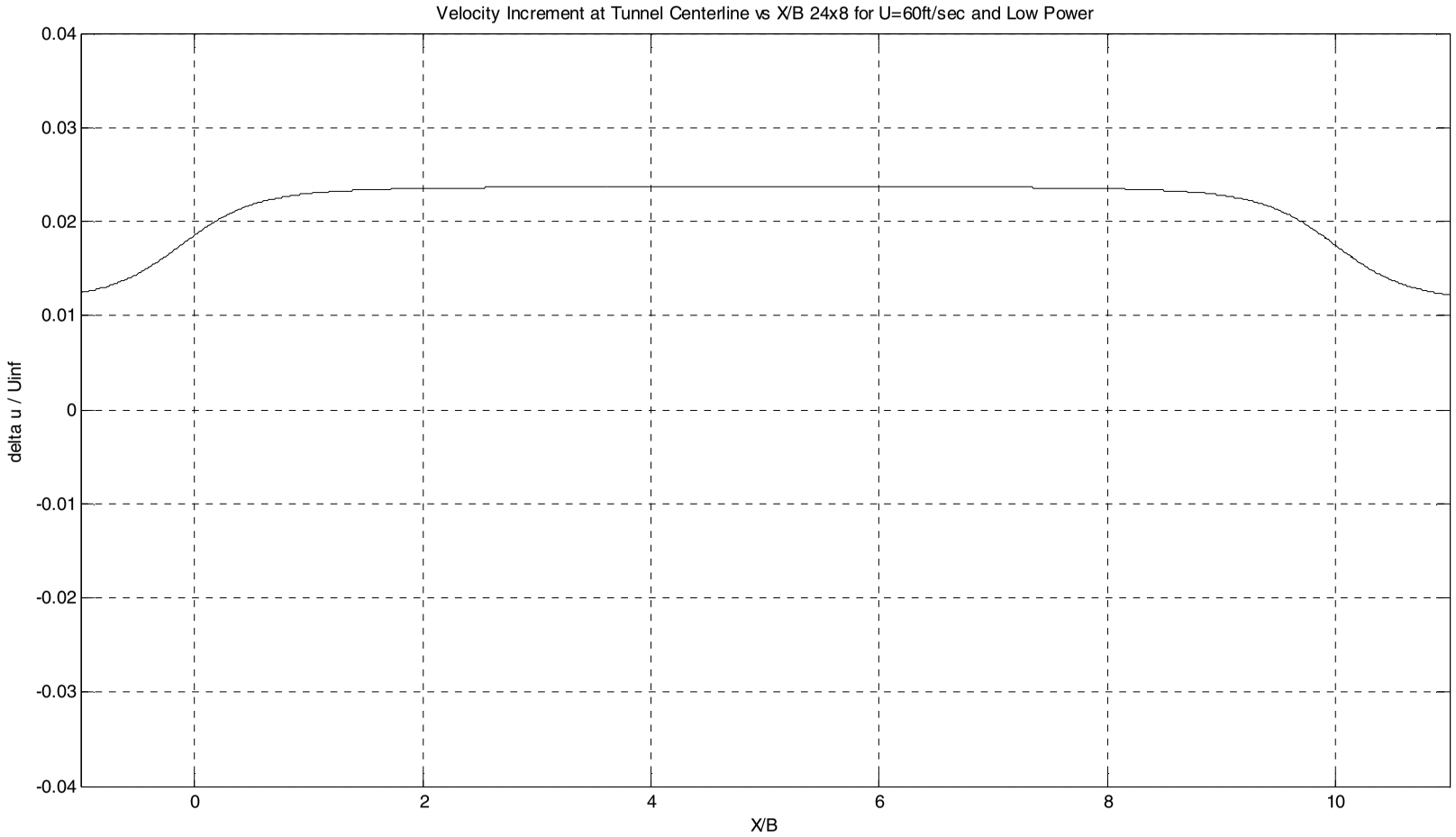

Centerline velocity increment for 24” x 8” propeller at 60ft/sec at low RPM.

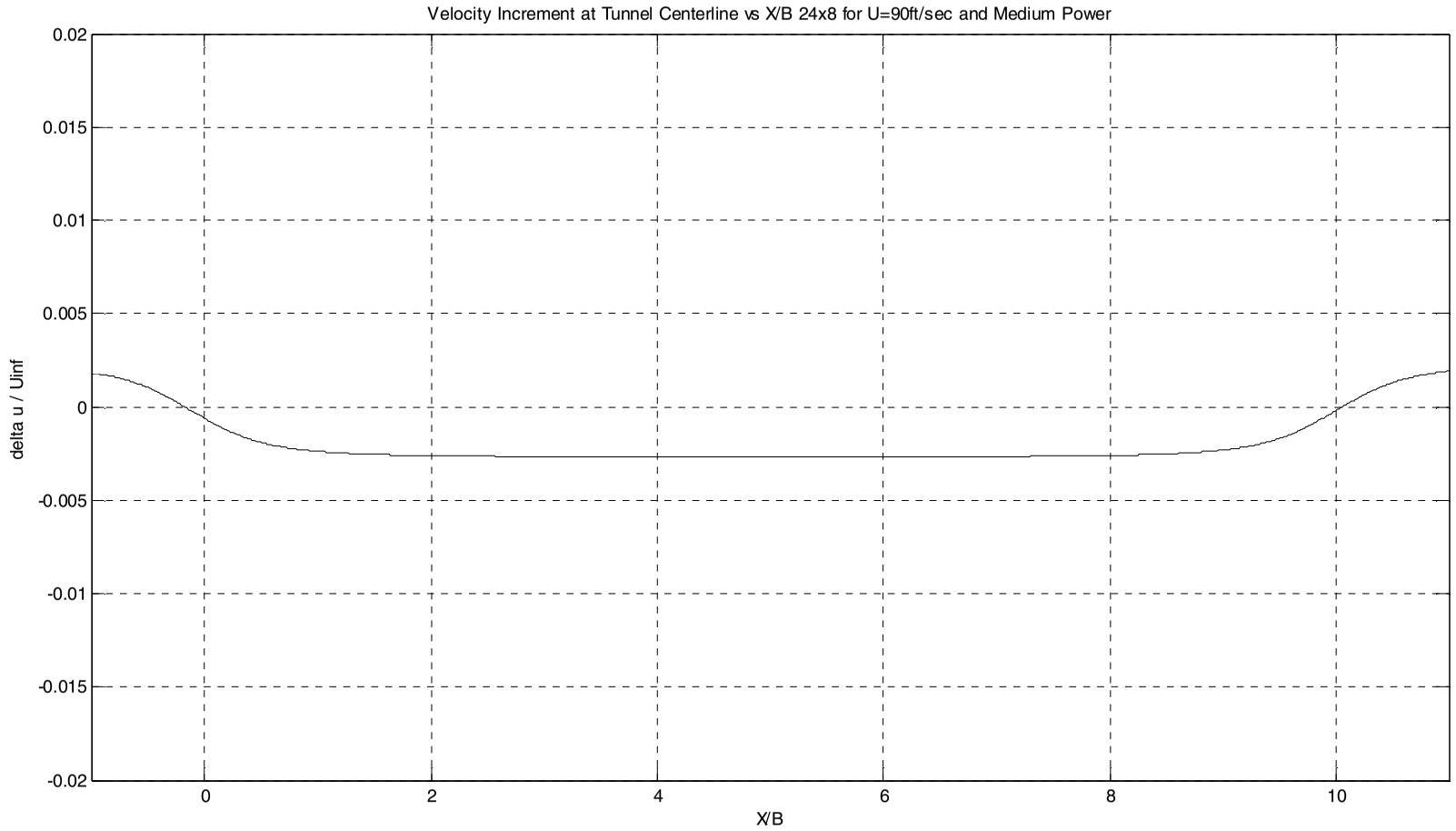

Centerline velocity increment for 24” x 8” propeller at 90ft/sec at medium RPM.

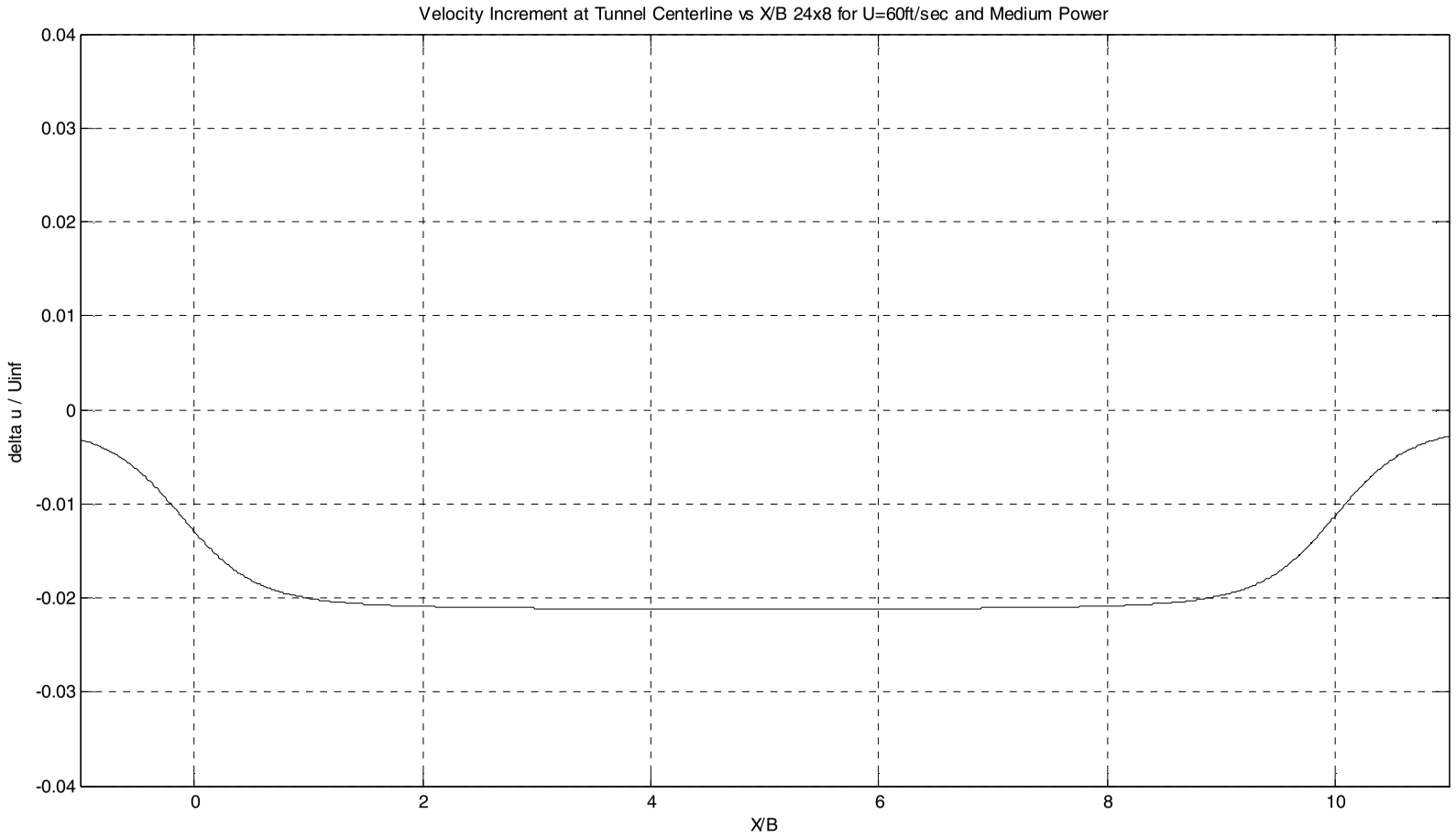

Centerline velocity increment for 24” x 8” propeller at 60ft/sec at medium RPM.

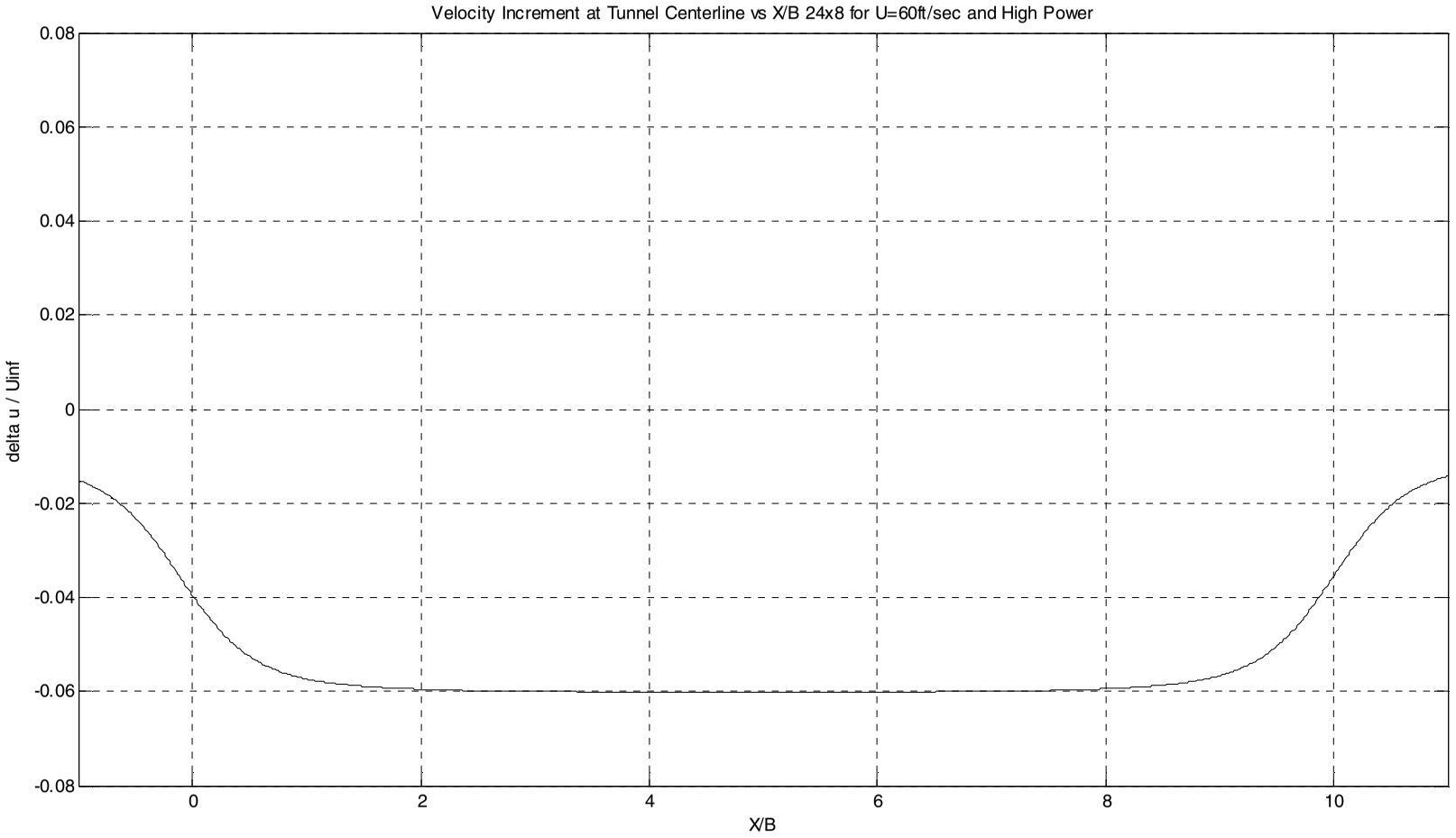

Centerline velocity increment for 24” x 8” propeller at 60ft/sec at high RPM.

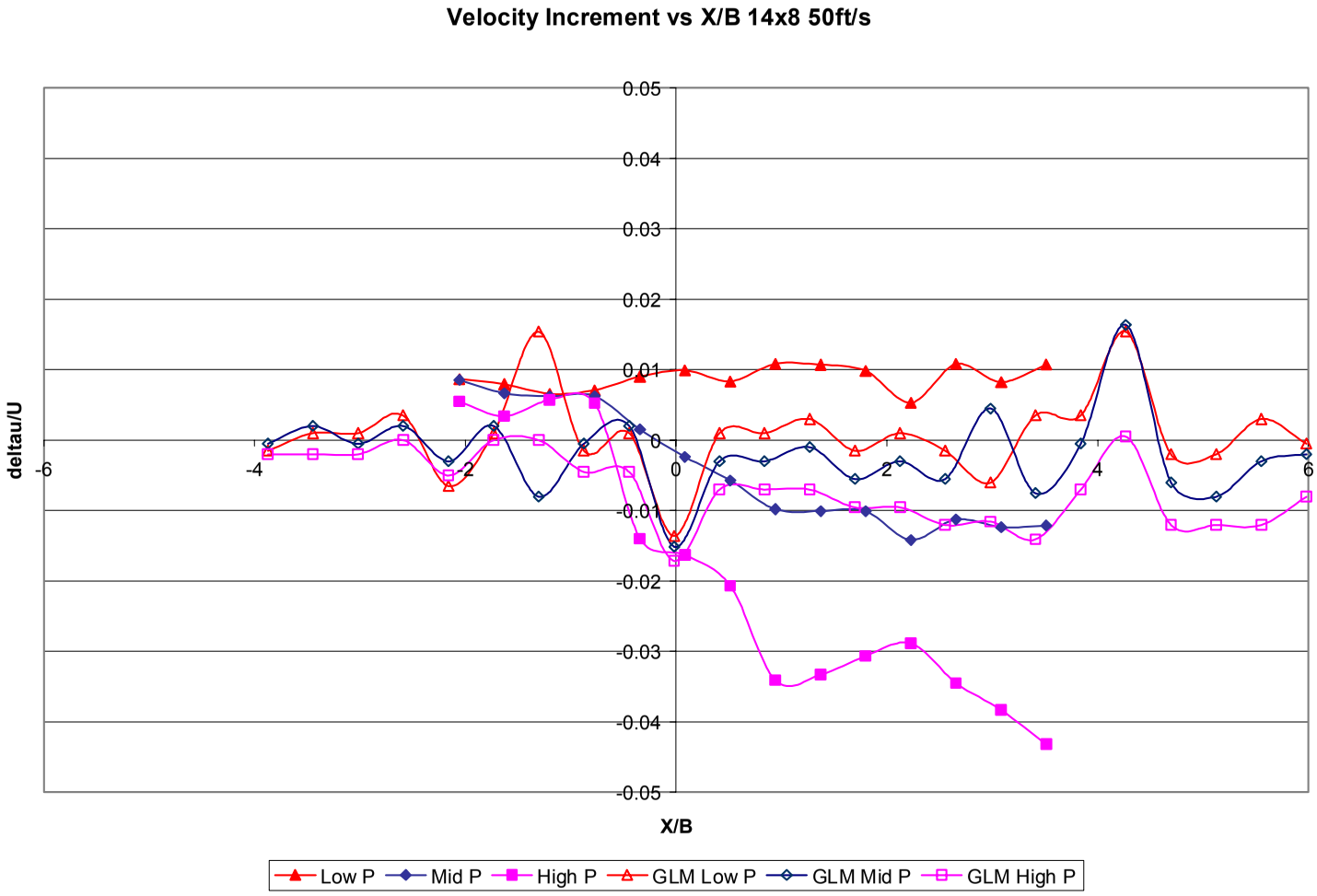

Velocity increment calculated from pressure data collected at NATF and GLMWT for the 14”x8” propeller and wind tunnel speed of 50ft/s.

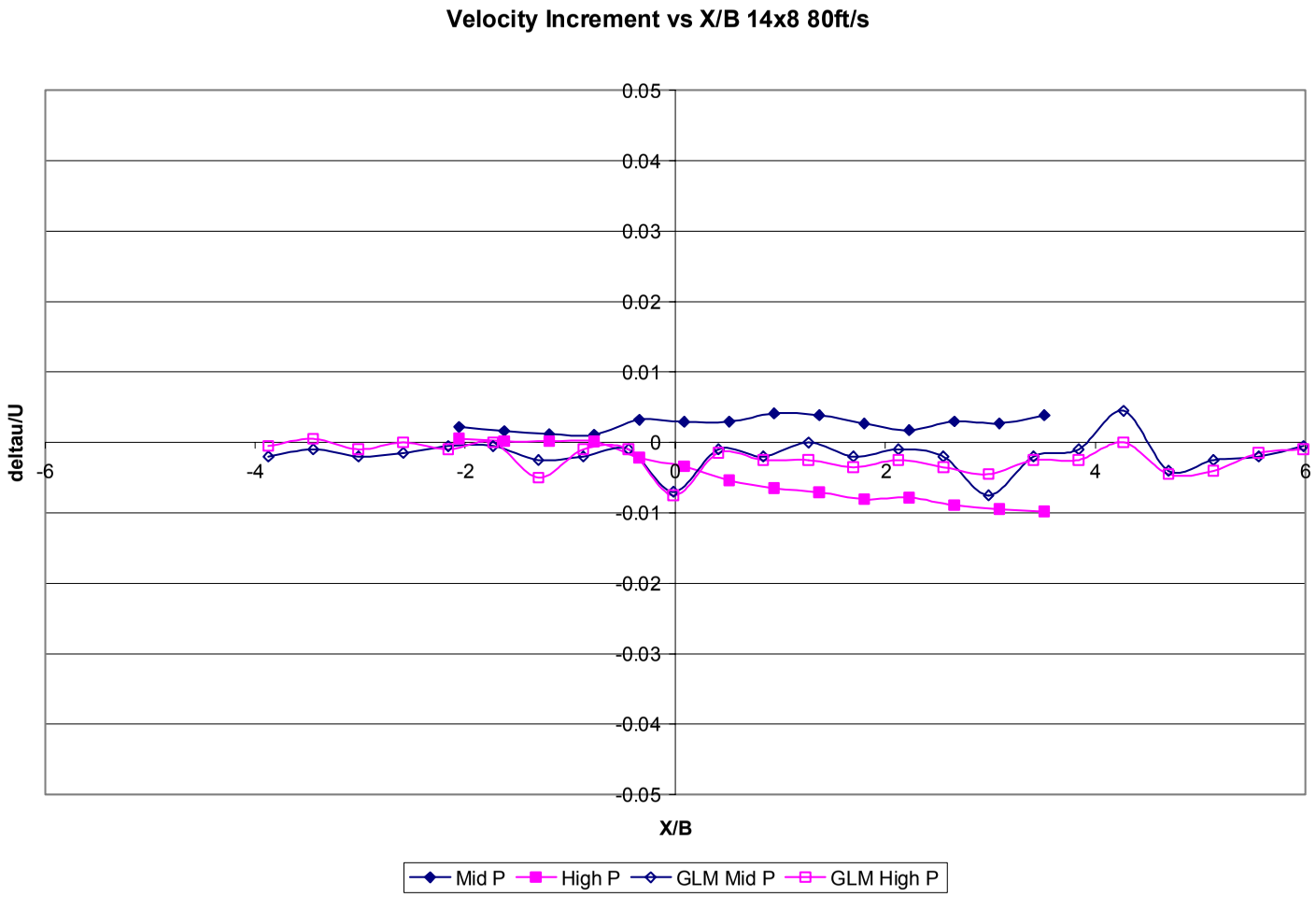

Velocity increment calculated from pressure data collected at NATF and GLMWT for the 14”x8” propeller and wind tunnel speed of 80ft/s.

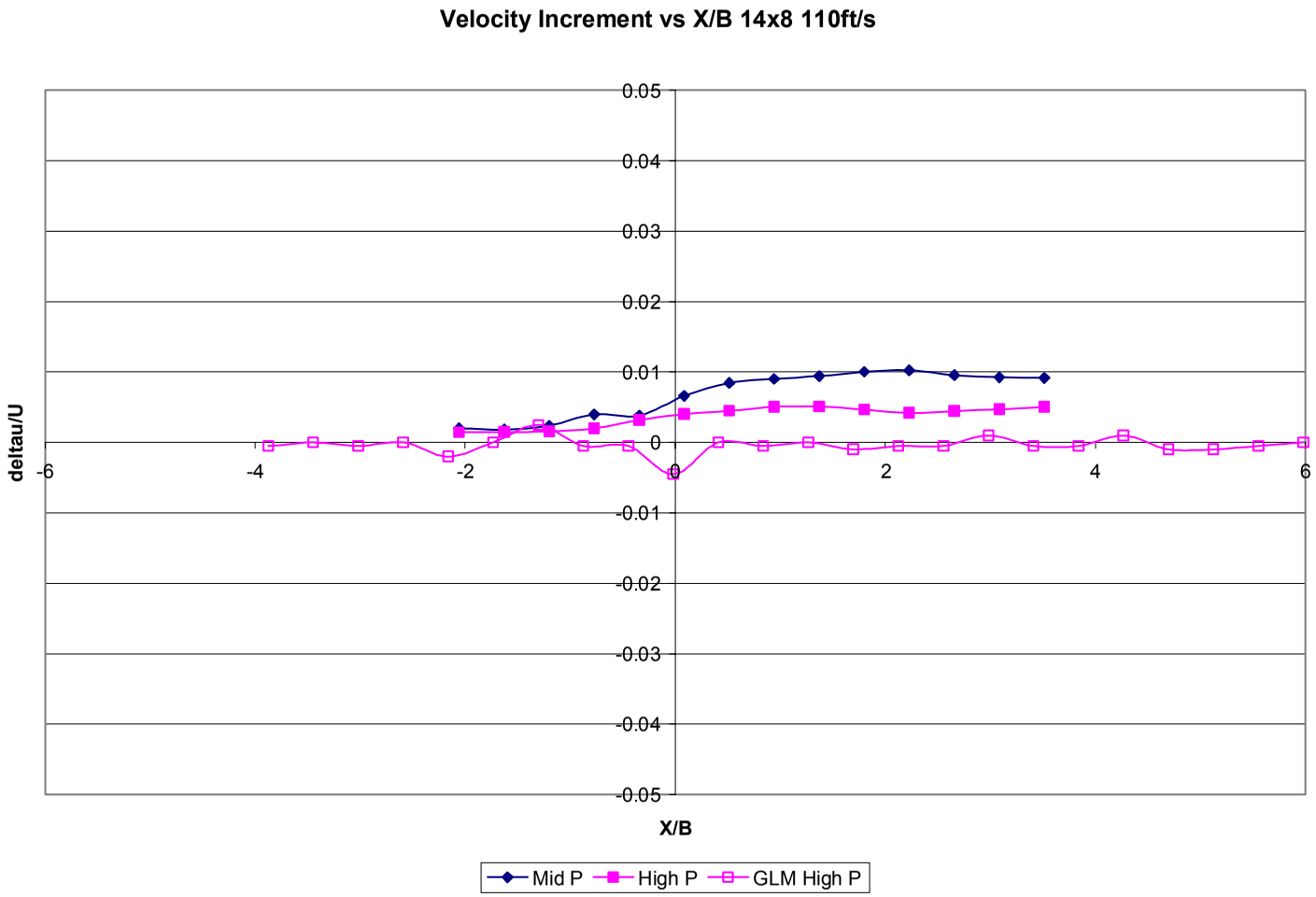

Velocity increment calculated from pressure data collected at NATF and GLMWT for the 14”x8” propeller and wind tunnel speed of 110ft/s.

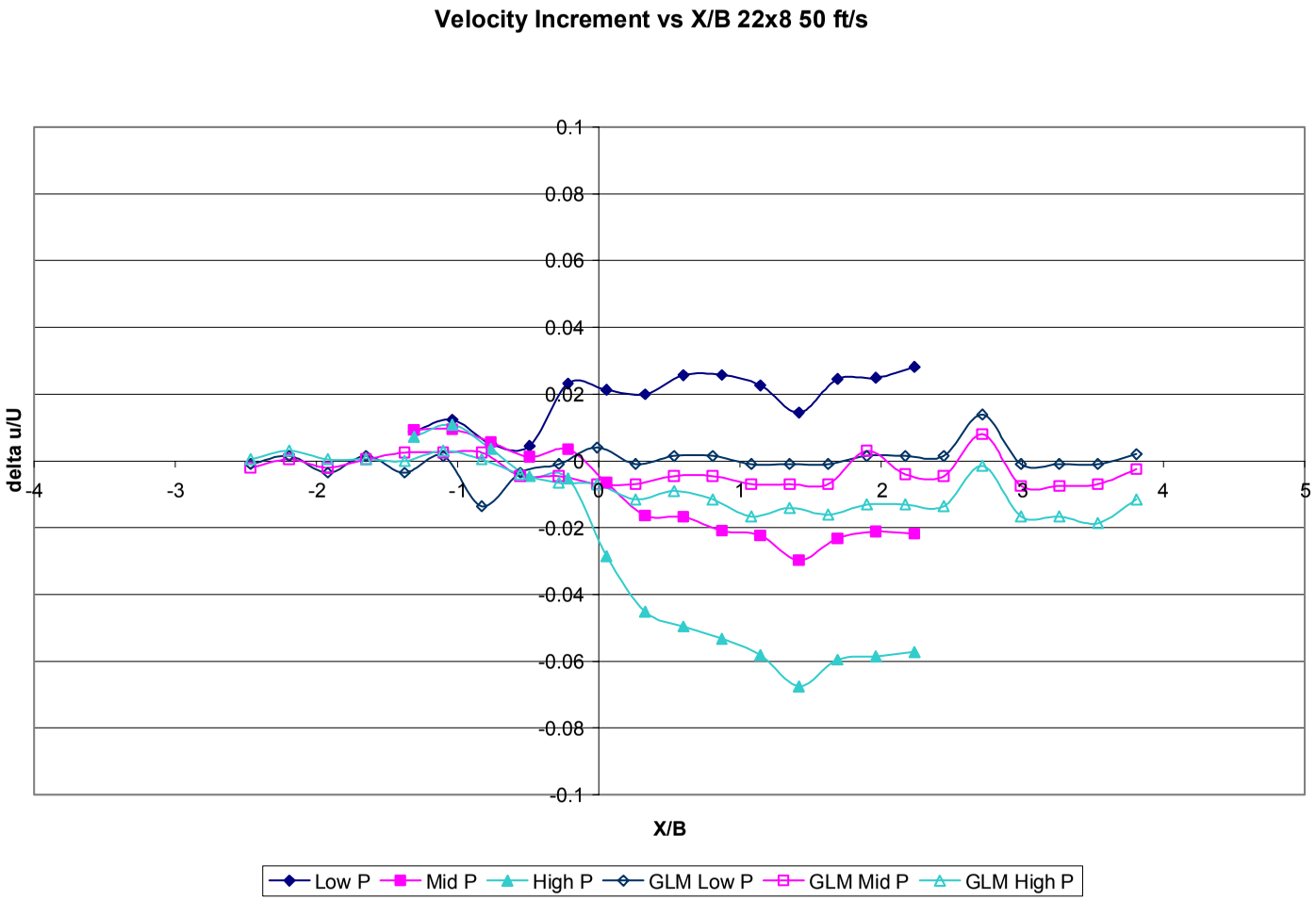

Velocity increment calculated from pressure data collected at NATF and GLMWT for the 22”x8” propeller and wind tunnel speed of 50ft/s.

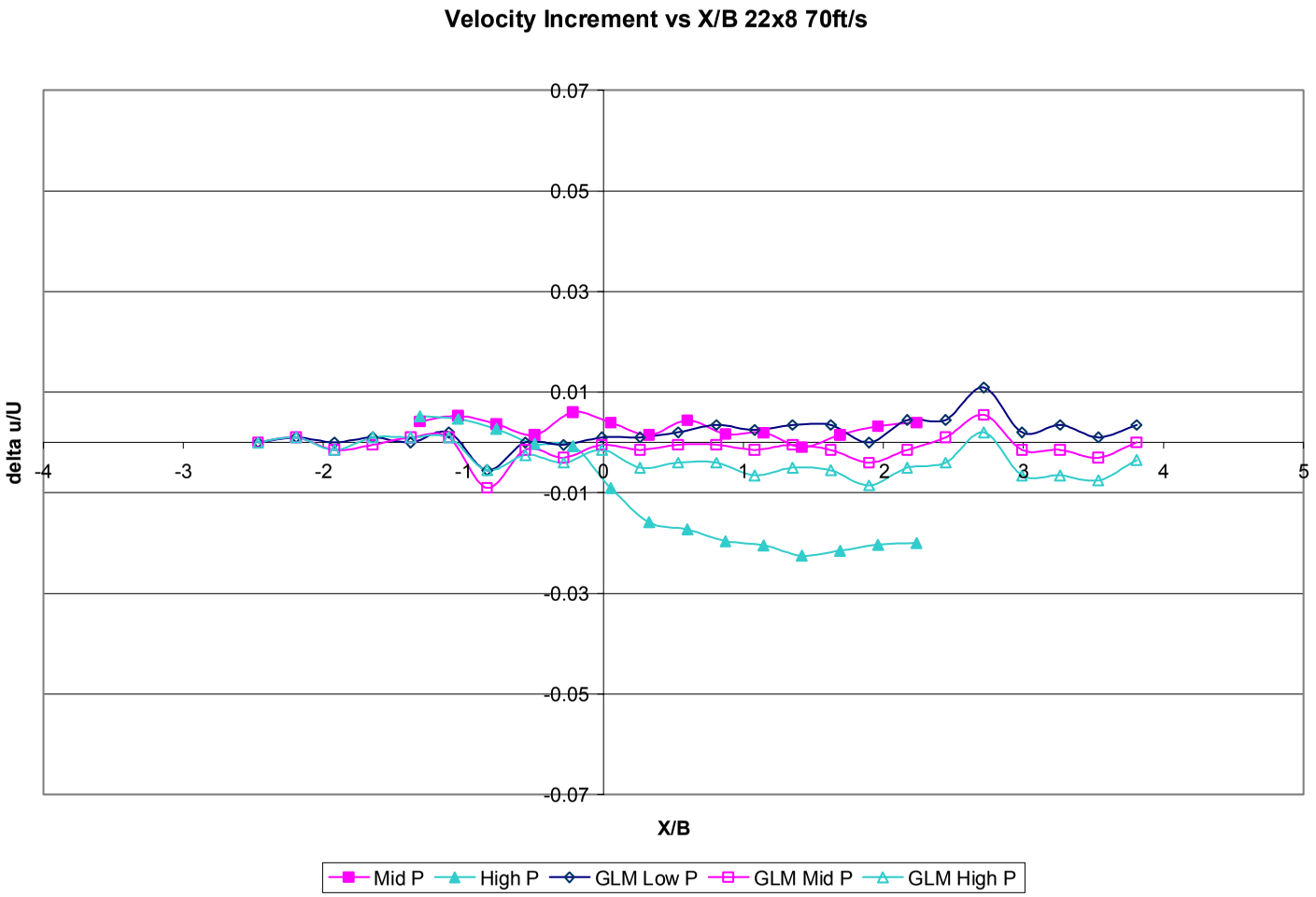

Velocity increment calculated from pressure data collected at NATF and GLMWT for the 22”x8” propeller and wind tunnel speed of 70ft/s.

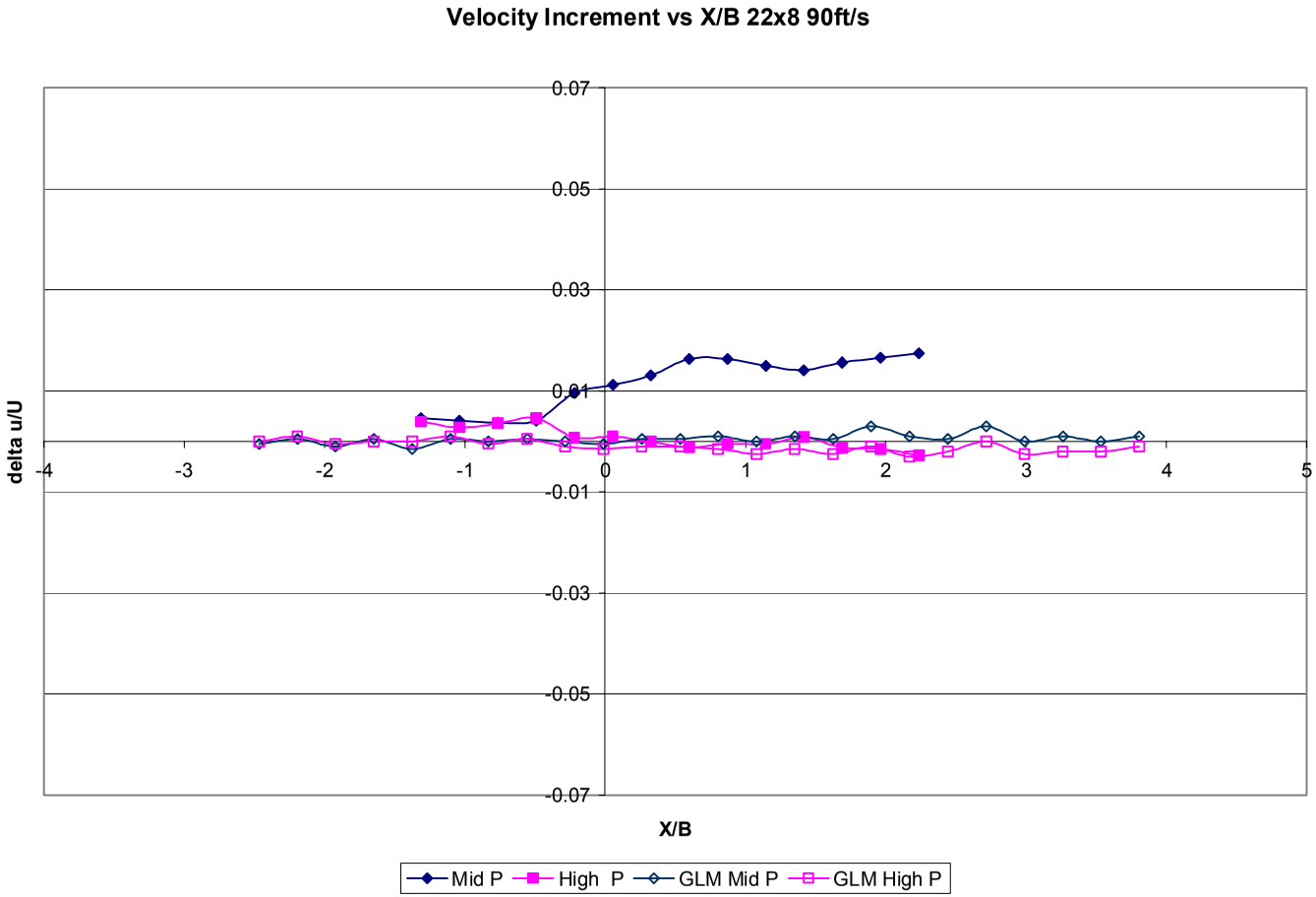

Velocity increment calculated from pressure data collected at NATF and GLMWT for the 22”x8” propeller and wind tunnel speed of 90ft/s.

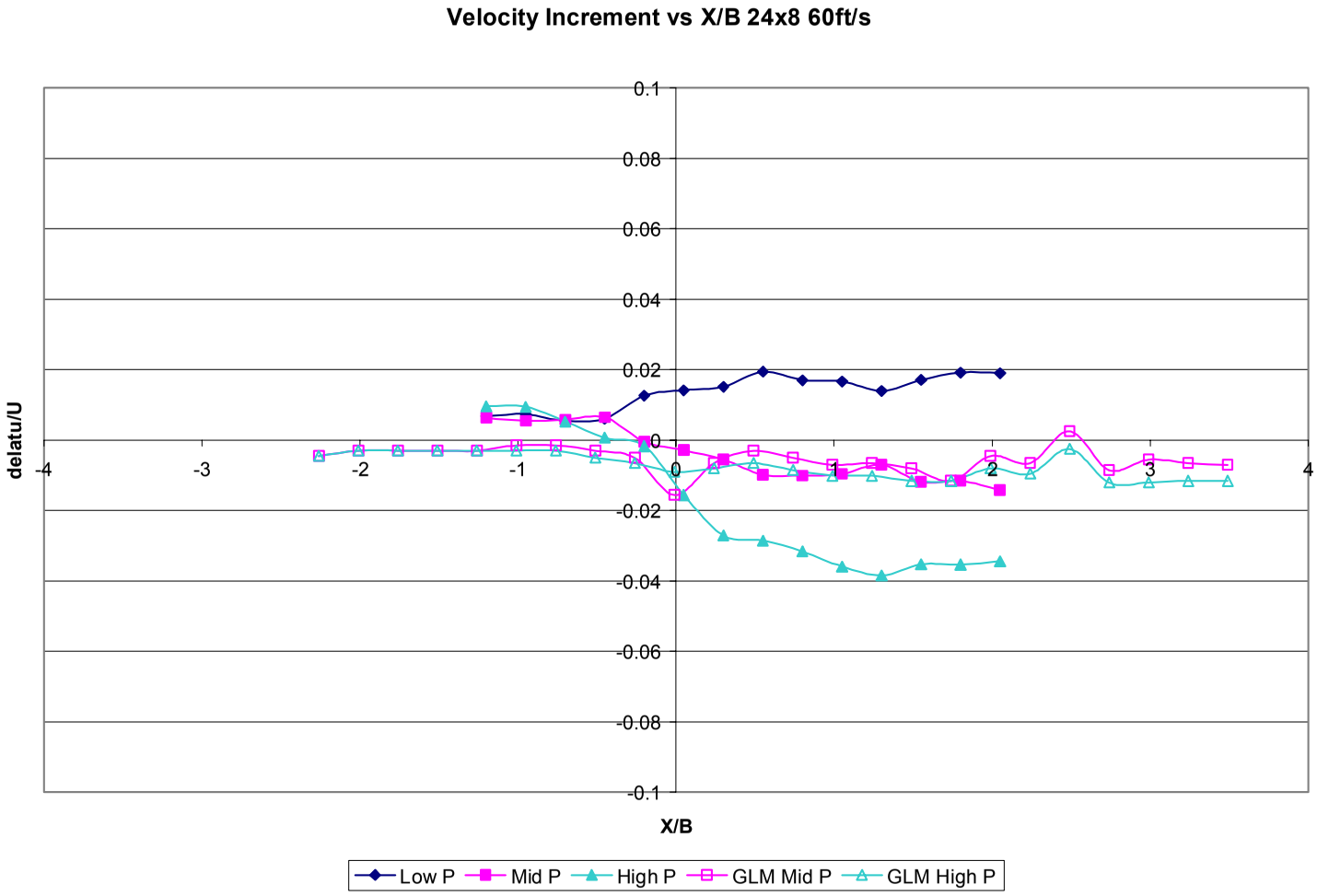

Velocity increment calculated from pressure data collected at NATF and GLMWT for the 24”x8” propeller and wind tunnel speed of 60ft/s

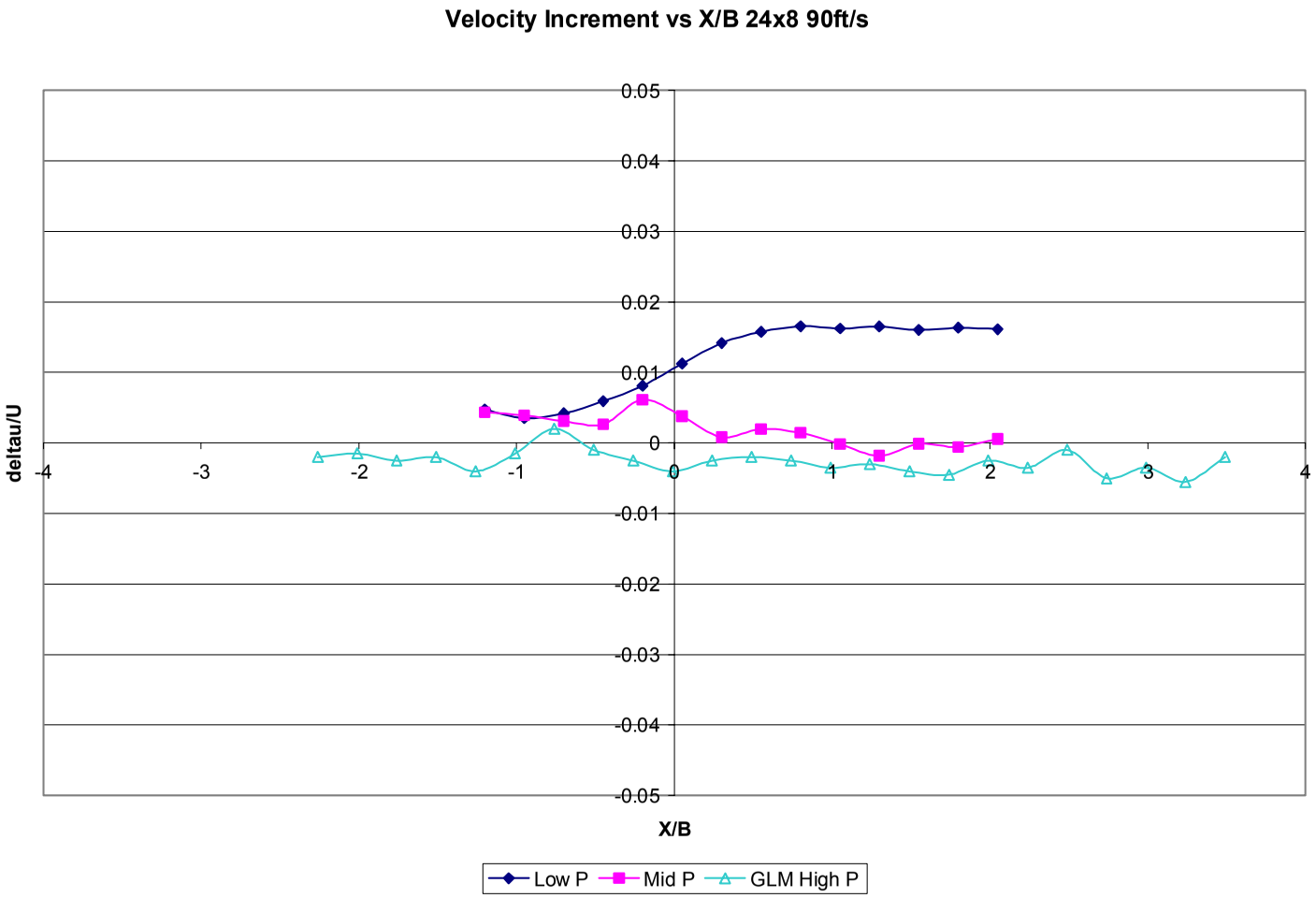

Velocity increment calculated from pressure data collected at NATF and GLMWT for the 24”x8” propeller and wind tunnel speed of 90ft/s

					Sorensen			Glauert		
Velocity (ft/sec)	Power Setting (1=L, 2=M, 3H)	Density (psf)	Thrust (pounds)	Ct	Delta P (psf)	Delta Cp	Deltau/U	Delta P	Delta Cp	Deltau/U
110.3070	2	0.002287	-7.38	-0.49617	0.33393	0.02400	-0.01207	-1.117251	-0.080299	0.039374
109.8700	3	0.002288	-5.03	-0.34072	0.00865	0.00063	-0.00031	-0.595769	-0.043141	0.021343
80.4289	2	0.002287	-2.18	-0.27568	3.23609	0.43748	-0.24999	-0.256562	-0.034685	0.017195
50.0125	1	0.002284	-0.88	-0.28819	-5.10874	-1.78851	0.66988	-0.103686	-0.036237	0.017957
80.1783	3	0.002288	0.9	0.114477	0.00718	0.00098	-0.00049	0.087988	0.0133	-0.0067
49.9617	2	0.002286	2	0.655731	0.07770	0.02723	-0.01371	0.162061	0.06	-0.0304
49.9712	3	0.002292	5.83	1.905728	0.49729	0.17378	-0.09103	0.311035	0.1043	-0.0536

Predicted pressure, coefficient of pressure, and velocity increment differentials as predicted by Sørensen and Mikkelsen and Glauert's methods for the 14"x8" propeller.

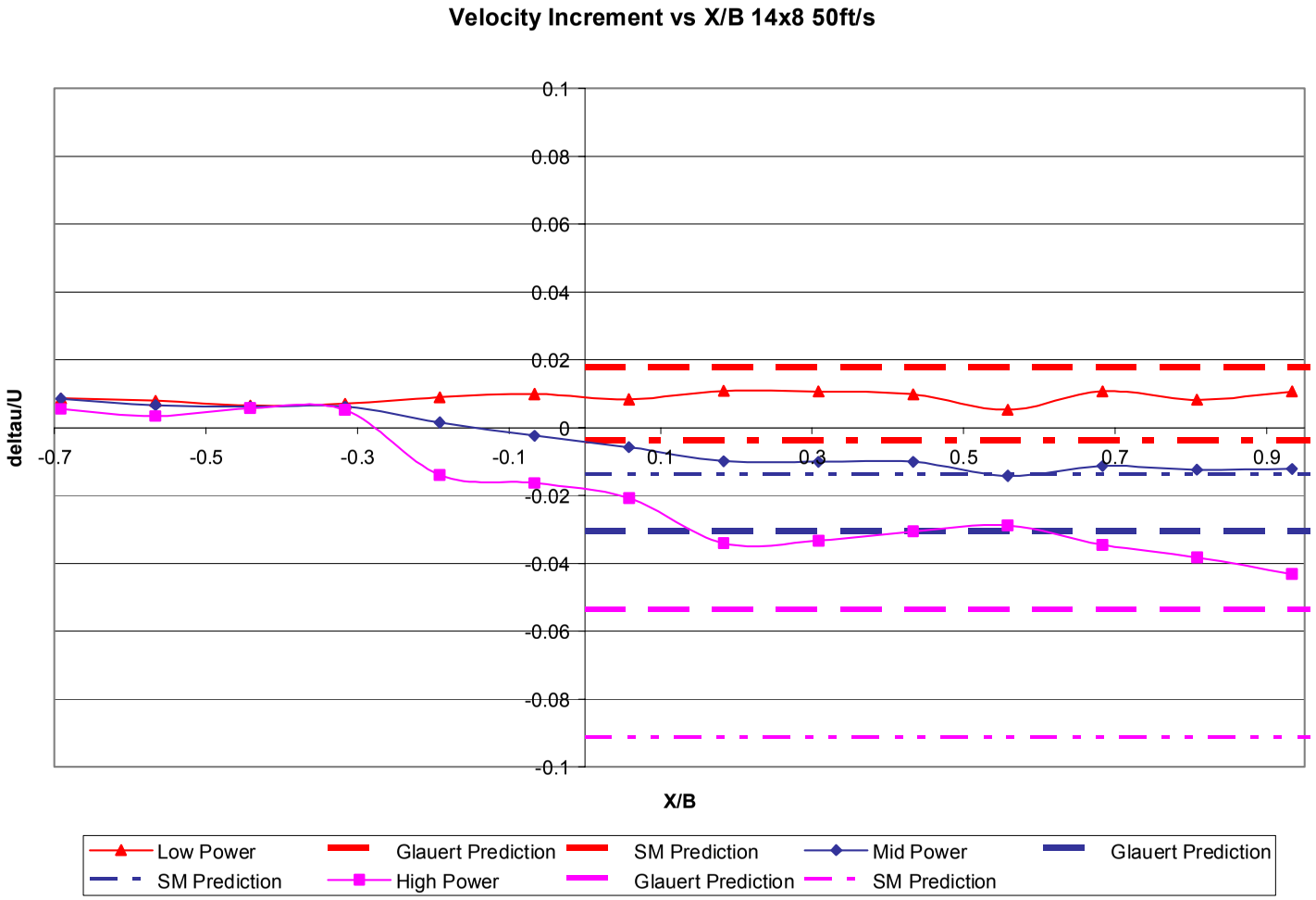

Predicted incremental velocity differentials plotted against velocity increments obtained from experimental data for the 14”x8” propeller and wind tunnel velocity of 50 ft/s.

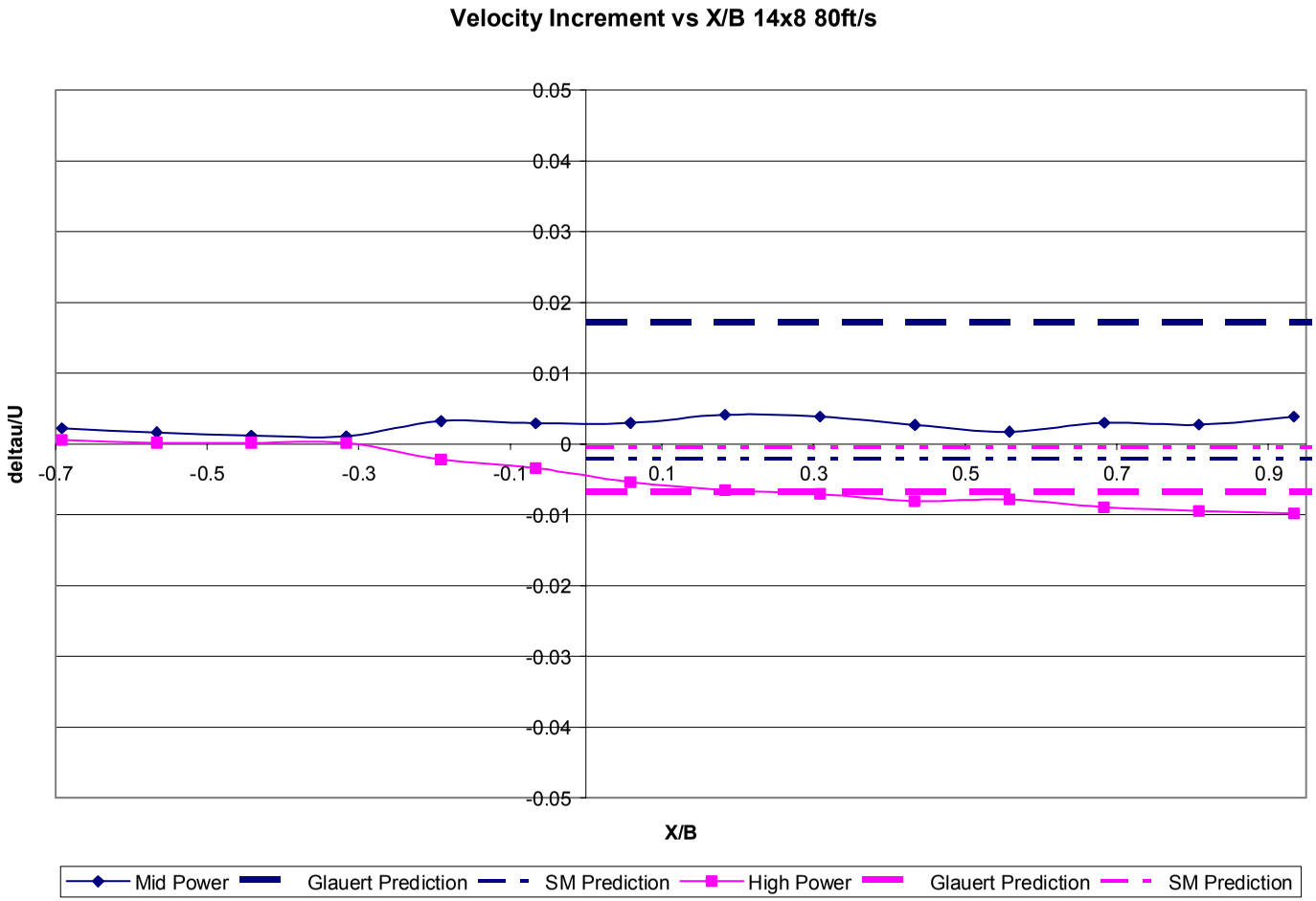

Predicted incremental velocity differentials plotted against velocity increments obtained from experimental data for the 14”x8” propeller and wind tunnel velocity of 80 ft/s.

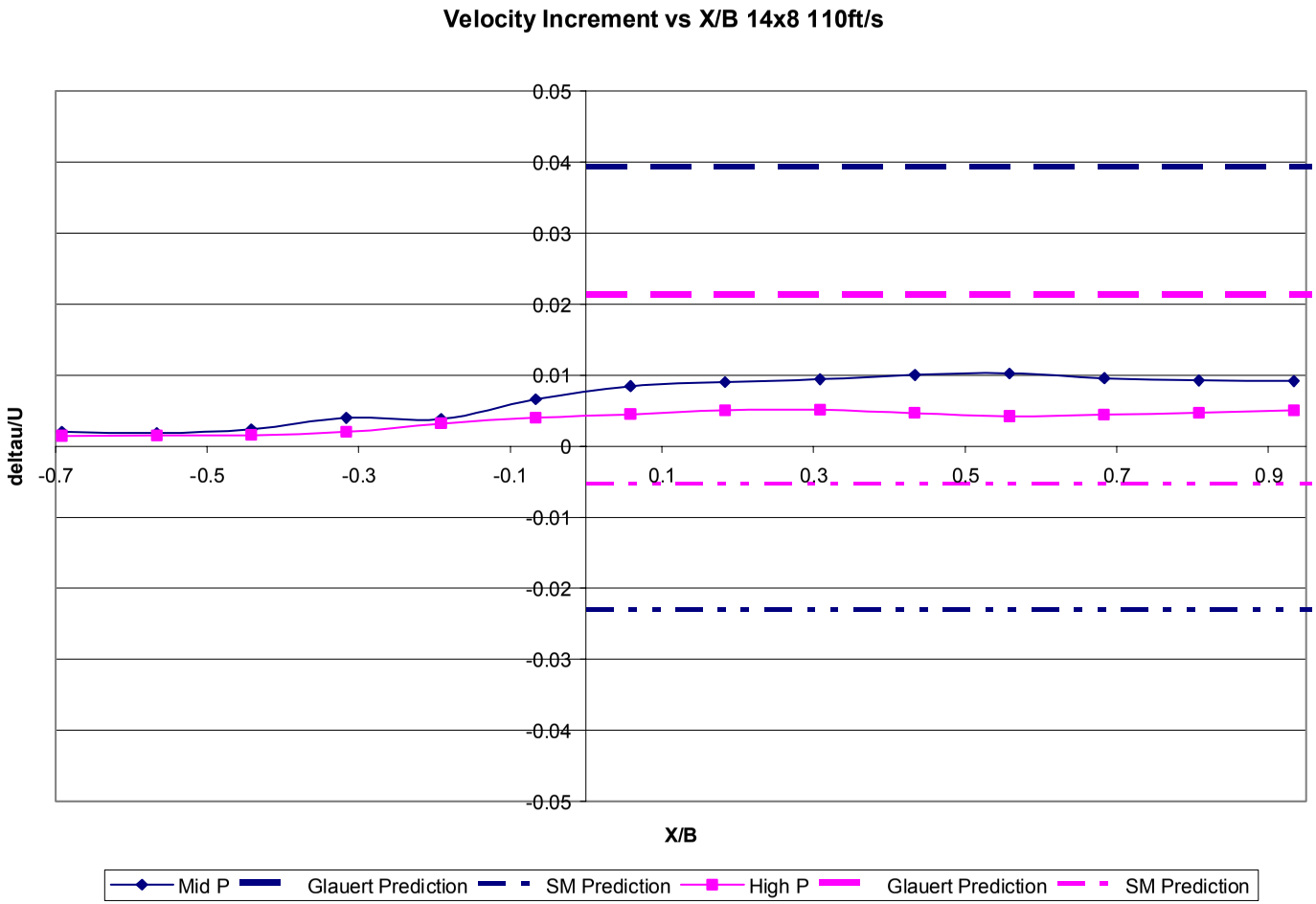

Predicted incremental velocity differentials plotted against velocity increments obtained from experimental data for the 14”x8” propeller and wind tunnel velocity of 110 ft/s.

					Sorensen			Glauert		
Velocity (ft/sec)	Power Setting (1=L, 2=M, 3H)	Density (psf)	Thrust (pounds)	Ct	Delta P (psf)	Delta Cp	Deltau/U	Delta P	Delta Cp	Deltau/U
89.9377	2	0.00229	-5.72	-0.23519	0.23078	0.02495	-0.01255	-0.87231	-0.07608	0.03734
90.0118	3	0.00228	-1.83	-0.07512	0.02000	0.00216	-0.00108	-0.86743	-0.02320	0.01153
50.1563	1	0.00229	-1.71	-0.22607	0.06569	0.02282	-0.01148	-0.97207	-0.07292	0.03582
69.0532	2	0.00229	-0.68	-0.04747	0.00472	0.00087	-0.00043	-0.97598	-0.01449	0.00722
50.4222	2	0.00229	3.18	0.415994	0.13087	0.04500	-0.02276	-1.19378	0.10687	-0.05495
69.8033	3	0.00229	4.9	0.33461	0.17039	0.03059	-0.01542	-1.15743	0.08878	-0.04542
50.3707	3	0.00229	9.46	1.239539	0.77548	0.26670	-0.14367	-1.54522	0.23040	-0.12270

Predicted pressure, coefficient of pressure, and velocity increment differentials as predicted by Sørensen and Mikkelsen and Glauert's methods for the 22"x8" propeller.

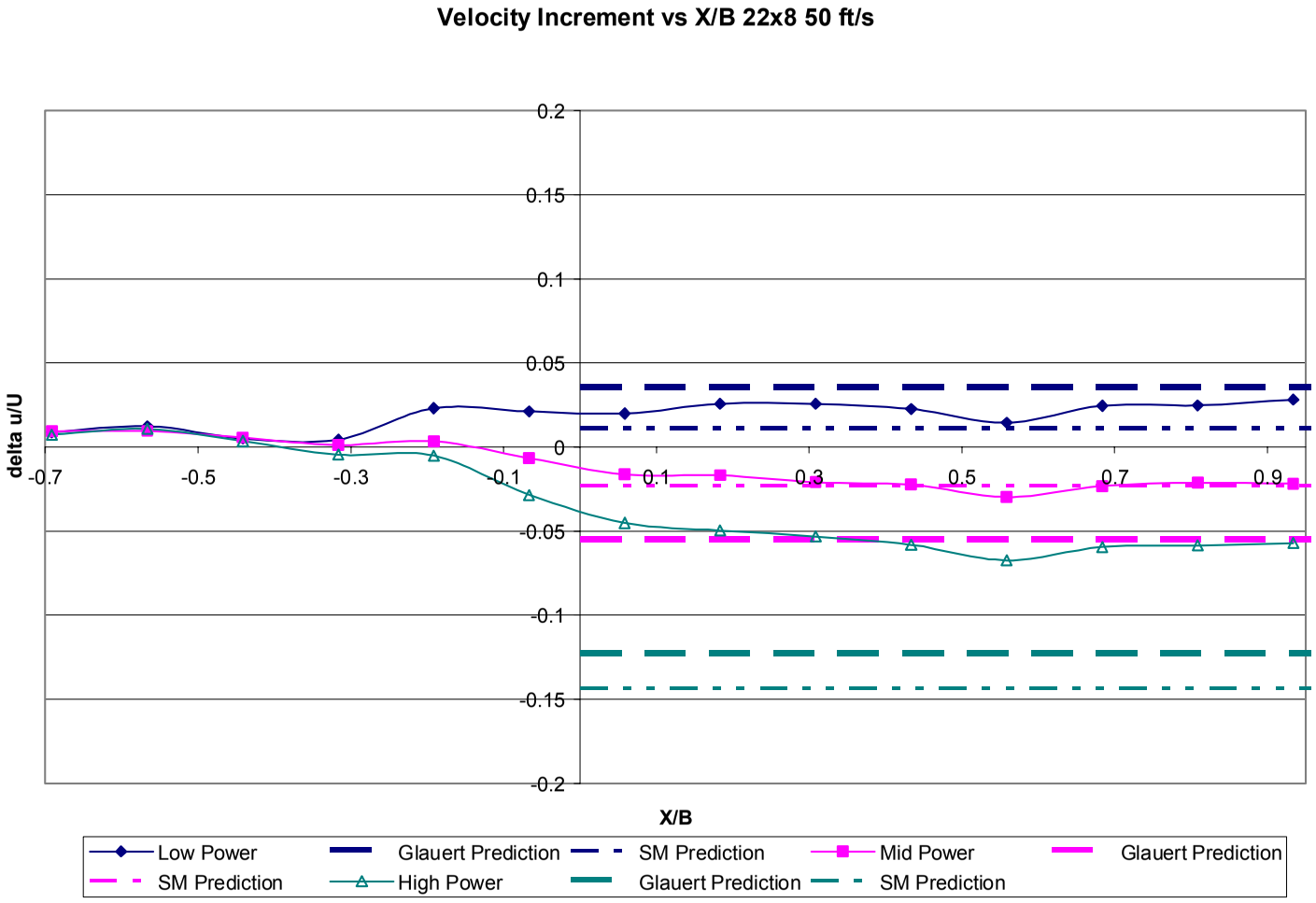

Predicted incremental velocity differentials plotted against velocity increments obtained from experimental data for the 22”x8” propeller and wind tunnel velocity of 50 ft/s.

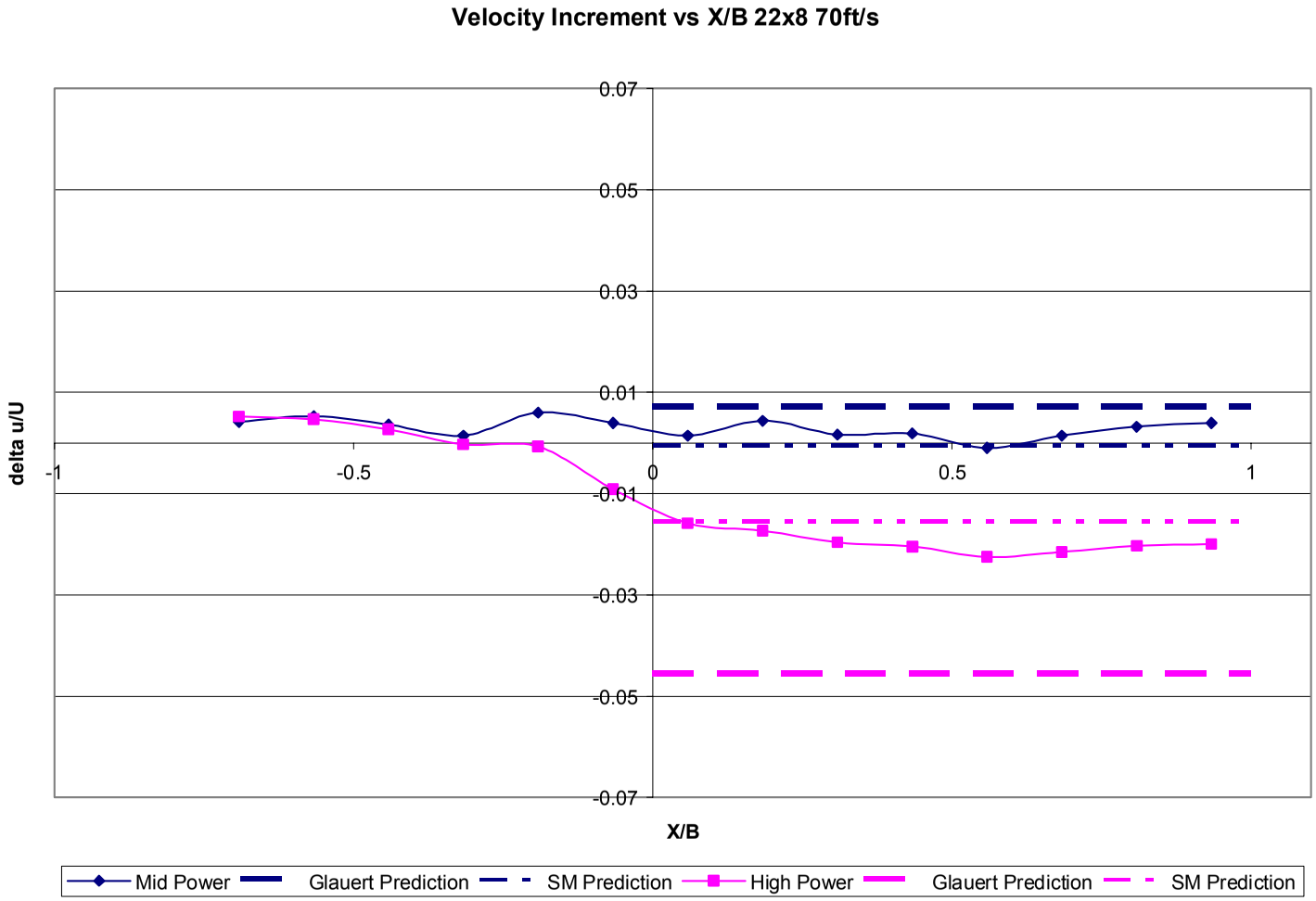

Predicted incremental velocity differentials plotted against velocity increments obtained from experimental data for the 22”x8” propeller and wind tunnel velocity of 70 ft/s.

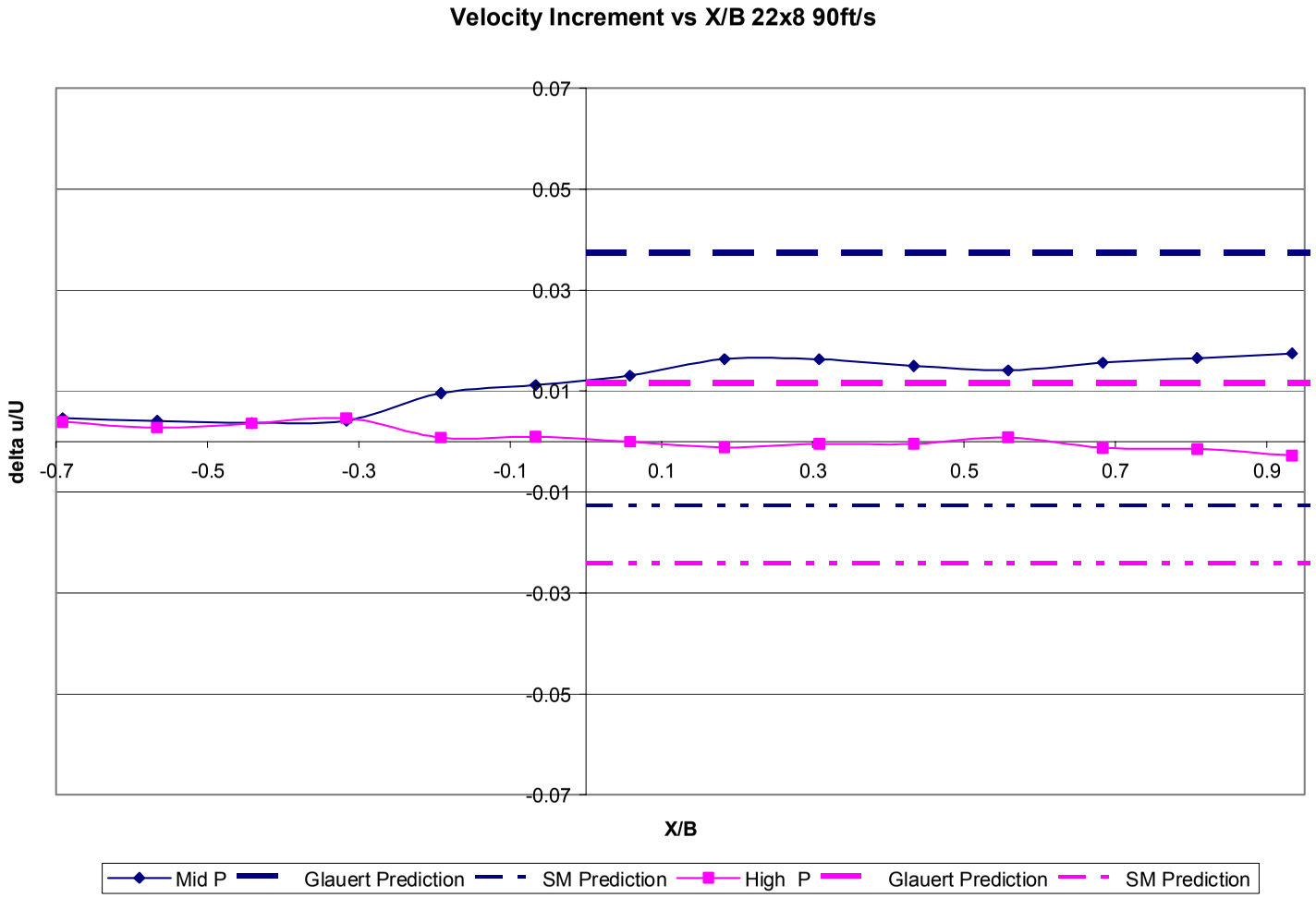

Predicted incremental velocity differentials plotted against velocity increments obtained from experimental data for the 22”x8” propeller and wind tunnel velocity of 90 ft/s.

					Sorensen			Glauert		
Velocity (ft/sec)	Power Setting (1=L, 2=M, 3H)	Density (psf)	Thrust (pounds)	Ct	Delta P (psf)	Delta Cp	Deltau/U	Delta P	Delta Cp	Deltau/U
120.1367	1	0.00229	-12.31	-0.23899	0.80576	0.04882	-0.02472	-0.86745	-0.09116	0.04459
120.0142	2	0.00229	-10.25	-0.19923	0.51634	0.03134	-0.01579	-0.89249	-0.07531	0.03697
90.7419	1	0.00228	-6.12	-0.20789	0.32519	0.03458	-0.01744	-0.88715	-0.07897	0.03874
59.0912	1	0.00229	-2.32	-0.18593	0.10620	0.02660	-0.01339	-0.90044	-0.07021	0.03451
89.9085	2	0.00229	-0.84	-0.02908	0.00495	0.00054	-0.00027	-0.98537	-0.01048	0.00523
60.3646	2	0.00229	1.65	0.126601	0.03251	0.00781	-0.00391	-1.06163	0.04343	-0.02196
60.6763	3	0.00229	6.94	0.528659	0.40604	0.09624	-0.04934	-1.24619	0.15563	-0.08111

Predicted pressure, coefficient of pressure, and velocity increment differentials as predicted by Sørensen and Mikkelsen and Glauert's methods for the 24"x8" propeller.

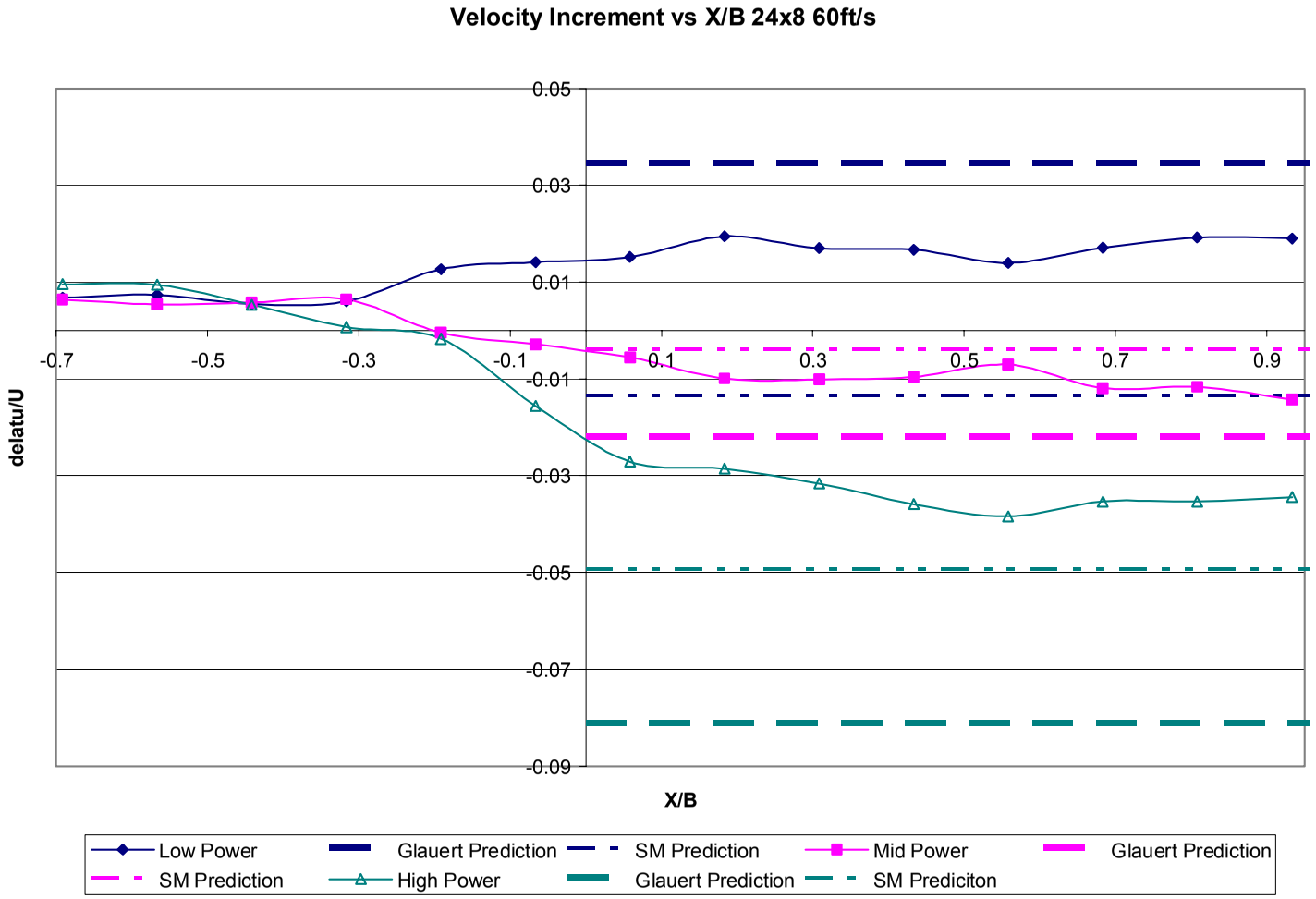

Predicted incremental velocity differentials plotted against velocity increments obtained from experimental data for the 24”x8” propeller and wind tunnel velocity of 60 ft/s.

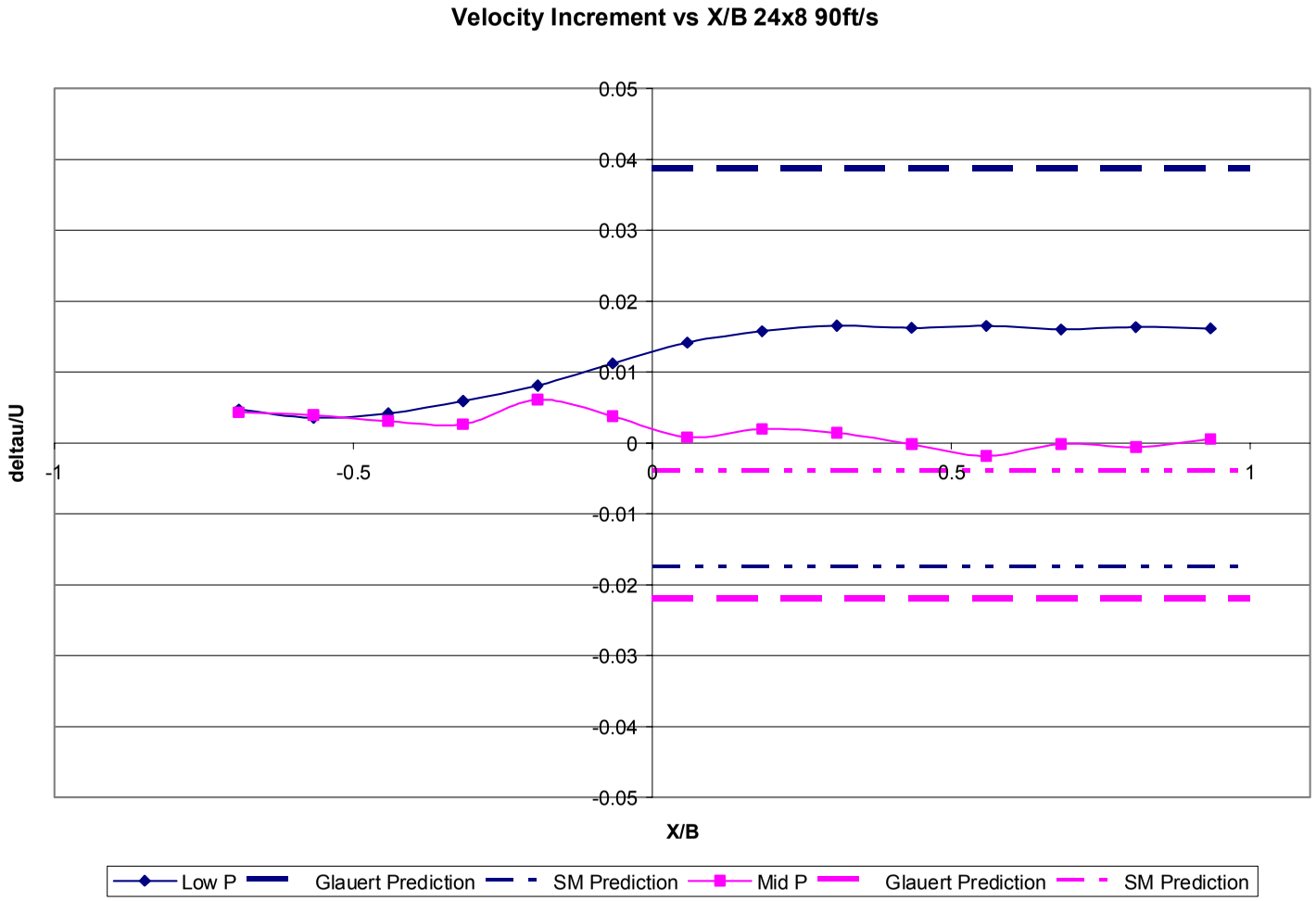

Predicted incremental velocity differentials plotted against velocity increments obtained from experimental data for the 24”x8” propeller and wind tunnel velocity of 90 ft/s.

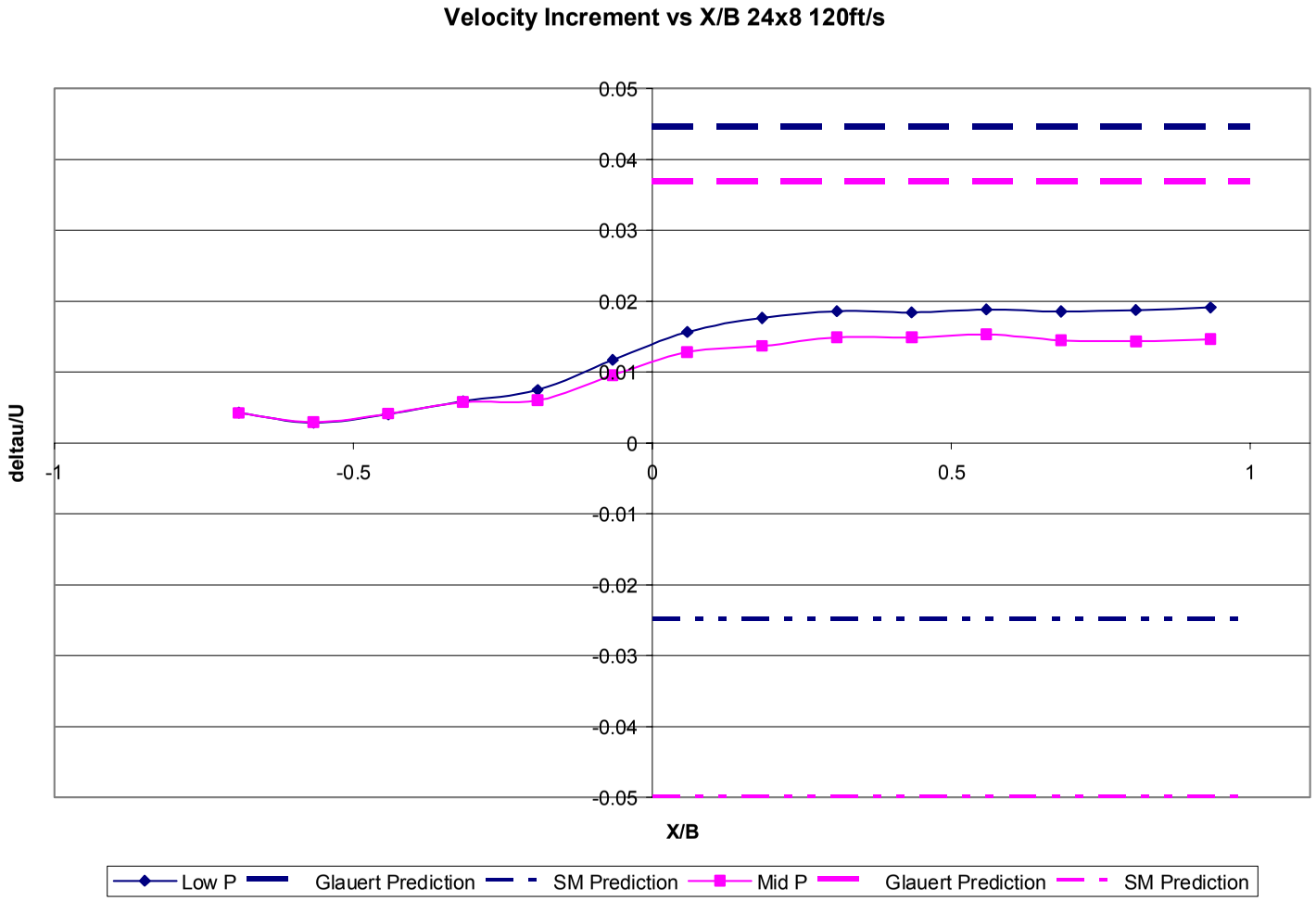

Predicted incremental velocity differentials plotted against velocity increments obtained from experimental data for the 24”x8” propeller and wind tunnel velocity of 120 ft/s.

APPENDIX C

Experimental Data				Glauert Correction			
Velocity (ft/sec)	Power Setting (1=L, 2=M, 3H)	Density (psf)	Thrust (pounds)	alpha	tau	Glauert Experimental	Glauert Theoretical
110.3070	2	0.002287	-7.38	0.0668	-0.2481	1.01168	1.01167361
109.8700	3	0.002288	-5.03	0.0668	-0.1704	1.00701	1.00700781
80.4289	2	0.002287	-2.18	0.0668	-0.1378	1.00541	1.0054068
50.0125	1	0.002284	-0.88	0.0668	-0.1441	1.00571	1.0057044
80.1783	3	0.002288	0.9	0.0668	0.0572	0.99819	0.99818908
49.9617	2	0.002286	2	0.0668	0.3279	0.99149	0.99148965
49.9712	3	0.002292	5.83	0.0668	0.9529	0.98133	0.98132976

Intermediate values and experimental and theoretical Glauert corrections for the 14”x8” propeller.

Experimental Data				Sorensen Correction								
Velocity (ft/sec)	Power Setting (1=L, 2=M, 3H)	Density (psf)	Thrust (pounds)	Ct	S1 (sq ft)	utilda	u	utilda1	u1 (ft/s)	utilda2	u2 (ft/s)	Sorensen Experimental
110.3070	2	0.002287	-7.38	-0.49617	1.28754	0.83342	91.93215	0.69197	76.32935	0.98742	108.91917	0.98226
109.8700	3	0.002288	-5.03	-0.34072	1.19280	0.89865	98.73425	0.80539	88.48783	0.99467	109.28445	0.99343
80.4289	2	0.002287	-2.18	-0.27568	1.16255	0.92124	74.09419	0.84712	68.13272	0.99664	49.84446	0.99605
50.0125	1	0.002284	-0.88	-0.28819	1.16804	0.91705	45.86414	0.83930	41.97569	0.99630	80.13157	0.99562
80.1783	3	0.002288	0.9	0.11448	1.04082	1.02740	82.37481	1.05523	84.60634	0.99951	80.13931	0.99954
49.9617	2	0.002286	2	0.65573	0.94990	1.13400	56.65640	1.27620	63.76094	0.98638	49.28124	0.98943
49.9712	3	0.002292	5.83	1.90573	0.84807	1.31018	65.47121	1.65151	82.52809	0.90651	45.29955	0.94654

Intermediate values and experimental and theoretical Sørensen and Mikkelsen corrections for the 14”x8” propeller.

Experimental Data				Hackett-Wilsden Correction				
Velocity (ft/sec)	Power Setting (1=L, 2=M, 3H)	Density (psf)	Thrust (pounds)	Ct	Sigma	bias	du (ft/sec)	Hackett-Wilsden Experimental
110.3070	2	0.00229	-7.38	-0.49617	0.008	0.005639	0.0136526500	1.00012377
109.8700	3	0.00229	-5.03	-0.34072	0.0039	0.003274	0.0071405820	1.000064991
80.4289	2	0.00229	-2.18	-0.27568	0.0054	0.004683	0.0101209640	1.000125837
50.0125	1	0.00228	-0.88	-0.28819	0.005	0.008	0.0130000000	1.000259935
80.1783	3	0.00229	0.9	0.11448	0.0117	-0.004537	0.0071714500	1.000089444
49.9617	2	0.00229	2	0.65573	0.0215	-0.0025	0.0190000000	1.000380291
49.9712	3	0.00229	5.83	1.90573	0.0475	-0.015	0.0325000000	1.000650374

Intermediate values and experimental Hackett-Wilsden corrections for the 14”x8” propeller.

Experimental Data				Glauert Correction			
Velocity (ft/sec)	Power Setting (1=L, 2=M, 3H)	Density (psf)	Thrust (pounds)	alpha	tau	Glauert Experimental	Glauert Theoretical
130.2705	1	0.002288	-11.07	0.1104	-0.1626	1.01093	1.01092742
129.9858	2	0.002284	-8.427	0.1104	-0.1633	1.01099	1.01098696
70.1400	1	0.002287	-2.93	0.1104	-0.1485	1.00978	1.0097783
50.9636	1	0.002287	-0.9104	0.1104	-0.0872	1.00530	1.00529929
70.2988	2	0.002288	2.246	0.1104	0.1132	0.99436	0.99435768
49.9574	2	0.002292	5.87	0.1104	0.5856	0.97805	0.97806188
70.2146	3	0.002286	7.112	0.1104	0.3582	0.98490	0.98490861
50.2740	3	0.00228	10.97	0.1104	1.1918	0.96400	0.96423543

Intermediate values and experimental and theoretical Glauert corrections for the 18”x8” propeller.

Experimental Data				Sorensen Correction								
Velocity (ft/sec)	Power Setting (1=L, 2=M, 3H)	Density (psf)	Thrust (pounds)	Ct	S1 (sq ft)	utilda	u	utilda1	u1 (ft/s)	utilda2	u2 (ft/s)	Sorensen Experimental
130.2705	1	0.002288	-11.07	-0.32281	1.95920	0.89617	116.74456	0.80832	112.03248	0.98925	129.50374	0.98690
129.9858	2	0.002284	-8.427	-0.24866	1.90293	0.92608	120.37715	0.86000	111.78773	0.99411	129.22074	0.99321
70.1400	1	0.002287	-2.93	-0.29694	1.93734	0.90779	63.67272	0.82804	58.07904	0.99126	69.52701	0.98957
50.9636	1	0.002287	-0.9104	-0.17445	1.85603	0.95113	48.47315	0.90558	46.15177	0.99726	50.82413	0.99699
70.2988	2	0.002288	2.246	0.22639	1.68143	1.05055	73.85270	1.10411	77.61732	0.99632	70.04022	0.99668
49.9574	2	0.002292	5.87	1.17111	1.48323	1.19547	59.72245	1.42430	71.15448	0.92603	46.26204	0.95056
70.2146	3	0.002286	7.112	0.71451	1.55837	1.13412	79.63161	1.28606	90.30001	0.96924	68.05506	0.99667
50.2740	3	0.00228	10.97	2.15922	1.38068	1.29987	65.34985	1.66372	0.78022	0.73599	37.00096	0.88460

Intermediate values and experimental and theoretical Sørensen and Mikkelsen corrections for the 18”x8” propeller.

Experimental Data				Hackett-Wilsden Correction				
Velocity (ft/sec)	Power Setting (1=L, 2=M, 3H)	Density (psf)	Thrust (pounds)	Ct	Sigma	bias	du (ft/sec)	Hackett-Wilsden Experimental
130.2705	1	0.00229	-11.07	-0.32281	0.01	0.008108	0.0181230000	1.000139118
129.9858	2	0.00228	-8.427	-0.24866	0.0061	0.003832	0.0099320000	1.000076408
70.1400	1	0.00229	-2.93	-0.29694	0.0105	0.0073	0.0178000000	1.000253778
50.9636	1	0.00229	-0.9104	-0.17445	0.005	0.017	0.0220000000	1.00043168
70.2988	2	0.00229	2.246	0.22639	-0.018	-0.00066	-0.0183600000	0.999738829
49.9574	2	0.00229	5.87	1.17111	-0.053	-0.0105	-0.0630000000	0.998738926
70.2146	3	0.00229	7.112	0.71451	-0.035	-0.01425	-0.0494500000	0.999295731
50.2740	3	0.00228	10.97	2.15922	-0.073	-0.01973	-0.0927300000	0.998155508

Intermediate values and experimental Hackett-Wilsden corrections for the 18”x8” propeller.

Experimental Data				Glauert Correction			
Velocity (ft/sec)	Power Setting (1=L, 2=M, 3H)	Density (psf)	Thrust (pounds)	alpha	tau	Glauert Experimental	Glauert Theoretical
89.9377	2	0.02278	-5.72	0.1650	-0.1176	1.01109	1.011093351
90.0118	3	0.002278	-1.83	0.1650	-0.0376	1.00322	1.003222085
50.1563	1	0.002278	-1.71	0.1650	-0.1130	1.01060	1.010600408
69.0532	2	0.002276	-0.68	0.1650	-0.0237	1.00201	1.00200637
50.4222	2	0.002278	3.18	0.1650	0.2080	0.98558	0.9855795
69.8033	3	0.002277	4.9	0.1650	0.1673	0.98805	0.988052275
50.3707	3	0.002279	9.46	0.1650	0.6198	0.96584	0.965833848

Intermediate values and experimental and theoretical Glauert corrections for the 22”x8” propeller.

Experimental Data				Sorensen Correction								
Velocity (ft/sec)	Power Setting (1=L, 2=M, 3H)	Density (psf)	Thrust (pounds)	Ct	S1 (sq ft)	utilda	u	utilda1	u1 (ft/s)	utilda2	u2 (ft/s)	Sorensen Experimental
89.9377	2	0.02278	-5.72	-0.23519	2.82917	0.92143	82.87130	0.85976	77.32464	0.98710	88.77776	0.98524
90.0118	3	0.002278	-1.83	-0.07512	2.69237	0.97972	88.18597	0.96059	86.46457	0.99893	89.91526	0.99888
50.1563	1	0.002278	-1.71	-0.22607	2.82026	0.92556	46.42286	0.86634	43.45265	0.98824	49.56667	0.98663
69.0532	2	0.002276	-0.68	-0.04747	2.67230	0.98756	68.19394	0.97555	67.36482	0.99958	69.02446	0.99957
50.4222	2	0.002278	3.18	0.41599	2.42911	1.07756	54.33288	1.17103	59.04568	0.97740	49.28255	0.98105
69.8033	3	0.002277	4.9	0.33461	2.46243	1.06528	74.36010	1.14202	79.71658	0.98468	68.73390	0.98675
50.3707	3	0.002279	9.46	1.23954	2.20189	1.16905	58.88510	1.40155	70.59717	0.85136	42.88354	0.90398

Intermediate values and experimental and theoretical Sørensen and Mikkelsen corrections for the 22”x8” propeller.

Experimental Data				Hackett-Wilsden Correction				
Velocity (ft/sec)	Power Setting (1=L, 2=M, 3H)	Density (psf)	Thrust (pounds)	Ct	Sigma	bias	du (ft/sec)	Hackett-Wilsden Experimental
89.9377	2	0.02278	-5.72	-0.49617	0.0134	0.010663	0.0240732000	1.000267665
90.0118	3	0.00228	-1.83	-0.34072	0.0061	0.002278	0.0083950000	1.000093266
50.1563	1	0.00228	-1.71	-0.27568	0.019	0.015	0.0340000000	1.000677881
69.0532	2	0.00228	-0.68	-0.28819	0.0061	0.003832	0.0099320000	1.000143831
69.8033	3	0.00228	4.9	0.11448	-0.029	-0.007438	-0.0363680000	0.999478993
50.4222	2	0.00228	3.18	0.65573	0.035	-0.0075	0.0275000000	1.000545395
50.3707	3	0.00228	9.46	1.90573	0.075	-0.025	0.0500000000	1.000992641

Intermediate values and experimental Hackett-Wilsden corrections for the 22”x8” propeller.

Experimental Data				Glauert Correction			
Velocity (ft/sec)	Power Setting (1=L, 2=M, 3H)	Density (psf)	Thrust (pounds)	alpha	tau	Glauert Experimental	Glauert Theoretical
120.1367	1	0.002272	-12.31	0.1963	-0.1195	1.01345	1.01344446
120.0142	2	0.002274	-10.25	0.1963	-0.09961	1.01093	1.010925816
90.7419	1	0.002276	-6.12	0.1963	-0.10395	1.01147	1.011463373
59.0912	1	0.002275	-2.32	0.1963	-0.0930	1.01012	1.010112757
89.9085	2	0.002275	-0.84	0.1963	-0.0145	1.00145	1.001448254
60.3646	2	0.002277	1.65	0.1963	0.0633	0.99415	0.994146553
60.6763	3	0.00227	6.94	0.1963	0.2643	0.97901	0.979016372

Intermediate values and experimental and theoretical Glauert corrections for the 24”x8” propeller.

Experimental Data				Sorensen Correction								
Velocity (ft/sec)	Power Setting (1=L, 2=M, 3H)	Density (psf)	Thrust (pounds)	Ct	S1 (sq ft)	utilda	u	utilda1	u1 (ft/s)	utilda2	u2 (ft/s)	Sorensen Experimental
120.1367	1	0.002272	-12.31	-0.23899	3.37143	0.90438	108.64959	0.84273	101.24280	0.97426	117.04441	0.97045
120.0142	2	0.002274	-10.25	-0.19923	3.32615	0.92821	111.39783	0.87670	105.21666	0.98378	118.06818	0.98186
90.7419	1	0.002276	-6.12	-0.20789	3.33573	0.92345	83.79580	0.86971	78.91889	0.98198	89.10676	0.97973
59.0912	1	0.002275	-2.32	-0.18593	3.31175	0.93509	55.25587	0.88705	52.41681	0.98630	58.28152	0.98480
89.9085	2	0.002275	-0.84	-0.02908	3.16494	0.99242	89.22687	0.98510	88.56857	0.99975	89.88576	0.99974
60.3646	2	0.002277	1.65	0.12660	3.05070	1.02712	62.00156	1.05772	63.84870	0.99608	60.12769	0.99630
60.6763	3	0.00227	6.94	0.52866	2.84127	1.08244	65.67852	1.19686	72.62080	0.95069	57.68418	0.96034

Intermediate values and experimental and theoretical Sørensen and Mikkelsen corrections for the 24”x8” propeller

Experimental Data				Hackett-Wilsden Correction				
Velocity (ft/sec)	Power Setting (1=L, 2=M, 3H)	Density (psf)	Thrust (pounds)	Ct	Sigma	bias	du (ft/sec)	Hackett-Wilsden Experimental
120.1367	1	0.00227	-12.31	-0.49617	0.0175	0.011	0.0285000000	1.00023723
120.0142	2	0.00227	-10.25	-0.34072	0.0135	0.009	0.0225000000	1.000187478
90.7419	1	0.00228	-6.12	-0.27568	0.014	0.01	0.0240000000	1.000264487
59.0912	1	0.00228	-2.32	-0.28819	0.0125	0.012	0.0245000000	1.000414613
89.9085	2	0.00228	-0.84	0.11448	0.005	0.002	0.0070000000	1.000077857
60.3646	2	0.00228	1.65	0.65573	0.02	-0.0025	0.0175000000	1.000289905
60.6763	3	0.00227	6.94	1.90573	0.05	-0.0135	0.0365000000	1.000601553

Intermediate values and experimental Hackett-Wilsden corrections for the 24”x8” propeller

REFERENCES

[1] Glauert, H., *The Elements of Aerofoil and Airscrew Theory*, Cambridge University Press, Cambridge, England, Second Edition, 1947.

[2] Barlow, J., Rae, W., Pope, A., *Low Speed Wind Tunnel Testing*, Jon Wiley & Sons, 1999.

[3] Maskell, E. C., "A Theory of Blockage Effects on Bluff Bodies and Stalled Wings in a Close Wind Tunnel," ARC R&M 3400, 1963.

[4] Ashill, P. R., and Keating, R. F. A., "Calculation of Tunnel Wall Interference from Wall Pressure Measurements," *Aeronaut. J.,* Jan. 1988.

[5] Hensel, R. W., "Rectangular Wind Tunnel Blocking Corrections Using the Velocity Ratio Method," NACA TN 2372, June 1951.

[6] Thom, A., "Blockage Corrections in a High Speed Wind Tunnel," ARC R&M 2033, 1943.

[7] Hackett J. E., Lilley, D. E., and Wilsden, D. J., "Estimation of Tunnel Blockage from Wall Pressure Signatures: A Review and Data Correlation" NASA CR 15,2241, March 1979.

[8] Mikkelsen, R., and Sørensen, J.N., "Modelling [sic] of Wind Tunnel Blockage," *Proceedings of the 2002 Global Windpower Conference and Exhibition* [CD-ROM], www.ewea.org.

[9] Stewart, V.R., "Naval Air Warfare Center, Warminster, PA Aerodynamic Test Facility Operation Instructions," *KSA Technology Report*, Columbus, OH, August 1996

[10] Parker, P. A., "NADC 3-Component Platform Balance Calibration Report," Sverdrup Technology, Inc., Newport News, VA., June 1992

[11] Katz J., and Plotkin A., *Low-Speed Aerodynamics: From Wing Theory to Panel Methods,* McGraw Hill, New York, 1991.